THERMAL RESPONSE OF PEDESTRIAN BRIDGE GIRDER SECTIONS UNDER FIRE EXPOSURE USING FINITE ELEMENT METHOD

BY

ORIAKHI, Sandra Omosigho

PG/ENG1403577

A PROJECT SUBMITTED IN PARTIAL FULFILMENT OF THE REQUIREMENS FOR THE AWARD OF MASTER OF ENGINEERING (M.Eng) DEGREE.

IN

THE DEPARTMENT OF CIVIL ENGINEERING, FACULTY OF ENGINEERING, UNIVERSITY OF BENIN, BENIN CITY, NIGERIA

DECEMBER, 2025

CERTIFICATION

This is to certify that this study was carried out by ORIAKHI, Sandra Omosigho, Mat. No PG/ ENG1403577, of the Department of Civil Engineering (Structural Engineering), Faculty of Engineering, University of Benin, in partial fulfilment of the requirement for the award of M.Eng. in Civil Engineering.

PROJECT SUPERVISIOR

Name: ENGR. PROF. O.R. OGIRIGBO

Signature: …… Date: …….

CO-PROJECT SUPERVISIOR

Name: ENGR. DR. I. INERHUNWA

Signature: …… Date: …….

HEAD OF DEPARTMENT

Name: ENGR. PROF. (MRS) N.I IHIMEKPEN

Signature: …… Date: …….

DEDICATION

I dedicate this work to God Almighty and my family for the enabling strength and courage to carry out this research.

ACKNOWLEDGEMENTS

I am deeply grateful to Almighty God for his wisdom and strength granted to me for consistency to completion of this research. I want to express my profound gratitude to my Supervisor, Engr. Prof. O.R. Ogirigbo, for his trust, support and direction he gave me to commence this research work and my Co-Supervisor, Engr. Dr. I. Inerhunwa for his detail scrutiny and undying encouragement in the course of this research work. I also want to extend my gratitude to the Head of Department; Engr. Prof. (Mrs) N.I Ihimekpen and the post graduate coordinators Engr. Prof. O.R. Ogirigbo and Engr. Dr. E.S. Okonofua. My gratitude also goes to all my lecturers; Engr. Prof. O.U. Orie, Engr. Prof. O.C. Izinyon, Engr. Prof. H. P. Audu, Engr. Prof. S.O. Osuji, Engr. Prof. R.I. Umasabor, Engr. Prof. (Mrs) N. Kayode-Ojo,Engr. Engr. Dr. A.I. Abonaye, Engr. Prof. S.D. Iyeke, Engr. Dr. R.I. Ilaboya, Engr. Dr. (Mrs) A. Rawlings, Engr. Dr. U. Ukeme, Engr. O. Oriakhi, Engr. B. E. Omosefe, Engr. N.K. Oghoyafedo, Engr. Dr. S.A. Adegbemileke, Engr. A. Musa, Engr. O. Osasu, Engr. E. Ambrose-Agabi, Engr. C.M. Okolie, Engr. Dr. P.N. Ogbeifun, Engr. Dr. L.O. Bobor, Engr. E.E. Oria-Usifo; of this great department who has been of great support during the course of this program.

My sincere thanks goes to my husband, Engr. O. Oriakhi for his guidance and support, whom in spite of all circumstances still believes in me and never get tired encouraging me to keep fighting until success is attained. And also, my children, for their patience and understanding in the course of this program. My thanks also go to my parents and siblings for their encouragement and support and also to all my course mate for their support.

ABSTRACT

Pedestrian bridges are essential components of urban transportation systems, yet their structural safety is significantly threatened when exposed to fire hazards. Recent incidents and limited available research on the fire performance of pedestrian bridge girders have highlighted the need for systematic research into their thermal response and post-fire behavior. This study was therefore conducted to examine the temperature distribution, degradation patterns, and fire endurance of three common girder types; steel I-beams, concrete I-beams, and concrete rectangular sections; together with a real-world evaluation of the composite girder used in the University of Benin pedestrian bridge. The overall aim was to understand how these girder systems behave under fire exposure.

A finite element modelling (FEM) framework was developed using Abaqus CAE, employing transient thermal analysis under the ISO 834 standard fire curve. Temperature-dependent material properties were defined according to Eurocode 2 and 3 provisions, and 2D thermal models of each girder section were created for computational efficiency. Boundary conditions included convection and radiation on fire-exposed surfaces, with analysis conducted at 1200 s, 2400 s, and 3600 s to capture progressive heat penetration. For the University of Benin case study, a composite girder was modelled to evaluate real structural behavior under elevated temperatures, focusing on heat migration, cracking zones, and the thermal protection offered by the concrete slab.

Results showed that steel I-beams heated rapidly and reached critical temperatures earliest due to high thermal conductivity, resulting in rapid loss of stiffness and structural stability. Concrete I-beams demonstrated moderate resistance, while rectangular concrete beams performed best, maintaining a cool core even at long exposure times. The composite girder exhibited heat concentration along its underside, with spalling and reinforcement weakening in exposed regions but retained strength in upper concrete zones.

TABLE OF CONTENTS

LIST OF TABLE

LIST OF FIGURE

CHAPTER ONE

INTRODUCTION

1.1 Background of the Study

Bridges are critical components of infrastructure, playing a pivotal role in facilitating transportation and connecting communities. They are essential for economic development, trade, and social integration. While bridges are vital for infrastructure and economic development, they are susceptible to fire incidents that can jeopardize their safety and longevity. Fire incidents pose a significant threat to the safety and longevity of bridges. Fires on bridges can occur due to various reasons, including accidents, arson, or natural disasters like wildfires (Abdulrahman & Kadir, 2022). The impact of fire on bridges depends on factors such as bridge design, materials used in construction, and the intensity of the fire. Fire can weaken structural components of bridges, such as steel beams and concrete decks (Bolina *et al*., 2021). High temperatures can cause steel to lose its strength and concrete to spall, crack, or even explode due to trapped moisture. This compromises the structural integrity of the bridge, increasing the risk of collapse. Proactive measures and investments in fire prevention, mitigation, and emergency preparedness are crucial in safeguarding bridges and ensuring the resilience of transportation networks. Bridge structural fire resistance can broadly be defined as the "ability of a bridge to fulfill its designed function for a period of time in the event of a fire" (Asadi *et al*., 2018).

One of the most complex and hence poorly understood behavioral characteristics in the reaction of concrete to high temperatures or fire is the phenomenon of 'explosive spalling' (Amran *et al*., 2022). The process of spalling is observed to start in the early stages of a fire with temperatures as low as 200˚C and can progress to high temperature of 1000˚C (Jincheng *et al*., 2018). If severe, spalling can have a deleterious effect on the strength of reinforced concrete structures, due to enhanced heating of the steel reinforcement. Spalling

may significantly reduce or even eliminate the layer of concrete cover on the reinforcement bars, thereby exposing the reinforcement to high temperatures, leading to a reduction of strength of the steel and hence a deterioration of the mechanical properties of the bridge structure as a whole (So, 2016). The residual condition of bridge structures after fire is mainly concerned with the strength and serviceability, as well as the long-term health of the structure.

Traditional post-fire assessment methods often involve visual inspections and manual calculations, which can be time-consuming, imprecise, and may not fully capture the extent of internal damage. When direct assessment is not possible, indirect assessment methods such as finite element modeling (FEM) may be used (Lourenço & Gaetani, 2022). Finite Element Modelling (FEM) presents a promising solution. FEM allows for a detailed and accurate simulation of the thermal and structural response of bridge components under fire conditions. By incorporating the non-linear behavior of materials at high temperatures and the interactions between different structural elements, FEM can provide comprehensive insights into potential failure mechanisms and inform the development of effective fire protection and mitigation strategies, as well as tailored remediation measures after a fire incident (Bernardi *et al*., 2020). FEM can simulate various fire scenarios and assess their impact on bridge integrity, helping engineers to predict possible points of failure and evaluate the effectiveness of different fire-resistant materials and designs. This advanced modeling technique can also aid in optimizing emergency response plans and improving the resilience of bridges to fire hazards (Gidaris *et al*., 2017).

1.2 Statement of the Problem

Bridges are critical components of transportation infrastructure, essential for the movement of people and goods. However, their exposure to fire poses significant risks, potentially leading

to severe structural damage, safety hazards, and economic losses. Instances of bridge failures due to fire hazards have been documented in various studies.

In Nigeria, several fire incidents have highlighted the vulnerability of bridges to hazards associated with flammable materials. Notable cases include the June 2018 Otedola Bridge fire in Lagos, caused by a fuel tanker explosion, which killed many people, destroyed 67 vehicles, and extensively damaged the bridge structure (Vanguard News Article, 2018). Similarly, in August 2018, a van fire on the Niger Third Mainland Bridge caused bridge deck damage (Punch News Article, 2018). In November 2020, a petrol tanker explosion on Kara Bridge, Lagos-Ibadan Expressway, caused significant structural damage, a temporary closure, severe traffic congestion, and two deaths (Punch News Article, 2020). Most recently, on May 25, 2024, a fuel tanker fire at the Ibafo/Aseese axis of the Lagos-Ibadan Expressway resulted in prolonged traffic delays and necessitated structural repairs (Punch News Article, 2024). These incidents underscore the need for stricter regulations and improved safety measures for transporting flammable materials on bridges.

These incidents in Nigeria echo global cases, such as the New Little Belt Suspension Bridge in Denmark experienced a serious truck fire in 2013, leading to rapidly rising flame temperatures above 1000 °C and necessitating fire protection measures for the main cables (Jensen *et al*., 2021). Additionally, research on steel bridges indicates that tanker fires underneath bridges can cause critical buckling stress, potentially resulting in buckling instability and failure of the bridge structure (Son *et al*., 2022). Moreover, studies on long-span cable-supported bridges highlight the significant impact of fire hazards on bridge hangers, with the failure of cables or hangers due to fire posing a risk of progressive structural failure (Zou *et al*., 2020).

Finite Element Modelling (FEM) greatly improves the efficiency of thermal assessments by enabling rapid evaluation of temperature distribution, heat penetration, and thermal gradients

in bridge girders exposed to fire. This faster analysis supports timely engineering decisions on safety measures and reduces delays in reopening critical pedestrian routes. In addition, FEM allows the simulation of multiple fire scenarios and heating conditions, offering detailed insight into how different temperature profiles affect steel and concrete components. Such thermal simulations are essential for identifying vulnerable regions, improving fire-resistant design choices, and developing appropriate protection strategies for various girder configurations.

1.3 Aim and Objectives of the Study

The aim of this study was to evaluate the thermal response of different pedestrian bridge girder sections when exposed to fire using Finite Element Modelling.

The objectives include:

I To develop and validate finite element thermal models capable of simulating temperature distribution, heat penetration, and thermal gradients in three girder sections (steel I-beam, concrete rectangular beam, and concrete I-beam).

II Comparative assessment of the post-fire condition of the three bridge girder sections (section type, and material type).

III Application to a case study to investigate the thermal behavior of the University of Benin pedestrian overhead bridge.

IV Provide recommendations for retrofitting techniques based on results of parametric study.

1.4 Scope of the Study

The scope of this study was restricted to examining how bridge girder sections respond to fire through thermal modeling using finite element analysis. The investigation concentrated exclusively on predicting temperature distribution, thermal gradients, and heating behavior within three girder sections exposed to elevated temperatures. Structural, mechanical, and

thermo-mechanical analyses were excluded to focus solely on thermal behavior, enabling clear evaluation of heat transfer without the influence of stress or deformation effects.

A review of existing literature was first conducted to understand how steel and concrete behave when subjected to high temperatures. Particular attention was given to temperature-dependent properties, heat transfer mechanisms, and degradation processes, including concrete spalling and changes in conductivity at elevated temperatures. This informed the development of three finite element thermal models; steel I-beam, concrete rectangular beam, and concrete I-beam, constructed using ABAQUS/CAE (Version 2017). The modelling phase involved defining each section's geometry, assigning appropriate thermal properties, specifying boundary conditions, applying fire exposure, and generating a mesh suitable for heat-transfer simulations.

A thermal parametric study was then performed to assess how variations in section geometry and material influence heat penetration during fire exposure. The simulations for different heating durations enabled a direct comparison of temperature profiles, thermal gradients, and heating rates across the three girder types. Although the analysis did not include structural response, the thermal outputs were interpreted to identify areas susceptible to weakening and potential material degradation. These insights offer a preliminary foundation for post-fire assessment and can guide future structural evaluation or rehabilitation strategies.

1.5 Justification of the Study

This study focuses on the application of Finite Element Modelling (FEM) for the post-fire assessment of bridge girders, a method that promises to enhance our ability to understand, evaluate, and mitigate fire-induced damage.

Traditional post-fire assessment methods such as visual inspection and manual estimation often provide only superficial information. They identify surface-level damage but fail to capture internal temperature rise, heat penetration patterns, and concealed thermal

degradation that occur within bridge beams during fire events. Such limitations can result in underestimating the severity of fire damage and may compromise the accuracy of subsequent structural evaluations.

Conventional assessment approaches also lack the capacity to simulate different fire exposure conditions or evaluate how various girder shapes respond to heating. As a result, important factors such as thermal gradients, hot-zone formation, and heat storage within different beam geometries are often overlooked. These thermal parameters are critical because they directly influence material degradation, spalling risk, and the residual capacity of bridge elements after a fire.

Finite Element Modelling (FEM), particularly thermal heat-transfer analysis, provides a more comprehensive and quantitative method for evaluating temperature development within bridge components. By incorporating temperature-dependent thermal properties and realistic fire boundary conditions, FEM enables the prediction of temperature distribution and heat flow patterns that cannot be measured through visual inspection alone. This analytical capability allows engineers to better understand how different beam geometries; such as steel I-beams, concrete I-beams, and concrete rectangular beams; respond to fire.

The use of thermal FEM also improves assessment efficiency. It allows for faster and more accurate thermal evaluation of fire-exposed bridge elements, supporting quicker decision-making on whether further structural assessment, repair, or replacement is required. Ultimately, this strengthens post-fire management, helps prevent unnecessary delays in reopening bridges, and enhances the overall safety and resilience of bridge infrastructure.

CHAPTER TWO

LITERATURE REVIEW

2.1 Assessment of Bridge Structures

Post-fire assessment of bridge structures is of paramount importance due to the critical role bridges play in transportation networks and public safety. Fires can inflict severe damage on bridge materials and structural components, compromising their integrity and functionality (Buchanan & Abu, 2017). The assessment ensures that any bridge exposed to fire is thoroughly evaluated for safety, serviceability, and necessary repairs, which is crucial for preventing catastrophic failures and ensuring the continuous flow of traffic and commerce. Bridges serve as vital links in transportation networks, enabling the movement of people, goods, and services (Rodrigue, 2020), and also, foot bridges makes it easier for people to commute from one end of the road to the other end of the road safely as shown in Figure 2.1. Any disruption in these links can have significant economic and social impacts. Fires, whether caused by accidents, natural events, or deliberate actions, can weaken structural elements, leading to potential collapses or reduced load-carrying capacity. Without a proper post-fire assessment, damaged bridges could remain in use, posing significant risks to public safety. The assessment process helps identify compromised components, recommend tailored repair measures and ensures that only safe structures remain operational.

Figure 2.1: Pedestrian Bridge (Rodrigue, 2020).

Materials commonly used in bridge construction, such as steel and concrete, behave differently under high temperatures. Steel may lose its strength and stiffness, while concrete can experience spalling and cracking, further reducing its load-bearing capacity (Aksoylu *et al*., 2022). The extent of this damage is often not visible to the naked eye and requires detailed investigation. Post-fire assessments typically involve a combination of visual inspections, non-destructive testing, and, increasingly, advanced computational methods like finite element modelling (FEM). These techniques allow engineers to understand the extent of the damage and the residual strength of the materials, providing a basis for informed decision-making regarding the bridge's future use (Pipinato *et al*., 2019). Another critical aspect of post-fire assessment is determining the repair strategies needed to restore the bridge to its original or acceptable condition (Nicoletta *et al*., 2020). Repairing fire-damaged structures can be complex and costly, involving the replacement of damaged components, strengthening of weakened areas, and sometimes, full or partial reconstruction. A thorough assessment provides the necessary data to develop effective and economical repair plans, ensuring that resources are used efficiently and the bridge can be returned to service as quickly as possible (Bocchini *et al*., 2014).

The importance of post-fire assessment also extends to long-term maintenance and monitoring. Fire damage can have lasting effects on the durability and fatigue life of bridge materials, potentially leading to premature failures if not properly addressed. By understanding the extent of the damage and the long-term implications, engineers can develop maintenance plans that include regular monitoring and inspections to detect any further deterioration early and take appropriate actions to mitigate risks (Frangopol & Soliman, 2019).

2.2 Overview of Bridge Fire Incidents

Bridge fire incidents, can have devastating consequences on infrastructure, traffic flow, and public safety. They highlight the vulnerabilities in our transportation network and the need for robust safety measures and rapid response strategies. Table 2.1 highlights but a few different bridge incidences that have occurred over the years, Nigeria inclusive and this contains details of the cause of the fire on the bridge, the type of materials used on the bridge, a description of the damage made, and the level of such damage to the bridge.

Table 2.1: Details of Bridges Exposed to Fire

Bridge/ Location	Date	Cause of Fire	Bridge Construction	Damage Description	Bridge Damage Level	Reference
Charilaos Trikoupis (Rio-Antirrio) Bridge, Greece	January 28, 2005	The cause of the fire is not ascertained, but it is believed that it could have been caused by a lightning	Cable-stayed bridge with a composite deck	One of cable caught fire and collapse, damaging the adjacent cable and crushing onto the deck	3	(Giuliani *et al*., 2012)
Bridge over the I-75 highway near Hazel Park, MI, USA	July 15, 2009	A gasoline tanker truck struck an overpass on the I-75	Composite deck (steel girders + reinforced concrete slab)	Complete collapse of the bridge which fell on the freeway below	5	(Mostafaei *et al*., 2014)
Highway 57, Dormagen, Germany	February 14, 2012	Plastic stored under the bridge	Concrete slab deck	Generalized spalling in a section of the	4	(Peris-Sayol *et al*., 2017)

Bridge/ Location	Date	Cause of Fire	Bridge Construction	Damage Description	Bridge Damage Level	Reference
		caught fire		structure. The bridge was demolished		
Pont Mathilde, Rouen, France	October 29, 2012	A tanker overturned and caught fire on the bridge. The fuel spill reached some trucks parked under the bridge that also caught fire	Steel deck with I-girders	Severe deformation of the girder in the section close to the fire. A section of the bridge had to be demolished	5	(Godart *et al*., 2015)
Ed Koch Queensboro Bridge, NY, USA	August 16, 2013	A 12-m tractor-trailer traveling on the outbound lower level of the bridge caught fire	Five-span cantilever truss bridge	Two stringers of the upper deck were severely deformed and damaged.	2	(Gong *et al*., 2015)
Overpass in El Cairo, Egypt	February 11, 2014	Gas cylinders in the shanty town underneath	Composite deck (steel girders + reinforced concrete slab)	One of the steel columns collapsed due to the high temperature.	5	(Peris-Sayol *et al*., 2017)

Bridge/ Location	Date	Cause of Fire	Bridge Construction	Damage Description	Bridge Damage Level	Reference
		exploded	supported by steel columns	Three sections of the bridge completely collapsed.		
Delta Steel Company Bridge, Warri, Nigeria	October 5, 2015	Spill and ignition of petroleum products	Steel bridge	Substantial damage to the steel structure of the bridge, compromising its load-bearing capacity and overall structural integrity.	4	(Ede *et al*., 2019)
Otedola Bridge, Lagos, Nigeria	June 29, 2018	Explosion of a petrol-laden tanker truck	Concrete and steel	Severe damage of the bridge's structural components, including significant heat-induced damage to the concrete and steel reinforcement.	4	(Punch News Article, 2018)
High Level Bridge, Edmonton, Alberta, Canada	August 24, 2019	A homeless encampment that accidentally ignited	Steel truss bridge with concrete piers	Damage to the protective paint coating on the steel components,	3	(Sharma *et al*., 2024)

Bridge/ Location	Date	Cause of Fire	Bridge Construction	Damage Description	Bridge Damage Level	Reference
		underneath the bridge		compromising of steel properties, damage to the electrical and lighting systems installed on the bridge.		
Ijora Bridge, Lagos, Nigeria	October 13, 2023	Overturning and ignition of a petrol tanker	Concrete and steel	Damage to both the concrete and steel reinforcements of the bridge. The high temperatures resulted in spalling of concrete and weakening of steel components	4	(Vanguard News Article, 2023)
Ibafo/Aseese axis of the Lagos-Ibadan Expressway, Nigeria	May 25, 2024	Fuel tanker truck overturned and ignited	Concrete and steel	Damage of bridge and underlying steel reinforcements. The heat led to cracks in the	3	(Punch News Article, 2024).

Bridge/ Location	Date	Cause of Fire	Bridge Construction	Damage Description	Bridge Damage Level	Reference
				concrete and loss of strength in the steel.		
Where: 1 = Manageable; 2 = Concerning; 3 = Serious; 4 = Severe; 5 = Catastrophic						

Figure 2.2 displays the number of bridge fire incidents over the years, revealing trends and patterns in their frequency and these data are shown in APPENDIX A. This data obtained from different source can help identify periods with higher occurrences, potentially linked to specific factors such as changes in traffic volume, maintenance practices, or environmental conditions. Together, these figures emphasize the critical need for ongoing research, preventive measures, and improved fire-resistant designs to enhance the safety and resilience of bridge infrastructure worldwide.

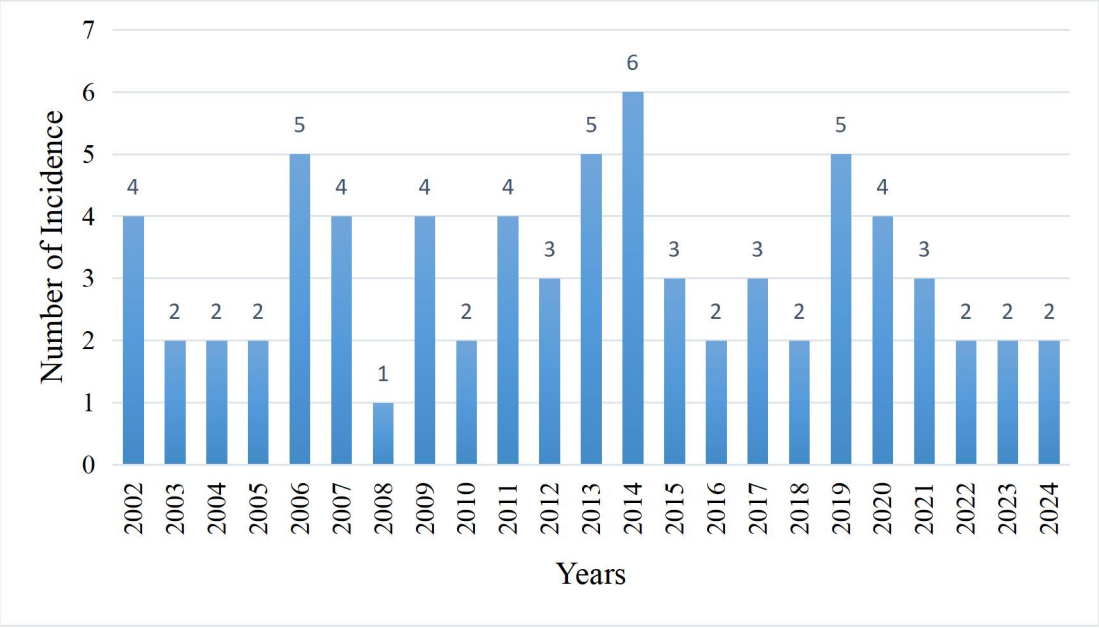

Figure 2.2: Number of Bridge Fire Incidence Over the Years

A study conducted by (Peris-Sayol *et al*., 2017) shows the percentage of different types of bridges which have been exposed to fire and this is given in Figure 2.3

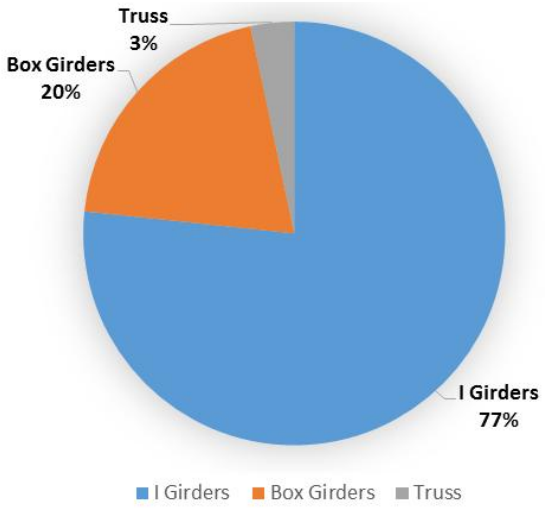

Figure 2.3: Percentage of Bridge Types Exposed to Fire (Peris-Sayol *et al*., 2017).

2.3 Material Behavior at Elevated Temperatures

Structural materials such as concrete and steel, when exposed to fire, undergo significant changes in their physical and mechanical properties. These changes can lead to severe structural damage, compromising the safety and functionality of bridge structure. Understanding the specific effects of fire on common structural materials for bridge construction such as reinforced concrete, steel, and plain concrete is essential for designing fire-resistant structures and for post-fire assessment and rehabilitation.

2.3.1 Reinforced Concrete

Reinforced concrete, composed of concrete and steel reinforcement, exhibits complex behavior under fire conditions due to the differing thermal properties of its constituents. The type of aggregate in the concrete, such as siliceous or calcareous, significantly affects its performance in fire. Siliceous aggregates, composed of materials like quartz, tend to experience a more pronounced reduction in strength at high temperatures compared to calcareous aggregates, which are primarily limestone-based. This difference is crucial because it influences the overall fire resistance of the concrete. Figure 2.4 illustrates the reduction in compressive strength of concrete at elevated temperature, as outlined in the European standard (Beeby *et al*., 2005). This figure, aids in understanding how different

aggregates affect the degradation rate of concrete under fire, impacting its structural integrity and load-bearing capacity.

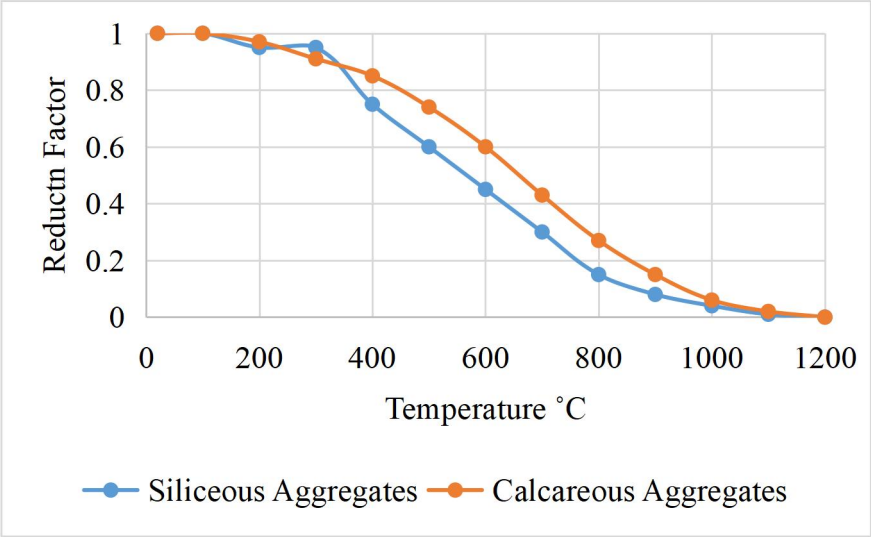

Figure 2.4: Reduction of Strength of Reinforced Concrete with High Temperature (Beeby *et al.*, 2005).

Concrete undergoes spalling, thermal expansion, and a reduction in strength when exposed to fire. Spalling reduces the effective cross-sectional area and exposes inner layers to direct fire, accelerating degradation (Amran *et al.*, 2022). Steel reinforcement loses strength and stiffness, experiences thermal expansion, and may undergo yielding or buckling when it is exposed to fire. The loss of yield strength can lead to the inability of the reinforcement to carry design loads, potentially leading to structural collapse (Memon *et al.*, 2019). The following subsections gives explanation of the behavior of concrete exposed to fire;

I. Thermal Expansion and Spalling:

Like reinforced concrete, plain concrete experiences thermal expansion when exposed to high temperatures. This can lead to spalling, where the surface layers of concrete break off due to the buildup of steam pressure within the pores. Spalling can significantly reduce the structural capacity and durability of concrete elements (Miah, 2017).

II. Strength Degradation:

The compressive strength of concrete diminishes with rising temperature. Up to 300˚C, concrete retains most of its strength, but beyond this point, strength degradation becomes significant. By 600˚C, concrete can lose up to 50% of its original strength, severely compromising its load-bearing capability (Memon *et al*., 2019).

III. Thermal Cracking:

Differential thermal expansion within the concrete can cause cracking, which compromises structural integrity. Cracks provide pathways for fire and heat to penetrate deeper into the concrete, exacerbating internal damage and potentially leading to structural failure (Golewski, 2023).

2.3.2 Steel

Steel structures are highly susceptible to fire due to steel's inherent properties, which change dramatically at increasing temperatures. According to the European standard (Beeby *et al*., 2005), Figure 2.5 shows the reduction of strength of steel under high temperature. This stress-strain relationship is defined by three parameters which includes; the proportional limit ($f_{sp,\Theta}$) , the maximum stress level ($f_{sy,\Theta}$), and, the slope of the linear elastic range ($E_{s,\Theta}$).

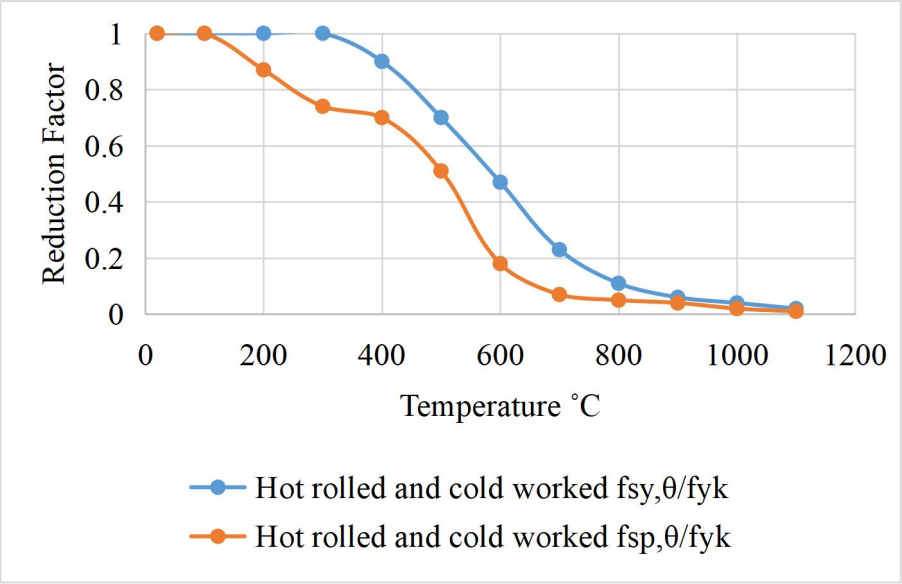

Figure 2.5: Reduction of Strength of Steel with High Temperature (Beeby *Et Al*., 2005).

Steel reinforcement loses strength and stiffness, experiences thermal expansion, and may undergo yielding or buckling when it is exposed to fire. The following subsections gives explanation of the behavior of steel exposed to fire;

I. Thermal Conductivity and Expansion:

Steel's high thermal conductivity means it heats up quickly when exposed to fire. Rapid heating can cause significant thermal expansion, leading to buckling and deformation of steel members. This expansion can also induce additional stresses in the structure, especially in restrained elements (Abambres *et al*., 2016).

II. Loss of Mechanical Properties:

The mechanical properties of steel degrade significantly at elevated temperatures. For example, at around 600˚C, structural steel retains only about 50% of its yield strength. Beyond 800˚C, it may retain as little as 10-20% of its original strength. This drastic reduction in strength and stiffness can result in large deflections, instability, and even collapse under load (Hamad *et al*., 2017).

III. Failure of Connections:

The connections (such as welds, bolts, and rivets) in steel structures can also be adversely affected by high temperatures, leading to partial or complete structural failure. Fire protection measures like intumescent coatings, spray-applied fire-resistive materials, and concrete encasement are often used to insulate steel from extreme heat, delaying the loss of strength and providing critical time for evacuation and firefighting (Hamad *et al*., 2017).

2.4 Bridge Girders at Elevated Temperature

Bridge girders are critical load-bearing components that span the length between bridge piers, transferring vehicular and structural loads to the substructure. Depending on design needs and site-specific factors, they are constructed from steel, reinforced concrete, pre-stressed concrete, or a composite of steel and concrete. Exposure to elevated temperatures particularly

during fire events can cause severe degradation of girder performance, leading to permanent deformation, strength loss, and potential collapse.

2.4.1 Steel Bridge Girders

Steel bridge girders, while known for their high strength-to-weight ratio and ductility, are particularly vulnerable to high-temperature exposure. At temperatures above 400˚C, steel begins to lose both its yield strength and modulus of elasticity. For example, experimental findings show that the yield strength of structural steel can reduce to about 50% at 600˚C and may drop to as low as 10–20% at 800˚C, rendering the steel ineffective in carrying design loads (Kodur *et al*., 2013). Figure 2.6 shows a graphical view of a steel bridge.

Figure 2.6: Steel Bridges (Kodur *et al*., 2013).

Fire scenarios involving hydrocarbon fuels, such as tanker truck accidents, can raise the temperature around bridge girders to over 1000˚C within minutes. During such incidents, the unprotected sections of steel girders, especially the bottom flange and web, heat up rapidly due to their slender geometry and exposure to direct flame. This leads to thermal gradients across the girder depth, which in turn results in thermal bowing a deformation mechanism where uneven expansion induces curvature and lateral movement even before mechanical degradation sets in (Zhang *et al*., 2024). The rapid deflection and loss of stiffness may cause local buckling, particularly in the web, and may lead to full collapse in as little as 15–30 minutes if fire protection is not present (Zhou, & Peng, 2024).

Recent advances in computational fluid dynamics (CFD) and finite element modeling have enabled more accurate simulations of how steel girders behave under fire loading. For instance, integrated fire-structure models have demonstrated that the highest stress concentrations develop at the mid-span and support regions, with fireproofing insulation playing a crucial role in delaying temperature rise and structural deterioration (Yu *et al*., 2021).

2.4.2 Composite Steel–Concrete Girders

Composite girders, which combine the compressive strength of concrete with the tensile efficiency of steel, are commonly used in modern bridge design due to their enhanced load distribution and fire resistance as seen in Figure 2.7. Under elevated temperatures, the thermal insulation provided by the concrete deck helps delay the temperature increase in the top flange of the steel beam. However, the web and bottom flange often less protected remain susceptible to rapid heating, leading to differential expansion within the girder (Kodur *et al*., 2013).

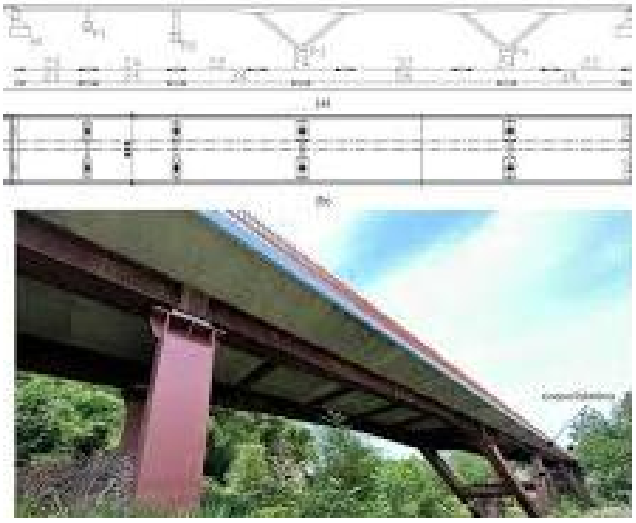

Figure 2.7: Composite Steel–Concrete Girders (Zhang *et al*., 2024).

The response of composite girders to fire is largely governed by the interface between steel and concrete. As heat penetrates the girder, the bond strength between these materials begins to deteriorate. Cracks form in the concrete slab due to thermal stress, and once the bond is

sufficiently compromised, composite action is lost, and the steel section begins to behave independently, hastening failure (Zhang et al., 2024). In computational models, deflections in composite girders increase dramatically after about 20 minutes of fire exposure, and global collapse is typically observed within 30–40 minutes in the absence of passive fire protection (Zhou, & Peng, 2024).

2.4.3 Reinforced and Pre-Stressed Concrete Girders

Concrete girders both reinforced and pre-stressed exhibit complex behavior under elevated temperatures. While concrete has a higher initial fire resistance than steel due to its low thermal conductivity, it suffers from internal micro-cracking, loss of strength, and a phenomenon known as spalling. Spalling occurs when pore pressure builds up inside the concrete as water vaporizes under heat, leading to explosive surface loss. This drastically reduces the effective cross-section and protective cover for embedded steel reinforcement or tendons (Gil, 2024).

The mechanical properties of concrete degrade with increasing temperature. Research has shown that compressive strength may reduce by up to 55% at 600˚C, and by more than 80% at 800˚C. Additionally, the bond between steel rebar's and the surrounding concrete weakens, compromising the girder's ability to sustain shear and bending loads (Babalola *et al*., 2021). Pre-stressed concrete girders are particularly vulnerable because the loss of pre-stress force either through tendon relaxation or rupture can result in sudden failure. Tendons located near the bottom of the section heat up quickly, especially in fire events that occur underneath the bridge, such as tanker truck fires.

Figure 2.8: Reinforced and Pre-Stressed Concrete Girders (Zhou, & Peng, 2024)

In segmental pre-stressed girders as seen in Figure 2.8, the joints between segments are another critical point of failure. Differential thermal expansion across segments can cause joint opening and eventual separation, as shown in numerical studies simulating standard fire curve and hydrocarbon fire curves (Zhou, & Peng, 2024). Despite being initially more fire-resistant than steel girders, concrete girders ultimately suffer from irreversible damage that necessitates extensive rehabilitation or replacement.

2.4.4 Long-Span Bridge Girders (Suspension and Cable-Stayed Systems)

Long-span bridges often utilize steel box girders or orthotropic decks supported by suspension cables or stay cables as seen in Figure 2.9. These girders, due to their slender sections and surface area, are highly sensitive to fire loading. For example, the Wuhan Yangtze River Bridge experienced a simulated tanker truck fire scenario where local temperatures at the girder soffit exceeded 1000˚C, causing serious strength reduction and distortion (Yu *et al*., 2021).

Figure 2.9: Suspension and Cable-Stayed (Liu et al., 2023)

Unlike typical girder failures, long-span systems face complex global behavior changes under fire. Localized heating near pylons or anchorages alters the internal force distribution, leading to unbalanced cable forces and increased bending moments. Additionally, thermal expansion in girder segments causes horizontal displacements that can push expansion joints and bearings beyond their limits, introducing secondary stresses and potential system-wide collapse (Liu et al., 2023). Due to their critical role in transport infrastructure, long-span bridge girders require proactive design measures such as fire-resistant coatings, thermal isolation barriers, and active fire suppression systems. While these methods can delay damage onset, the magnitude and duration of fire exposure remain the decisive factors in determining post-fire survivability.

2.5 Design Fire

A design fire is a conceptual representation of a fire scenario used to analyze and predict the fire's impact on a structure. It provides a basis for evaluating the thermal and structural performance of buildings, bridges, and other infrastructures under fire conditions (Nicoletta *et al*., 2020). In structural fire engineering, the design fire is crucial because it defines the heat flux, temperature distribution, and duration of a fire, which are essential for determining the structural response and ensuring safety and resilience.

Developing design fire scenarios for bridge structures involves a thorough understanding of potential fire hazards and risks specific to the bridge's environment and surroundings. Engineers consider factors such as nearby industrial facilities, traffic conditions, and the likelihood of accidents involving flammable materials (Decò *et al*., 2011). Based on this assessment, the key characteristics of the design fire, including the fire load, growth rate, peak temperature, and duration are defined.

Once the design fire scenario is established, engineers use fire modeling tools and techniques to simulate how the fire would develop and spread within and around the bridge structure. This involves modeling factors such as wind conditions, ventilation effects, and the thermal properties of bridge materials. Computational fluid dynamics (CFD) simulations are often employed to predict fire behavior, including flame spread, heat transfer, and smoke movement (Kashi *et al*., 2020).

The results of the fire modeling simulations are then used to assess the structural response of the bridge to the design fire scenario. Thermal analysis is conducted to determine how the fire would affect the temperature distribution within the bridge components, including beams, decks, and cables. Structural analysis is then performed to evaluate the mechanical response of the bridge materials to the elevated temperatures, including changes in stiffness, strength, and deformation (Aziz *et al*., 2015).

2.5.1 Fire Parameters

Fire scenarios and parameters include fire load, growth rate, duration, and temperature-time curves. Scenarios like standard fire, natural fire, and hydrocarbon fire help model realistic conditions, impacting structural integrity assessments and safety measures in buildings and bridges during and after fire exposure. A study carried out by (Ariyanayagam *et al*., 2014), gave brief summary of the different fire parameters used when designing for fire and are discussed in the following subsections.

I. Fire Load

The fire load is the total energy content of the combustible materials within a compartment, usually expressed in MJ/m². High fire loads lead to more intense fires, requiring structures to have higher fire resistance to maintain structural integrity.

II. Growth Rate

The growth rate is the speed at which the fire develops, often classified as slow, medium, fast, or ultra-fast. Rapid fire growth rates require structures to withstand quickly escalating temperatures and heat fluxes, which can challenge the thermal stability of materials.

III. Duration

The duration of a fire is the length of time the fire burns. Longer fire durations mean prolonged exposure to high temperatures, potentially weakening structural components over time and necessitating designs that can endure extended heat exposure

2.5.2 Design Fire Curves

Different types of design fires include standard fires, hydrocarbon fire, external fire and natural fires. Standard fires follow a fixed temperature-time curve; external fires deal with fires that occur outside of a structure or nearby bridge but have the potential to impact it; hydrocarbon fires involve intense, rapid temperature rises and, natural fires vary based on real scenarios.

When designing fire, it is grouped into two main types which are nominal fire curve and natural fire curve. Nominal fire curve is made up of; Standard fire curve; External fire curve and Hydrocarbon fire curve (Cook & Cook, 2007).

I. Standard Fire

The standard fire is a simplified, time-temperature curve used in fire resistance testing. It is defined by the ISO 834 curve, which specifies a consistent rise in temperature over time as

shown in Figure 2.10. Standard fire equation in accordance to (Cook & Cook, 2007) is given in Equation 2.1;

$$T = 20 + 345 \log(8t + 1) \quad (2.1)$$

Where; T = Temperature in Degree Celsius (˚C).

t = Time (minutes)

This type of fire is used to test and rate the fire resistance of construction materials and components. It provides a benchmark for evaluating structural elements' performance under a controlled, repeatable fire scenario (Oliveira *et al*., 2021).

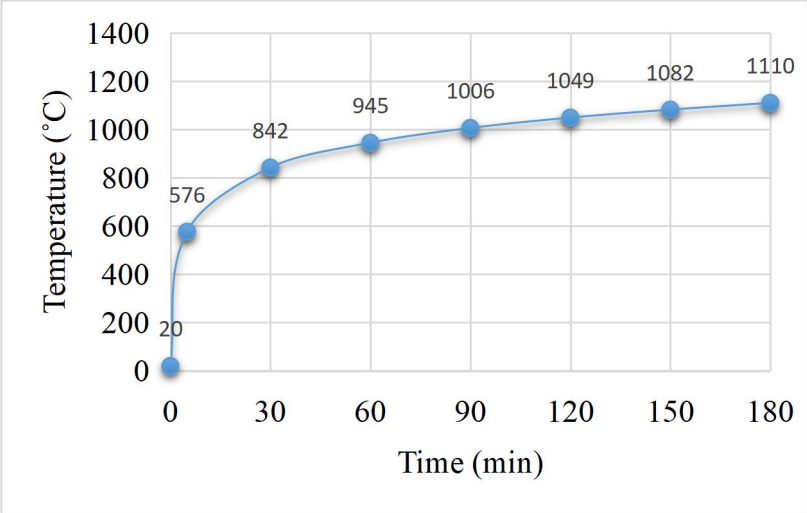

Figure 2.10: Standard Fire Curve (Cook & Cook, 2007)

II. External Fire

External fires refer to fires that occur outside of a structure or nearby bridge but have the potential to impact it. These fires can be caused by vehicle fires near the bridge structure, or any adjacent fire source. The temperature-time curve for external fires is highly variable, depending on factors such as wind conditions, fuel type, and proximity to the bridge. This can cause significant thermal exposure to the outer surfaces of bridge and other structures around, leading to potential structural damage. For instance, wildfires can cause prolonged exposure to high temperatures, affecting materials like concrete and steel. External fire equation in accordance to (Cook & Cook, 2007) is given in Equation 2.2.

$$T = 20 + 660\ (\mathbf{1 - 0.687e^{-0.32t} - 0.313e^{-3.8t}}) \quad (2.2)$$

Where; T = temperature in Degree Celsius (˚C).

t = Time (minutes)

External fire models are used to assess the risk and impact of external fire scenarios on bridge structures. These models help in designing protective measures such as fire-resistant cladding, barriers, and enhanced firefighting strategies. However, predicting the behavior of external fires can be challenging due to the many variables involved, such as environmental conditions and fuel types (Silva *et al*., 2023). Figure 2.11 gives a graphical illustration of external fire curve.

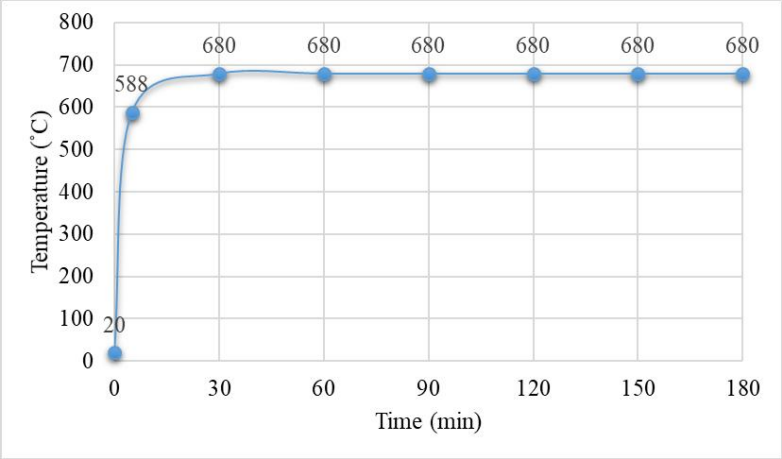

Figure 2.11: External Fire Curve (Cook & Cook, 2007)

III. Hydrocarbon Fire

Hydrocarbon fires are characterized by rapid temperature rise and high peak temperatures, typical of fires involving flammable liquids and gases, such as those found in petrochemical facilities. Hydrocarbon fire equation in accordance to (Cook & Cook, 2007) is given in Equation 2.3 which results in hydrocarbon fire curve in Figure 2.12 while an example of this type fire is explosion of fuel or diesel tankers, car explosion e.t.c as shown in Figure 2.13. Designing for hydrocarbon fires ensures that critical infrastructure can survive severe fire conditions without catastrophic failure (Gernay *et al*., 2019).

$$T = 20 + 1080\ (\mathbf{1 - 0.325e^{-0.167t} - 0.675e^{-2.5t}}\ ) \quad (2.3)$$

Where; T = Temperature in Degree Celsius (˚C).

t = Time (minutes)

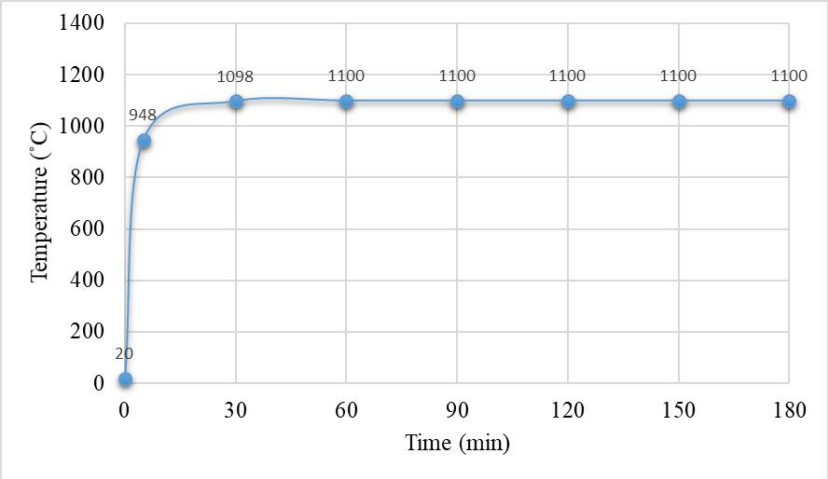

Figure 2.12: Hydrocarbon Fire Curve (Cook & Cook, 2007)

Figure 2.13: Tanker Explosion Under Bridge in Lagos, Nigeria (Daily Trust, 2021)

IV. Natural Fire

Natural fire models represent more realistic fire scenarios that consider the actual fire development within a compartment with the inclusion of a decay/cooling phase as shown in Figure 2.14. Other examples of this type of fire is wildfire and fire caused by lighting as shown in Figure 2.15. Natural fire models offer a more accurate prediction of fire behavior in

real-life conditions, helping engineers design bridge structures that can withstand the specific fire risks associated with their environment (Craig & Naser, 2023).

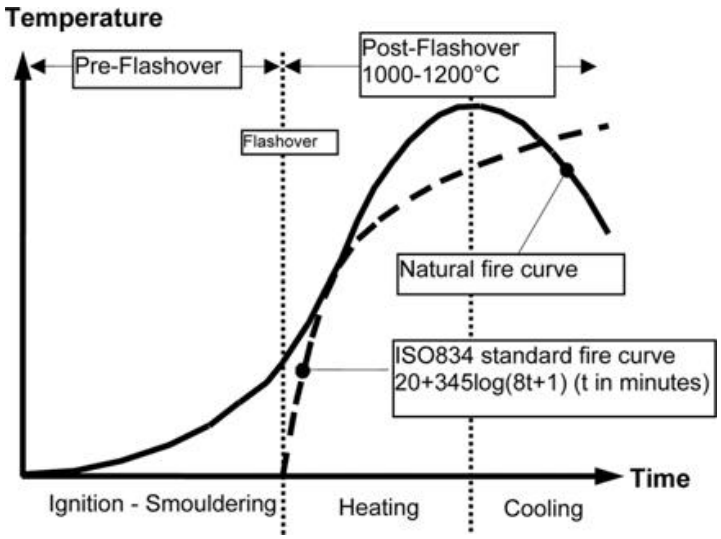

Figure 2.14: Natural Fire and Nominal Fire Curve (Zehfuß *et al.*, 2007)

Figure 2.15: Canyon Bridge, Northern California on Fire due to wildfire (InsideTrack News Article, 2021)

2.6 Post-Fire Damage Assessment Techniques

Assessing post-fire damage in bridge structures is critical to ensure safety, determine the extent of repairs needed, and restore functionality (Nicoletta *et al.*, 2020). Various techniques are utilized in post-fire evaluation, each with its own set of advantages and limitations. These include; visual inspection, Non-Destructive Testing (NDT), Digital Image Correlation (DIC),

Thermal Imaging and Finite Element Modeling (FEM) and they are discussed in the following subsection (Adamczak-Bugno *et al*., 2024);

2.6.1 Visual Inspection

Visual inspection is often the first step in assessing fire damage to bridge structures. It involves a thorough examination of the visible components of the bridge, including concrete surfaces, steel elements, and other materials affected by the fire. Inspectors look for signs of spalling, cracking, discoloration, deformation, and other indicators of damage.

2.6.2 Non-Destructive Testing (NDT)

NDT methods, such as ultrasonic testing, radiography, thermography, and ground-penetrating radar, are used to evaluate the internal condition of bridge materials without causing damage. These techniques can provide a more detailed assessment of the extent of fire damage.

2.6.3 Digital Image Correlation (DIC)

DIC is a technique used to measure deformation, displacement, and strain on the surface of materials by comparing digital images taken before and after a fire.

2.6.4 Thermal Imaging

Thermal imaging uses infrared cameras to detect temperature variations on the surface of bridge components, which can indicate areas of damage or internal defects caused by fire.

2.6.5 Finite Element Modeling (FEM)

FEM is an advanced computational technique used to simulate the structural behavior of bridges under various conditions, including post-fire scenarios. By creating a detailed model of the bridge, engineers can predict how the structure has been affected by the fire and identify critical stress points.

FEM complements these techniques by providing a comprehensive analysis that incorporates detailed modeling and simulation, leading to a more thorough understanding of the structural condition. FEM allows for a detailed and accurate analysis of how structures respond to fire.

It can model complex geometries and material behaviors, providing insights into temperature distributions, thermal stresses, and structural deformations that simpler methods cannot achieve. This detailed analysis is critical for understanding how fire affects different parts of a structure and predicting potential failure points (Luo *et al*., 2018). Materials exhibit complex behaviors at high temperatures, including changes in strength, stiffness, and thermal conductivity. FEM can incorporate these non-linear material properties and provide a more realistic simulation of how materials will perform under fire conditions. This is particularly important for materials like steel and concrete, which undergo significant changes when exposed to high heat.

2.6.6 Summary of Fire Damage Assessment Techniques

A summary of different post-fire damage assessment techniques with its advantages and limitations is give below in Table 2.2.

Table 2.2: Summary of post-fire damage assessment techniques.

S/N	Techniques	Advantage	Limitation
1	Visual Inspection	Immediate assessment, Cost-Effective, and Simple Implementation.	Subjectivity, Surface-Level Only, and Inconsistent Results.
2.	Non-Destructive Testing (NDT)	Internal Assessment, Precision, and Safety.	Specialized Equipment and Training, Interpretation of Results, and Environmental Sensitivity.
3.	Digital Image Correlation (DIC)	Non-Contact Measurement, High Precision, and Real-Time Monitoring	Surface Preparation, Environmental Factors, and Complex Data Analysis.
4.	Thermal Imaging	Quick Identification, Non-Destructive, and Wide	Surface-Only, Interpretation Challenges,

S/N	Techniques	Advantage	Limitation
		Area Coverage.	and Limited Penetration
5.	Finite Element Modelling	Comprehensive Analysis, Predictive Capability, and Customizable.	Complexity and Cost, and Accuracy of Input Data.

2.7 Fundamentals of Finite Element Method (FEM)

The Finite Element Method (FEM) is a numerical technique for solving complex engineering and mathematical problems. It is particularly valuable for analyzing structures, heat transfer, fluid dynamics, and electromagnetic fields. The following subsections present a detailed explanation of FEM, including its principles, operation, types of finite elements, meshing strategies, and boundary conditions (Reddy & Reddy, 2015).

2.7.1 Principles of FEM

The fundamental principle of FEM is to break down a large, complex problem into smaller, simpler parts called finite elements. These elements, connected at points known as nodes, form a mesh that approximates the geometry of the structure or domain being analyzed. The process of FEM begins with discretization, where the structure or domain is divided into a finite number of elements. The choice of element type such as 1D elements for beams, 2D elements for plates and shells, or 3D elements for solid structures depends on the nature of the problem and the desired accuracy. The mesh density, or the number of elements, is crucial as it influences both the precision of the results and the computational resources required (Kuna & Kuna, 2013).

Once the mesh is established, the next step involves deriving the element equations. These equations are based on physical principles such as equilibrium, compatibility, and material constitutive laws, which describe the behavior of the material under various loads. For each

element, a set of equations is formulated to relate the nodal displacements (or other field variables) to the applied forces as shown in Equation 2.4.

$$P = K \cdot U \tag{2.4}$$

Where P is applied nodal forces in Newton (N), K is stiffness matrix, and U is displacement in meter (m).

These individual element equations are then assembled into a global system of equations that represents the entire problem. The assembly process takes into account the connectivity of the elements and ensures that the global system accurately reflects the interactions between adjacent elements as shown in Equation 2.5 and Equation 2.6. Boundary conditions and external loads are applied to the global system to simulate real-world constraints and forces.

$$\begin{Bmatrix} \boldsymbol{P_1} \\ \boldsymbol{P_2} \end{Bmatrix} = \begin{bmatrix} \boldsymbol{k_{11}} & \boldsymbol{k_{12}} \\ \boldsymbol{k_{21}} & \boldsymbol{k_{22}} \end{bmatrix} \cdot \begin{Bmatrix} \boldsymbol{d_1} \\ \boldsymbol{d_2} \end{Bmatrix} \tag{2.5}$$

Where P is applied nodal forces in Newton (N), K is stiffness matrix, and D is nodal displacement in meter (m)

Solving the global system of equations typically involves numerical methods such as matrix inversion or iterative techniques, depending on the size and nature of the problem. The solution yields the primary unknowns, such as nodal displacements, which can then be used to calculate secondary quantities like stresses and strains within the elements. The final step in FEM is post-processing, where the computed results are analyzed and visualized. This step is critical for interpreting the physical behavior of the system, identifying areas of high stress or deformation, and making informed decisions about design modifications or improvements (Dalémat *et al*., 2019). The global stiffness matrix is given in below in Equation 2.6

$$\begin{Bmatrix} \boldsymbol{P_1} \\ \boldsymbol{P_2} \\ \boldsymbol{P_3} \\ \dots \end{Bmatrix} = \begin{bmatrix} \boldsymbol{k_{11}} & \boldsymbol{k_{12}} & \boldsymbol{k_{13}} & \dots \\ \boldsymbol{k_{21}} & \boldsymbol{k_{22}} & \boldsymbol{k_{23}} & \dots \\ \boldsymbol{k_{31}} & \boldsymbol{k_{32}} & \boldsymbol{k_{33}} & \dots \\ \dots & \dots & \dots & \boldsymbol{k_{nn}} \end{bmatrix} \cdot \begin{Bmatrix} \boldsymbol{d_1} \\ \boldsymbol{d_2} \\ \boldsymbol{d_3} \\ \dots \end{Bmatrix} \tag{2.6}$$

Where P is applied nodal forces in Newton (N), K is stiffness matrix, and D is nodal displacement in meter (m)

2.7.2 FEM Resolution

FEM resolution refers to the level of detail and accuracy in a finite element model, determined by the size and number of elements in the mesh. High-resolution FEM models use a large number of small elements, providing detailed and accurate results by capturing complex geometries and stress variations more precisely. This is essential for analyzing regions with high gradients in stress, strain, or temperature, ensuring that critical areas are accurately represented (Marcé-Nogué *et al*., 2020).

However, increasing the resolution also increases computational requirements, as more elements result in larger systems of equations to solve. This trade-off between accuracy and computational efficiency is a key consideration in FEM. The resolution of an FEM model is often guided by mesh convergence studies, where the mesh is progressively refined until the results stabilize, indicating that further refinement will not significantly change the outcome. This approach ensures that the model provides reliable results without unnecessary computational expense. Properly resolved FEM models are crucial for making informed design decisions, optimizing structural performance, and ensuring the safety and reliability of engineering systems (Chi *et al*., 2015).

2.7.3 Types of Finite Elements

Finite elements come in various types, each suited for specific applications and types of analysis. Proper selection and application of these elements are crucial for the effectiveness and efficiency of FEM analyses. Each type of element is chosen based on the problem's geometry, loading conditions, and desired accuracy, ensuring that the finite element model accurately represents the physical system being analyzed. Figure 2.16 shows some examples of element shapes both the first and the second order.

I. 1D Elements:

These are used for structures like beams, trusses, and frames. Beam elements can model bending and axial deformations and are defined by their length, cross-sectional properties, and the material's elastic modulus. Truss elements are only capable of withstanding axial forces and are typically used in frameworks like bridges and towers (Gayed *et al*., 2021).

II. 2D Elements:

These include triangles and quadrilaterals and are used for plane stress, plane strain, and shell problems. Plane stress elements are ideal for thin structures where stresses in the thickness direction are negligible, such as in thin plates. Plane strain elements are used for thick structures where deformation in one direction is negligible compared to the other two, like in dams or tunnels. Shell elements, a subset of 2D elements, are used for thin-walled structures where both bending and membrane actions are significant. They combine the characteristics of plates (bending) and membranes (in-plane forces) (Gayed *et al*., 2021).

III. 3D Elements:

These elements, such as tetrahedrons and hexahedrons (brick elements), are used for solid mechanic’s problems involving complex geometries. Tetrahedral elements are preferred for meshing complex shapes due to their flexibility, while hexahedral elements are preferred for their accuracy and efficiency in regular geometries. These elements can model volumetric stress and strain in three-dimensional space, making them suitable for detailed stress analysis in components like engine blocks, structural components, and pressure vessels (Gayed *et al*., 2021).

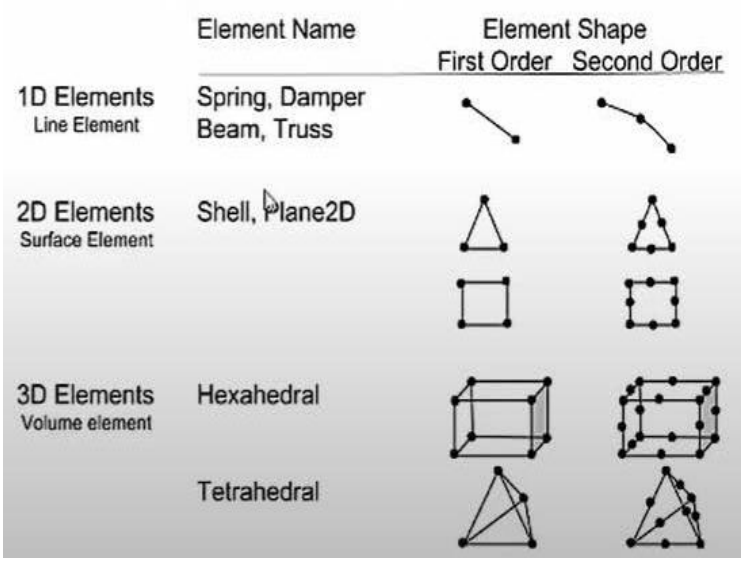

Figure 2.16: Examples and Types of Element (Hearn & Hearn, 1997)

IV. Axisymmetric Elements:

These are specialized 2D elements used for problems with rotational symmetry around an axis, simplifying 3D problems into 2D ones. They are useful for analyzing structures like tanks, pipes, and rotating machinery where the geometry and loading are symmetrical about an axis. By reducing a 3D problem to a 2D plane, computational efficiency is significantly improved while still capturing the essential behavior of the structure (Vaxman *et al*., 2016).

2.7.4 Meshing Strategies

Meshing strategies are crucial in finite element analysis as they significantly influence the accuracy and computational efficiency of the simulation. A good meshing strategy involves selecting the appropriate element type, size, and distribution for the given problem. Structured meshes use regular, grid-like patterns, ideal for simple geometries and regions with uniform stress distribution as seen in Figure 2.17. They offer high accuracy and computational efficiency but may struggle with complex shapes. Unstructured meshes, composed of irregularly shaped elements like triangles or tetrahedrons, adapt better to complex geometries and varying stress fields, although they can be more computationally intensive (More & Bindu, 2015).

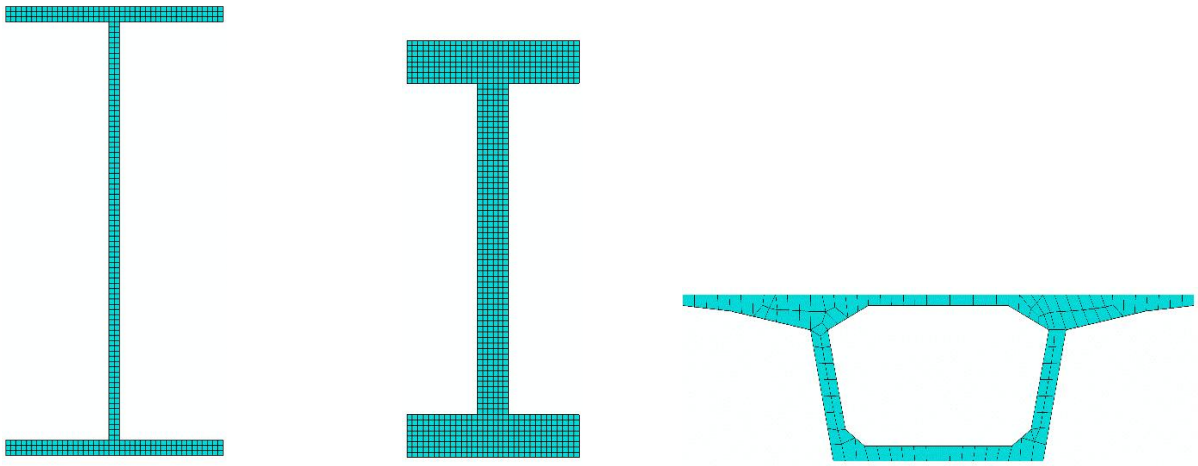

Figure 2.17: Meshed Bridge Girders Both Concrete and Steel

Adaptive meshing refines the mesh iteratively, focusing on areas with high error estimates or stress gradients. This approach balances accuracy and efficiency by allocating computational resources where they are needed most. Mesh convergence studies, where the mesh is progressively refined until the results stabilize, ensure that the solution is independent of the mesh size (Baiges *et al*., 2020).

2.7.5 Boundary Conditions

Boundary conditions in finite element analysis (FEA) define how a structure interacts with its surroundings and are crucial for simulating real-world behavior accurately. They specify constraints, loads, and displacements that the structure experiences during analysis. Essential boundary conditions restrict degrees of freedom (DOFs) of selected nodes, such as fixing nodes to prevent translation or rotation. These conditions simulate structural supports like fixed supports or rollers (Lourenço & Gaetani, 2022).

Natural boundary conditions apply loads and external forces to the structure, such as applied forces, pressures, or thermal gradients. These conditions represent the applied loads and environmental effects that the structure experiences during operation. In FEA, boundary conditions must be carefully defined to reflect the actual structural behavior while ensuring computational efficiency. Improper boundary conditions can lead to unrealistic results or

computational errors. Engineers typically validate boundary conditions by comparing simulation results with physical tests or analytical solutions, ensuring the accuracy and reliability of the FEA model (Lourenço & Gaetani, 2022).

2.8 Application of FEM in Structural and Fire Engineering

The Finite Element Method (FEM) is a foundational analytical tool in structural engineering due to its capability to model complex geometries, diverse material behaviors, and varied loading conditions. Its use spans across multiple domains, from static and dynamic structural analysis to thermal assessments and stability evaluations (Craig, & Naser, 2023). FEM's adaptability makes it essential for both design and diagnostic tasks within structural engineering projects.

2.8.1 Static Structural Analysis

FEM plays a central role in static structural analysis by enabling the calculation of stress distributions and deformations under constant load conditions. In bridge engineering, for instance, FEM is used to model structural components such as beams and trusses. Engineers apply static equilibrium equations within the FEM framework to evaluate internal forces and displacements. This process helps ensure that structures can sustain operational vehicular loads without undergoing excessive deformation or structural failure (Reddy & Reddy, 2015).

2.8.2 Thermal Analysis

Thermal analysis using FEM is critical in understanding how structural components respond to temperature variations. A typical application can be seen in power plants, where FEM is used to assess thermal expansion in pipelines. By simulating thermal loads, engineers can predict temperature distributions and the resulting thermal stresses as seen in Figure 2.18. These predictions are essential to maintain structural integrity under fluctuating operational temperatures (Hesien *et al*, 2025).

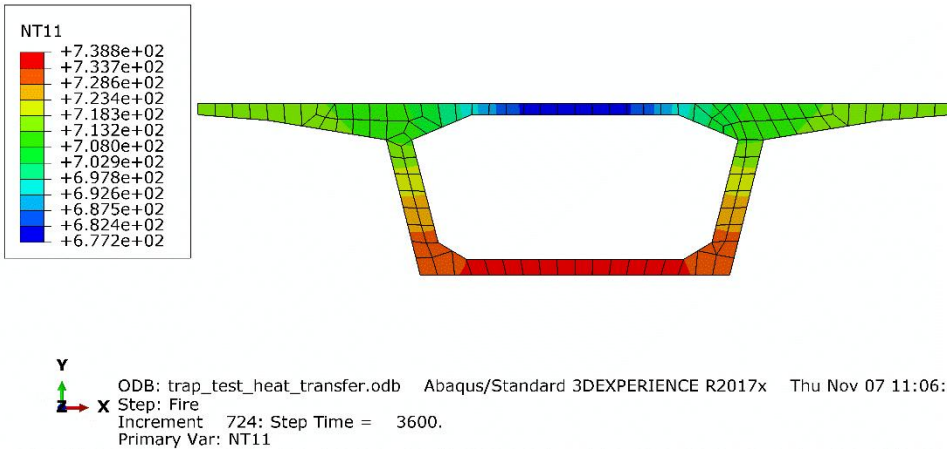

Figure 2.18: Thermal Analysis of a Bridge Girder Using FEM

2.8.3 Buckling and Stability Analysis

FEM is also employed for evaluating the buckling behavior and overall stability of structures, particularly in elements vulnerable to compressive loading. Slender columns and beams in bridge designs, for example, are assessed for their critical buckling loads and mode shapes. Such evaluations ensure that structures are provided with appropriate safety margins to prevent sudden and catastrophic buckling failures (Memon *et al*., 2019).

2.8.4 Application in Structural Fire Engineering

In structural fire engineering, FEM extends its utility to simulate the behavior of structures under fire exposure. This involves complex interactions between thermal and mechanical responses. One key application is thermal response analysis, which predicts temperature distribution within structural elements during fire incidents. For instance, transient thermal analysis of a steel beam subjected to fire can simulate the heat flux and determine resulting thermal stresses and deformation over time (Hodges *et al*., 2017).

2.8.5 Structural Health Monitoring

FEM is widely used in structural health monitoring (SHM) to evaluate both the current condition and the projected performance of infrastructure systems. In bridges, sensor data—such as strain and temperature readings are integrated with FEM models to provide real-time structural assessments. This allows for continuous updates to the analysis model, aiding in

early detection of potential issues like fatigue or material degradation and enabling proactive maintenance measures (Millard & Pimienta, 2019).

2.8.6 Damage Prediction and Failure Analysis

Finally, FEM is indispensable in predicting damage and analyzing failure mechanisms in structural components. Nonlinear FEM models are especially useful in simulating crack initiation and material degradation under varied loading conditions. For example, when assessing a bridge's long-term durability, these models help identify locations susceptible to damage propagation, thus guiding reinforcement strategies to enhance the structure's longevity and safety.

2.9 Finite Element Method for Post-Fire Assessment of Structures

The Finite Element Method (FEM) is a powerful computational technique used to simulate fire exposure and predict the structural response of materials under elevated temperatures. By developing detailed models, FEM incorporates the thermal and mechanical behavior of materials during and after fire events, enabling accurate assessment of damage and structural integrity.

2.9.1 Thermal Analysis Using FEM

The FEM process begins with thermal analysis, where the software simulates heat transfer through conduction, convection, and radiation across the structural elements (Hodges *et al*., 2017). This analysis is guided by a fire's time-temperature curve and tracks how heat penetrates and evolves throughout the structure. The resulting temperature distribution data serves as the basis for further mechanical assessment.

2.9.2 Mechanical Analysis and Material Behavior

Following the thermal analysis, a mechanical analysis evaluates the impact of elevated temperatures on the structural materials. Concrete and steel lose strength and stiffness at high temperatures, and FEM models can incorporate these temperature-dependent material

properties (Ye *et al*., 2022). The simulation calculates thermal stresses, strains, and deformations, which are essential for identifying vulnerable zones, possible collapse mechanisms, and excessive displacements.

2.9.3 Application of FEM in Bridge Fire Cases

FEM has been widely applied in the post-fire assessment of bridge structures. For example, Hamad *et al*. (2017) modeled a steel bridge exposed to fire, focusing on how thermal gradients induced by the fire led to significant internal stresses and local buckling. This enabled the formulation of reinforcement strategies to recover structural performance. Similarly, Watson *et al*. (2012) applied FEM to analyze a fire-damaged concrete bridge. Their thermal simulations revealed extensive concrete spalling and exposure of reinforcing steel, while the mechanical assessment confirmed a severe reduction in load-bearing capacity, prompting urgent repair recommendations such as concrete replacement and enhanced fireproofing.

2.9.4 Limitations of FEM

Despite its advantages, FEM is not without limitations. A major challenge is the computational complexity of high-fidelity models. Simulating large structures with detailed geometries requires significant computing power and time (Zhou *et al*., 2024). Additionally, simplifications such as assuming uniform material properties or omitting boundary conditions may reduce model accuracy and affect the reliability of the predictions.

2.10 Thermal Finite Element Analysis Using Abaqus Software

Thermal finite element modelling in ABAQUS has been widely applied to study heat transfer in fire-exposed structural components such as beams, columns, slabs, and composite sections. The following subsections summaries the standard procedures, highlighting key modelling steps.

2.10.1 Introduction to Thermal Analysis in Abaqus

Abaqus is widely employed for conducting both steady-state and transient thermal analyses, particularly in fire engineering applications where temperature evolution over time is critical. According to Neupane (2020), Abaqus provides robust numerical procedures for modelling heat transfer through solid materials under conduction, convection, and radiation boundary conditions. In structural fire engineering, it is commonly used to simulate temperature distribution in steel, concrete, and composite elements exposed to defined fire curves such as standard fire curve (Hesien *et al*, 2025).

2.10.2 Geometry Modelling of Structural Components

Thermal analysis begins with the creation of geometric models representing the structural component of interest. Abaqus/CAE allows users to construct 2D or 3D representations of beams, slabs, or full structural assemblies seen in Figure 2.19. For heat-transfer studies, simplified 2D cross-sections are often used to capture thermal gradients efficiently while reducing model complexity (Kodur, & Dwaikat, 2008).

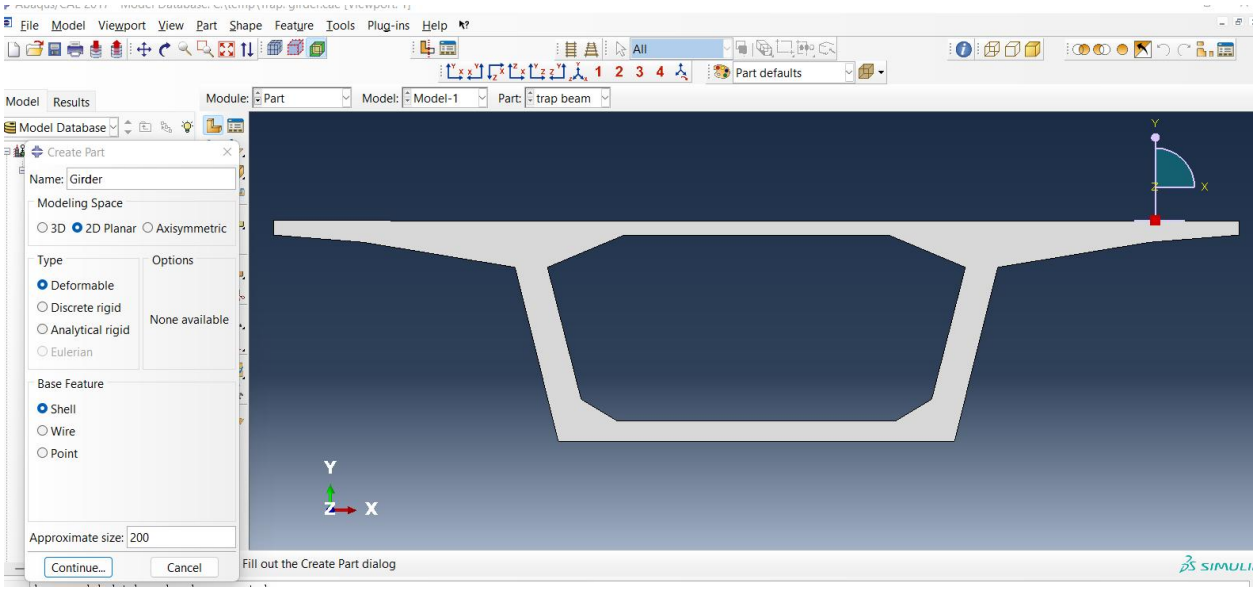

Figure 2. 19 - 2D Cross-Section Geometry of a Girder Modelled in ABAQUS.

2.10.3 Temperature-Dependent Material Property Definition

Accurate thermal modelling requires defining temperature-dependent material properties. Abaqus supports tabular inputs for thermal conductivity, specific heat capacity, density, and emissivity, which vary with temperature. For concrete and steel, these values may be sourced from Eurocode 2 (Beeby *et al*., 2005) and Eurocode 3 (Brown 2018), which provide standardized thermal property curves under fire exposure. Temperature-dependent degradation (e.g., loss of conductivity or density changes) is essential for predicting realistic temperature distributions and thermal delay within the section seen in Figure 2.20.

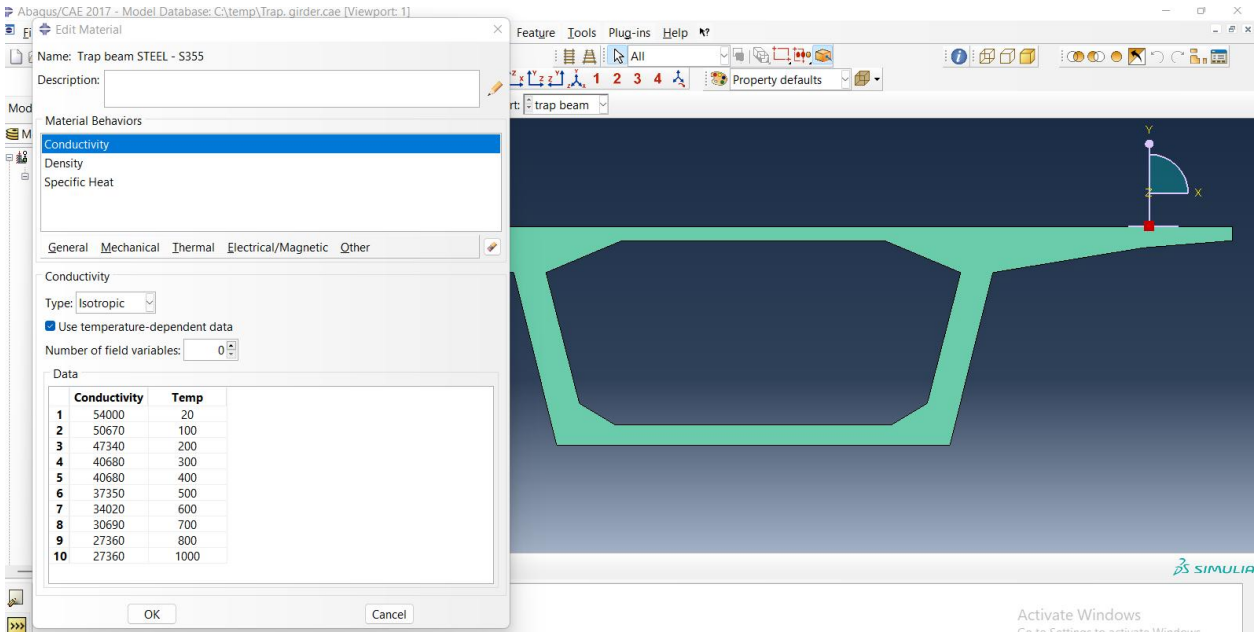

Figure 2. 20 - Temperature-Dependent Thermal Conductivity of Concrete as Defined in ABAQUS.

2.10.4 Step Definition for Transient Thermal Analysis

In Abaqus, a transient heat-transfer step is used to simulate the evolution of temperature in structural components subjected to fire exposure seen in Figure 2.21. This step governs how heat propagates through the model over time, capturing the nonlinear and time-dependent nature of thermal loading (Koric *et al*., 2009). Researchers typically define the heating duration, time increments, and automatic stabilization controls to ensure numerical accuracy

during rapid temperature rises in the early fire stage (Watson *et al*, 2012). The transient step also accounts for temperature-dependent thermal properties, allowing the software to update conductivity, specific heat, and density at each increment to reflect material degradation under elevated temperatures. This approach has been widely adopted in structural fire engineering studies because it provides a reliable representation of thermal gradients and heating patterns in steel, concrete, and composite members (Hesien *et al*, 2025).

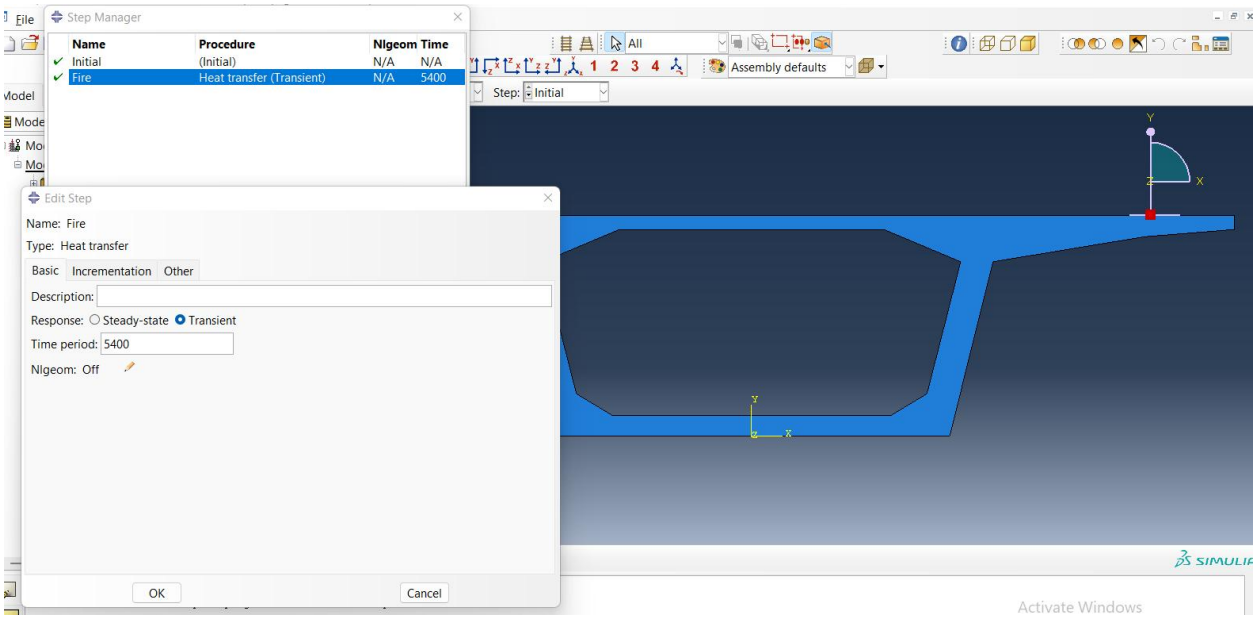

Figure 2. 21 - Transient Heat-Transfer Step Setup for Simulating Fire Exposure.

2.10.5 Fire Exposure and Thermal Boundary Conditions

Fire exposure is introduced into Abaqus as a time-dependent thermal boundary condition applied to the member's exposed surfaces seen in Figure 2.22. These boundary conditions define the thermal environment acting on the structure, including gas temperature, convection film coefficients, and radiation emissive properties (Abdelrahman *et al*., 2025). The applied temperatures follow predefined curves representing standardized or real fire scenarios. Abaqus allows the user to assign different boundary conditions to different surfaces for example, applying fire exposure on the bottom flange while keeping the top flange insulated or unexposed. This flexibility is useful for modelling asymmetric heating observed in bridge girders, slabs, and beams subjected to localized fires (Kodur & Gil, 2024). The boundary

conditions simulate how heat flux enters the material and determine the rate at which thermal gradients develop across the section.

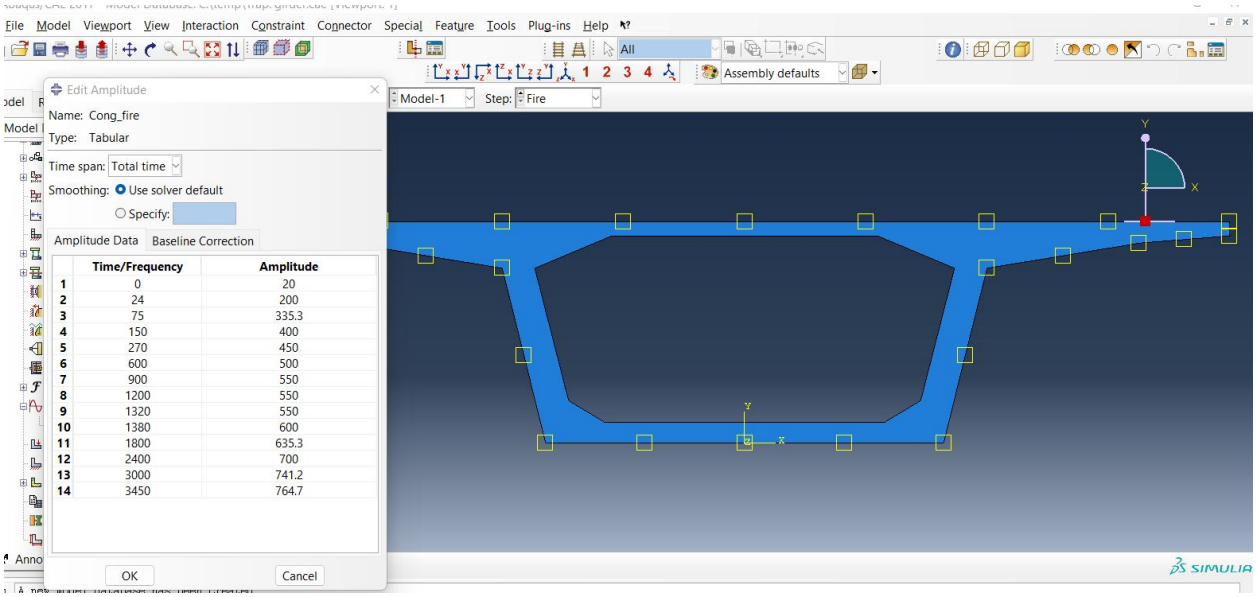

Figure 2. 22 - Application of ISO 834 Fire Curve as Surface Thermal Loading in ABAQUS.

2.10.6 Thermal Interactions and Heat Transfer Mechanisms

Thermal analysis in Abaqus incorporates the three primary heat-transfer mechanisms conduction, convection, and radiation. Heat conduction is modelled through the bulk of the material using Fourier's Law, representing temperature diffusion within steel and concrete elements (Banerjee, 2021). Convection and radiation are applied to the exposed surfaces to simulate heat exchange between the member and the surrounding fire environment seen in Figure 2.23. Convection coefficients and emissivity values are typically selected according to design codes such as Eurocode 1 (Cook & Cook, 2007). Combined radiation–convection interactions are particularly important at high temperatures, where radiative heat exchange dominates heat absorption (Buchanan, 2001). By modelling these interactions simultaneously, Abaqus captures realistic heating behavior consistent with experimental fire-test results.

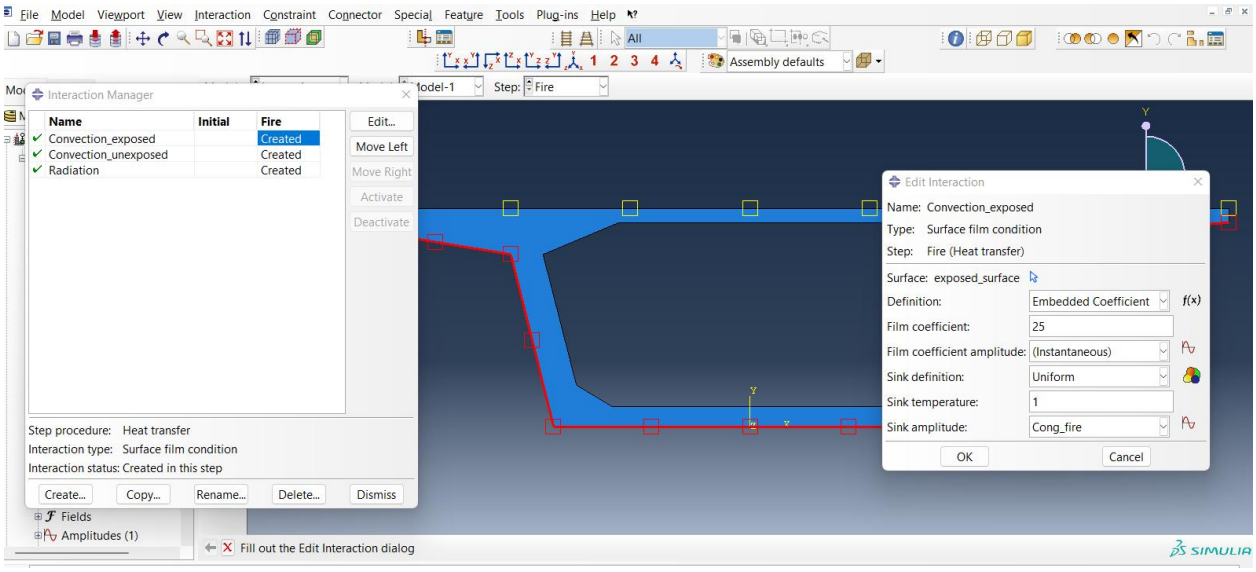

Figure 2. 23 - Application of ISO 834 Fire Curve as Surface Thermal Loading in ABAQUS.

2.10.7 Mesh Generation for Thermal Analysis

Mesh generation is a crucial step in achieving accurate temperature predictions. Abaqus offers 2D and 3D thermal elements such as DC2D4 (2D heat-transfer quadrilateral) and DC3D8 (3D heat-transfer brick) for modelling thermal conduction (Tang *et al*., 2020). Finer mesh densities are typically used near fire-exposed surfaces to capture steep temperature gradients that occur during heating, while coarser meshes may be assigned to insulated or cooler regions to reduce computational cost (Hodges *et al*, 2017). Mesh refinement is especially important in concrete sections where spalling-prone zones require detailed thermal resolution. Several studies have demonstrated that insufficient mesh resolution leads to significant underestimation of temperature peaks and delayed thermal penetration (Miah, 2017). Thus, mesh configuration directly influences the fidelity of the thermal results.

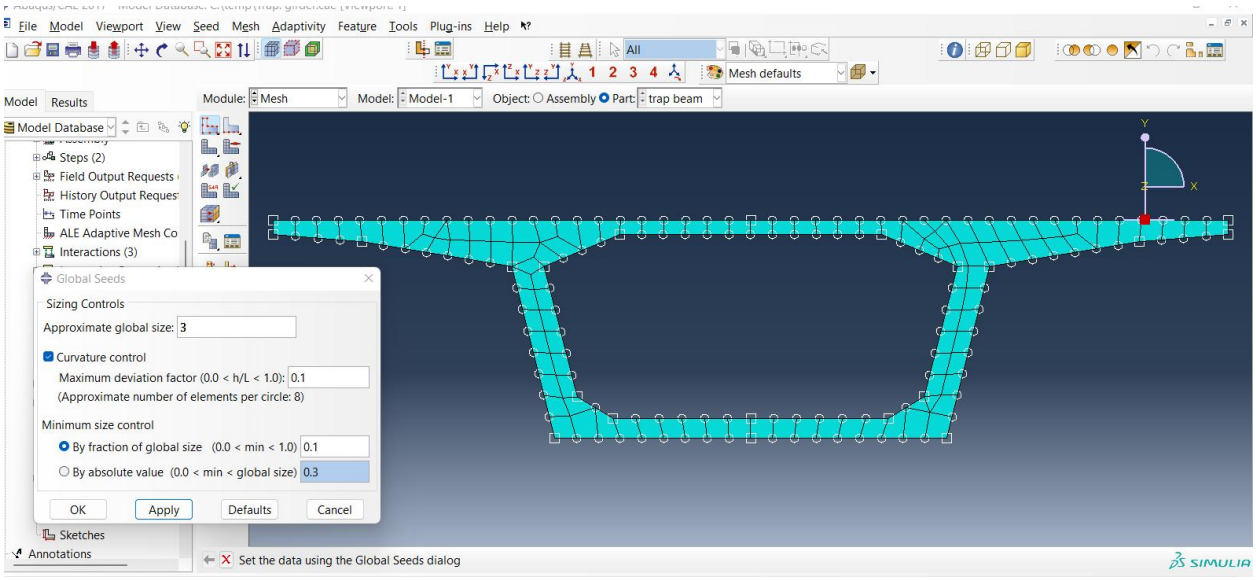

Figure 2. 24 - Finite Element Mesh Showing Refinement Near Fire-Exposed Surfaces.

2.10.8 Analysis Execution and Solver Settings

The thermal analysis is executed using the Abaqus heat-transfer solver, which processes the transient step and evaluates temperature fields over time (Aziz & Kodur, 2013). Solver settings such as automatic time stepping, maximum increment size, and convergence tolerances determine the stability and accuracy of the simulation, particularly during rapid temperature rises early in the fire. Nonlinear temperature-dependent properties are updated at each iteration, and the solver uses implicit integration to ensure stable results during long-duration heating (Hesien *et al.,* 2025). Output requests typically include nodal temperatures, heat flux, and thermal gradients, allowing researchers to extract temperature–time histories for critical elements such as reinforcement, flanges, and core regions (Curto *et al*., 2022). These results, Figure 2.25 are then used to evaluate structural fire resistance and compare behaviors across different section geometries.

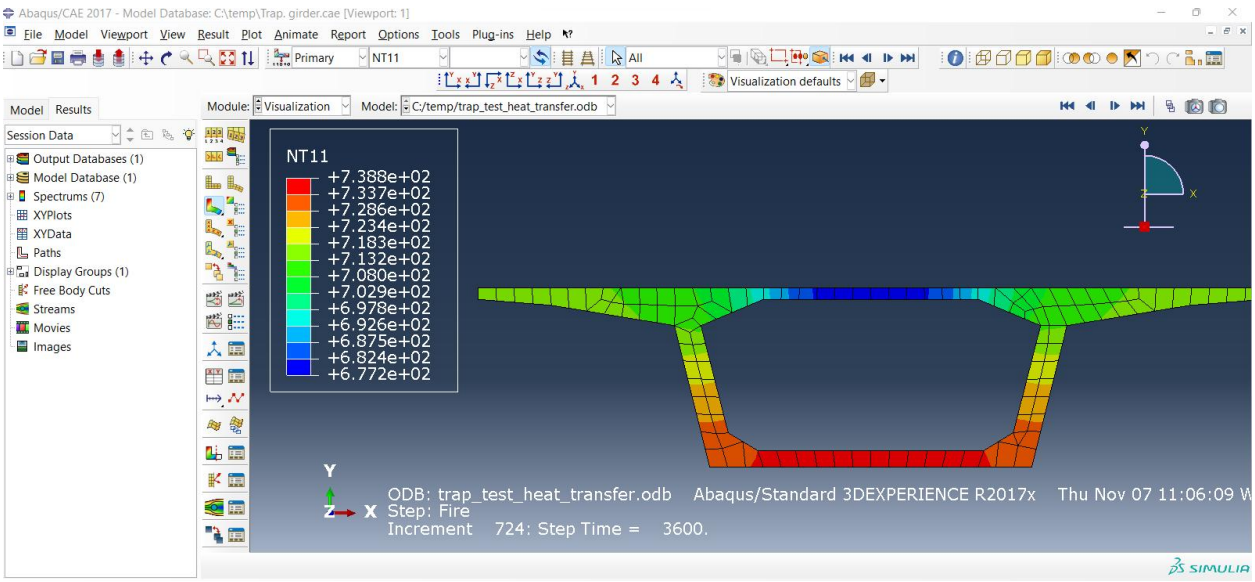

Figure 2. 25 - Temperature Contour Illustrating Heat Penetration into a Concrete Section After 3600sec of Fire Exposure.

2.11 Case Studies of FEM Application in Post-Fire Bridge Assessment

Several bridge projects have successfully employed FEM to assess and improve their structural integrity. Reviewing and comparing these cases provides insight into the practical application of FEM and highlights its benefits and challenges.

2.11.1 Case Study 1: New Little Belt Bridge, Denmark (Kragh *et al.*, 2020).

In 2013, a truck fire on the New Little Belt Suspension Bridge caused significant damage due to rapidly rising temperatures above 1000˚C. Engineers used FEM to simulate the thermal effects of the fire on the steel cables and other structural components. The model included detailed thermal properties of the materials and the geometric configuration of the bridge. The FEM analysis indicated that the fire caused substantial thermal stress, leading to potential weakening of the main cables. The simulation helped identify the need for fire protection measures, such as insulating materials to protect the cables from future fires. While the FEM provided valuable insights into the thermal effects, the accuracy of the simulation depended heavily on the precise thermal properties of the materials and the exact fire conditions, which are often difficult to determine accurately.

2.11.2 Case Study 2: Apapa-Oshodi Expressway Bridge, Lagos, Nigeria (Okunola & Okunola, 2019).

The Apapa-Oshodi Expressway bridge experienced severe fire damage from a tanker explosion in 2019. FEM was employed to assess the fire's impact on the concrete and steel reinforcements of the bridge. The model simulated the thermal effects and the resulting mechanical stresses on the structural components. The analysis revealed critical stress points where the material integrity was compromised. The FEM guided the repair strategies, ensuring that the rehabilitated bridge could withstand future incidents. The simulation's accuracy was limited by the availability of precise data on the fire's temperature and duration. Additionally, the complex interactions between the thermal and mechanical effects posed modeling challenges.

2.11.3 Case Study 3: I-85 Bridge Collapse, Atlanta (Park *et al*., 2018).

The I-85 bridge collapse in Atlanta due to a fire in 2017 is a prominent example. FEM was used extensively to assess the damage and guide the reconstruction process. The model helped engineers understand the thermal effects of the fire on the steel and concrete components, allowing them to identify critical areas that needed replacement or reinforcement. The detailed analysis provided by FEM ensured that the rebuilt sections would be more resilient to similar incidents in the future.

2.11.4 Case Study 4: Polcevera Viaduct (Morandi Bridge), Genoa, Italy (Petrini *et al*., 2020).

The Morandi Bridge collapsed on August 14, 2018, resulting in 43 fatalities. The collapse was due to the failure of the stays in the southern end of the bridge, which were made of prestressed concrete and steel cables. FEM was used to model the bridge and analyze the failure mechanisms of the stays. The model incorporated the complex geometry of the stays and the material properties of both concrete and steel. The FEM analysis demonstrated that

the stays had deteriorated over time due to corrosion and material fatigue. This deterioration led to a significant reduction in the load-carrying capacity of the stays, ultimately causing the collapse. The analysis highlighted the challenge of accurately modeling the long-term effects of corrosion and fatigue on structural components. Additionally, the complexity of the bridge's design made it difficult to simulate all possible failure modes accurately.

2.11.5 Case Study 5: I-35W Mississippi River Bridge Collapse, Minnesota, USA (Zhu *et al.*, 2010).

The I-35W Mississippi River Bridge in Minneapolis collapsed on August 1, 2007, leading to the deaths of 13 people and injuring 145 others. The collapse was attributed to a combination of design flaws and the additional weight of construction materials placed on the bridge. FEM was used to model the bridge structure and analyze the stresses and forces that led to its failure. The model included detailed representations of the steel truss elements and the concrete deck. The FEM analysis revealed that gusset plates in the bridge, which were undersized due to a design error, experienced excessive stress. The additional construction loads further exacerbated the stress on these plates, leading to their failure. The FEM analysis was conducted post-collapse, which means the insights gained could not prevent the incident. Additionally, accurate modeling of the complex interactions between various structural elements and the dynamic loading conditions was challenging.

2.12 Previous Research Done

Bridges, especially pedestrian girders, are vulnerable to fire-induced damage that affects structural performance through mechanisms like deflection, spalling, and material degradation. While significant research exists on highway bridge structures under fire exposure, pedestrian girder-specific studies are less common. This report examines previous work related to fire response of concrete girders and identifies research gaps relevant to pedestrian bridge assessments using finite element modeling.

2.12.1 Post-Fire Behavior of Concrete Bridge Girders

Miah, J. (2017) developed validated finite element models to simulate pre stressed and conventional concrete girders under fire exposure. Their work integrated thermal-mechanical behavior, hydro-thermal processes, and spalling to assess section loss in slender members. The study emphasized that smaller cross-sectional areas and web zones are more susceptible to failure and that UHPC in I-girders is particularly vulnerable to shear failure at elevated temperatures. However, the analyses focused on highway-scale girders, leaving limited insight into smaller, pedestrian-scale girders.

2.12.2 Hydro-Thermal-Cracking and Material Degradation

Batoma Sosso *et al*. (2021) presented an advanced finite element model capturing the hydro-thermal-mechanical response of concrete under fire. Their findings suggest critical coupling between moisture transport, pore pressure development, and cracking/spalling mechanisms. While their simulations detailed property degradation such as reduced stiffness, creep, and crack growth they primarily addressed building-scale structural members rather than bridge girders. Nonetheless, their methodological framework lays a strong foundation for pedestrian girder assessment.

2.12.3 Case-Specific Girder Fire Reconstructions

Gernay *et al.,* (2024) conducted a numerical reconstruction of a real-world fire incident involving a concrete T-girder bridge. Their study employed CFD-derived thermal inputs and finite element modeling to capture temporal temperature gradients, spalling evolution, and structural deflection. Significant degradation was observed in thin web regions, confirming the need to incorporate realistic fire scenarios into girder modeling. However, these insights were largely based on highway applications; pedestrian girders may exhibit distinct response behaviors due to geometry and span.

2.12.4 Spalling Mechanisms and Persistent Damage

Izzet *et al.,* (2021) investigated spalling in concrete specimens, highlighting the rapid onset of thermal–hydro spalling (within 10 minutes of heating) followed by thermal–chemical spalling at higher temperatures (700 - 800˚C). Their experimental observations align with thermodynamic models showing pore-pressure-induced cracking as a primary degradation driver. Although focused on testing specimens rather than bridge girders, these results emphasize the importance of modeling spalling in bridge components with adequate moisture coupling.

2.13 Research Gaps and Opportunities

In reviewing different literatures, while most FEM-based studies (e.g., Hamad *et al*., 2017; Watson *et al*., 2012) have concentrated on large vehicular or highway bridges, pedestrian bridges remain underexplored. These lighter structures may respond differently to fire due to their typically smaller cross-sections, lighter reinforcement, and different usage patterns. This creates a gap in understanding how pedestrian bridge girders specifically behave under post-fire conditions and what unique vulnerabilities they present.

Additionally, there is a scarcity of detailed post-fire case studies providing empirical data for validating FEM predictions, and the complexity of FEM software can be a barrier for practitioners, hindering broader adoption in post-fire assessments.

CHAPTER THREE

METHODOLOGY

3.1 Thermal Modelling Procedures

This chapter provides a comprehensive description of the methodology employed to model the thermal behavior of three beam configurations, a steel I-beam, a concrete I-beam, and a rectangular concrete beam when subjected to fire. The analysis was carried out using the ABAQUS finite element software, with the objective of developing reliable 2D thermal models capable of capturing temperature distribution and thermal gradients within each structural section during fire exposure.

The modelling procedure for each beam type is presented in a structured manner, detailing the processes of geometry creation, assignment of temperature-dependent material properties, specification of boundary conditions, application of thermal loading, and mesh formulation (Neupane, 2020). Particular emphasis is placed on accurately defining elevated-temperature material characteristics and heat-transfer parameters, as these are essential for reproducing realistic thermal responses under fire conditions.

3.2 Modelling Framework

This subsection presents the general workflow (Figure 3.1), adopted in developing the thermal finite element models for the steel I-beam, concrete I-beam, and rectangular concrete beam. The modelling framework ensures consistency, accuracy, and clarity across all simulations. The process follows the sequential steps outlined below:

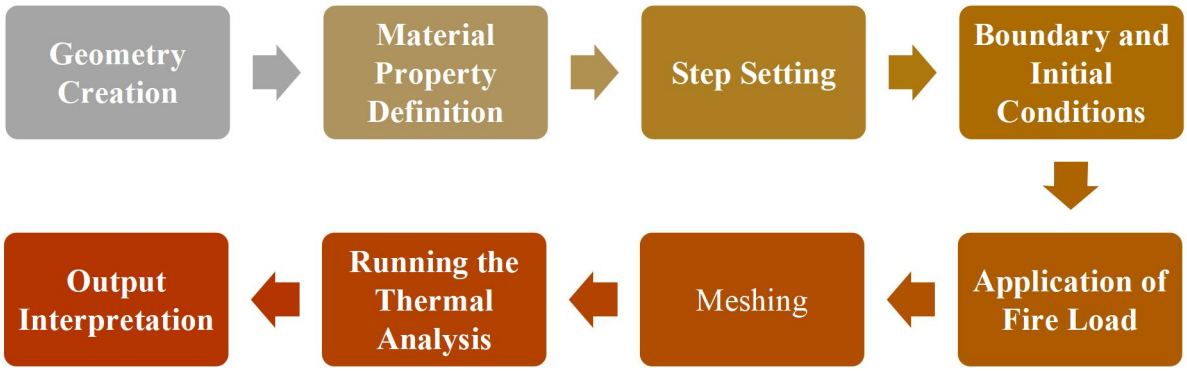

Figure 3. 1 – Modelling Workflow

I. Geometry Creation

This involved developing the 2D cross-sectional representations of the steel I-beam, concrete I-beam, and concrete rectangular beam seen in Figure 3.2. The dimensions used reflect realistic structural proportions and are consistent with the requirements of thermal analysis. Only the cross-section is modelled since heat transfer is evaluated in the plane of the section (Piekarska *et al*., 2010).

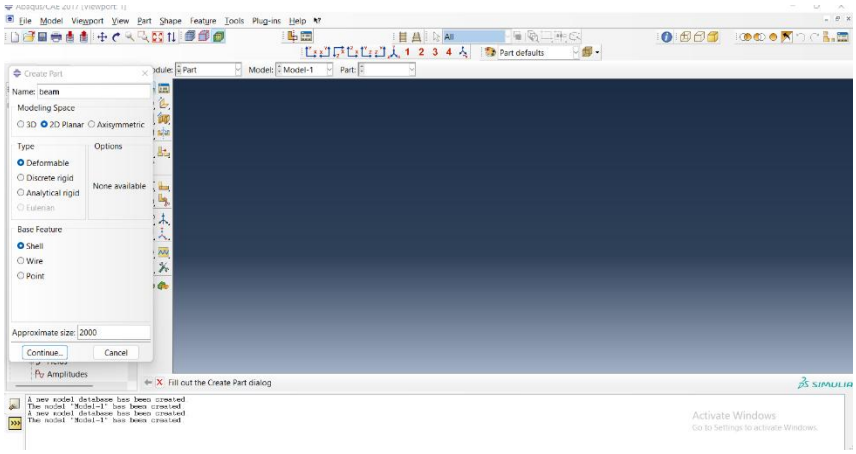

Figure 3. 2 – Development of Geometry in Abaqus

II. Material Property Definition

Temperature-dependent thermal properties such as thermal conductivity, specific heat capacity, density were assigned to each beam material (Neupane, 2020) seen in Figure 3.3. These properties govern how heat travels through steel and concrete during fire exposure and are defined in accordance with Eurocode standards and established literature.

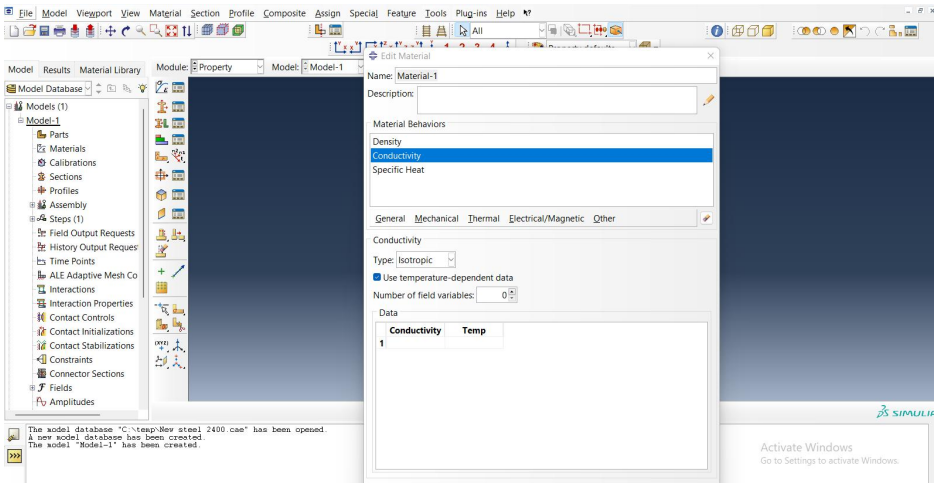

Figure 3. 3 – Thermal Properties in Abaqus

III. Step Setting

This involves the time frames for the fire exposure on the beam seen in Figure 3.4. Also, stating the type of analysis to be carried out i.e transient heat transfer for the analysis (Watson *et al*, 2012). Elements needed such as nodal temperature, reaction flux and heat flux are also selected for the thermal analysis.

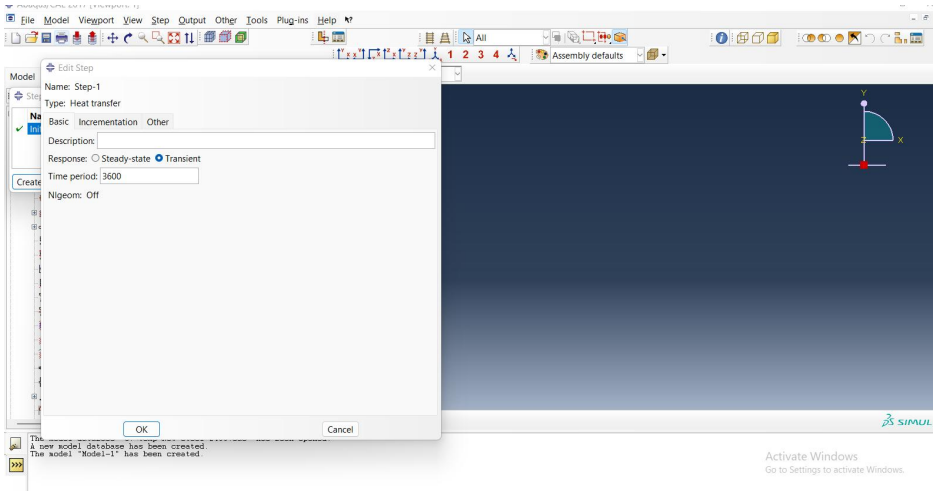

Figure 3. 4 – Step Module

IV. Boundary and Initial Conditions

Initial conditions specify the starting temperature (usually ambient temperature). Boundary conditions define the type of heat transfer occurring at exposed surfaces such as convection to the fire environment and radiation to fire gases. Non-exposed boundaries may be insulated or

assigned reduced heat flux depending on realistic exposure scenarios (Maragkos & Beji, 2021) as seen in Figure 3.5.

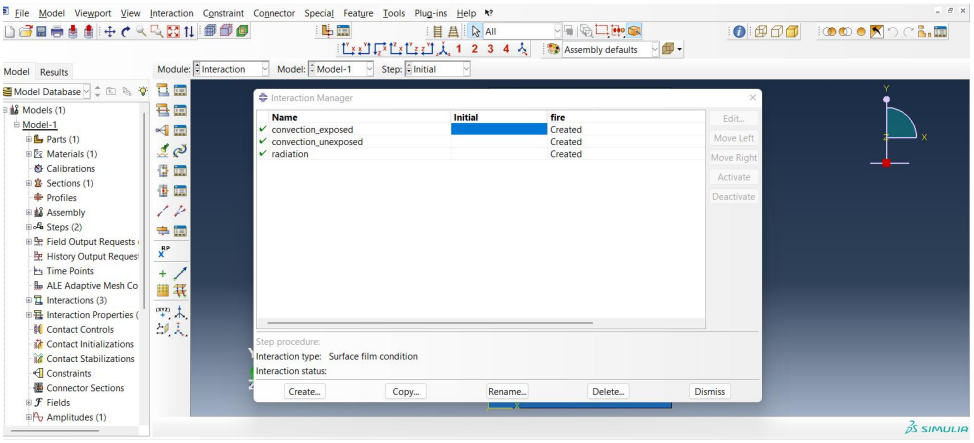

Figure 3. 5 – Thermal Boundary Conditions in Abaqus

V. Application of Fire Load (Temperature–Time Data)

The temperature-time curve (such as ISO 834 or any selected curve) is applied as the external thermal load. This fire load in Figure 3.6, determines how temperature rises on exposed surfaces over time and acts as the primary input driving the thermal response of the beams (Selden & Varma, 2016).

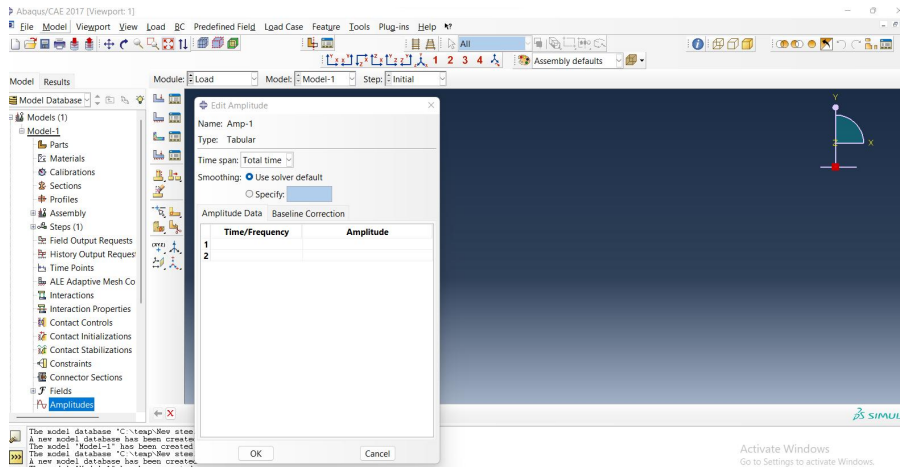

Figure 3. 6 – Fire Load, Amplitude in Abaqus

VI. Meshing

The geometry is discretized into finite elements to enable numerical heat transfer calculations. A structured mesh with refined element sizes around flanges, webs, and edges is used to

capture steep temperature gradients. The global seed is a key component in the meshing (Tang *et al*., 2020) which determines how large or how small the mesh will be and it also determines how big or little the number of elements and nodes will be. In selecting this global seed, there are no criterial but on what it is intended to achieve as seen in Figure 3.7.

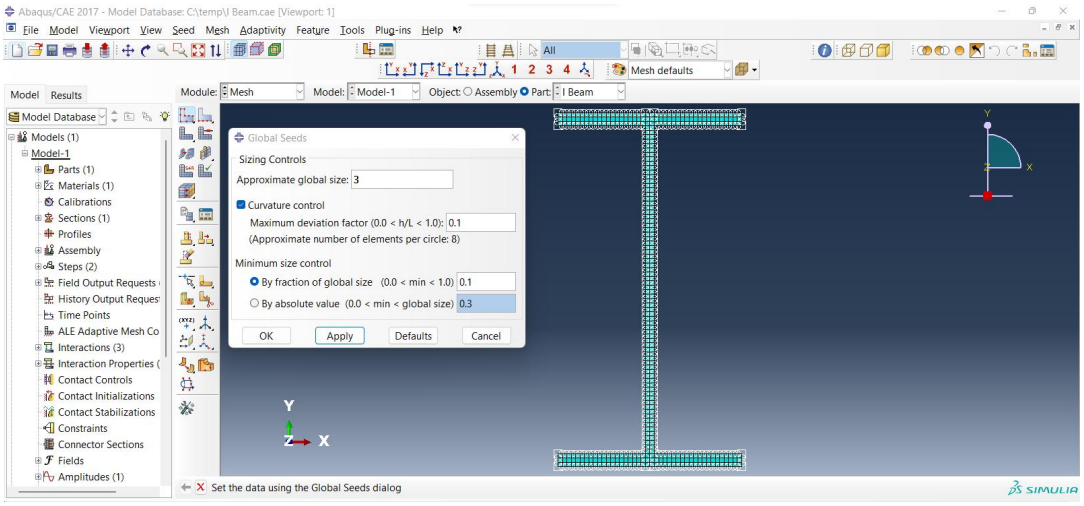

Figure 3. 7 – Meshing in Abaqus

VII. Running the Thermal Analysis

A transient heat transfer step seen in Figure 3.8 is executed to simulate temperature evolution over the fire duration. ABAQUS solves the heat transfer equations using the defined materials, mesh, and fire boundary conditions (Hodges *et al*, 2017). The simulation outputs temperature contours and time-dependent thermal gradients.

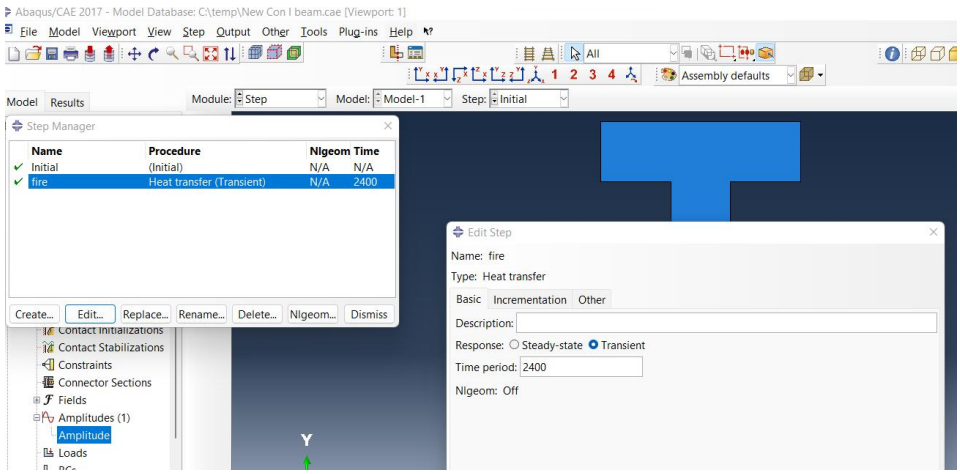

Figure 3. 8 – Transient Heat Transfer in Abaqus

VIII. Output Interpretation

The results obtained from the thermal analysis, including temperature distribution patterns, thermal gradients, and heating rates were extracted and organized for comparative assessment across the three beam configurations (Wang *et al*, 2013). These outputs provided the fundamental basis for evaluating the thermal performance of each beam type and formed the core of the discussion presented in Chapter Four.

3.3 Model Geometry

This section presents the geometric modelling of the three beam types used for the thermal analysis; the steel I-beam, the concrete I-beam, and the concrete rectangular beam. Each beam was modelled as a 2D cross-section as seen in Figure 3.9, representing the plane where heat transfer is most critical during fire exposure.

A 2D modelling approach was adopted instead of a full 3D model for the following reasons: Bridges exposed to fire typically experience relatively uniform heating along their longitudinal axis. Therefore, temperature variation primarily occurs across the cross-sectional depth and width, not along the span (Liu *et al*, 2023). This makes a 2D thermal section sufficient to capture realistic heat penetration. 2D cross-sectional model reduces simulation time while maintaining accuracy in temperature prediction (Zhang & Haghighat 2009). This study focuses specifically on temperature distribution, thermal gradients, and heat transfer mechanisms, all of which are governed by the cross-section's geometry rather than the beam length. Eurocode fire design methods and several FEM thermal studies show that 2D modelling is adequate for structural fire analysis when heat exposure is uniform along the member length (Rackauskaite *et al*., 2019).

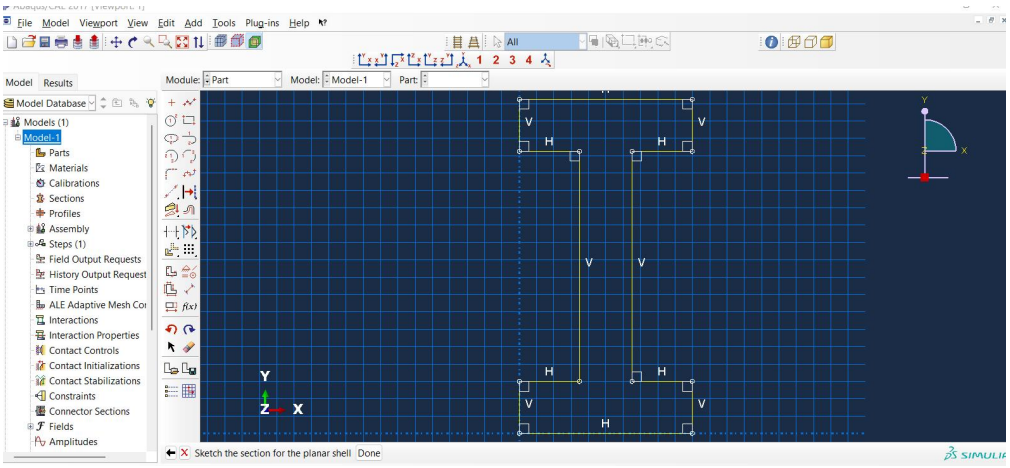

Figure 3. 9 - 2D Modelling Concept for Thermal Analysis.

3.3.1 Steel I-Beam Model

The suitable steel I-beam section selected for the analysis was the UKB 533 × 312 × 150 section, with a yield strength of 355 MPa. This section type was obtained using Tekla Tedds software where the bridge's length and width (from the case study) was modeled, and the most suitable steel beam details provided was UKB 533 × 312 × 150 as seen in APPENDIX B, also, the result of the increment analysis in Abaqus is seen in APPENDIX C. The steel grade of S275 failed in bending moment calculated though the shear force and deflection passed. The steel beam passed for bending moment, shear force and deflection with steel grade of S355 which aligned with eurocode 3 (Franssen & Zaharia, 2005) on recommended steel grade commonly used for bridges. Lower beam details selected failed in bending moment and shear force calculations, while suitable beam grades were UKB 533 × 312 × 150 and above. The overall dimension is given in Figure 3.10.

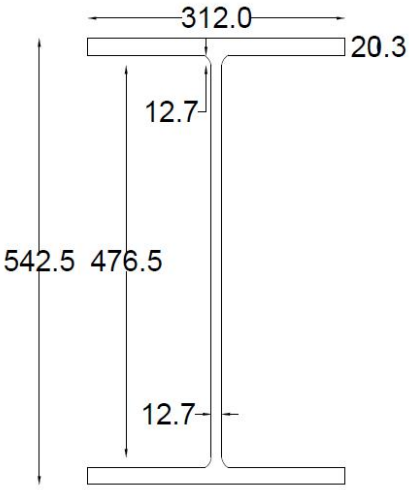

Figure 3. 10 – Geometry of Steel I Beam

3.3.2 Concrete I-Beam Model

The concrete I-beam was developed using realistic dimensions for a reinforced concrete girder (Beeby *et al*., 2005). The length of the case study bridge was incorporated in Tekla Tedds software to give a recommended dimension for the concrete I beam while adjustment where made in accordance to eurocode 2 (Beeby *et al*., 2005). The section was evaluated using standard high-yield steel grades (410, 460, and 500 N/mm²) to verify its capacity against flexural and shear failure. The analysis confirmed that Grade 460 steel reinforcement with C35 concrete satisfied all structural requirements. Details of the selected configuration and section dimensions are provided in Appendix D and Figure 3.11 respectively. Also, the result of the increment analysis in Abaqus is seen in APPENDIX E.

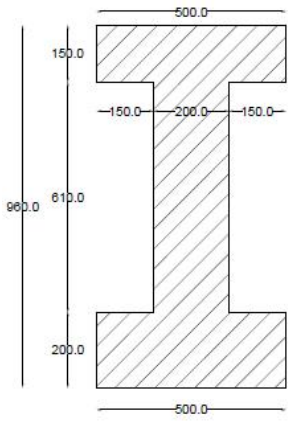

Figure 3. 11 – Geometry of Concrete I Beam

Since the simulation focuses only on thermal behavior, reinforcement bars were not explicitly modelled. Instead, the concrete region containing reinforcement was treated as a homogeneous thermal material, which is standard practice for heat-transfer-only analysis (Millard, & Pimienta, 2019).

3.3.3 Concrete Rectangular Beam Model

The dimensions for the concrete rectangular beam was obtained from onsite measurements of the University of Benin overhead pedestrian bridge (case study). These measurements were cross verified using Tekla Tedds software to assess reinforcement stability and determine the appropriate yield strength of the reinforced steel, which was found to be 460 MPa as lower yield strength didn't satisfy some checks in the reinforcement calculations seen in APPENDIX F, also, the result of the increment analysis in Abaqus is seen in APPENDIX G. The rectangular beam, Figure 3.12 provides an essential contrast because it lacks flanges, thin web regions, and complex contours present in the I-shaped sections.

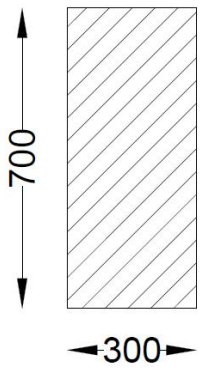

Figure 3. 12 – 2D Geometry of Rectangular Concrete Beam Dimension

3.4 Material Properties

This section presents the thermal material properties used in modelling the steel I-beam, concrete I-beam, and concrete rectangular beam. Since the study focuses purely on thermal analysis in ABAQUS, only temperature-dependent heat transfer properties were assigned, no mechanical or thermo-mechanical parameters were included. All properties were obtained

from Eurocode 3 (for steel) (Brown, 2018), Eurocode 2 (for concrete) (Beeby *et al.*, 2005), and supporting literature.

3.4.1 Thermal Properties of Steel

Steel properties were defined as temperature-dependent seen in Figure 3.13, to accurately capture heat penetration and the rapid temperature rise typical of structural steel under fire exposure.

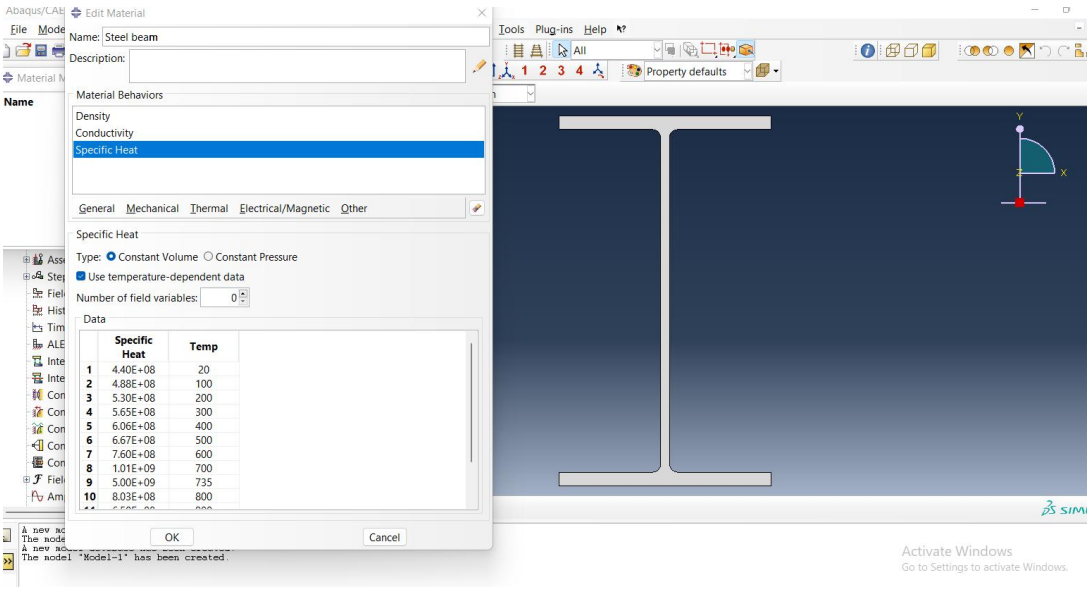

Figure 3. 13 - Thermal Properties of Steel

I. Density

ρ = 7850 kg/m³

(Constant with temperature)

II. Specific Heat Capacity (Cp)

The specific heat capacity for steel according to Eurocode 3 (Brown, 2018) is given in Equation 3.1 to Equation 3.4.

$20°C \leq \theta < 600°C$

$$C_a = 425 + 7.73 \times 10^{-1}\theta - 1.69 \times 10^{-3}\theta^2 + 2.22 \times 10^{6}\theta^3 \ J/KgK \quad (3.1)$$

$600°C \leq \theta < 735°C$

$$C_a = 666 + \frac{13002}{738 - \theta} \quad J/KgK \tag{3.2}$$

$735°C \leq \theta < 900°C$

$$C_a = 545 + \frac{17820}{\theta - 731} \quad J/KgK \tag{3.3}$$

$900°C \leq \theta \leq 1200°C$

$$C_a = 650 \ J/KgK \tag{3.4}$$

The results are shown in Table 3.1;

Table 3. 1 - Specific Heat Capacity Results from Eurocode 3

Specific Heat	Temperature
4.40E+08	20
4.88E+08	100
5.30E+08	200
5.65E+08	300
6.06E+08	400
6.67E+08	500
7.60E+08	600
1.01E+09	700
5.00E+09	735
8.03E+08	800
6.50E+08	900
6.50E+08	1000
6.50E+08	1100
6.50E+08	1200

III. Thermal Conductivity (k)

Thermal conductivity decreases with temperature as steel becomes less efficient in transferring heat. The thermal conductivity for steel according to Eurocode 3 (Brown, 2018) is given in Equation 3.5 to Equation 3.6 which gives results shown in Table 3.2

$20°C \leq \theta < 800°C$

$$\lambda_a = 54 - 3.33 \times 10^{-2}\theta \quad W/Mk \tag{3.5}$$

$900°C \leq \theta \leq 1200°C$

$$\lambda_a = 27.3 \quad W/Mk \tag{3.6}$$

where; Θ_a = Steel temperature (˚C).

Table 3. 2 - Thermal Conductivity Results from Eurocode 3

Thermal Conductivity	Temperature
53334	20
50670	100
47340	200
44010	300
40680	400
37350	500
34020	600
30690	700
27360	800
27300	1000
27300	1100
27300	1200

3.4.2 Thermal Properties of Concrete

Concrete was modelled as a temperature-dependent thermal material seen in Figure 3.14, reflecting its changing conductivity, and heat capacity, under fire exposure.

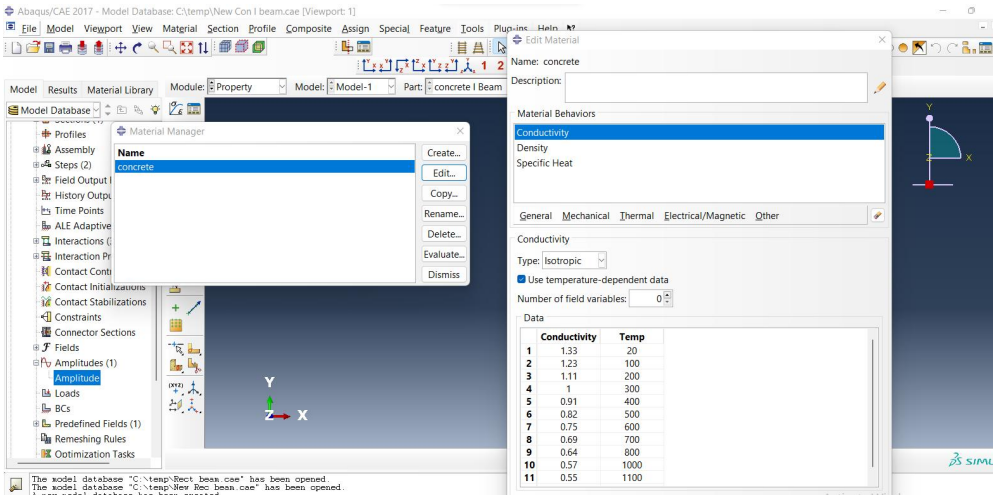

Figure 3. 14 - Thermal Properties of Concrete

I. Density

ρ = 2500 kg/m³

(Normal-weight concrete)

II. Specific Heat Capacity (Cp)

Concrete exhibits a peak in Cp between 100–200°C due to moisture evaporation. The specific heat capacity for concrete according to Eurocode 2 (Beeby *et al.*, 2005) is given in Equation 3.7 to Equation 3.10 which gives results shown in Table 3.3;

$20°C \leq \theta \leq 100°C$

$$\boldsymbol{C_p = 900\ J/KgK} \tag{3.7}$$

$100°C < \theta \leq 200°C$

$$\boldsymbol{C_p = 900 + (\theta - 100)\ J/KgK} \tag{3.8}$$

$200°C < \theta \leq 400°C$

$$\boldsymbol{C_p = 1000 + \frac{(\theta - 200)}{2}\ J/KgK} \tag{3.9}$$

$400°C < \theta \leq 1200°C$

$$\boldsymbol{C_p = 1100\ J/KgK} \tag{3.10}$$

Table 3. 3 - Specific Heat Capacity Results from Eurocode 2

Specific Heat	Temperature
900	20
900	100
1000	200
1050	300
1100	400
1100	500
1100	600
1100	700
1100	800
1100	1000
1100	1100
1100	1200

III. Thermal Conductivity (k)

Conductivity reduces as temperature increases concrete becomes more insulating during fire. The thermal conductivity for concrete according to Eurocode 2 (Beeby *et al*., 2005) is given in Equation 3.11 which gives results shown in Table 3.4;

$20°C \leq \theta \leq 1200°C$

$$\boldsymbol{\lambda_c = 1.36 - 0.136\left(\frac{\theta}{100}\right) + 0.0057\left(\frac{\theta}{100}\right)^2 \quad W/Mk} \tag{3.11}$$

where; Θ = Steel temperature (˚C).

Table 3. 4 - Thermal Conductivity Results from Eurocode 2

Thermal Conductivity	Temperature
1.33	20
1.23	100
1.11	200
1.00	300
0.91	400
0.82	500
0.75	600
0.69	700
0.64	800
0.57	1000
0.55	1100
0.54	1200

3.5 Thermal Load, Boundary Conditions and Fire Exposure

This section outlines the thermal loading conditions, fire curve definition, and boundary constraints used in modelling the thermal response of the steel I-beam, concrete I-beam, and rectangular concrete beam. Since the study focuses exclusively on temperature distribution, the applied loads consist only of convection, radiation, and temperature-time boundary conditions.

3.5.1 Fire Curve Definition

The fire exposure applied in this study was based on standard cellulosic fire curve, which is widely used in structural fire engineering (Neupane, 2020). The curve defines the evolution of gas temperature inside a fire compartment and follows the mathematical relationship:

Standard fire equation in accordance to eurocode 1 (Cook & Cook, 2007) is given in equation 3.12;

$$T = 20 + 345 \log(\mathbf{8}t + \mathbf{1}) \quad (3.12)$$

where; T = fire gas temperature (˚C)

t = time (minutes)

This fire curve represents a rapid temperature rise typical of a cellulosic fire (wood, paper, and normal building contents) (Neupane, 2020). The fire exposure was applied for 1200 seconds (20 min), 2400 seconds (40 min), and 3600 seconds (60 min) to capture short-, medium-, and long-duration heating phases.

In the finite element model, the fire temperature was applied using three thermal load components (Abdelrahman *et al*., 2025):

I. **Convection (film condition):** Representing hot gases interacting with the beam surfaces.
II. **Surface radiation:** Accounting for heat transfer by thermal radiation
III. **Temperature boundary condition (from ISO curve):** Applied as a time-dependent amplitude

This combination allows realistic simulation of heat transfer into the beam cross-section.

3.5.2 Thermal Boundary Application

To simulate realistic bridge fire exposure, the bottom flange and side faces of each girder were subjected to fire heating. These regions typically experience the highest temperatures (Aziz & Kodur, 2013) as the beams where modeled as an overhead bridge. The boundary conditions used for the thermal analysis includes convection and radiation as per Eurocode 1 (Cook & Cook, 2007).

I. **Convection – exposed surface**

Film condition coefficient (α_c) = 25w/m^{2}k

Surface film condition; sink temperature = 1

II. Convection – unexposed surface

Film condition coefficient (α_c) = 9w/m^{2}k

Surface film condition; sink temperature = 1

III. Radiation

Surface radiation as seen in Figure 3.15 – shows;

Emissivity = 0.7

Ambient temperature = 1

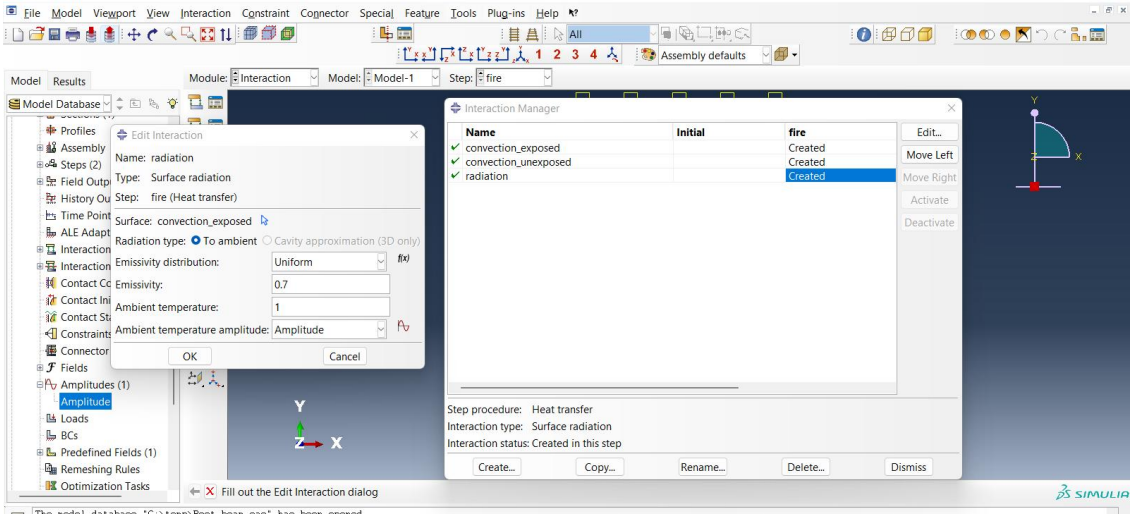

Figure 3. 15 – Surface Radiation

IV. Absolute Zero Temperature and Stefan-Boltzmann Constant

The absolute zero temperature of -273.16˚C was also used to develop the model. A Stefan-Boltzmann radiation constant was applied to simulate radiative heat transfer as per Eurocode 1 (Cook and Cook, 2007) and the value is 5.67×10^{-8} seen in Figure 3.16.

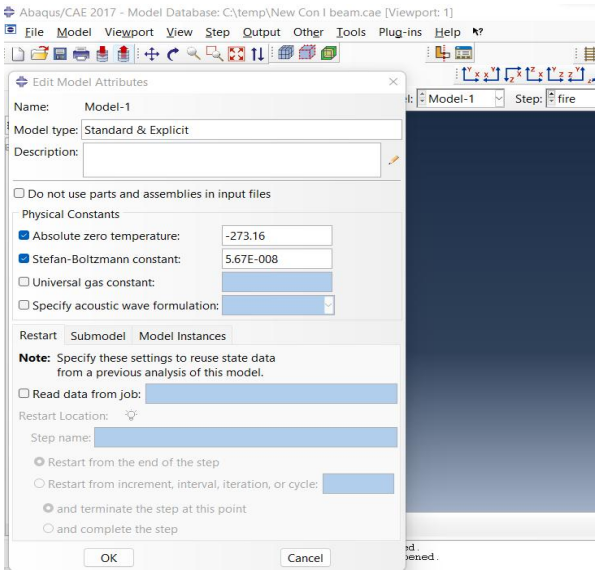

Figure 3. 16 - Absolute Zero Temperature and Stefan-Boltzmann Constant

V. Initial Temperature

Ambient temperature = 20˚C seen in Figure 3.17

In ABAQUS:

- The **film condition** was assigned to exposed surfaces to model convection.
- The **surface radiation interaction** was defined to account for radiative heat transfer between the fire gases and beam surfaces.

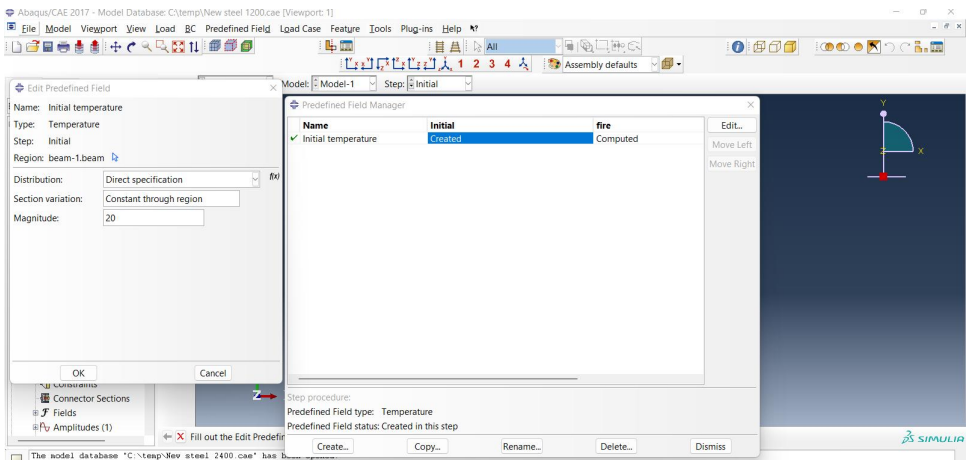

Figure 3. 17 – Initial Thermal Load

The upper surface of all beams (representing the deck interface) was assumed insulated (Al-Ansari *et al*., 2023), since it is not directly exposed to fire in typical bridge scenarios.

3.5.3 Amplitude Definition for Fire Curve

The fire curve temperature - time relationship was implemented in ABAQUS using a tabular amplitude definition following equation 3.12. The amplitude table, Table 3.5, contains pairs of values representing the frequency to gas temperature:

$$(t_i, T_i) \tag{3.12}$$

where; t = simulation time and T = corresponding gas temperature.

Table 3. 5 - Amplitude Table for Fire Curve

Time/frequency (t)	Amplitude (T)
0	20
300	948
600	1034
900	1071
1200	1087.6
1500	1095
1800	1098
2100	1099
2400	1100
2700	1100
3000	1100
3300	1100
3600	1100

This amplitude function ensures that the temperature applied to the beam surfaces increases gradually with time exactly according to the ISO curve (Xia *et al*., 2012) as seen in Figure 3.18

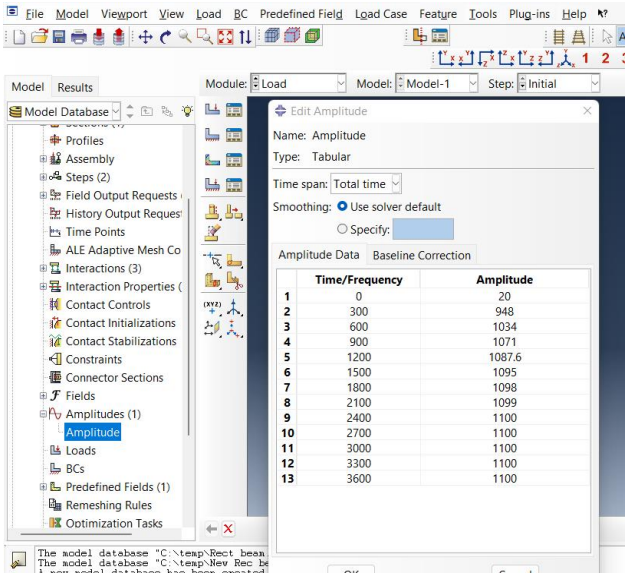

Figure 3. 18 - Thermal Load, Amplitude

ABAQUS then automatically interpolates between data points to apply a continuous heating profile throughout the analysis. This method allows accurate simulation of transient temperature fields and helps predict realistic thermal gradients within each beam type (Neupane, 2020).

3.6 Thermal Analysis Setup

This section describes the analysis procedures adopted for simulating the temperature distribution within the steel I-beam, concrete I-beam, and rectangular concrete beam. All simulations were carried out using a transient thermal analysis in ABAQUS to evaluate the evolution of temperature within each girder during fire exposure.

3.6.1 Analysis Type

A transient heat transfer analysis was selected for this study rather than a steady-state approach. Transient analysis captures the progression of heat penetration from the exposed surfaces into the beam depth, which is essential for understanding thermal gradients and insulation performance (Parthasarathi, 2024). Steady-state analysis assumes temperatures no longer change with time, which is unrealistic for fire behavior and unsuitable for modelling short- and medium-term thermal response (Parthasarathi, 2024). Transient heat transfer

therefore provides a more accurate representation of actual fire conditions, particularly during the first hour when temperature gradients are most severe.

3.6.2 Initial and Step Settings

All models were assigned an initial uniform temperature of 20˚C to represent ambient environmental conditions before fire exposure (Hesien *et al.*, 2025).

I. Total Time

The total simulation time was set within a realistic fire duration as seen in Figure 3.19;

- 1200 seconds (20minutes)
- 2400 seconds (40minutes)
- 3600 seconds (60minutes; 1 hour)

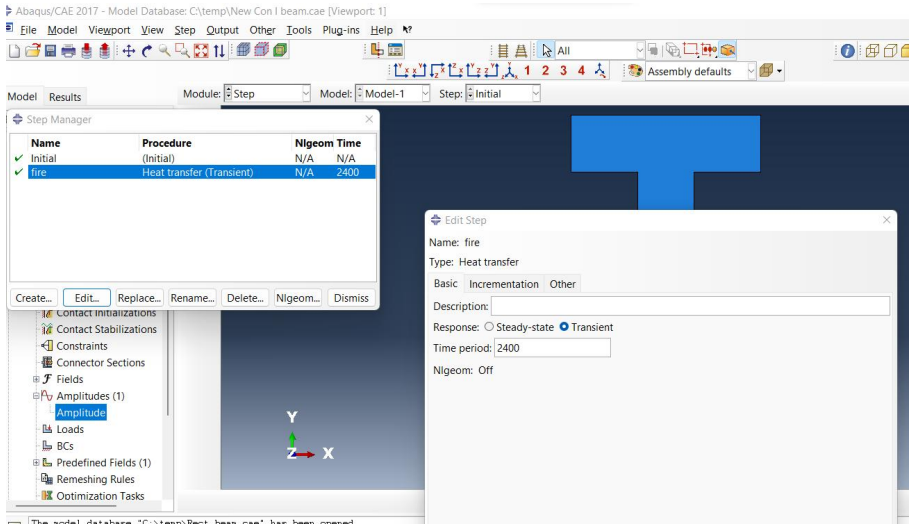

Figure 3. 19 - Total Time for Fire Exposure

II. Time Increment Settings

ABAQUS automatic time incrementation was used, allowing the solver to adjust step size based on heat transfer stability limits seen in Figure 3.20. Finer increments were applied in the early stage of heating because temperature rises rapidly in the first few minutes of the ISO 834 curve (Koric *et al.*, 2009).

Role of Increment Size:

- Ensures numerical stability of the solution.

- Improves accuracy by capturing steep temperature gradients.
- Prevents divergence when sudden thermal changes occur.
- Allows the software to take larger increments later when the temperature increase becomes gradual.

Proper increment control is therefore essential to obtaining realistic thermal histories throughout the beam's cross-section.

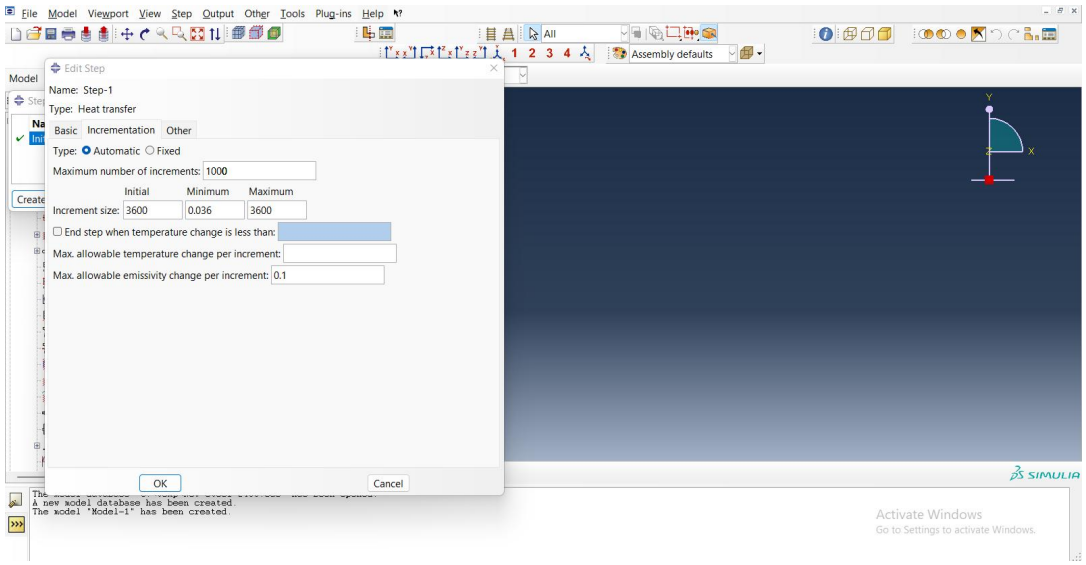

Figure 3. 20 - Increment Sizes Setting

3.6.3 Meshing and Element Type

Meshing is a critical step in thermal analysis, as it influences the accuracy of heat flow predictions. A suitable global seed size, seen in Figure 3.21 was applied to ensure uniform mesh distribution while maintaining computational efficiency (Tang *et al*., 2020).

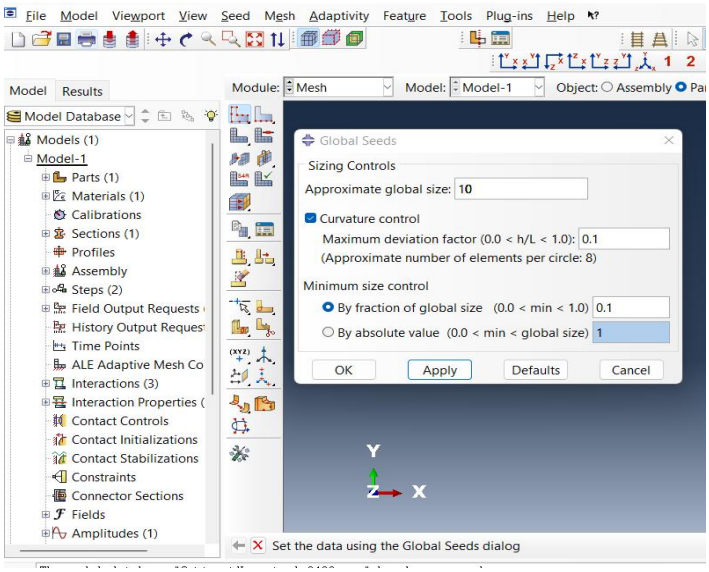

Figure 3. 21 - Meshing with Global Seed

I. Element Type

Because the study focuses solely on temperature distribution through the beam cross-section, a 2D planar heat transfer element was used: DC2D4 - 4-node bilinear heat transfer quadrilateral element; seen in Figure 3.22. This element type is appropriate for modelling transient heat conduction in solid sections (Dal-Sasso, *et al*., 2023).

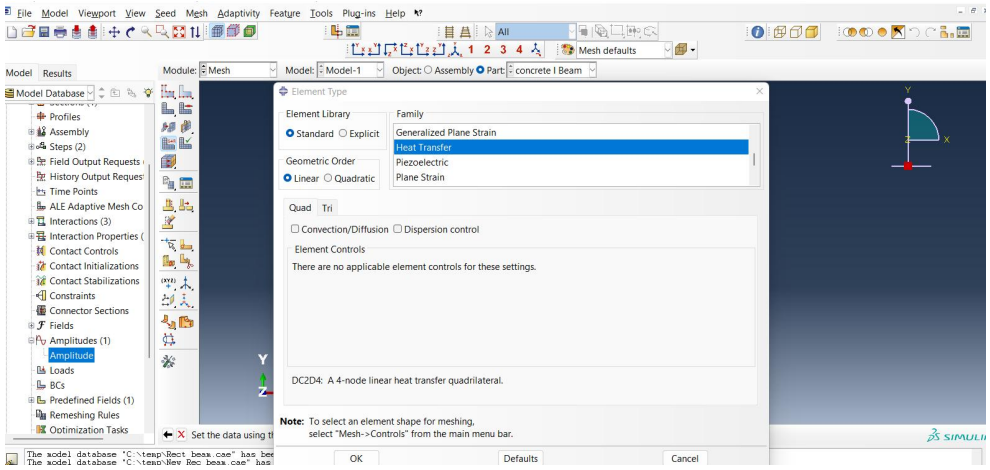

Figure 3. 22- Element Type

3.7 Model Steps for Each Beam Type

This section outlines the modeling procedure adopted for the three beam configurations analyzed in the thermal study. Although all models followed the same general workflow;

geometry creation, assignment of thermal properties, application of fire boundary conditions, and transient heat-transfer simulation; the specific considerations for each beam type differed based on geometry and material behavior.

3.7.1 Steel I-Beam Model

I. Geometry

The steel beam, Figure 3.23 was modeled as a standard I-section consisting of a top flange, bottom flange, and web. Only the cross-section was required since the analysis focused on two-dimensional heat transfer.

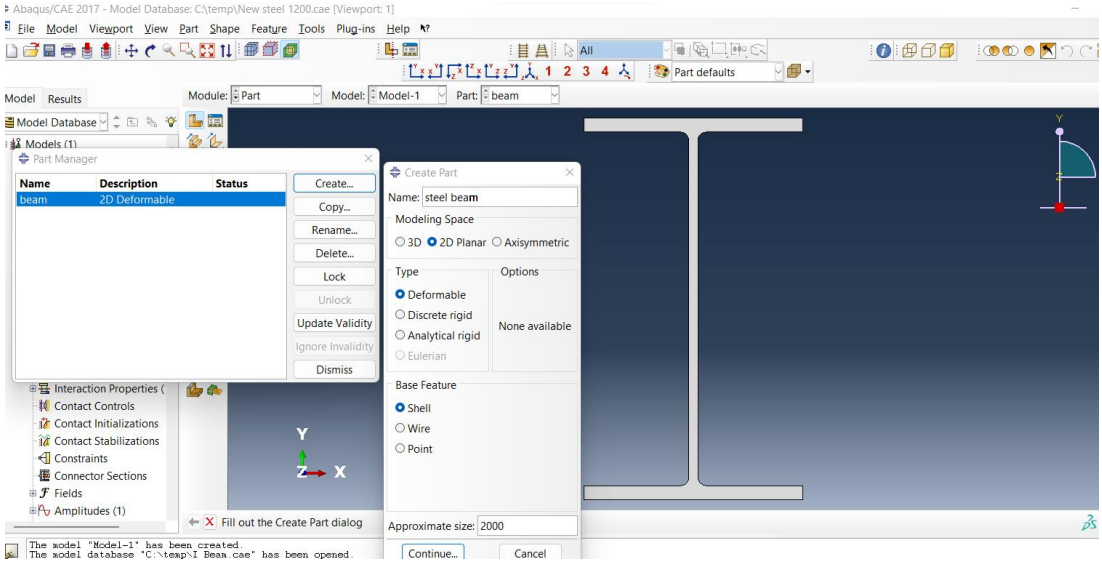

Figure 3. 23 – Steel I-Beam Model

II. Material Definition:

Temperature-dependent thermal properties for structural steel; thermal conductivity, specific heat, and density; were assigned as seen in Figure 3.24. This is important because steel's conductivity increases heat penetration speed and strongly influences temperature distribution.

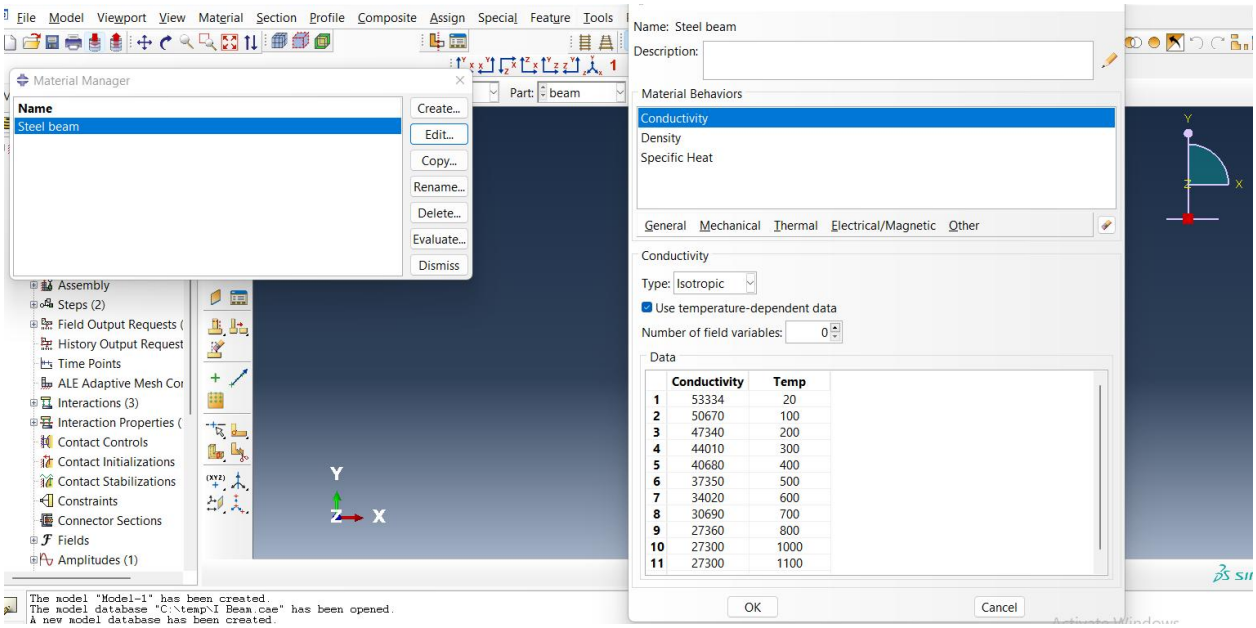

Figure 3. 24 – Material Properties of Steel I-Beam

III. Step Time

Different step time simulations were carried out; 1200 seconds (20minutes), 2400 seconds (40minutes), 3600 seconds (60minutes; 1 hour) seen in Figure 3.25. This relates the amount of time the beam was exposed to fire while other parameters remained the same.

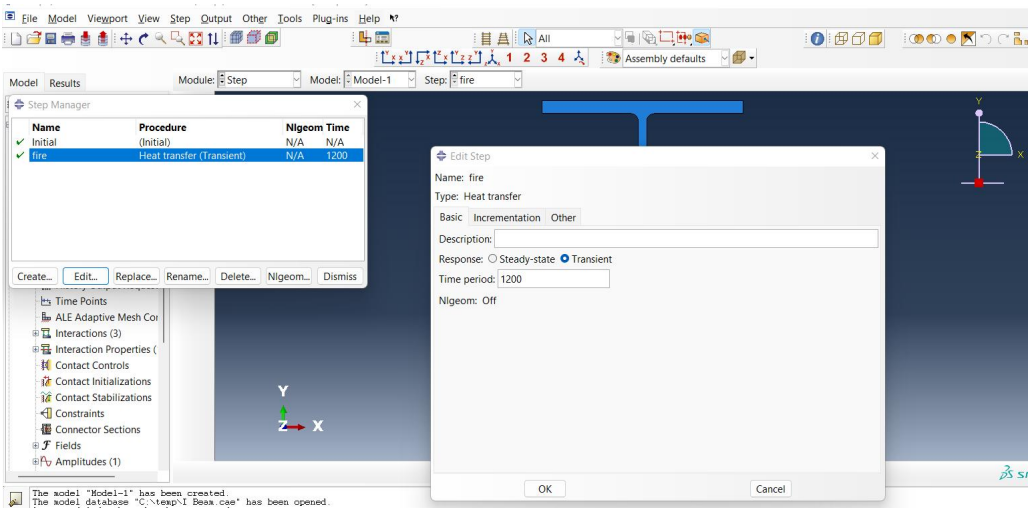

Figure 3. 25 – Step Time for Fire Exposure

IV. Fire Exposure:

After the thermal load was applied, the amplitude, fire action was applied along the bottom flange and the two sides of the web, representing typical exposure conditions in real bridge or

building fires. These surfaces seen in Figure 2.26 received both convection and radiation heat fluxes derived from the standard fire curve, while the unexposed surface of the beam is seen in Figure 3.27.

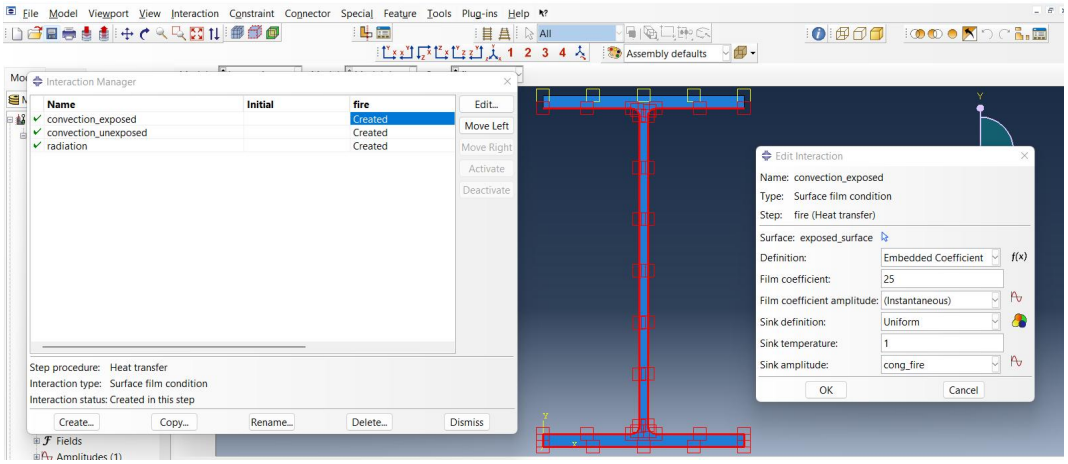

Figure 3. 26 – Exposed Surface

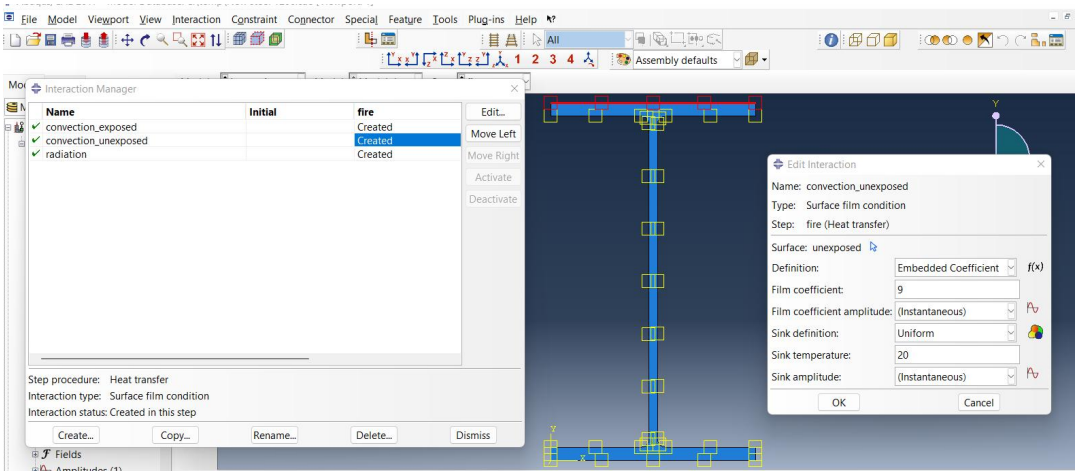

Figure 3. 27 – Unexposed Surface

V. Meshing

The meshing of the steel I-beam was done using global seed size of 8 which after analysis produced results of total number of element to be 446 and total number of nodes to be 606.

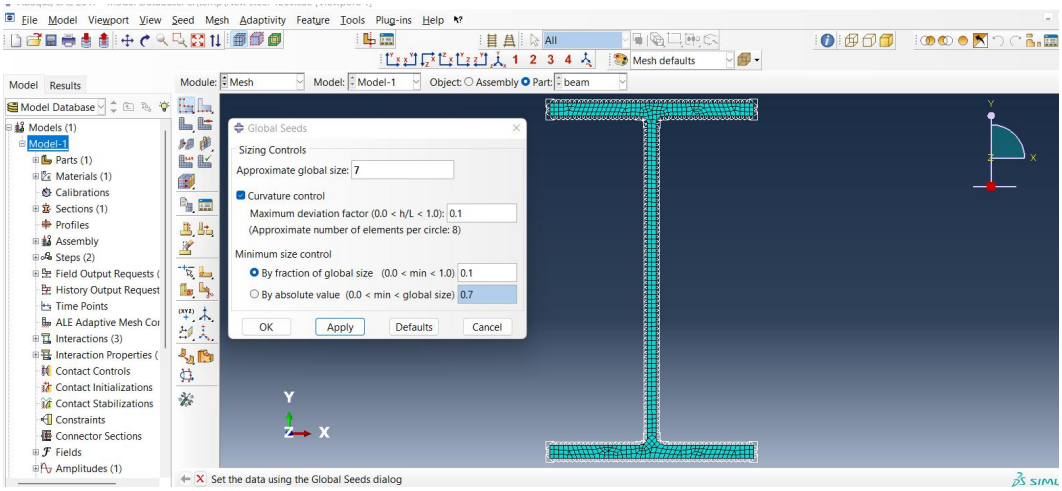

Figure 3. 28 – Meshed Steel I-Beam

VI. Job Module

This phase involved the checking of all data inputted into the software and submitting them for simulation as seen in Figure 2.29 and this is what produces the thermal results which will be discussed in the next chapter.

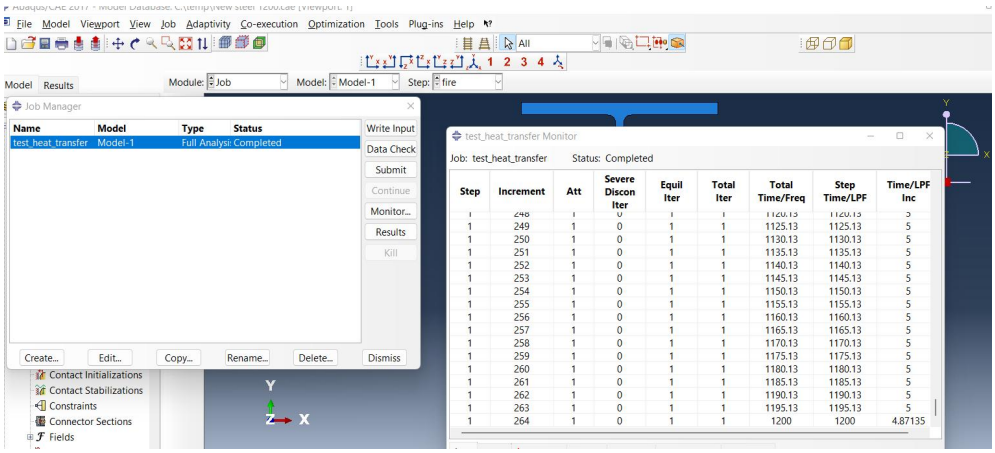

Figure 3. 29 - Job Module

3.7.2 Concrete I-Beam Model

I. Geometry:

This section was modeled as a reinforced concrete I-beam comprising a wide top flange and a thicker web. The concrete's heterogeneous nature was simplified into a homogeneous equivalent material for thermal analysis seen in Figure 3.30.

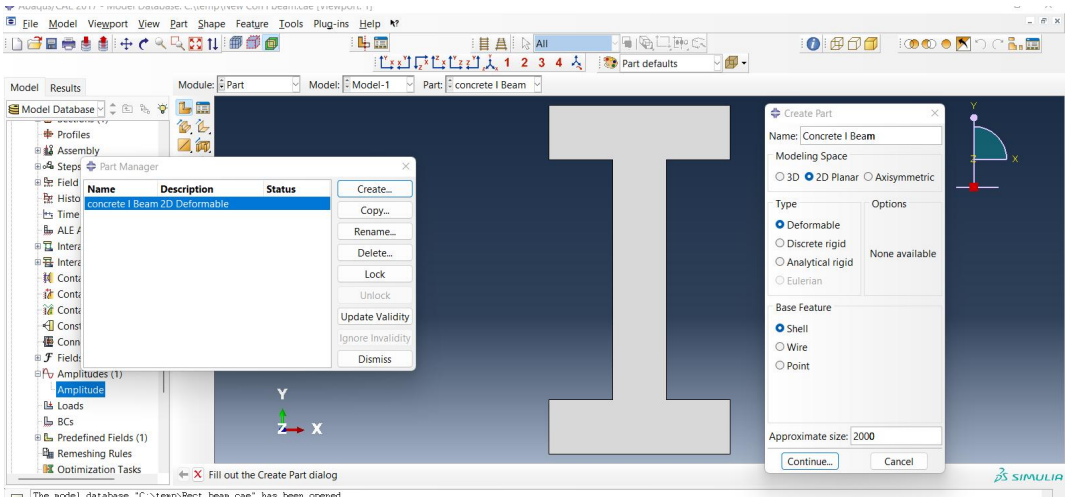

Figure 3. 30 – Concrete I-Beam Model

II. Material Definition:

Concrete thermal properties; thermal conductivity, density, and specific heat, were defined as temperature-dependent seen in Figure 3.31. Concrete exhibits relatively low thermal conductivity, which slows heat penetration.

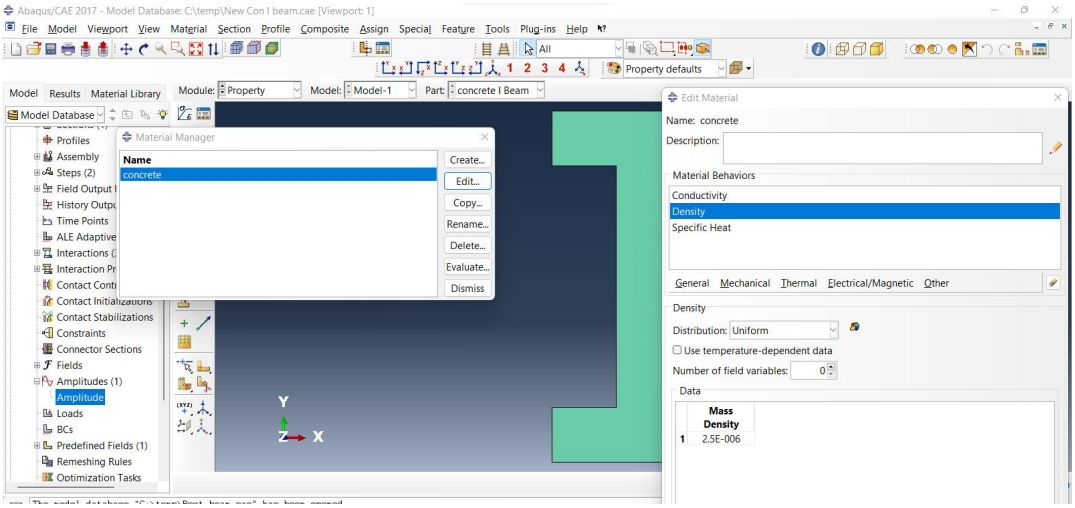

Figure 3. 31 – Material Definition

III. Step Setting

Different step time simulations as performed in the Steel I-beam were also carried out; 1200 seconds (20minutes), 2400 seconds (40minutes), 3600 seconds (60minutes; 1 hour) seen in Figure 3.32. This relates the amount of time the beam was exposed to fire while other parameters remained the same.

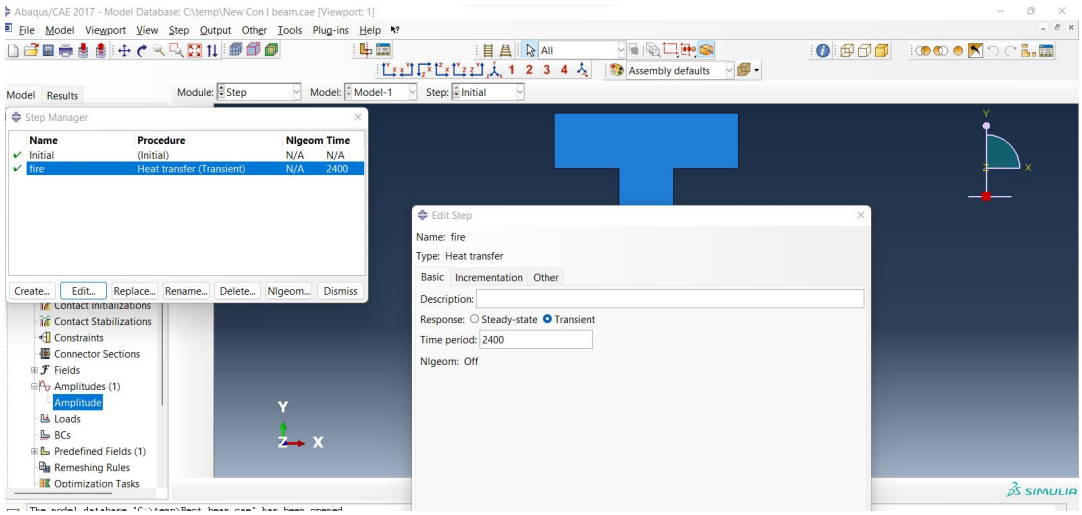

Figure 3. 32 – Step Time for Fire Exposure

IV. Fire Exposure:

The beam was exposed on the bottom surface and the two vertical web surfaces, Figure 3.33 following realistic exposure of the over-head bridge, while the unexposed surface was also noted as seen in Figure 3.34. thermal load was applied before the analysis was carried out.

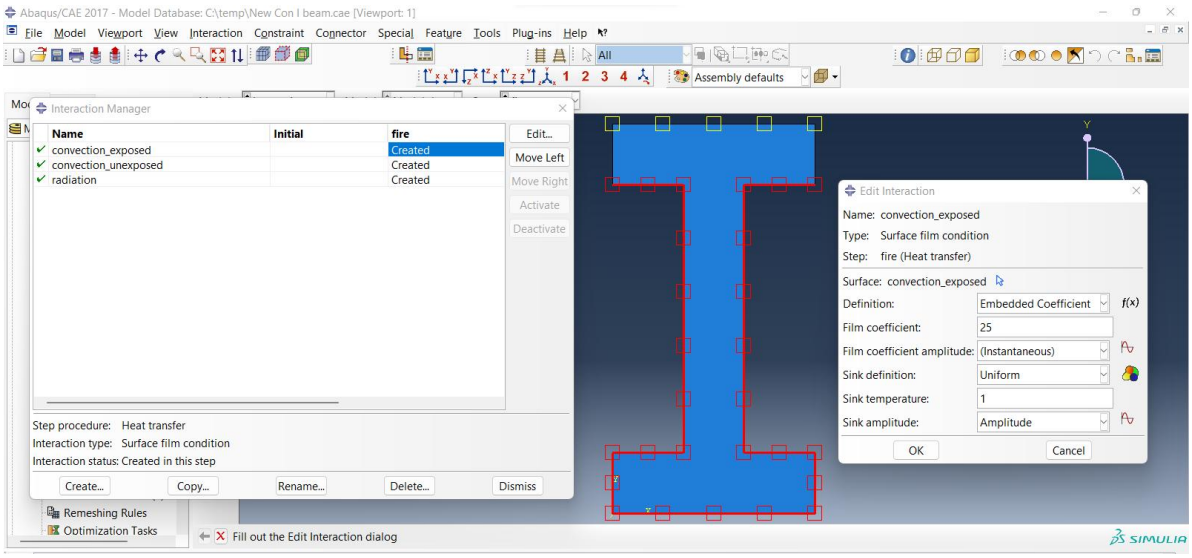

Figure 3. 33 – Exposed Surface

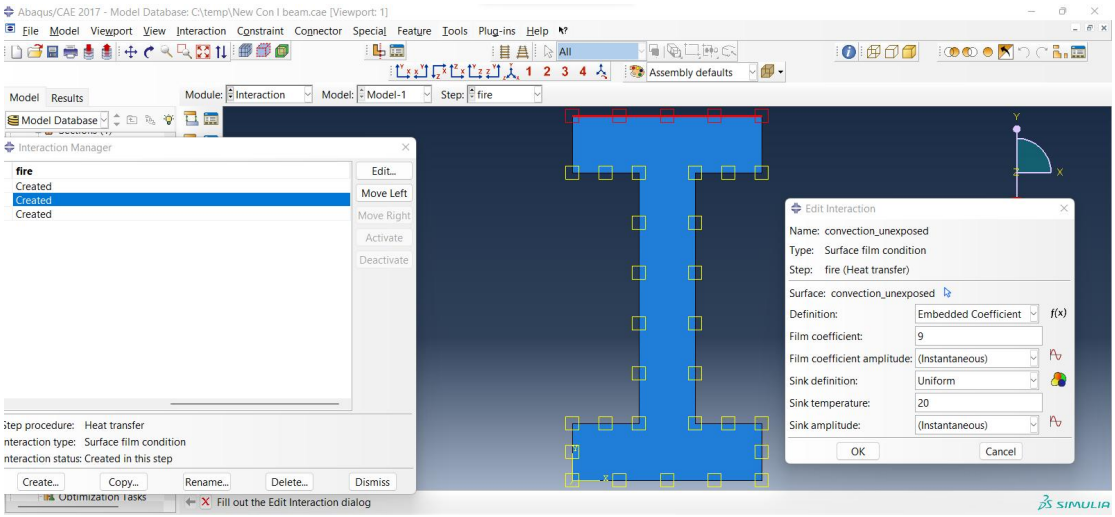

Figure 3. 34 – Unexposed Surface

V. Meshing

The meshing of the concrete I-beam was done using global seed size of 15 seen in Figure 3.35 which after analysis produced results of total number of element to be 1195 and total number of nodes to be 1307.

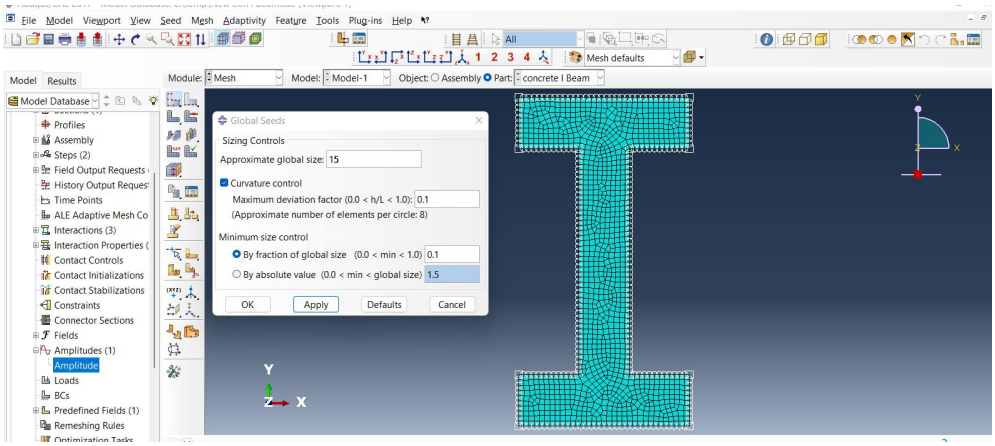

Figure 3. 35 – Meshed Concrete I-Beam

VI. Job Module

This phase involved the checking of all data inputted into the software and submitting them for simulation as seen in Figure 3.36 and this is what produces the thermal results which will be discussed in the next chapter.

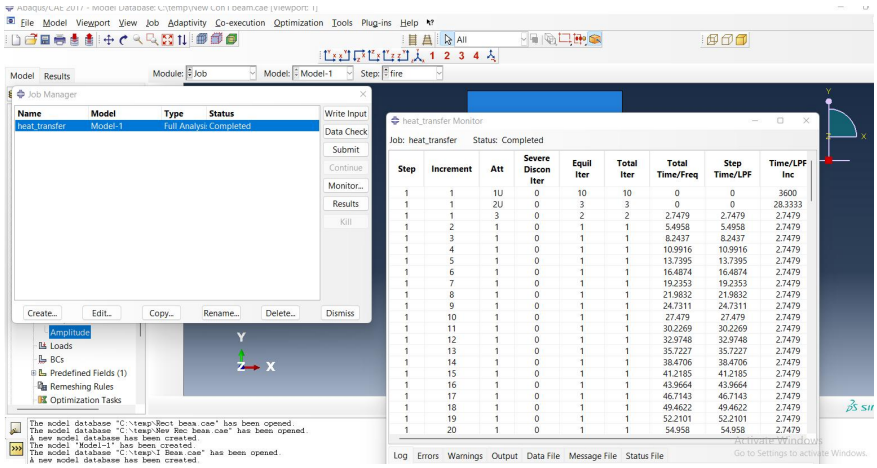

Figure 3. 36 - Job Module

3.7.3 Rectangular Concrete Beam

I. Geometry:

This section was modeled as a rectangular concrete beam. The concrete's heterogeneous nature was simplified into a homogeneous equivalent material for thermal analysis seen in Figure 3.37.

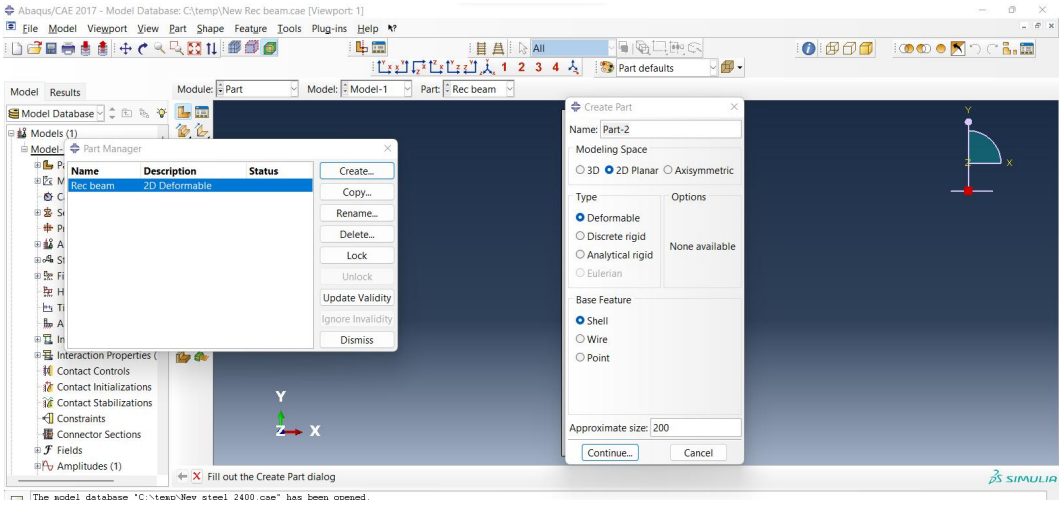

Figure 3. 37 – Rectangular Concrete Beam Model

II. Material Definition:

Thermal properties identical to the concrete I-beam model were used, in Figure 3.38. This allows a meaningful comparison of temperature distribution across different geometrical forms.

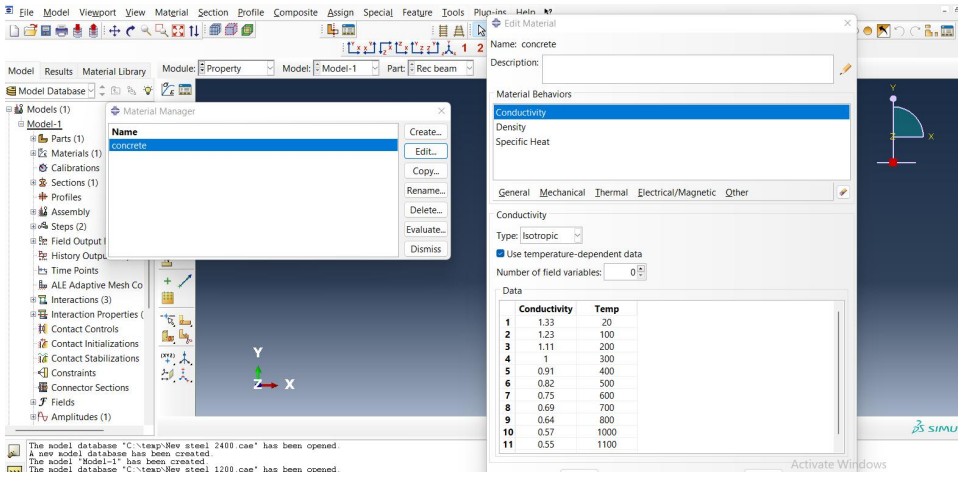

Figure 3. 38– Material Definition

III. Step Setting

Different step time simulations as performed in the Concrete I-beam were also carried out; 1200 seconds (20minutes), 2400 seconds (40minutes), 3600 seconds (60minutes; 1 hour) seen in Figure 3.39.

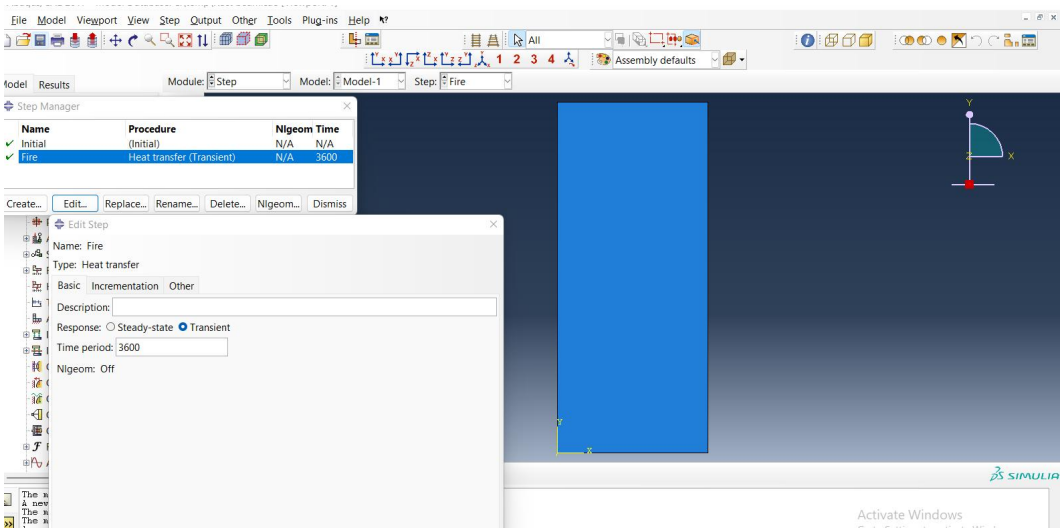

Figure 3. 39– Step Time for Fire Exposure

IV. Fire Exposure:

The same boundary conditions used in the previous models as well as the thermal load, amplitude were applied to ensure consistency bottom and sides exposed to convection and radiation as seen in Figure 3.40 and in Figure 3.41.

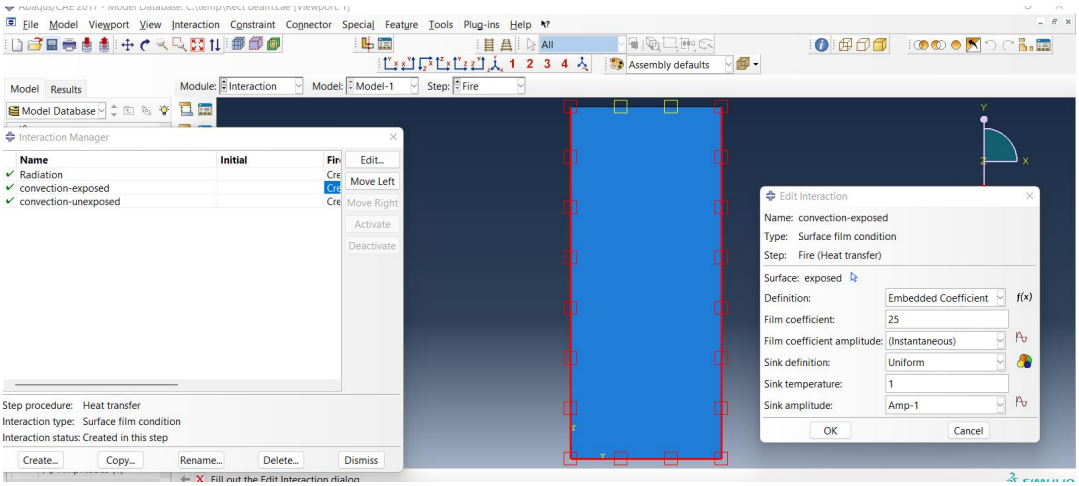

Figure 3. 40– Exposed Surface

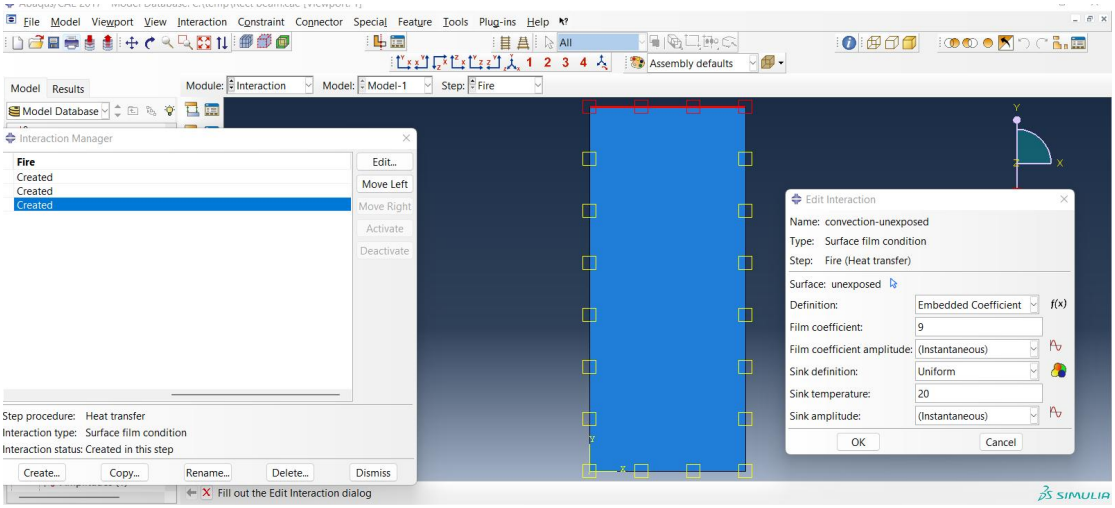

Figure 3. 41 – Unexposed Surface

V. Meshing

The meshing of the concrete rectangular beam was done using global seed size of 10, Figure 3.42 which after analysis produced results of total number of element to be 2100 and total number of nodes to be 2201.

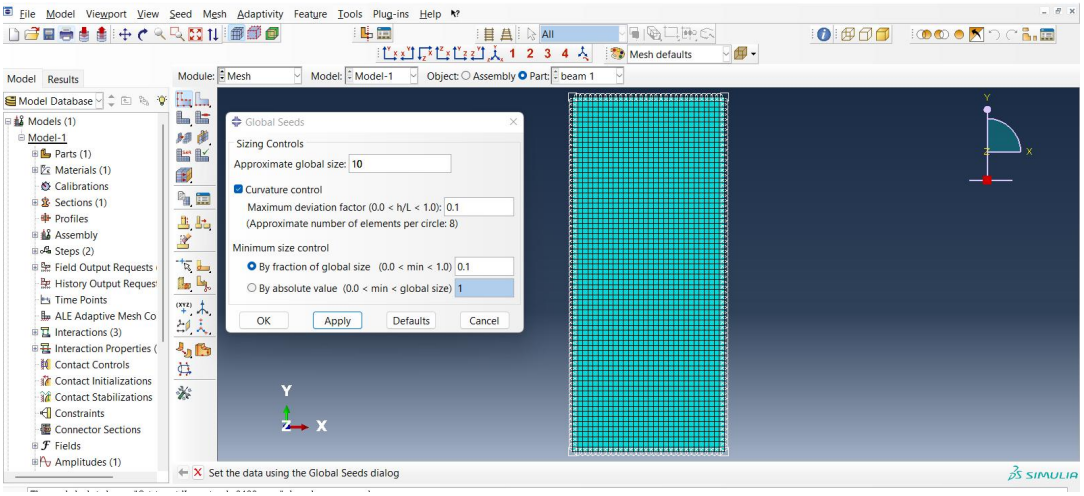

Figure 3. 42– Meshed Rectangular Concrete Beam

VI. Job Module

This phase involved the checking of all data inputted into the software and submitting them for simulation as seen in Figure 3.43 and this is what produces the thermal results which will be discussed in the next chapter.

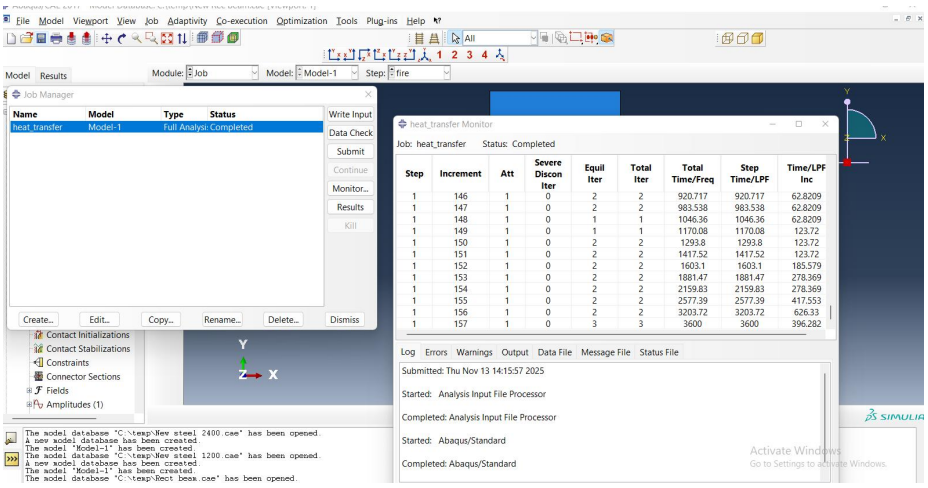

Figure 3. 43- Job Module

3.8 Model Validation

During the model validation phase, the accuracy and reliability of the developed finite element model (FEM) were assessed by comparing its output with established data from existing literature. The objective was to ensure that the FEM model could accurately predict the thermal effects, material degradation, and structural responses of bridge components

under fire conditions. Validation served as a crucial step in verifying that the model could be used confidently for further analysis and design recommendations (Hicks *et al*., 2015).

3.8.1 Comparison of Different Model Data

This process ensured that the validation comparisons of the different models were both meaningful and applicable. In the thermal response validation, simulated temperature distributions were compared with observed values from selected literature or experiments. This comparison evaluated the FEM model's ability to replicate heat transfer and the temperature rise in key bridge components over time (Curto *et al*., 2022).

3.8.2 Thermal Response Analysis:

The thermal response analysis focused on evaluating how heat affected the bridge structure during fire exposure. Key outputs from this analysis includes:

I. Temperature Contours:

This involved visualizing the heat distribution within the bridge components. Temperature contours showed how heat spread through the structure, identifying areas that experienced the highest temperatures, which helped in predicting potential points of failure (Abid *et al*., 2022). This was summarized in the temperature legend in the final result.

3.9 Parametric Study

The parametric analysis assessed the effect of bridge section type and material type on the behavior and performance of the girder after fire exposure (Song *et al*., 2021). The analysis covered the loss of load-bearing capacity and the residual strength of the girder section.

3.9.1 Section Type

The geometry of each girder section had a major influence on its thermal response. Beams with larger surface-area-to-volume ratios, such as steel I-sections, heated up faster because more of their surface was directly exposed to fire (Saari, 2019). This rapid heat absorption led to quicker temperature rise and faster reduction in strength. In contrast, compact sections like

rectangular concrete beams showed slower heat penetration, as their thicker cross-section provided better insulation and delayed the temperature increase at the core (Siebers *et al*., 2016). The section shape also affected thermal deformation, with open sections experiencing more distortion under uneven heating (Golewski, 2023). Overall, the geometry strongly influenced how quickly each girder reached critical temperatures and how much residual strength it retained after exposure.

3.9.2 Material Type

Material type also played a critical role in how each girder behaved during thermal loading. Steel, with its high thermal conductivity, heated rapidly and lost strength quickly as temperatures increased (Zhou *et al*., 2024). Concrete heated more slowly due to its lower conductivity and higher heat capacity, but it was susceptible to cracking or surface spalling as moisture expanded (Amran *et al*. 2022). Reinforced concrete had an additional concern: elevated temperatures weakened the bond between steel reinforcement and concrete, affecting its load-carrying performance. Each material experienced reductions in stiffness and strength as temperatures increased, but at different rates (Abambres *et al*., 2016). These differences determined how much residual capacity remained after heating and influenced whether the girder could continue serving its function or required strengthening.

3.10 Post-Fire Damage Assessment

Post-fire assessment was a critical process used to evaluate the material properties, and overall safety of bridge structures after exposure to fire. It involved determining the extent of thermal damage, residual strength of materials, and functionality of the bridge components (Nicoletta *et al*., 2020). Several post-fire conditions were assessed for proper evaluation, and these included the following:

3.10.1 Percentage of Residual Strength

The assessment of the percentage of residual strength in fire-exposed bridge structures using Abaqus involved simulating the thermal responses to determine the remaining load-bearing capacity (Gil, 2024). The process began with the creation of a detailed finite element model of the bridge component, incorporating accurate material properties and geometric details. Fire exposure was simulated by applying thermal loads, allowing Abaqus to compute the resulting temperature distribution within the structure. The temperature profiles produced after the simulation were used to adjust material properties, reflecting the degradation due to elevated temperatures (Abid *et al*., 2022). Using Eurocode 3 (for steel) (Brown, 2018), Eurocode 2 (for concrete) (Beeby *et al*., 2005), the reduction factor (*k*) was obtained in line its respective temperature looked out for and was multiplied by 100% to get the percentage strength seen in Equation 3.13. This reduction factor was multiplied by the compressive strength of the concrete and the yield strength of the steel in order to obtain the remain residual strength left in the beam after exposure to fire as seen in Equation 3.14.

$$\textbf{Percentage of Residual Strength} = \textbf{Reduction Factor } (\mathbf{k}) \times \mathbf{100}\% \tag{3.13}$$

$$\textbf{Residual Strength} = \textbf{ Reduction Factor } \times \textbf{ Yield or Compressive Strength} \tag{3.14}$$

3.10.2 Spalling of Concrete

The assessment of spalling in concrete structures exposed to fire using Abaqus software involved simulating the thermal behavior that led to surface layer detachment. The process began with the development of a detailed finite element model of the concrete component, incorporating its geometric and material properties (Mohammed *et al*., 2022). The results from the simulation provided insights into the extent and severity of spalling. According to literature by Amran *et al*. (2022), spalling typically began at temperatures around 300˚C (572˚F) and became more pronounced as temperatures increased.

3.11 Application to a Case Study Bridge

The case study investigated the thermal behavior of the University of Benin pedestrian flyover bridge, Figure 3.44, by analyzing the 2D temperature response of its girder cross-sections under simulated fire exposure. The finite element model was developed to represent only the girder section rather than the complete bridge structure, enabling a focused assessment of heat transfer, temperature gradients, and heating patterns within the steel and concrete components.

Figure 3. 44 - University of Benin Pedestrian Bridge

The dimensions for the composite girder was obtained from onsite measurement which was cross checked using Tekla Tedds software in order to cross check its reinforcement stability and provide suitable yield strength of the reinforced steel which gave 450Mpa and the result from this analysis is found in APPENDIX H with Figure 3.45 and Figure 3.46 showing graphical detail of the measurement used for the calculation. Also, the result of the increment analysis in Abaqus is seen in APPENDIX I. The dimensions as shown in Figure 3.45 was used to model the composite girder and with meshed model as seen in Figure 3.47. After the simulation, the number of nodes which formed the mesh for the composite girder was 3456 nodes and 3288 elements.

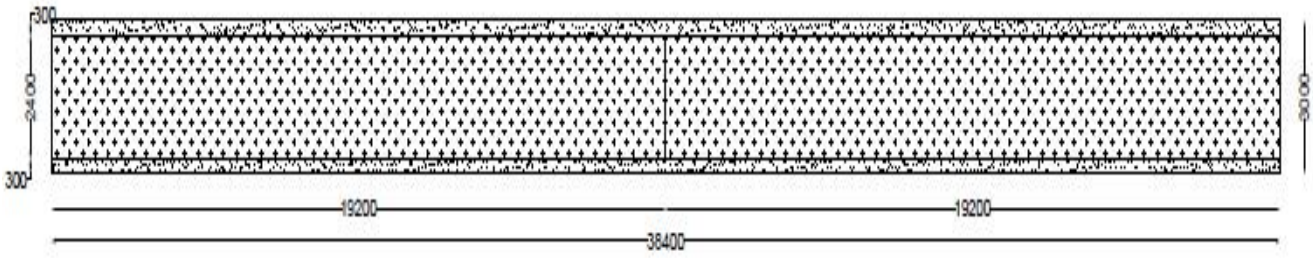

Figure 3. 45 - Bridge Dimension (mm)

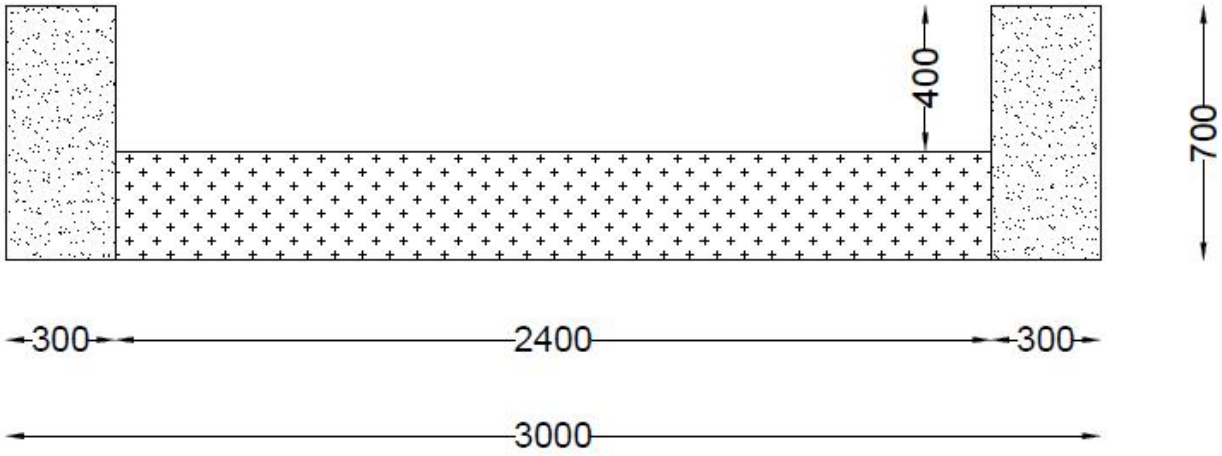

Figure 3. 46 - Dimension (in mm) of the Composite Girder Cross-Section

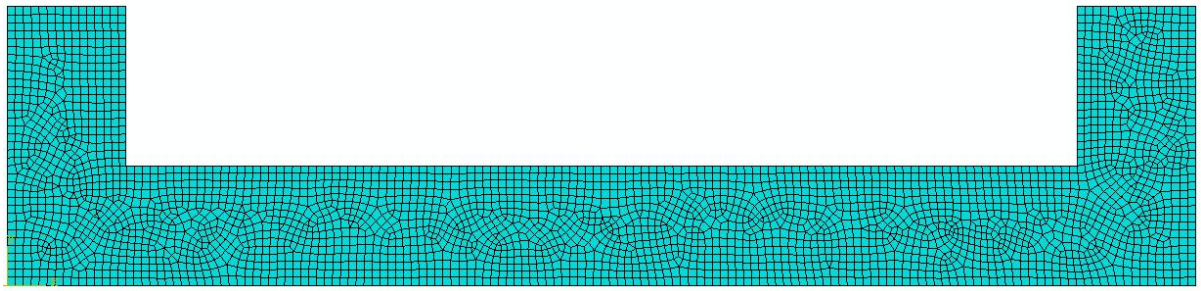

Figure 3. 47 - Meshed Model of the Composite Girder

I. Geometry:

The composite girder cross-section was modelled in 2D in which the geometry was drawn to capture accurate dimensions, interface regions, and heat-transfer paths across the section seen in Figure 3.48.

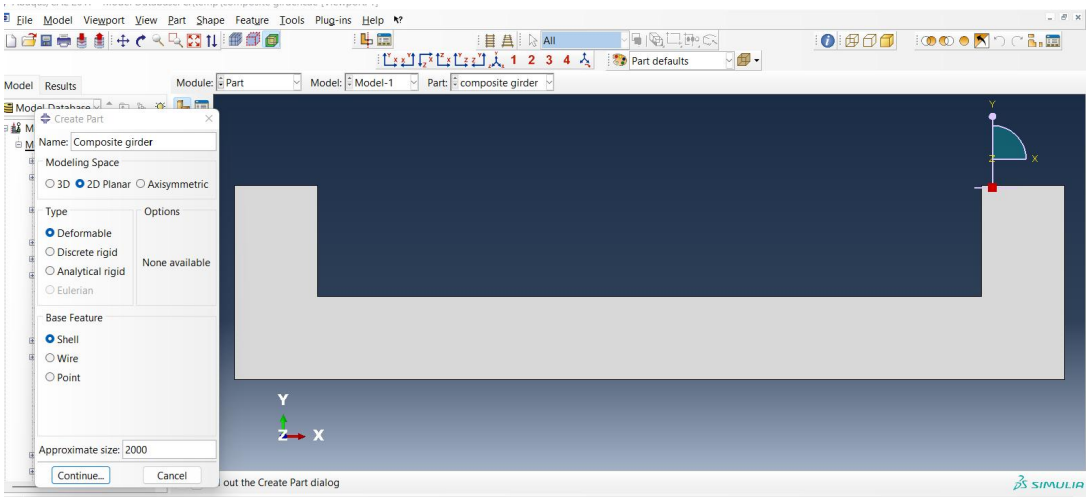

Figure 3. 48 - Composite Girder Model

II. Material Definition:

Temperature-dependent thermal properties were assigned to the composite girder, including thermal conductivity, specific heat capacity, and density seen in Figure 3.49. These properties ensured that the model captured realistic heat penetration, insulation effects, and variations in thermal behavior at elevated temperatures.

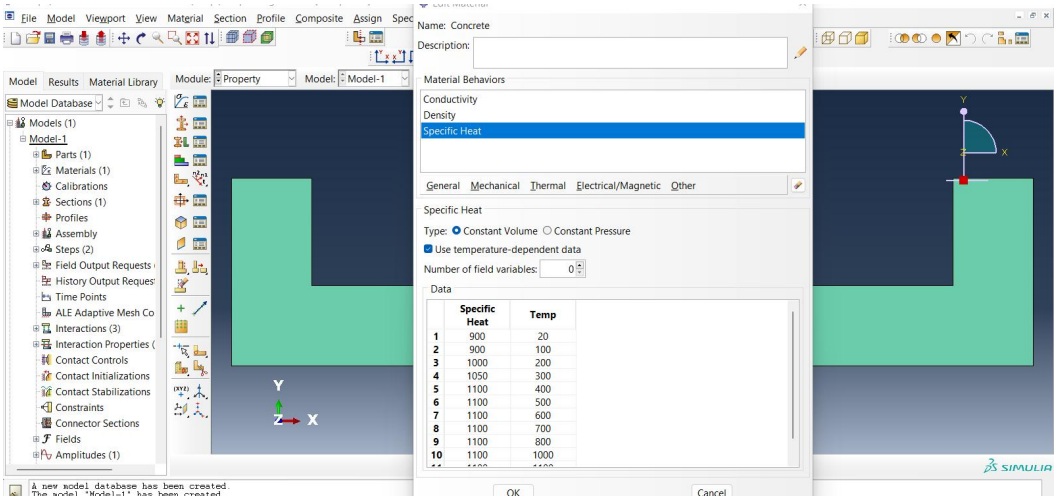

Figure 3. 49 – Material Definition

III. Step Setting

A transient heat-transfer step was created to simulate the time-dependent temperature response during fire exposure. The step controlled the duration of heating, the increment size,

and the solution procedure required to track temperature evolution throughout the girder section seen in Figure 3.50.

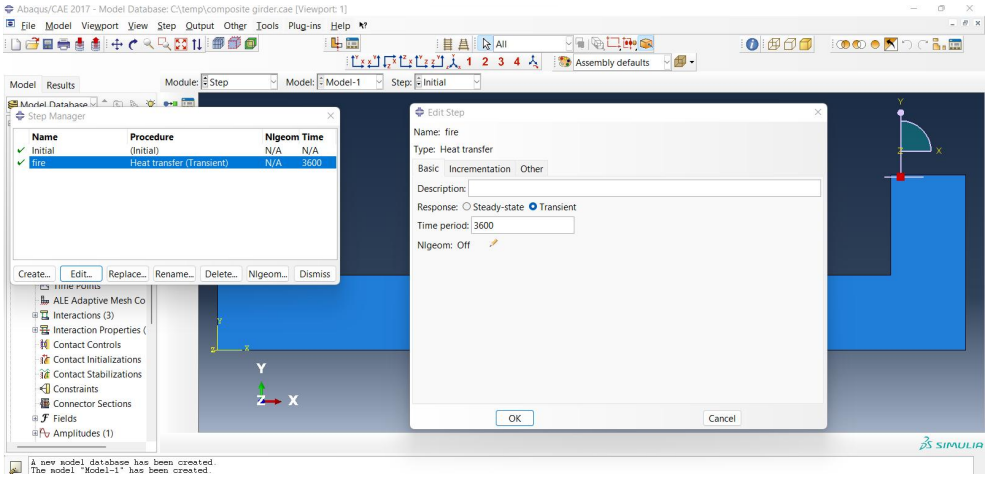

Figure 3. 50 – Step Time for Fire Exposure

IV. Fire Exposure:

Fire loading was applied using the ISO standard fire curve, introduced as a temperature-time boundary condition on the exposed surfaces, Figure 3.51 and identifying the unexposed surface, Figure 3.52. Convection and radiation coefficients were included to reflect external heat transfer, while conduction governed internal heat flow within the composite section.

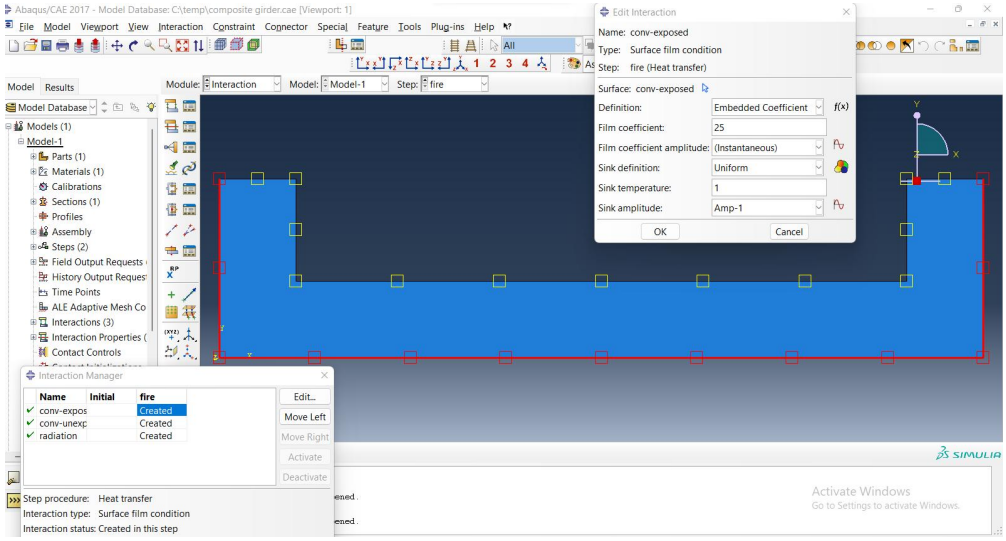

Figure 3. 51– Exposed Surface

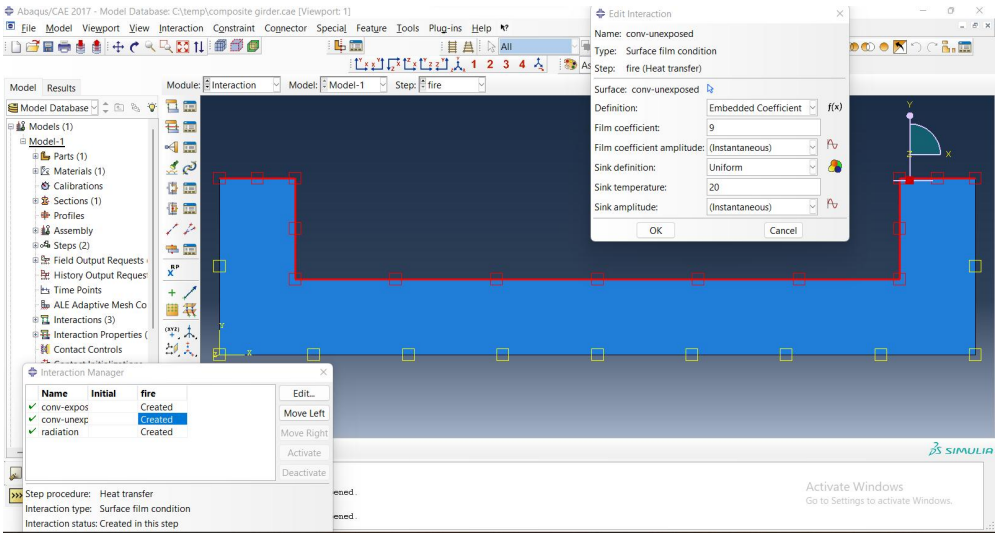

Figure 3. 52 – Unexposed Surface

V. Meshing

The geometry was discretized using structured quadrilateral heat-transfer elements with global seed size of 10 as seen in Figure 3.53. After analysis, the results produced, total number of element to be 2100 and total number of nodes to be 2201.

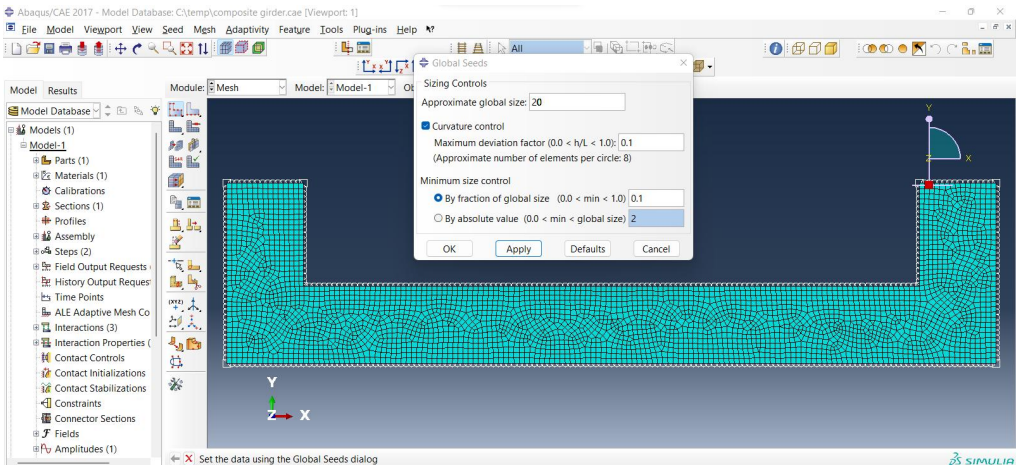

Figure 3. 53– Meshed Composite Girder

VI. Job Module

This phase involved the checking of all data inputted into the software and submitting them for simulation as seen in Figure 3.54 and this is what produces the thermal results which will be discussed in the next chapter.

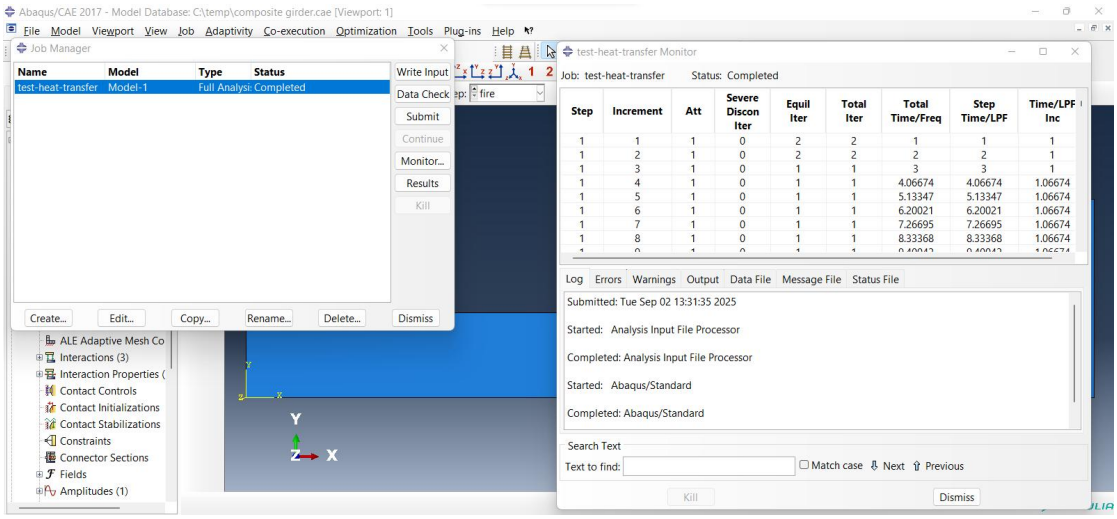

Figure 3. 54- Job Module

CHAPTER FOUR

RESULT AND DISCUSSION

4.1 Temperature Contour Results

This section presents the temperature contour results obtained from the thermal finite element analysis of the three girder sections under fire exposure. The contours illustrate how heat was distributed across the cross-sections over time (1200 sec, 2400sec, and 3600sec).

4.1.1 Steel I-Beam Temperature Contours

This subsection presents the thermal response of the steel I-beam under fire exposure at 1200 seconds, 2400 seconds, and 3600 seconds. For each fire duration, the corresponding temperature contour from Abaqus is inserted and discussed.

I Temperature Distribution at 1200 Seconds

The heat penetration pattern at 1200 seconds showed that most of the steel section had become substantially heated, indicating that it had absorbed a significant amount of thermal energy over the exposure period. The web and bottom flange recorded the highest and most uniform temperatures of 994.2˚C, reflecting their prolonged direct exposure to fire as seen in Figure 4.1. Heat had penetrated through the entire web and into both flanges, suggesting that the temperature distribution across the cross-section was approaching thermal equilibrium, even though the innermost regions may still have been slightly cooler (Vácha *et al*., 2016).

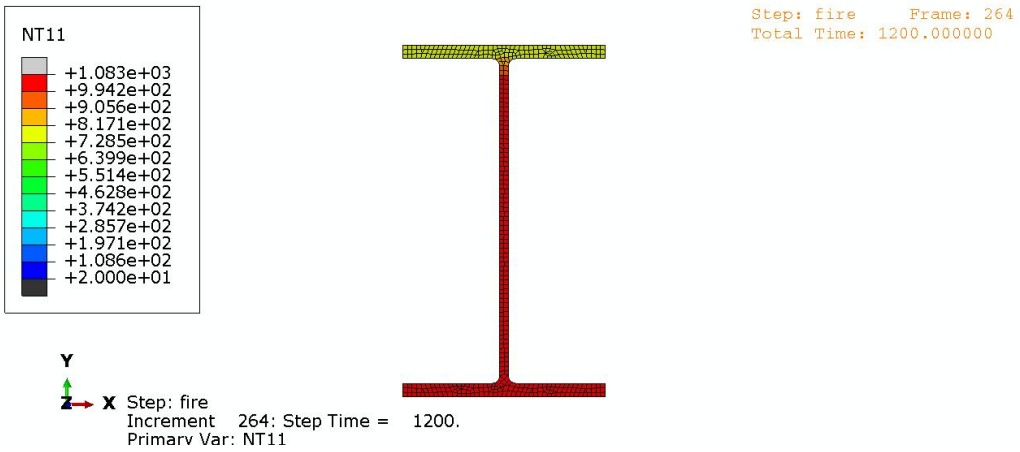

Figure 4. 1 - Nodal Temperature of Steel I-Beam at 1200seconds

The hottest zones at 1200 seconds were identified in the bottom flange and the web. The bottom flange, being the most directly exposed to fire, heated up first and reached the highest temperature levels (Ebrahimzadeh, & Rezaeian, 2022). The web, due to its thinner profile, also heated rapidly and maintained temperatures close to those of the bottom flange 905.6˚C. Although the top flange experienced less direct exposure with temperature of 639.9˚C, the high thermal conductivity of steel ensured that it also reached elevated temperatures, resulting in only minor temperature gradients across the section (Awoyera, & Naser, 2024).

The thermal distribution at 1200 seconds further demonstrated the influence of steel's high thermal conductivity. Heat had been rapidly and efficiently transmitted throughout the entire section, causing the temperature differences between the most exposed and less exposed areas to become minimal after twenty minutes of heating (Siddique *et al*., 2010). This rapid equalization of temperature across the cross-section was characteristic of steel's behaviour under fire conditions (Rzeszut, & Lukasz, 2013).

II Temperature Distribution at 2400 Seconds

At 2400 seconds, the steel section had reached a state of near-complete thermal saturation, with the entire cross-section engulfed in high temperatures seen in Figure 4.2. At this stage of heating, the entire section effectively became the hottest zone at temperature of 1041˚C.

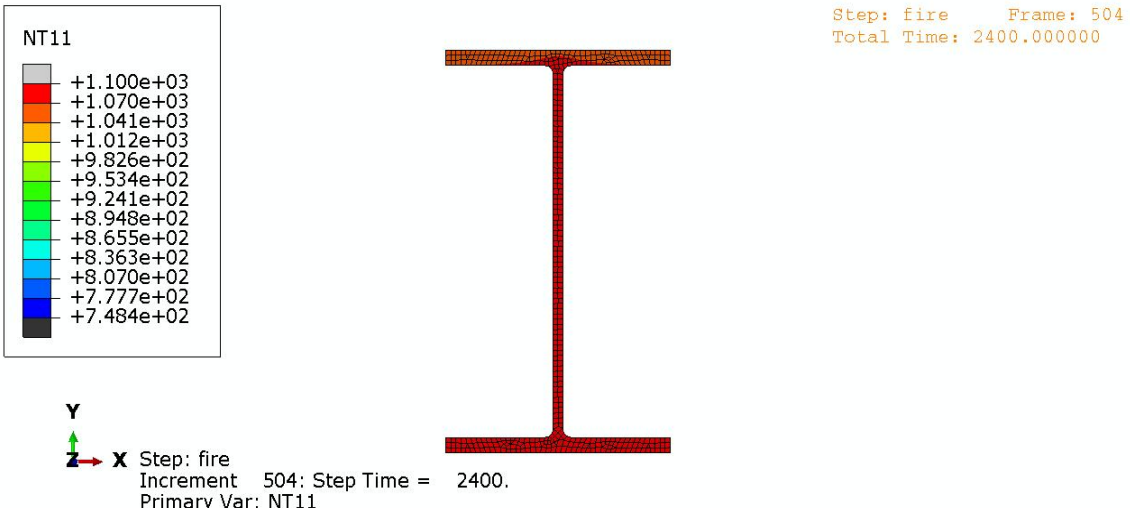

Figure 4. 2 - Nodal Temperature of Steel I-Beam at 2400seconds

Although the bottom flange and web initially recorded the highest temperatures because of direct fire exposure, the top flange and inner regions had eventually reached similar temperature levels at 1012˚C (Akagwu, 2021).

By 2400 seconds, the distribution of heat across the steel section demonstrated the strong influence of steel's high thermal conductivity over an extended heating period. After 40 minutes of exposure, the component had reached temperatures that drastically reduced its strength, producing a significant risk of structural failure (Narang, 2005).

III Temperature Distribution at 3600 Seconds

At 3600 seconds, Figure 4.3, the heat penetration pattern showed that the steel section had reached a state of complete thermal saturation or near-equilibrium with the surrounding fire environment. The temperature appeared uniform across the entire cross-section at 1010˚C, indicating that heat had fully penetrated the web, bottom flange, and top flange (Liu *et al.*, 2025), with a drop in temperature from 1041˚C stating the reduction of heat supply. The thermal contour was dominated by colors representing the highest temperature range, demonstrating that the member had been fully engulfed in intense heat for a prolonged period.

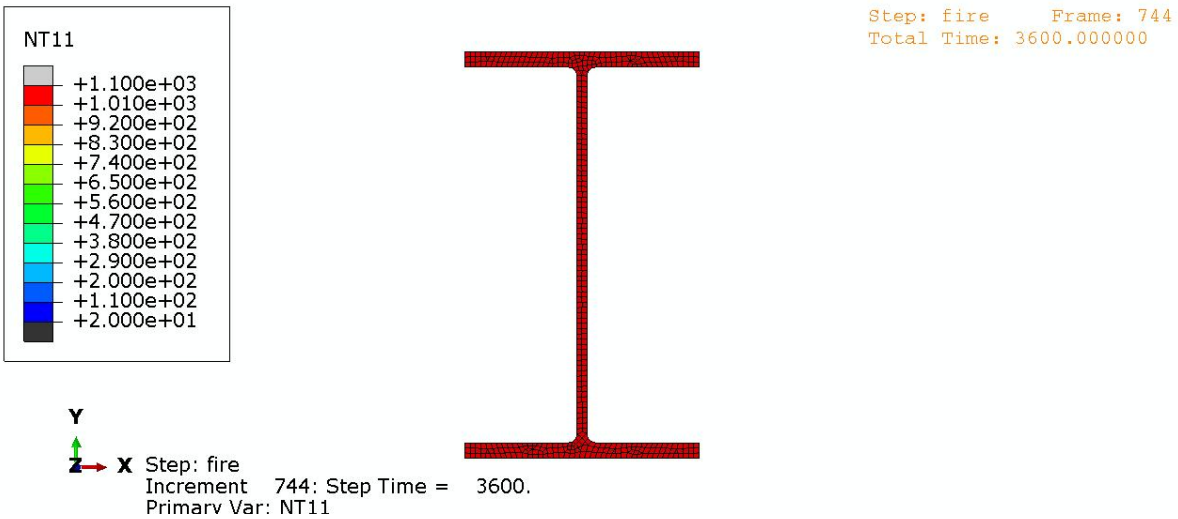

Figure 4. 3 – Nodal Temperature of Steel I-Beam at 3600seconds

At this stage of extended exposure, the entire section represented the hottest zone, with temperatures closely matching those of the furnace environment (Han *et al.*, 2011). All parts

of the cross-section; the bottom flange, web, and top flange were at a uniformly high and critical temperature. Under a standard ISO 834 fire curve (Cook & Cook, 2007).

By 3600 seconds, the uniform temperature distribution provided clear evidence of steel's high thermal conductivity (Li *et al*., 2015). Heat absorbed at the exposed surfaces had been quickly and efficiently transmitted throughout the entire cross-section, eliminating any internal temperature variation. After one hour of heating, the steel member had reached a state of thermal equilibrium and had exceeded its critical temperature threshold (Wong, 2017), typically around 920˚C.

4.1.2 Concrete I-Beam Temperature Contours

This subsection presents the thermal response of the concrete I-beam at 1200 seconds, 2400 seconds, and 3600 seconds under ISO 834 fire exposure. For each duration, the temperature contour produced in Abaqus is included and interpreted.

I Temperature Distribution at 1200 Seconds

The thermal analysis of the concrete I-beam carried out is shown in Figure 4.4 which depicts the concrete I-beam after fire exposure.

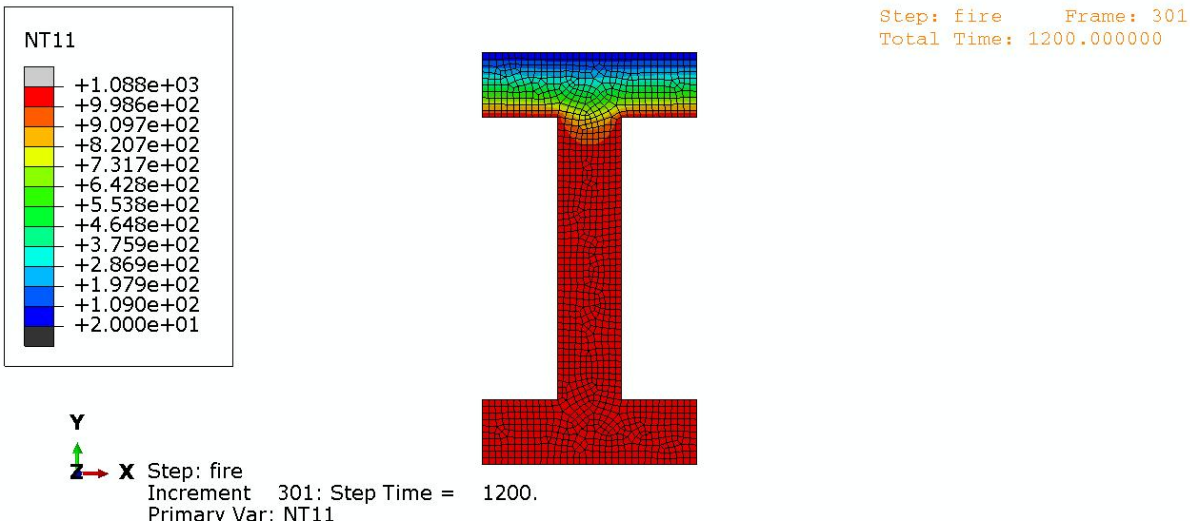

Figure 4. 4 - Nodal Temperature of Concrete I-Beam at 1200seconds

The thermal behavior of the beam at 1200sec was strongly influenced by the insulating effect of concrete. Its naturally low thermal conductivity and high thermal capacity caused the

material to act as an effective barrier to heat transfer (Asadi *et al*, 2018). This slowed the movement of heat from the fire-exposed surfaces toward the interior of the concrete I-beam and ensured that the embedded reinforcement remained at a much lower temperature.

At 1200 seconds, the conditions also fell within the time window in which concrete spalling was most likely to occur. The potential spalling zones were located within the concrete cover of the bottom flange with temperature of 820.7˚C and along the sides of the web of the exposed surface (Yun *et al*., 2013).

II Temperature Distribution at 2400 Seconds

The beam's ability to retain structural integrity at 40 minutes was largely attributed to the insulating effect of concrete (Asadi *et al*, 2018). Due to its low thermal conductivity and high thermal capacity, concrete acted as an effective thermal barrier, substantially slowing the transfer of heat from the exposed surfaces to the interior in Figure 4.5.

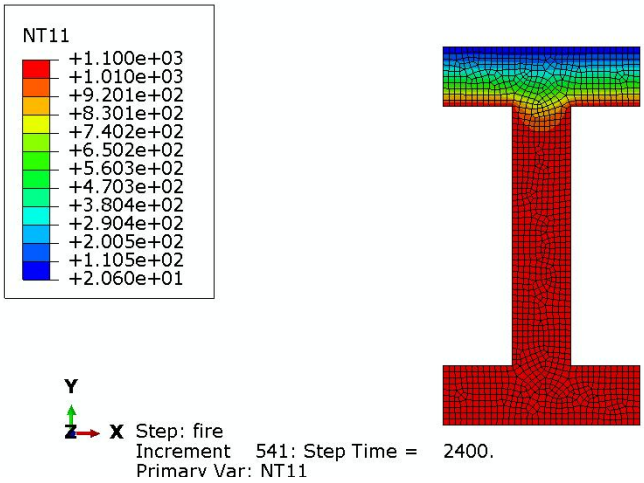

Figure 4. 5 - Nodal Temperature of Concrete I-Beam at 2400seconds

The temperature at 2400sec continued to increase along the bottom flange and the web up to 830.1˚C while the top flange though responding to the temperature rise, remained cool. The concrete insulating nature continued to resist and absorb the heat.

Spalling remained a potential concern, although the nature of the risk shifted from sudden explosive failure to continued surface degradation (Mohammed, *et al*., 2022). Temperature

entered 920.1˚C supporting Amran *et al* (2022) at the bottom flange and web which indicated that spalling has occurred.

III Temperature Distribution at 3600 Seconds

At 3600 seconds of fire exposure, the concrete I-beam, Figure 4.6 displayed a deeply penetrated temperature gradient. Heat had moved significantly into the member due to the prolonged exposure, resulting in elevated temperatures across much of the concrete cross-section.

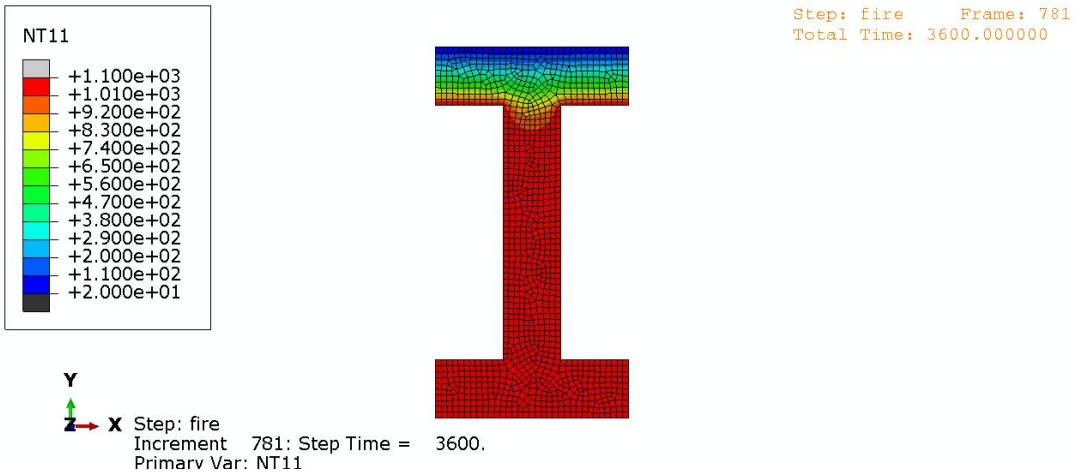

Figure 4. 6 - Nodal Temperature of Concrete I-Beam at 3600 seconds

The beam's ability to sustain load for such an extended period was directly attributed to the insulating effect of concrete (Yun *et al*., 2013). It's low thermal conductivity, combined with its high heat capacity, continued to act as an effective thermal barrier and significantly slowed the transfer of heat toward the embedded reinforcement. This behavior delayed the reinforcement from reaching critical temperature levels, as a result, the beam maintained its stability for a longer period during fire exposure (Rashid, *et al*., 2023). The evaporation of moisture within the concrete most active between 100˚C and 300˚C also contributed to slowing the advance of the heat front earlier in the fire, although this effect would have diminished significantly by 3600 seconds as most near-surface moisture would already have been expelled (Ali, *et al*., 2023).

According to a literature by (Amran *et al*., 2022), spalling will typically begin at temperatures around 300°C (572°F) and will become more pronounced as temperatures rise. Based on Figure 4.6, it was inferred that spalling of concrete likely occurred in areas where the temperature reaches approximately 830˚C or higher. This is because the concrete beam's cross-section is primarily red, indicating high temperatures, and has reached up to 1010˚C. Spalling would have started long before 3600sec (1hrs).

4.1.3 Concrete Rectangular Beam Temperature Contours

This subsection presents the thermal response of the concrete rectangular beam at 1200 seconds, 2400 seconds, and 3600 seconds under ISO 834 fire exposure.

I Temperature Distribution at 1200 Seconds

The rectangular concrete beam, Figure 4.7 demonstrated a delayed structural failure under fire exposure at 1200seconds**,** which clearly indicates its superior fire resistance compared to the concrete I-beam. This enhanced performance attributed to both its geometry and material behavior during thermal loading (Kamil, *et al*., 2019).

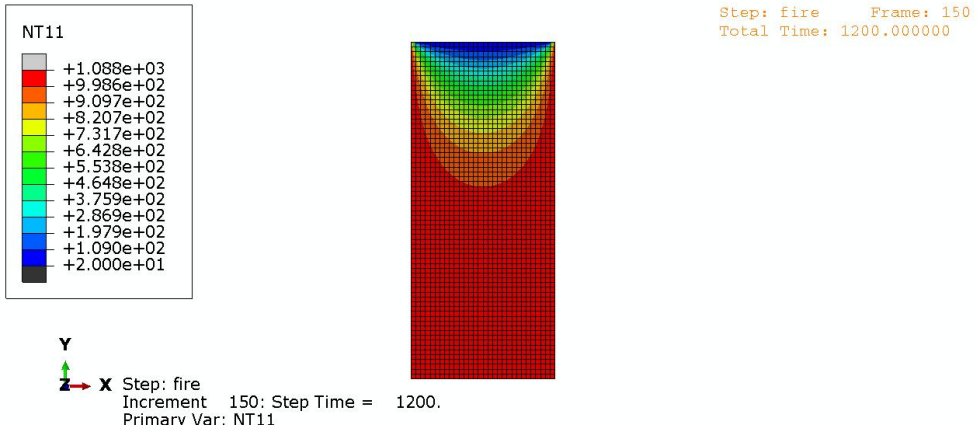

Figure 4. 7 - Nodal Temperature of Concrete Rectangular Beam at 1200 seconds

The concrete rectangular beam's behavior at 1200 seconds was characterized by a strong resistance to heat transfer due to the insulating properties of the concrete material. The core of the beam remained significantly cooler, in many cases staying below 375.9˚C (Liu *et al*., 2024), which ensured that the embedded reinforcing steel retained a large portion of its

mechanical strength. This reduced temperature rise was primarily attributed to the low thermal conductivity of concrete reported to be up to 25 times lower than steel (Asadi *et al*., 2018) combined with its high heat capacity, which slowed the inward movement of thermal energy. Additional energy loss occurred through the vaporization of moisture within the concrete between 100˚C and 300˚C, further restricting heat penetration (Zhang, 2011).

Spalling was considered highly likely at 1200 seconds, as this duration fell within the critical window in which explosive surface failure typically occurred (Li, 2018). The most vulnerable region was the bottom of the beam where temperature reached 909.7˚C.

II Temperature Distribution at 2400 Seconds

At 2400 seconds of fire exposure, Figure 4.8, the thermal response of the concrete rectangular beam was still largely controlled by the insulating capacity of the concrete. The material's low thermal conductivity continued to restrict the movement of heat toward the interior. The exposed surface temperature in a standard fire can approach approximately 925˚C (Wickström, 2016), with the analysis aligning by temperature reaching 920˚C at the bottom of the beam.

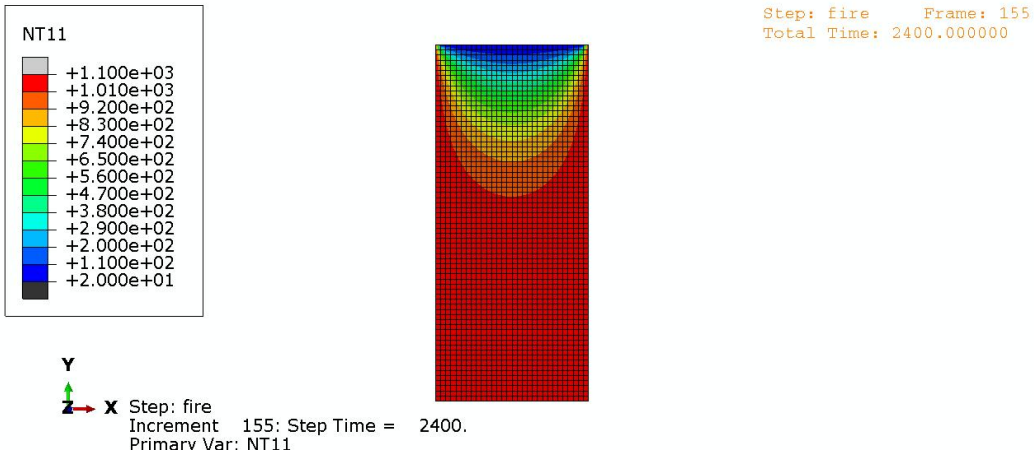

Figure 4. 8 - Nodal Temperature of Concrete Rectangular Beam at 2400 seconds

Despite the prolonged exposure, the central core of the beam remained the coolest region with temperature of 200˚C, demonstrating the persistence of thermal lag (Zhang, 2011). Although the heat front had moved deeper into the section compared to earlier stages, the

cooler core helped delay the temperature rise of the embedded reinforcement, thereby contributing to the temporary preservation of structural capacity.

The potential for spalling at this stage depended strongly on the earlier thermal history of the beam. Explosive spalling typically occurred within the first 15 to 30 minutes of fire exposure (Klingsch, 2014). Spalling occurred from 830˚C and above from the temperature gradient of the analysis (Li, 2018).

III Temperature Distribution at 3600 Seconds

At 3600 seconds, Figure 4.9, the thermal response of the concrete rectangular beam was governed by the continued insulating effect of the concrete. The material's naturally low thermal conductivity restricted the inward movement of heat, even after prolonged exposure to fire, consistent with established thermal behavior of concrete reported in fire design standards (Eurocode 1, 2002). The slower heat transfer, initially helped preserve the mechanical properties of the embedded reinforcement, however, by this one-hour mark, the steel temperature was likely approaching or exceeding its critical strength-loss threshold of about 830˚C, suggesting that significant degradation of load-carrying capacity had already occurred (Winful, 2018).

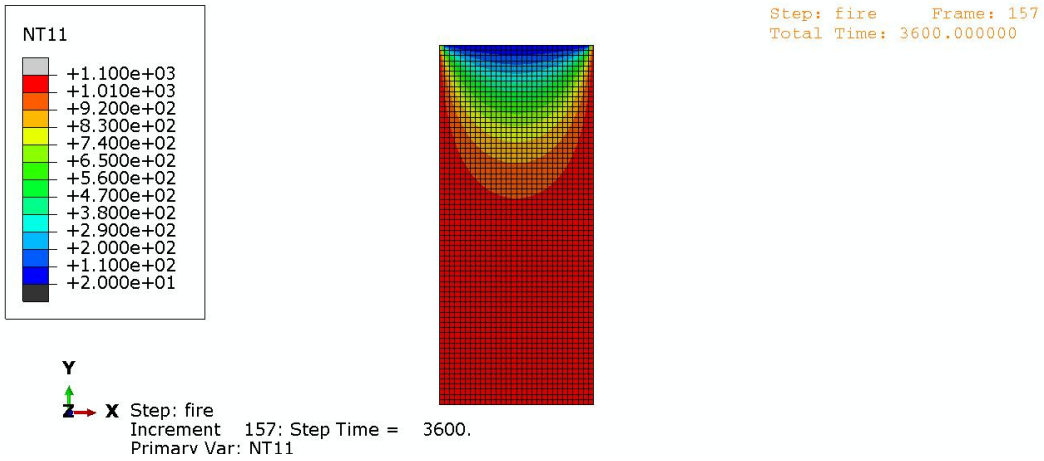

Figure 4. 9 - Nodal Temperature of Concrete Rectangular Beam at 3600 seconds

Spalling behavior at this time was influenced by earlier thermal events. Explosive spalling typically occurred within the first 15 to 30 minutes of heating (Li, 2018), when pore pressure

from vaporizing moisture was at its peak. However, the continuous exposure to high temperatures can cause severe material deterioration on the exposed surfaces before cooling phase occur (Jhavar, *et al*, 2013). In cases where early spalling had exposed the reinforcement, structural failure likely occurred before this stage.

4.1.4 Interpretation of Graphs of the Beams

The graphs provide a comprehensive insight into the structural behavior of the three beams exposed to fire.

I Steel I- Beam

- **Interpretation at 1200 Seconds**

Figure 4.10 shows the temperature – time graph for steel I-beam at 1200 seconds. The temperature curve shows a gradual and steady increase between 0 and 200 seconds, rising from approximately 200˚C to 400˚C. This indicates a typical early-stage heating phase where the exposed material begins absorbing heat, resulting in a smooth thermal rise. Between 200 and 400 seconds, the temperature continues to increase toward 700˚C, although a slight dip is observed within this interval. This temporary reduction suggests short-term thermal fluctuation, likely caused by local heat redistribution or transient surface heating effects (Awoyera, & Naser, 2024). Following this minor drop, the temperature resumes an upward trend, indicating continued heat input and sustained fire exposure. Overall, the curve reflects a rapidly progressing heating regime with brief instability before stabilizing again into a rising thermal pattern (Matlock, *et al*, 2020).

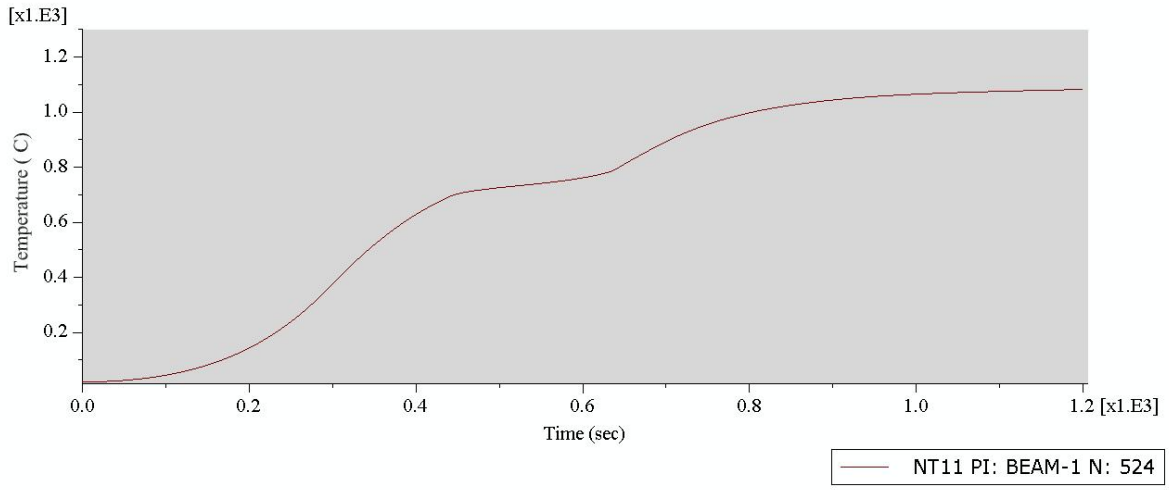

Figure 4. 10 - Graph of Temperature against Time for Steel I-Beam at 1200 seconds

- **Interpretation at 2400 Seconds**

The temperature curve, Figure 4.11 shows a progressive rise from 0 to 400 seconds, increasing smoothly from approximately 200˚C to 650˚C. This trend reflects a continuous heat absorption phase typical of early to mid-duration fire exposure, during which the material steadily accumulates thermal energy. From 400 to 700 seconds, the temperature continues to rise toward about 900˚C, although a slight drop is observed near 700 seconds. This minor decline suggests a brief thermal fluctuation, potentially caused by localized heat redistribution or short-term instability in the heating environment (Akagwu, 2021). After this dip, the temperature resumes its upward trajectory, indicating sustained heating and ongoing thermal escalation. Overall, the curve demonstrates an accelerating fire-induced heating process with a short-lived interruption before continuing its rise toward higher temperatures (Awoyera, & Naser, 2024).

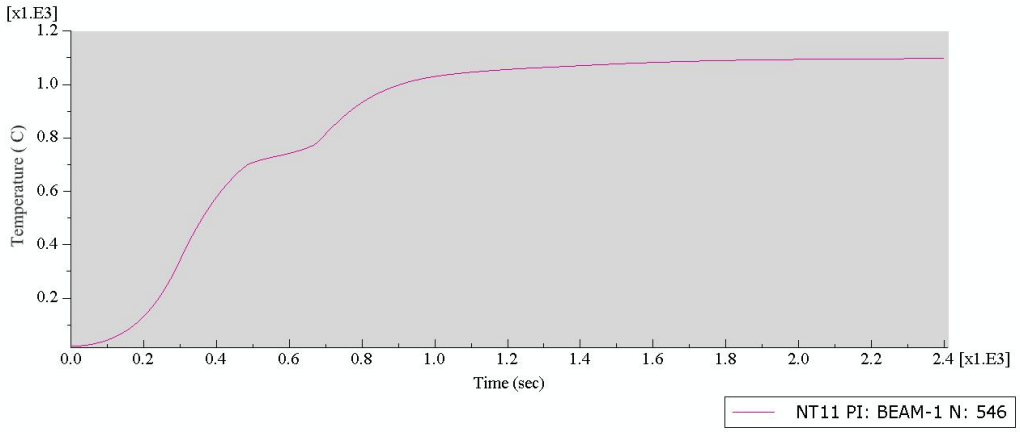

Figure 4. 11 - Graph of Temperature against Time for Steel I-Beam at 2400 seconds

- **Interpretation at 3600 Seconds**

The temperature–time curve, Figure 4.12, shows a steady increase in temperature from 0 to 600 seconds, rising from approximately 0˚C to 650˚C. This gradual upward trend reflects the typical early heating phase in which the material continuously absorbs thermal energy. Beyond 600 seconds, the temperature continues to rise toward 900˚C, although a slight dip is observed near 700 seconds. This brief decrease indicates a temporary thermal fluctuation, possibly due to localized heat redistribution or momentary changes in the heating environment (Dossett & Totten, 2013). After this short decline, the temperature resumes its upward trend, eventually reaching 1000˚C, suggesting sustained heating and progression into a more severe fire exposure phase.

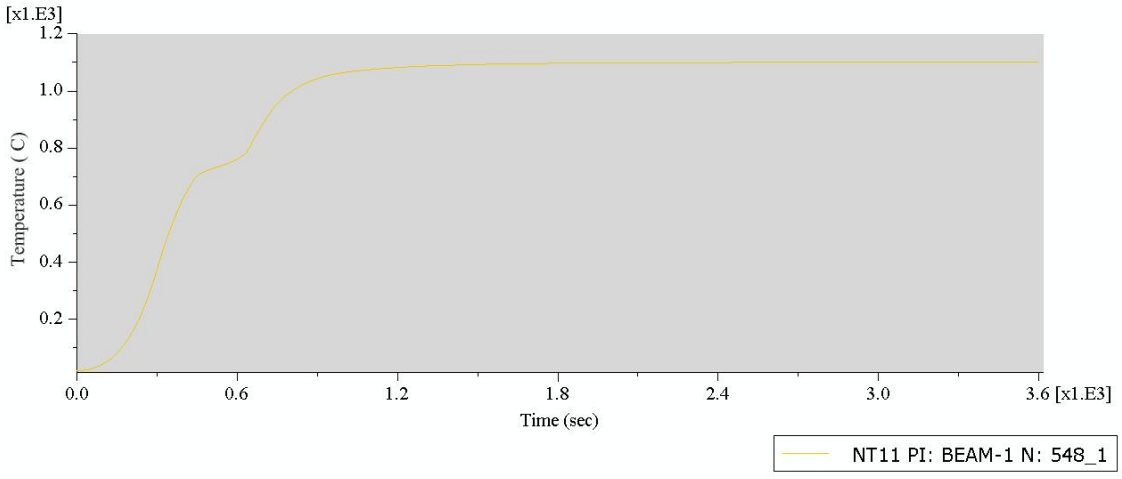

Figure 4. 12- Graph of Temperature against Time for Steel I-Beam at 3600 seconds

II Concrete I Beam

- **Interpretation at 1200 Seconds**

The temperature–time curve, Figure 4.13, indicates an initial linear increase in temperature from 0 to 300 seconds, rising steadily from 0˚C to approximately 300˚C. This straight-line trend reflects a uniform and controlled heating rate during the early exposure period. Beyond 300 seconds, the curve transitions into another linear segment, where the temperature continues to rise from 600˚C to about 650˚C over the period from 300 to 1200 seconds. This phase suggests a slower, more gradual heating rate compared to the initial stage, likely representing a stabilized fire environment in which heat input remains relatively consistent (Yun *et al*., 2013). Overall, the graph displays two distinct heating phases: a rapid initial rise followed by a prolonged period of moderate, near-linear temperature increase (Lacković, 2021).

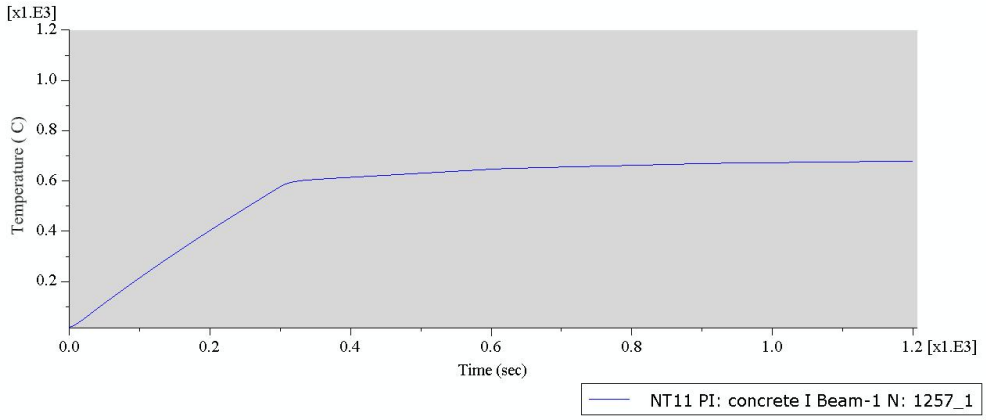

Figure 4. 13 - Graph of Temperature against Time for Concrete I-Beam at 1200 seconds

- **Interpretation at 2400 Seconds**

The temperature–time graph, Figure 4.14, shows an initial rapid and linear rise in temperature from 0˚C at 0 seconds to approximately 700˚C at 300 seconds. This steep, straight-line trend indicates a high and consistent heating rate during the early stage of fire exposure, characteristic of a rapidly developing fire environment (Asadi *et al*, 2018). Beyond 300

seconds, the curve transitions into a second straight-line segment where the temperature remains approximately constant at 700˚C up to 1200 seconds.

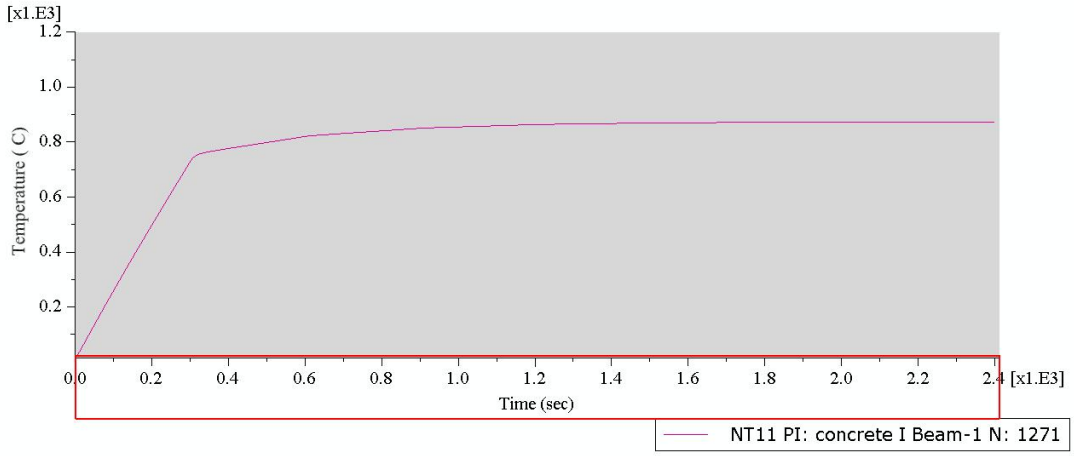

Figure 4. 14- Graph of Temperature against Time for Concrete I-Beam at 2400 seconds

- **Interpretation at 3600 Seconds**

The temperature–time curve shows an initial rapid and linear rise in temperature, increasing from 0 °C at 0 seconds to approximately 900˚C at 300 seconds. This steep linear trend indicates a period of intense heating, where the fire temperature increases at a nearly constant rate, reflecting the rapid growth phase of a fully developing fire (Gil, 2024). From 300 seconds to 3600 seconds, the curve transitions into a second straight-line segment in which the temperature remains approximately constant at 900˚C or slightly above. This plateau signifies that the system has entered a quasi-steady or fully developed fire stage, where the thermal input to the surface becomes balanced by heat losses, resulting in minimal further temperature increase (Lacković, 2021).

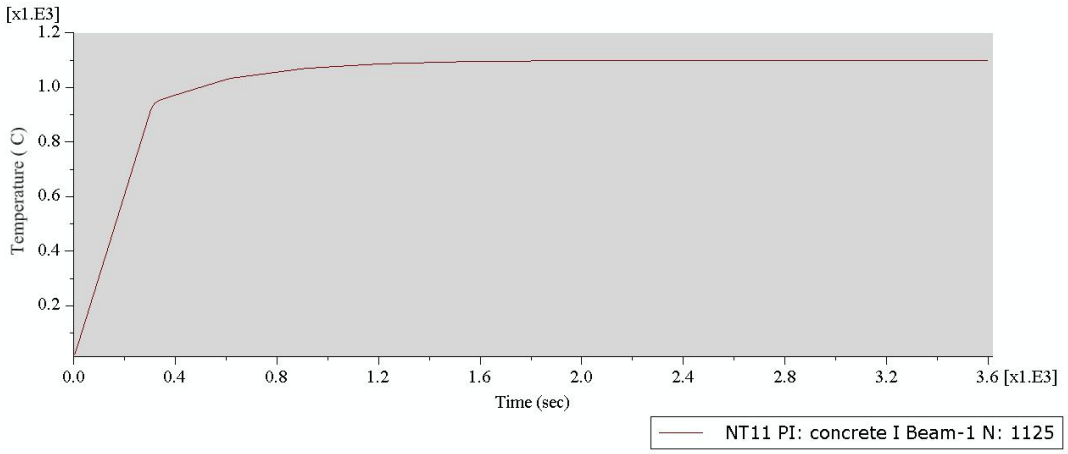

Figure 4. 15- Graph of Temperature against Time for Concrete I-Beam at 3600 seconds

III Concrete Rectangular Beam

- **Interpretation at 1200 Seconds**

The temperature–time curve shows an initial linear rise from 0 to 300 seconds, with temperatures increasing steadily from 0˚C to around 300˚C. This straight-line pattern indicates a consistent and uniform heating rate during the early phase of exposure. After 300 seconds, the curve shifts into a second linear trend, where temperatures continue to increase more gradually from roughly 600˚C to 650˚C between 300 and 1200 seconds. This stage reflects a slower heating rate, characteristic of a stabilizing fire condition in which the thermal input becomes more uniform (Gil, 2024). Overall, the graph demonstrates two distinct heating stages: a rapid initial increase followed by an extended period of moderate, near-linear temperature growth.

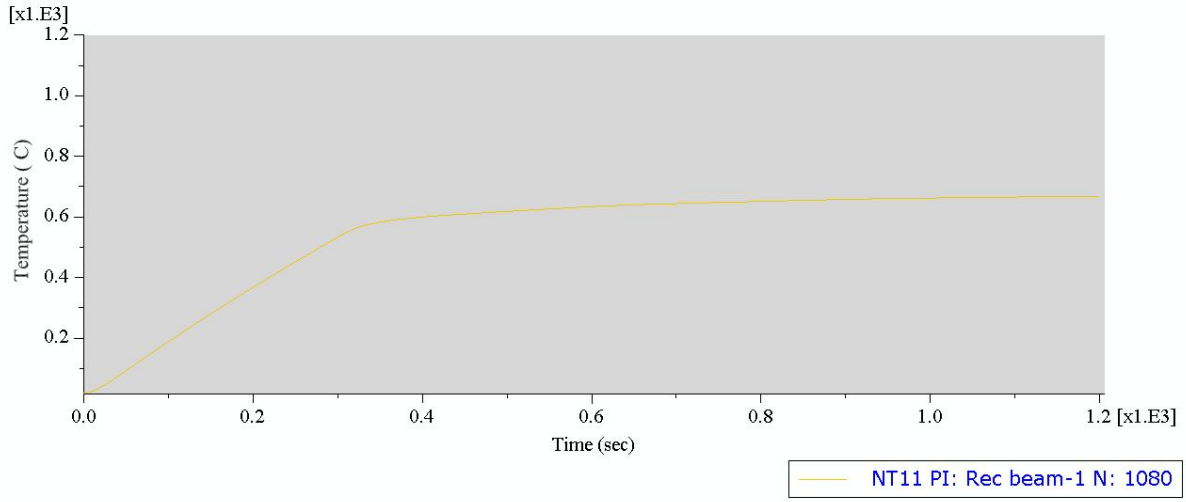

Figure 4. 16- Graph of Temperature against Time for Concrete Rectangular Beam at 1200 seconds

- **Interpretation at 2400 Seconds**

The temperature–time curve exhibits an initial steep and linear temperature increase, rising from 0˚C at the onset to approximately 900˚C by 300 seconds. This pronounced linear rise signifies an intense heating phase characteristic of the rapid growth stage of a developing fire, during which temperatures escalate at a nearly constant rate (Asadi *et al*, 2018). Beyond 300 seconds, the curve transitions into a second linear segment, where the temperature stabilizes at around 900˚C or slightly higher up to 3600 seconds. This extended plateau indicates entry into a quasi-steady or fully developed fire phase, in which the rate of heat input becomes balanced by heat dissipation, resulting in little to no additional temperature rise (Zhang *et al*., 2021).

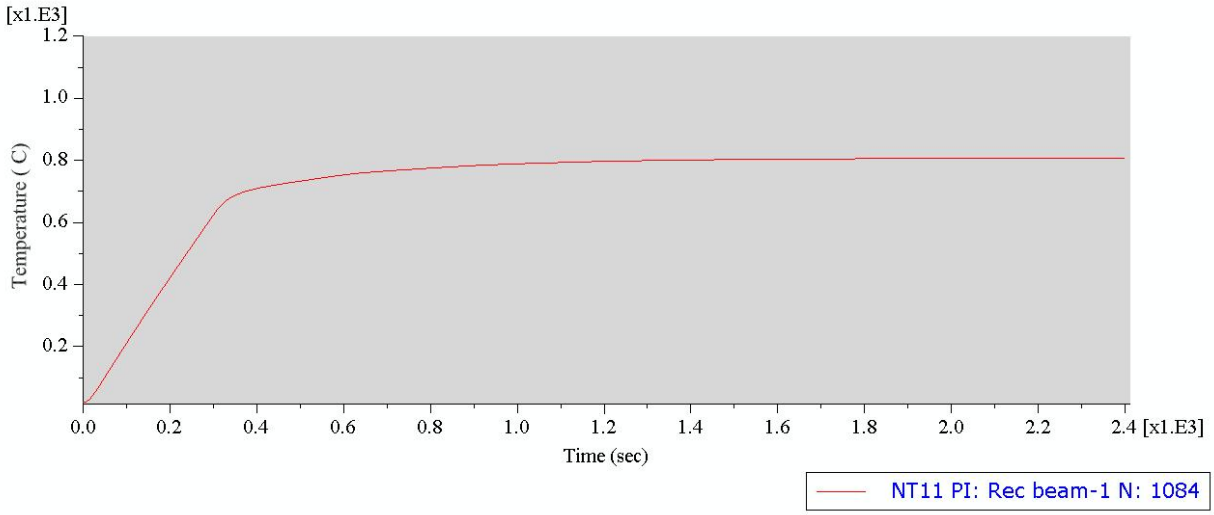

Figure 4. 17- Graph of Temperature against Time for Concrete Rectangular Beam at 2400 seconds

- **Interpretation at 3600 Seconds**

The temperature–time curve demonstrates an initial sharp and linear increase in temperature, rising from 0˚C at the start to roughly 900˚C by 300 seconds. This steep ascent reflects a period of intense heating, characteristic of the rapid growth stage of a developing fire, during which temperatures rise at an almost constant rate (Kamil, *et al*., 2019). After 300 seconds, the curve enters a second linear phase, where the temperature remains nearly constant at about 900˚C, extending up to 3600 seconds. This prolonged plateau indicates a transition into a quasi-steady or fully developed fire condition, during which the heat supplied to the surface is largely balanced by heat losses, resulting in little additional temperature rise (Zhang *et al*., 2021).

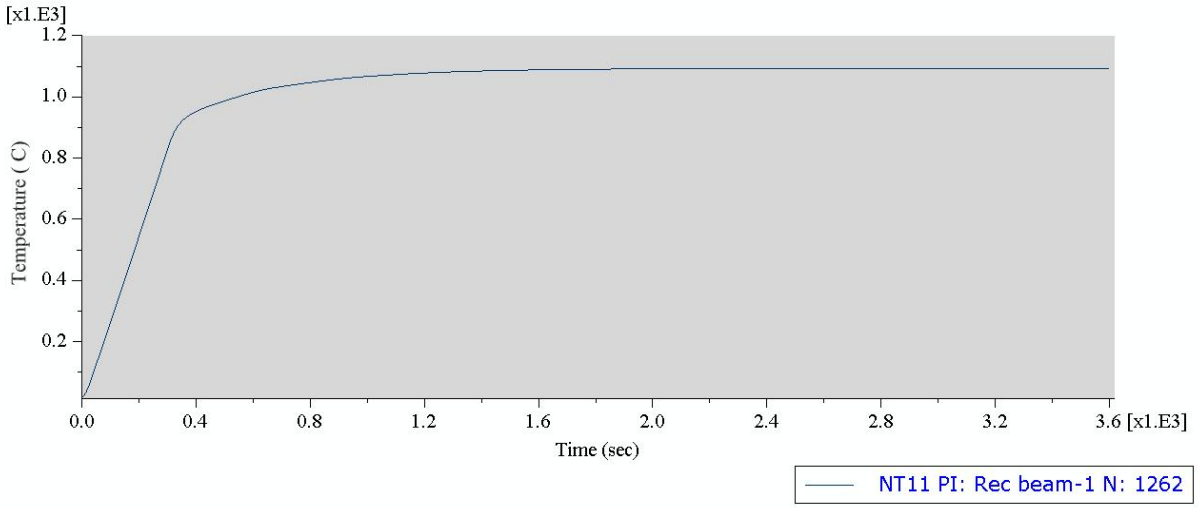

Figure 4. 18- Graph of Temperature against Time for Concrete Rectangular Beam at 3600 seconds

4.1.5 Validation of Results Using Existing Research

The following validation of the results obtained from the three different models are as follows;

I Steel I-Beam

The validation of the steel I-beam (1200 sec, 2400 sec, 3600 sec) is given in Table 4.1;

Table 4. 1 - Validation of Steel I-Beam Model with Existing Research

Authors	Research Focus	Key Findings	Model Validation
EN 1993-1-2 (Franssen & Zaharia, 2005)	Temperature-dependent behavior of structural steel under ISO 834 fire; strength reduction and temperature evolution.	Showed that exposed steel heats rapidly, with temperatures approaching furnace levels within 30 - 60 minutes; steel strength drops sharply beyond 400 - 600˚C; temperature gradients reduce quickly due to high thermal conductivity.	Simulation results align with Eurocode trends: rapid heating of web/flange at 1200 s, near-uniform temperatures by 2400 - 3600sec, and steel reaching critical temperature of 920˚C after prolonged fire, indicating near-complete loss of load-bearing capacity.
Issa, &	Experimental and	Identified fast temperature	Validates simulation

Authors	Research Focus	Key Findings	Model Validation
Izadifard, (2021)	numerical evaluation of fire behavior of steel and concrete members; heating rates, thermal penetration, and structural response.	rise in unprotected steel due to high conductivity; deeper heat penetration with time; steel temperatures rapidly approach furnace values beyond 30 - 40 minutes; structural failure occurs once steel reaches critical temperature.	observations of steep gradients at 1200 s, full thermal penetration by 2400 - 3600 s, and critical strength loss at high temperatures. The study supports the model's heating trends and structural degradation sequence.
Buchanan (2001)	Fire behaviour of steel structures, thermal response, and ISO 834 heating model.	Describes uniform section heating of exposed steel within one hour; bottom flange and web heat fastest; thermal equilibrium reached under continuous heating; near-total strength loss when steel approaches furnace temperature.	Confirms simulated behaviour where the I-beam showed high temperatures in flanges/web at 1200 s, near equilibrium by 2400 s, and complete thermal saturation by 3600 s, consistent with ISO 834 heating curves. Validates predicted loss of stiffness and strength.

II Concrete I-Beam

The validation of the concrete I-beam (1200 s, 2400 s, 3600 s) is given in Table 4.2;

Table 4. 2 - Validation of Concrete I-Beam Model with Existing Research

Authors	Research Focus	Key Findings	Model Validation
Mohammed *et al*., 2022	Thermal behaviour, spalling mechanisms, and reinforcement protection in concrete under fire.	Concrete exhibited a slow rate of temperature rise because of its low thermal conductivity and high heat-storage capacity. The embedded reinforcement generally remained relatively cool during the initial stages of heating. However, spalling was likely to occur once surface temperatures entered the 200 - 400˚C range, particularly in highly exposed tensile regions.	At 1200 seconds, the beam showed cool reinforcement and hot surfaces, indicating early thermal lag and spalling risk. By 2400 seconds, the hotter bottom flange and cooler top flange demonstrated steep temperature gradients. At 3600 seconds, surface temperatures exceeded 1000˚C while reinforcement heating remained delayed, aligning with Mohammed et at., 2022.
Amran *et al*. (2022)	Temperature thresholds for spalling, moisture-driven failure, and degradation of concrete at elevated temperatures.	Concrete spalling initiates at 300˚C and becomes more severe at 600 - 800˚C. When exposed to temperatures above 800˚C, the concrete surface experiences significant degradation and material loss.	At 1200 secs, the bottom flange reaches 830˚C, placing it within the severe spalling range noted by Amran. By 2400 secs, temperatures peak near 920˚C, indicating spalling has occurred. At 3600 secs, the beam reaches about 1010˚C, consistent with advanced thermal damage,

Authors	Research Focus	Key Findings	Model Validation
			and ongoing surface deterioration.
Eurocode 2 (Beeby *et al*., 2005).	Fire design principles for concrete structures, thermal properties, reinforcement protection, and spalling behavior.	Concrete's low thermal diffusivity caused slow heat penetration, keeping reinforcement cooler than the exposed surfaces for an extended period. Early spalling usually occurred within the first 15–30 minutes, while prolonged fire exposure resulted in significant surface degradation.	At 1200 secs, the beam's strong insulation kept the reinforcement cool, aligning with Eurocode heat-transfer predictions. By 2400 seconds, the hot bottom flange and cooler top flange reflected the expected thermal gradient. At 3600 seconds, near-uniform high surface temperatures and significant material degradation corresponded to long-duration fire behavior described in Eurocode.

III Concrete Rectangular Beam

The validation of the concrete rectangular beam (1200 s, 2400 s, 3600 s) is given in Table 4.3;

Table 4. 3 - Validation of Concrete Rectangular Beam Model with Existing Research

Authors	Research Focus	Key Findings	Model Validation
Mohammed *et al*., 2022	Thermal behaviour of concrete members, reinforcement protection, and spalling mechanisms under fire.	Concrete heats slowly because of its low thermal conductivity, keeping the embedded reinforcement cool during the early stages of fire. Spalling is likely when surface or cover temperatures reach 200 - 400˚C, while the core remains comparatively cool even after prolonged exposure.	At 1200 s, the beam exhibited a hot surface of 910˚C with a much cooler core, reflecting thermal lag and early spalling. By 2400 s, steep thermal gradients persisted, with the core around 200˚C, indicating slow inward heat transfer. At 3600 s, the reinforcement approached critical temperatures while surface deterioration continued, consistent with long-duration fire behavior
Amran *et al*. (2022)	Concrete spalling thresholds, temperature-induced surface degradation, and fire-induced material loss.	Spalling typically starts near 300˚C and becomes more severe above 600 - 800˚C. Surface areas exceeding 800˚C are highly susceptible, and extended exposure leads to progressive material loss and surface sloughing.	At 1200 s, the bottom flange reached 910˚C, indicating high spalling risk. By 2400 s, temperatures around 920˚C suggested ongoing spalling and surface drying. At 3600 s, peak temperatures of 1010˚C corresponded with advanced degradation..
Eurocode 2 (EN 1992-1-2, 2004)	Fire design of concrete structures, thermal properties, heat	Concrete's low thermal conductivity produced steep temperature gradients, keeping reinforcement cool for	At 1200 s, thermal gradients with cool reinforcement reflected Eurocode thermal delay predictions; at 2400 s, the core remained cool,

Authors	Research Focus	Key Findings	Model Validation
	transfer, and reinforcement protection.	long periods. Explosive spalling typically occurred within the first 15–30 minutes, while prolonged exposure led to significant surface deterioration.	200˚C showing slow heat penetration; by 3600 s, reinforcement approached critical temperatures and surfaces showed severe damage, consistent with Eurocode long-duration fire behavior.

4.2 Comparative Assessment of Post-Fire Condition Based on Material Type

This section provides a comparative evaluation of the post-fire condition of concrete and steel I-beams. The analysis considers thermal response during the fire, the observed degradation mechanisms, and the residual capacity after cooling, highlighting how material type governs post-fire safety and repair potential.

4.2.1 Thermal Properties

The thermal properties of concrete and steel, significantly influence their post-fire performance. Table 4.4 shows concrete and steel I-beams post-fire condition based on their ability to conduct heat and retain internal strength backed by existing research.

Table 4. 4 - Tabular Representation on the Thermal Analysis Based on Material Type

Material	Thermal Properties (Post-Fire Behavior)
Concrete I-Beam	After fire exposure at 3600sec, the concrete I-beam retained a considerable portion of its internal strength because concrete's low thermal conductivity slowed heat transfer from the surface toward the

	core. Research showed that concrete's conductivity decreased after high-temperature exposure, reducing residual heat flow (Ali, *et al*., 2023). Because of its high heat capacity, the concrete absorbed and stored a lot of thermal energy, which delayed temperature rise in the reinforcement and preserved much of its load-bearing capacity. However, post-fire, the concrete's mechanical strength was significantly reduced. Studies found that residual compressive strength can drop dramatically with increasing temperature exposure, particularly above 600˚C (Rashid, *et al*., 2023). Spalling occurred at 3600sec. The steep thermal gradients caused by the low conductivity generated internal stresses, and decomposition reactions inside concrete contributed to strength loss (Amran *et al*., 2022).
Steel I-Beam	After fire exposure at 3600sec, the steel I-beam heated very rapidly because of high thermal conductivity, causing its cross-section temperature to equalize quickly and reach damaging levels. This behavior was consistent with findings in high-temperature steel research, which showed that residual capacity of steel dropped sharply as exposure temperature increased (Awoyera, & Naser, 2024). The residual strength of steel was significantly compromised. Studies on high-strength steel after fire revealed large reductions in yield strength and residual load capacity due to thermal exposure (Bailey, 2005).

4.2.2 Residual Strength

Residual strength was used as an indicator of whether structural recovery was feasible after the fire. Table 4.5 compares the remaining strength of concrete and steel I-beams after they experienced peak fire temperatures during simulation.

Table 4. 5 - Residual Strength after Elevated Temperature Based on Material Type

Material	Residual Yield Strength	% Strength Retained	Post-Fire Conditions

Material	Residual Yield Strength	% Strength Retained	Post-Fire Conditions
Concrete I-beam	At 1200sec = 322MPa (from 460 MPa)	70%	The results obtained closely match findings from similar research which shows that, concrete typically retains 65-75% of its strength in the early stages of heating and drops to 35-45% by mid-exposure, before falling to around 20-30% after 3600sec, of standard fire conditions (Golewski, 2023).
	At 2400sec = 184MPa (from 460 MPa)	40%	
	At 3600sec = 115 MPa (from 460 MPa)	25%	
Steel I-beam	At 1200sec = 129 MPa (from 355 MPa)	36%	The strength at 1200sec aligns with Eurocode 3 and other studies showing steel retains only 30–40% strength once temperatures reach about 600˚C. By 2400sec, strength dropped, consistent with research indicating that steel loses over 90% of its capacity as temperatures exceed 750-800˚C. At 3600sec, the beam strength matches Eurocode-based predictions of 2-5% residual strength at 900-1000˚C (Brown, 2018).
	At 2400sec = 13.5 MPa (from 355 MPa)	3.8%	
	At 3600sec = 15 MPa (from 355 MPa)	4%	

4.3 Comparative Assessment of Post-Fire Condition Based on Section Type

This section presents a comparative analysis of structural performance between concrete I-beam and concrete rectangular beam post-fire conditions. By examining differences in

thermal response, behavior under fire exposure, and residual strength, it highlights how the section type influences fire resistance and failure behavior.

4.3.1 Thermal Properties

Concrete's thermal performance under fire is influenced by its mass, geometry, and material composition. Table 4.6 shows a tabular representation on the thermal analysis on both bridge girders post-fire condition.

Table 4. 6 - Tabular Representation on the Thermal Analysis Based on Section Type

Section Type	Thermal Properties (Post-Fire Behavior)
Concrete I-Beam	After fire exposure, the concrete I-beam heated slowly at its core because its low thermal conductivity restricted heat flow from the flanges and web into the interior. Its high thermal capacity further delayed temperature rises in the reinforcement, keeping the inner region cooler for longer (Asadi *et al*, 2018). Spalling occurred, as internal moisture created pore pressure under high temperatures especially along exposed flange surfaces leading to potential surface loss (Mohammed, *et al*., 2022).
Concrete Rectangular Beam	The concrete rectangular beam experienced a gradual rise in internal temperature, with heat remaining concentrated near the outer surfaces. Prior studies reported that larger concrete sections and thicker cover delayed heat movement, allowing the beam's interior to stay much cooler for longer periods (Asadi *et al*., 2018). Its geometry further slowed heat flow, creating a distinct temperature difference between the hot exterior and the cooler core an effect supported by numerical fire-resistance analyses showing that section size plays a major role in retaining structural capacity (Winful, 2018). Spalling occurred after 3600sec of exposure to fire.

4.3.2 Residual Strength

Residual strength was used as an indicator to see the strength retained after the fire exposure. Table 4.7 compares the remaining strength of the two section type, concrete I-beam and concrete rectangular beam after they experienced peak fire temperatures during simulation.

Table 4. 7 - Residual Strength after Elevated Temperature Based on Section Type

Material	Residual Yield Strength	% Strength Retained	Post-Fire Conditions
Concrete I-Beam	At 1200sec = 322MPa (from 460 MPa)	70%	The results obtained closely match findings from similar research which shows that, concrete typically retains 65-75% of its strength in the early stages of heating and drops to 35-45% by mid-exposure, before falling to around 20-30% after 3600sec of standard fire conditions (Golewski, 2023).
	At 2400sec = 184MPa (from 460 MPa)	40%	
	At 3600sec = 115 MPa (from 460 MPa)	25%	
Concrete Rectangular Beam	At 1200sec = 340.4 MPa (from 460 MPa)	74%	The high strength retained initially was due to slow heat penetration and compact geometry, which dropped to 50% at mid-exposure as internal temperatures rose, and maintained 40% after 3600sec, reflecting its superior fire performance from reduced spalling and better thermal insulation (Gil, 2024).
	At 2400sec = 230 MPa (from 460 MPa)	50%	
	At 3600sec = 184 MPa (from 460 MPa)	40%	

4.4 Case Study Bridge

This section presents the temperature contour results obtained from the thermal finite element analysis of the composite girder sections under fire exposure

4.4.2 Thermal Analysis

The thermal analysis of the composite girder carried out is shown in Figure 4.19;

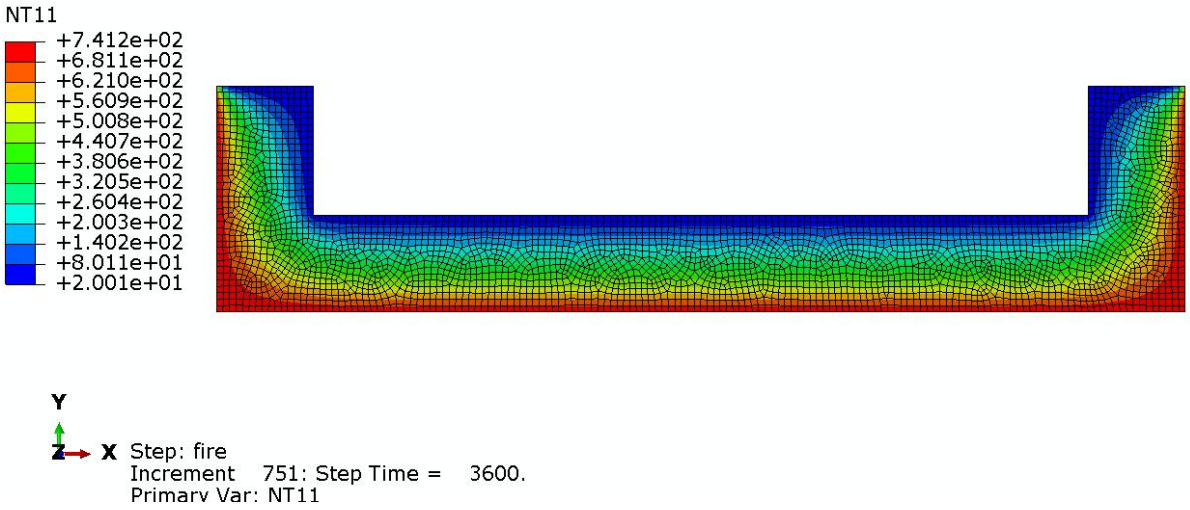

Figure 4. 19 - Composite Girder Thermal Analysis

The thermal analysis of the composite girder indicates a progressive heat distribution where the bottom and side of the composite girder were most affected. The temperature contour represented by the deep red zones shows that these areas exceeded critical thresholds above 600˚C, a level at which both steel and concrete undergo strength loss (Amran *et al*., 2022). The top surface of the girder retained relatively lower temperatures, indicating some degree of thermal insulation due to concrete's low conductivity, which is consistent with prior studies on composite members under ISO 834 fire curves (Ding *et al*., 2023).

4.4.3 Spalling of Concrete

According to a literature by (Amran *et al*., 2022), spalling will typically begin at temperatures around 300˚C (572˚F) and will become more pronounced as temperatures rise. Based on Figure 4.19, it was inferred that spalling of concrete likely occurred in bottom and side area of the girder which is the exposed surface where the temperature reaches

approximately 561˚C or higher. Spalling in this region not only reduced the protective concrete cover but also exposed reinforcing steel, accelerating degradation. This aligns with recent fire tests on composite decks, where spalling initiated after 30 - 40 minutes of standard fire exposure (Fan *et al*., 2020).

4.4.4 Percentage of Residual Strength:

From the temperature legend provided after the analysis, the composite girder section was only affected at the bottom and at the side but progressing upward, it was seen that the mass of the girder was able to withstand the heat and the temperature of 380˚C from the temperature legend was were the strength retained was taken. This was because the girder was still at a cool region. It, therefore retained 75% of its original strength after fire exposure.

$$\text{Yield Strength} = 460 \times 0.75 = 345\text{Mpa}.$$

The yield strength of the reinforced steel reduced from 460Mpa to 345Mpa.

4.4.5 Implication of Structural Integrity

The girder lost strength at the exposed area leading to material degradation at the bottom of the beam which is signified by “red color” and progressing upwards, it showed areas not affected. The combined effects of concrete spalling, reinforcement exposure, and severe steel heating compromised the structural integrity at the bottom of the girder. Cracking and delamination in the slab reduced stiffness of the concrete (Abdulrahman, 2019). Moreover, spalling led to localized reduction in cross-sectional area, which, in turn, increased stress concentration. This suggests that the girder would be affected post-fire without retrofitting interventions (Abdulrahman, *et al*., 2021).

4.4.6 Validation of Result

The thermal gradient observed in the composite girder severe heating concentrated at the bottom flange and sides with much lower temperatures toward the top slab matches typical behavior reported for composite members under standard fire exposure. Numerical and

experimental studies show that steel elements heat and conduct temperature faster than the overlying concrete slab, producing pronounced through-depth stratification and bottom-up failure patterns under ISO curves (Ding *et al*., 2023). Performance-based reviews also emphasize that concrete's lower thermal conductivity provides a degree of insulation for upper regions, producing the kind of cool zone (380˚C) noted in your legend (Kodur & Gil, 2024).

The inference of spalling at the exposed soffit and side faces is also supported by contemporary research. Spalling is commonly initiated in the 300-400˚C range and becomes pronounced as temperatures increase and pore pressures build particularly in dense or high-strength concretes and at edges/corners where restraint and gradients are largest (Amran *et al*., 2022). Reported fire tests on composite decks demonstrate spalling onset within 30–40 minutes (1800sec – 2400sec) under standard fire loading, producing cover loss and early exposure of reinforcement as observed (Fan *et al*., 2020).

The residual strength estimate (75% retained at 380˚C) is consistent with both codified reduction factors and recent experimental summaries. Eurocode 2 (Beeby *et al*., 2005) and Eurocode 3 give temperature-dependent reduction factors for concrete and steel respectively, indicating modest loss of capacity in the mid-300˚C range (reduction factors typically 0.7-0.85 depending on aggregate and steel grade) which supports a retained strength on the order of 70–80% near 380˚C (Brown, 2018). Empirical studies similarly report residual concrete compressive strength and reinforcement yield factors falling within this band for temperatures of 300-400˚C (Mohammed *et al*., 2022). Thus, the computed steel yield of 460 → 345MPa (75% retention) is reasonable for the stated temperature regime and aligns with experimental/numerical findings (Ding *et al*., 2023).

4.5 Recommended Retrofitting Techniques Based on Parametric Study

The findings from the thermal analysis emphasize the importance of both preventive and recovery-oriented retrofitting strategies in improving the fire resistance of pedestrian bridge girders. These measures aim to delay temperature rise, limit thermal damage during fire exposure, and restore structural performance where heat effects have already caused deterioration.

4.5.1 Fire Mitigation Techniques (Preventive Methods)

Preventive retrofitting methods are essential for reducing the rate of temperature rise and slowing heat penetration during a fire. For steel girders, passive fire protection systems such as intumescent coatings and spray-applied fire-resistive materials (SFRMs) have proven effective in delaying critical temperature escalation and maintaining lower steel temperatures for longer periods (Structures, 2024). These materials expand or insulate when heated, creating a barrier that reduces thermal exposure. For concrete girders, improved fire resistance can be achieved by increasing cover thickness, using heat-resistant aggregate types, or applying protective layers such as mineral plasters or fire-resistant cladding. These methods help reduce surface heating and limit early spalling, enabling the core and reinforcement to remain cooler for extended durations (Kaya, 2025). Overall, preventive measures improve the thermal performance of bridge girders and reduce the risk of rapid deterioration during fire events (Khan *et al*., 2021).

4.5.2 Post-Fire Structural Retrofitting (Recovery Methods)

Where fire exposure has already caused thermal damage such as spalling, cracking, or loss of material strength recovery techniques may be required to restore the structural capacity of the girder. For concrete members, strengthening methods such as fibre-reinforced polymer (FRP) wraps, steel plate bonding, shotcrete overlays, and epoxy injection can help recover a significant portion of the lost capacity (Structures, 2024). These systems provide additional

confinement, replace damaged material, or seal heat-induced cracks, improving post-fire performance.

For steel members, methods such as heat straightening, localized section replacement, or reinforcement with external plates can be used to restore the member's stiffness and strength after high-temperature exposure (Garlock *et al*, 2012). These actions help compensate for thermal distortion, loss of section thickness, and reduced material properties.

In summary, both preventive and recovery-based retrofitting strategies are essential for improving the thermal resilience of pedestrian bridges. Preventive measures help slow heat penetration and delay degradation during fire exposure, while recovery techniques offer practical means of restoring serviceability and extending the lifespan of fire-affected structures.

CHAPTER FIVE

CONCLUSION AND RECOMMENDATION

5.1 Conclusion

The development and validation of a finite element thermal model in Abaqus successfully demonstrated the capability to simulate temperature distribution, heat penetration, and thermal gradients in both steel and concrete girder sections. The model accurately captured the distinct thermal behaviors of each material, with steel exhibiting rapid temperature rise and early deterioration due to its high thermal conductivity, while concrete displayed slower heating rates and delayed degradation. The steel I-beam's quick progression to critical temperatures aligned with its material properties and early strength loss characteristics, whereas concrete beams maintained lower internal temperatures over extended periods. These findings validate the effectiveness of the developed FE models in reproducing realistic thermal responses, confirming their reliability for assessing structural performance following fire exposure.

A comprehensive comparative assessment revealed substantial differences in thermal resistance among the three girder types, directly influenced by material composition and cross-sectional configuration. Steel I-beams demonstrated the greatest vulnerability to fire exposure, experiencing rapid heat penetration and significant strength degradation within the initial hour. Concrete I-beams exhibited improved performance, retaining appreciable residual strength owing to slower internal heating, though they remained prone to surface cracking and elevated web temperatures. The concrete rectangular beam displayed the highest resistance to fire-induced deterioration, with its compact geometry and favorable surface-area-to-volume ratio effectively retarding thermal ingress and preserving greater structural capacity. This evaluation underscores the enhanced fire resilience of concrete sections and highlights the critical role of geometric configuration in determining thermal performance.

Application of the validated thermal modelling approach to the University of Benin pedestrian overhead bridge effectively demonstrated its practical utility for real-world structures. The analysis successfully characterized the thermal response of the bridge's girder system under fire conditions, yielding temperature distribution patterns consistent with controlled simulation results. The concrete elements exhibited gradual heating profiles and retained substantial structural integrity over extended durations, while steel components showed susceptibility to rapid temperature escalation, indicating the necessity for protective interventions. This case study confirms the modelling framework's applicability to actual fire safety evaluations and its value in supporting informed decision-making for pedestrian bridge infrastructure.

The study successfully fulfilled its intended scope by developing reliable thermal models, establishing a definitive hierarchy of fire performance among girder configurations, and demonstrating practical applicability through real-world bridge analysis. The collective findings emphasize the superior fire resistance inherent in concrete girder sections and provide valuable guidance for fire-resilient structural design and post-fire condition assessment of bridge infrastructure.

5.2 Recommendations for Further Studies

Based on the findings and analyses conducted in this study, several recommendations are proposed to guide future research efforts and practical applications. First, it is recommended that the current two-dimensional thermal models be extended to full three-dimensional simulations of the University of Benin pedestrian bridge. A 3D model would allow for a more realistic representation of the bridge geometry, including diaphragms, cross-bracing, deck–girder interaction, and boundary conditions that influence thermal behavior. Incorporating various load combinations; such as dead load, pedestrian live load, environmental loads, and accidental actions; both with and without fire exposure would provide deeper insight into the

structural response of the bridge under realistic service and extreme scenarios. Such an approach would also allow the evaluation of deformation patterns, load redistribution, and potential failure mechanisms that cannot be captured adequately in a 2D analysis. This progression from 2D to 3D modelling represents a logical continuation of the present work and would significantly strengthen the overall predictive capacity of the modelling framework.

Furthermore, it is also recommended that a parametric study be carried out to identify the key factors that affect the thermal and post-fire performance of the girder sections. This should include variations in material properties, fire duration, fire curve type, insulation thickness, and section geometry. The results from this study can then be used to suggest practical retrofitting methods that will improve the fire resistance of the girders. Possible measures include applying fire-protection coatings to steel girders, adding fire-resistant concrete layers, increasing concrete cover, or strengthening members with fibre-reinforced polymer (FRP) materials. These recommendations should be based on the sensitivity results to ensure that the most critical weaknesses are addressed. Overall, such retrofitting measures would improve the safety and post-fire performance of pedestrian bridges.

1. Union Pacific. (2021, August 5). *Rising from the ashes: Dry Canyon Bridge rebuilt in one month*. Inside Track. https://www.up.com/aboutup/community/inside_track/dry-canyon-bridge-repens-early.htm
2. Abimbola, O. (2018, August 8). Photos: Mini van catches fire on Third Mainland Bridge. *Punch Newspapers*. https://punchng.com/photos-mini-van-catches-fire-on-third-mainland-bridge/
3. Hanafi, A. (2020, November 7). Petrol tanker explodes on Kara Bridge along Lagos-Ibadan Expressway. *Punch Newspapers*. https://punchng.com/breaking-petrol-tanker-explodes-on-kara-bridge-along-lagos-ibadan-expressway/
4. Oyediran, T. (2024, May 25). Fuel tanker explodes on Lagos-Ibadan Expressway. *Punch Newspapers*. https://punchng.com/updated-fuel-tanker-explodes-on-lagos-ibadan-expressway/

MLA Style:

Union Pacific. "Rising from the Ashes: Dry Canyon Bridge Rebuilt in One Month." *Inside Track*, 5 Aug. 2021, www.up.com/aboutup/community/inside_track/dry-canyon-bridge-repens-early.htm.

Abimbola, Oluwakemi. "Photos: Mini Van Catches Fire on Third Mainland Bridge." *Punch Newspapers*, 8 Aug. 2018, punchng.com/photos-mini-van-catches-fire-on-third-mainland-bridge/.

Hanafi, Afeez. "Petrol Tanker Explodes on Kara Bridge along Lagos-Ibadan Expressway." *Punch Newspapers*, 7 Nov. 2020, punchng.com/breaking-petrol-tanker-explodes-on-kara-bridge-along-lagos-ibadan-expressway/.

Oyediran, Tosin. "Fuel Tanker Explodes on Lagos-Ibadan Expressway." *Punch Newspapers*, 25 May 2024, punchng.com/updated-fuel-tanker-explodes-on-lagos-ibadan-expressway/.

INACCESSIBLE SOURCES (Format Based on URL):

APA Style:

Tanker explosion: Lagos bridge remains closed as repair work begins. Daily Trust. https://dailytrust.com/tanker-explosion-lagos-bridge-remains-closed-as-repair-work-begins/

2022 Crimean Bridge explosion. Wikipedia. https://en.m.wikipedia.org/wiki/2022_Crimean_Bridge_explosion

2023 Crimean Bridge explosion. Wikipedia. https://en.m.wikipedia.org/wiki/2023_Crimean_Bridge_explosion

Lagos State Fire Service. (2020, June 23). *Lagos Fire Service averts escalation of multiple fire incident on Kara Bridge*. https://fireservice.lagosstate.gov.ng/2020/06/23/lagos-fire-service-averts-escalation-of-multiple-fire-incident-on-kara-bridge/

Fuel tanker rams into vehicle on Niger Bridge, catches fire. *Punch Newspapers*. https://punchng.com/fuel-tanker-rams-into-vehicle-on-niger-bridge-catches-fire/

(2018, June). *Vanguard News*. https://www.vanguardngr.com/2018/06/1012631/

(2023, October). No casualty recorded in Ijora tanker explosion, Lagos Fire Service confirms. *Vanguard News*. https://www.vanguardngr.com/2023/10/no-casualty-recorded-in-ijora-tanker-explosion-lagos-fire-service-confirms/

Chi, H.-L., Chi, H.-L., Wang, X., Wang, X., Jiao, Y., & Jiao, Y. (2015). BIM-Enabled Structural Design: Impacts and Future Developments in Structural Modelling, Analysis and Optimisation Processes. *Archives of Computational Methods in Engineering*, *22*(1), 135–151. https://doi.org/10.1007/s11831-014-9127-7

Cook, N., & Cook, N. J. (2007). *Designers' Guide to EN 1991-1-4 Eurocode 1: Actions on structures, general actions part 1-4. Wind actions*. https://doi.org/10.1680/dgte1.31524

Craig, D., & Naser, M. Z. (2023). A primer and success stories on performance-based fire design of structures. *Journal of Structural Fire Engineering*. https://doi.org/10.1108/jsfe-01-2023-0002

Dalémat, M., Dalémat, M., Coret, M., Coret, M., Leygue, A., Leygue, A., Erwan Verron, & Verron, E. (2019). Measuring stress field without constitutive equation. *Mechanics of Materials*, *136*, 103087. https://doi.org/10.1016/j.mechmat.2019.103087

Decò, A., Decò, A., Frangopol, D. M., & Frangopol, D. M. (2011). Risk assessment of highway bridges under multiple hazards. *Journal of Risk Research*, *14*(9), 1057–1089. https://doi.org/10.1080/13669877.2011.571789

Ede, A. N., Ede, A. N., Nwankwo, C. O., Nwankwo, C. O., Oyebisi, S., Oyebisi, S., Olofinnade, O. M., Olofinnade, O. M., Okeke, A. C., Okeke, A., Busari, A. A., Busari, A., & Busari, A. A. (2019). Failure Trend of Transport Infrastructure in Developing Nations: Cases of Bridge Collapse in Nigeria. *IOP Conference Series: Materials Science and Engineering*, *640*(1), 012102. https://doi.org/10.1088/1757-899x/640/1/012102

Frangopol, D. M., & Soliman, M. (2019). Life-cycle of structural systems: Recent achievements and future directions. In *Structures and infrastructure systems* (pp. 46–65). Routledge.

Gayed, R. B., Gayed, R. B., Ghali, A., & Ghali, A. (2021). *Structural Analysis Fundamentals*. https://doi.org/10.1201/9780429286858

Gernay, T., Gernay, T., Khorasani, N. E., & Khorasani, N. E. (2019). Resilience of the Built Environment to Fire and Fire-Following-Earthquake. *Resilient Structures and Infrastructure*, 417–449. https://doi.org/10.1007/978-981-13-7446-3_16

Giuliani, L., Giuliani, L., Crosti, C., Crosti, C., Gentili, F., & Gentili, F. (2012). *Vulnerability of bridges to fire*. https://doi.org/10.1201/b12352-225

Godart, B., Godart, B., Godart, B., Berthellemy, J., Berthellemy, J., Berthellemy, J., Lucas, J. P., & Lucas, J. P. (2015). Diagnosis, assessment and repair of the Mathilde bridge close to collapse during a fire. *Structural Engineering International*, *25*(3), 331–338. https://doi.org/10.2749/101686615x14210663188691

Golewski, G. L. (2023). The Phenomenon of Cracking in Cement Concretes and Reinforced Concrete Structures: The Mechanism of Cracks Formation, Causes of Their Initiation, Types and Places of Occurrence, and Methods of Detection—A Review. *Buildings*, *13*(3), 765–765. https://doi.org/10.3390/buildings13030765

Gong, X., Gong, X., Agrawal, A. K., & Agrawal, A. K. (2015). Numerical Simulation of Fire Damage to a Long-Span Truss Bridge. *Journal of Bridge Engineering*, *20*(10), 04014109. https://doi.org/10.1061/(asce)be.1943-5592.0000707

Hamad, R. J., Johari, M. M., & Haddad, R. H. (2017). Mechanical properties and bond characteristics of different fiber reinforced polymer rebars at elevated temperatures. *Construction and Building Materials*, *142*, 521–535.

Jiayu, H., Hu, J., Carvel, R., Carvel, R. O., Carvel, R., Usmani, A., & Usmani, A. (2021). Bridge fires in the 21st century: A literature review. *Fire Safety Journal*, *126*, 103487. https://doi.org/10.1016/j.firesaf.2021.103487

Kashi, E., Kashi, E., Bahoosh, M., Bahoosh, M., & Bahoosh, M. (2020). Jet fire assessment in complex environments using computational fluid dynamics. *Brazilian Journal of Chemical Engineering*, *37*(1), 203–212. https://doi.org/10.1007/s43153-019-00003-y

Kragh, E., Kragh, E., Narasimhan, H., Narasimhan, H., Jensen, J., & Jensen, J. L. (2020). Fire Protection of Bridge Cables. *Structural Engineering International*, *30*(4), 530–533. https://doi.org/10.1080/10168664.2020.1716653

Kuna, M., & Kuna, M. (2013). *Finite Elements in Fracture Mechanics*. https://doi.org/10.1007/978-94-007-6680-8

Lourenço, P. B., & Gaetani, A. (2022). *Finite element analysis for building assessment: Advanced use and practical recommendations*. Routledge.

Luo, Z., Luo, Z., Luo, Z., Zhao, Y. F., & Zhao, Y. (2018). A survey of finite element analysis of temperature and thermal stress fields in powder bed fusion Additive Manufacturing. *Additive Manufacturing*, *21*, 318–332. https://doi.org/10.1016/j.addma.2018.03.022

Marcé-Nogué, J., Nogué, J. M., Terricabras, J. F., Terricabras, J. F., Espert, L. G., Espert, L. G., Romero, M. S., & Romero, M. S. (2020). *Improving mesh generation in finite element analysis for functional morphology approaches*. *30*(1), 117–132. https://doi.org/10.7203/sjp.30.1.17227

Memon, S. A., Shah, S. F. A., Khushnood, R. A., & Baloch, W. L. (2019). Durability of sustainable concrete subjected to elevated temperature–A review. *Construction and Building Materials*, *199*, 435–455.

Miah, J. (2017). *The effect of compressive loading and cement type on the fire spalling behaviour of concrete*. Université de Pau et des Pays de l'Adour-Laboratoire SIAME.

More, S. T., & Bindu, Dr. R. S. (2015). *Effect of Mesh Size on Finite Element Analysis of Plate Structure*.

Mostafaei, H., Mostafaei, H., Kashef, A., Kashef, A., Sultan, M. A., Sultan, M., McCartney, C., McCartney, C., Leroux, P., Leroux, P., Cowalchuk, R., & Cowalchuk, R. (2014). *Resilience of Critical Infrastructure to Extreme Fires—Gaps and Challenges*.

Nicoletta, B., Kotsovinos, P., & Gales, J. (2020). Review of the fire risk, hazard, and thermomechanical response of bridges in fire. *Canadian Journal of Civil Engineering*, *47*(4), 363–381.

Okunola, O. H., & Okunola, O. H. (2019). Spatial analysis of disaster statistics in selected cities of Nigeria. *International Journal of Emergency Management*, *15*(4), 299. https://doi.org/10.1504/ijem.2019.10025949

Oliveira, P., Oliveira, P. N., Fonseca, E. M. M., Fonseca, E. M. M., Campilho, R. D. S. G., Campilho, R. D. S. G., Campilho, R. D. S. G., Piloto, P. A. G., & Piloto, P. A. G. (2021). Analytical Equations Applied to the Study of Steel Profiles under Fire According to Different Nominal Temperature-Time Curves. *Mathematical & Computational Applications*, *26*(2), 48. https://doi.org/10.3390/mca26020048

Peris-Sayol, G., Peris-Sayol, G., Payá-Zaforteza, I., Paya-Zaforteza, I., Balasch-Parisi, S., Balasch-Parisi, S., Alós-Moya, J., & Alos-Moya, J. (2017). Detailed Analysis of the Causes of Bridge Fires and Their Associated Damage Levels. *Journal of Performance of Constructed Facilities*, *31*(3), 04016108. https://doi.org/10.1061/(asce)cf.1943-5509.0000977

Petrini, F., Francesco, P., Gkoumas, K., Konstantinos, G., Rossi, C., Claudio, R., Bontempi, F., & Franco, B. (2020). Multi-Hazard Assessment of Bridges in Case of Hazard Chain: State of Play and Application to Vehicle-Pier Collision Followed by Fire. *Frontiers in Built Environment*. https://doi.org/10.3389/fbuil.2020.580854

Reddy, J. N., & Reddy, J. N. (2015). *An Introduction to Nonlinear Finite Element Analysis: With applications to heat transfer, fluid mechanics, and solid mechanics*.

Rodrigue, J.-P. (2020). *The geography of transport systems*. Routledge.

Sharma, D. P., Beigi-Mohammadi, N., Geng, H., Dixon, D., Madro, R., Emmenegger, P., Tobar, C., Li, J., & Leon-Garcia, A. (2024). Statistical and Machine Learning Models for Predicting Fire and Other Emergency Events in the City of Edmonton. *IEEE Access*. https://doi.org/10.1109/access.2024.3390089

Silva, D. de, Gallo, M., Falco, L. D., & Nigro, E. (2023). Fire risk assessment of bridges: From state of the art to structural vulnerability mitigation. *Journal of Civil Structural Health Monitoring*. https://doi.org/10.1007/s13349-023-00670-z

Vaxman, A., Vaxman, A., Campen, M., Campen, M., Diamanti, O., Diamanti, O., Panozzo, D., Panozzo, D., Bommes, D., Bommes, D., Hildebrandt, K., Hildebrandt, K., Ben-Chen, M., & Ben-Chen, M. (2016). Directional field synthesis, design, and processing. *Computer Graphics Forum*, *35*(2), 545–572. https://doi.org/10.1111/cgf.12864

Zhu, S., Zhu, S., Levinson, D., Levinson, D., Liu, H., Liu, H. X., Harder, K. A., & Harder, K. A. (2010). The Traffic and Behavioral Effects of the I-35W Mississippi River Bridge Collapse. *Transportation Research Part A-Policy and Practice*. https://doi.org/10.1016/j.tra.2010.07.001

REFERENCES

Abambres, M., Abambres, M., Quach, W.-M., & Quach, W. M. (2016). Residual stresses in steel members: A review of available analytical expressions. *International Journal of Structural Integrity*, *7*(1), 70–94. https://doi.org/10.1108/ijsi-12-2014-0070

Abdelrahman, M., Khaloian-Sarnaghi, A., & van de Kuilen, J. W. (2025). Fire performance of

wood–steel hybrid elements: finite element analysis and experimental validation. *Wood Science and Technology*, *59*(1), 23

Abdulrahman, A. S., & Kadir, M. R. A. (2022). Behavior and flexural strength of fire damaged

high strength reinforced rectangular concrete beams after strengthening with CFRP laminates. *Ain Shams Engineering Journal*, *13*(6), 101767.

Abid, S. R., Xue, J., Liu, J., Tayşi, N., Liu, Y., Özakça, M., & Briseghella, B. (2022, March). Temperatures and gradients in concrete Bridges: Experimental, finite element analysis and design. In *Structures* (Vol. 37, pp. 960-976). Elsevier.

Adamczak-Bugno, A., Lipiec, S., Koteš, P., Bahleda, F., & Adamczak, J. (2024). Detection of

Destructive Processes and Assessment of Deformations in PP-Modified Concrete in an Air-Dry State and Exposed to Fire Temperatures Using the Acoustic Emission Method, Numerical Analysis and Digital Image Correlation. *Polymers*. https://doi.org/10.3390/polym16081161.

Aksoylu, C., Özkılıç, Y. O., & Arslan, M. H. (2022). Mechanical Steel Stitches: An innovative approach for strengthening shear deficiency in undamaged reinforced concrete beams. *Buildings*, *12*(10), 1501.

Al-Ansari, A. A., Kharnoob, M. M., & Kadhim, M. A. (2023). Abaqus simulation of the fire's impact on reinforced concrete bubble deck slabs. In *E3S Web of Conferences* (Vol. 427, p. 02001). EDP Sciences.

Ali, H. K., Abid, S. R., & Tayşi, N. (2023). Thermal behaviour and microstructure of self-

cured high-strength plain and fibrous geopolymer concrete exposed to various fire scenarios. *Buildings*, *13*(10), 2444

Amran, M., Amran, M., Huang, S., Huang, S.-S., Onaizi, A. M., Onaizi, A. M., Murali, G., Murali, G., Abdelgader, H. S., & Abdelgader, H. S. (2022). Fire spalling behavior of high-strength concrete: A critical review. *Construction and Building Materials*, *341*, 127902–127902. https://doi.org/10.1016/j.conbuildmat.2022.127902

Amran, Y. H. M., Fediuk, R., Lee, Y. H., Vatin, N., & Abdelgader, H. S. (2022). Fire resistance of concrete elements: mechanisms and prevention strategies. Construction and Building Materials, 319, 126030. https://doi.org/10.1016/j.conbuildmat.2021.126030.

Ariyanayagam, A., Ariyanayagam, A. D., Mahendran, M., & Mahendran, M. (2014). Development of realistic design fire time-temperature curves for the testing of cold-formed steel wall systems. *Frontiers of Structural and Civil Engineering*, *8*(4), 427–447. https://doi.org/10.1007/s11709-014-0279-1

Asadi, I., Shafigh, P., Hassan, Z. F. B. A., & Mahyuddin, N. B. (2018). Thermal conductivity of concrete–A review. *Journal of Building Engineering*, *20*, 81-93.

Awoyera, P. O., & Naser, M. Z. (Eds.). (2024). *Construction Materials and Their Properties for Fire Resistance and Insulation*. Elsevier.

Aziz, E., & Kodur, V. (2013). An approach for evaluating the residual strength of fire exposed bridge girders. *Journal of Constructional Steel Research*, *88*, 34-42.

Aziz, E. M., Aziz, E. M., Kodur, V., Kodur, V., Glassman, J. D., Glassman, J. D., Garlock, M. E. M., & Garlock, M. E. M. (2015). Behavior of steel bridge girders under fire conditions. *Journal of Constructional Steel Research*, *106*, 11–22. https://doi.org/10.1016/j.jcsr.2014.12.001

Kodur, V., Aziz, E., & Dwaikat, M. (2013). Evaluating fire resistance of steel girders in bridges. Journal of Bridge Engineering, 18(7), 633-643.

Babalola, O. E., Awoyera, P. O., Le, D. H., & Romero, L. B. (2021). A review of residual strength properties of normal and high strength concrete exposed to elevated temperatures: Impact of materials modification on behaviour of concrete composite. Construction and Building Materials, 296, 123448. https://doi.org/10.1016/j.conbuildmat.2021.123448.

Baiges, J., Baiges, J., Chiumenti, M., Chiumenti, M., Moreira, C. A., Moreira, C. A., Cervera, M., Cervera, M., Codina, R., & Codina, R. (2020). An adaptive Finite Element strategy for the numerical simulation of additive manufacturing processes. *Additive Manufacturing*, *37*, 101650. https://doi.org/10.1016/j.addma.2020.101650

Bailey, C. G. (2005). Fire engineering design of steel structures. *Advances in Structural Engineering*, *8*(3), 185-202.

Banerjee, D. K. (2021). A review of models for heat transfer in steel and concrete members during fire. *Journal of research of the National Institute of Standards and Technology*, *126*, 126030.

Batoma Sosso, P. Z., Gutierrez, F. M. P., & Berke, P. Z. (2021). Computational analysis of reinforced concrete structures subjected to fire using a multilayered finite element formulation. Fire Safety Journal.

Beeby, A. W., Beeby, A. W., Gulvanessian, H., Narayanan, R., & Narayanan, R. S. (2005). *Designers Guide to EN 1992-1-1 and EN 1992-1-2 Eurocode 2: Design of Concrete Structures. General rules and rules for buildings and structural fire design*. https://doi.org/10.1680/dgte2docs.31050.

Bernardi, P., Michelini, E., Sirico, A., Rainieri, S., & Corradi, C. (2020). Simulation methodology for the assessment of the structural safety of concrete tunnel linings

based on CFD fire–FE thermo-mechanical analysis: A case study. *Engineering Structures*, *225*, 111193.

Bocchini, P., Frangopol, D. M., Ummenhofer, T., & Zinke, T. (2014). Resilience and sustainability of civil infrastructure: Toward a unified approach. *Journal of Infrastructure Systems*, *20*(2), 04014004.

Bolina, F. L., Tutikian, B., & Rodrigues, J. P. C. (2021). Experimental analysis on the structural continuity effect in steel decking concrete slabs subjected to fire. *Engineering Structures*, *240*, 112299.

Brown, D. (2018). Eurocode 3: Design of steel structures. *Design of Structural Elements*, 508–577. https://doi.org/10.1201/9781315273433-19

Buchanan, A. H., & Abu, A. (2001). *Structural design for fire safety* (Vol. 273). New York: Wiley.

Buchanan, A. H., & Abu, A. K. (2017). *Structural design for fire safety*. John Wiley & Sons.

Chi, H.-L., Chi, H.-L., Wang, X., Wang, X., Jiao, Y., & Jiao, Y. (2015). BIM-Enabled Structural Design: Impacts and Future Developments in Structural Modelling, Analysis and Optimisation Processes. *Archives of Computational Methods in Engineering*, *22*(1), 135–151. https://doi.org/10.1007/s11831-014-9127-7

Cook, N., & Cook, N. J. (2007). *Designers' Guide to EN 1991-1-4 Eurocode 1: Actions on structures, general actions part 1-4. Wind actions*. https://doi.org/10.1680/dgte1.31524

Craig, D., & Naser, M. Z. (2023). A primer and success stories on performance-based fire design of structures. *Journal of Structural Fire Engineering*. https://doi.org/10.1108/jsfe-01-2023-0002

Curto, D., Franzitta, V., Guercio, A., & Martorana, P. (2022). FEM analysis: A review of the most common thermal bridges and their mitigation. *Energies*, *15*(7), 2318.

Dalémat, M., Dalémat, M., Coret, M., Coret, M., Leygue, A., Leygue, A., Erwan Verron, & Verron, E. (2019). Measuring stress field without constitutive equation. *Mechanics of Materials*, *136*, 103087. https://doi.org/10.1016/j.mechmat.2019.103087

Dal-Sasso, M. F., Assis, L. S. D., Farage, M. C. R., Bastos, F. D. S., & Beaucour, A. L. (2023). Numerical evaluation of aggregate size influence on concrete mechanical damage under high temperatures. *Revista IBRACON de Estruturas e Materiais*, *16*(6), e16605.

Decò, A., Decò, A., Frangopol, D. M., & Frangopol, D. M. (2011). Risk assessment of highway bridges under multiple hazards. *Journal of Risk Research*, *14*(9), 1057–1089. https://doi.org/10.1080/13669877.2011.571789.

Dossett, J. L., & Totten, G. E. (Eds.). (2013). *Steel heat treating fundamentals and processes*. Asm International.

Ebrahimzadeh, M., & Rezaeian, A. (2022). Fire response of steel beams with bolted flange plate connections. *Fire Technology*, *58*(1), 479-501.

Ede, A. N., Ede, A. N., Nwankwo, C. O., Nwankwo, C. O., Oyebisi, S., Oyebisi, S., Olofinnade, O. M., Olofinnade, O. M., Okeke, A. C., Okeke, A., Busari, A. A., Busari, A., & Busari, A. A. (2019). Failure Trend of Transport Infrastructure in Developing Nations: Cases of Bridge Collapse in Nigeria. *IOP Conference Series: Materials Science and Engineering*, *640*(1), 012102. https://doi.org/10.1088/1757-899x/640/1/012102

Fan, S., Zhang, Y., & Tan, K. H. (2020). Experimental and analytical studies of reinforced concrete short beams at elevated temperatures. *Engineering Structures*, *212*, 110445

Frangopol, D. M., & Soliman, M. (2019). Life-cycle of structural systems: Recent achievements and future directions. In *Structures and infrastructure systems* (pp. 46–65). Routledge.

Franssen, J. M., & Zaharia, R. (2005). *Design of Steel Structures subjected to Fire. Background and Design Guide to Eurocode 3*. Les Éditions de l'Université de Liège, Liège, Belgium.

Garlock, M., Paya-Zaforteza, I., Kodur, V., & Gu, L. (2012). Fire hazard in bridges: Review, assessment and repair strategies. *Engineering structures*, *35*, 89-98.

Gayed, R. B., Gayed, R. B., Ghali, A., & Ghali, A. (2021). *Structural Analysis Fundamentals*. https://doi.org/10.1201/9780429286858.

Gernay, T., Gernay, T., Khorasani, N. E., & Khorasani, N. E. (2019). Resilience of the Built Environment to Fire and Fire-Following-Earthquake. *Resilient Structures and Infrastructure*, 417–449. https://doi.org/10.1007/978-981-13-7446-3_16.

Gernay, T., Pei, J. Q., & Tong, Q. (2024). Damage analysis and assessment of concrete T-girder bridge based on fire scene numerical reconstruction. Advances in Bridge Engineering, 5(28).

Gidaris, I., Gidaris, I., Padgett, J. E., Padgett, J. E., Fragiacomo, M., Barbosa, A. R., Barbosa, A. R., Chen, S., Chen, S., Cox, D. T., Cox, D. T., Webb, B. M., Webb, B. M., Cerato, A. B., & Cerato, A. B. (2017). Multiple-Hazard Fragility and Restoration Models of Highway Bridges for Regional Risk and Resilience Assessment in the United States: State-of-the-Art Review. *Journal of Structural Engineering-Asce*, *143*(3), 04016188–04016188. https://doi.org/10.1061/(asce)st.1943-541x.0001672

Gil, A. M. (2024). *Response of fire exposed concrete bridge girders* (Doctoral dissertation). Michigan State University.

Giuliani, L., Giuliani, L., Crosti, C., Crosti, C., Gentili, F., & Gentili, F. (2012). *Vulnerability of bridges to fire*. https://doi.org/10.1201/b12352-225

Godart, B., Godart, B., Godart, B., Berthellemy, J., Berthellemy, J., Berthellemy, J., Lucas, J. P., & Lucas, J. P. (2015). Diagnosis, assessment and repair of the Mathilde bridge

close to collapse during a fire. *Structural Engineering International*, *25*(3), 331–338. https://doi.org/10.2749/101686615x14210663188691

Golewski, G. L. (2023). The Phenomenon of Cracking in Cement Concretes and Reinforced Concrete Structures: The Mechanism of Cracks Formation, Causes of Their Initiation, Types and Places of Occurrence, and Methods of Detection; A Review. *Buildings*, *13*(3), 765–765. https://doi.org/10.3390/buildings13030765

Gong, X., Gong, X., Agrawal, A. K., & Agrawal, A. K. (2015). Numerical Simulation of Fire Damage to a Long-Span Truss Bridge. *Journal of Bridge Engineering*, *20*(10), 04014109. https://doi.org/10.1061/(asce)be.1943-5592.0000707

Hamad, R. J., Johari, M. M., & Haddad, R. H. (2017). Mechanical properties and bond characteristics of different fiber reinforced polymer rebars at elevated temperatures. *Construction and Building Materials*, *142*, 521–535

Han, S. H., Chang, D., & Huh, C. (2011). Efficiency analysis of radiative slab heating in a walking-beam-type reheating furnace. *Energy*, *36*(2), 1265-1272.

Hearn, E. J., & Hearn, E. J. (1997). Chapter 9 – Introduction to the Finite Element Method. *Finite Element Analysis*, 300–380. https://doi.org/10.1016/b978-075063266-9/50010-x.

Hesien, M., Youssef, M. A., & El-Fitiany, S. (2025). Finite Element Analysis of Flat Plate Structures in Fire. *Fire*, *8*(7), 252.

Hicks, J. L., Uchida, T. K., Seth, A., Rajagopal, A., & Delp, S. L. (2015). Is my model good enough? Best practices for verification and validation of musculoskeletal models and simulations of movement. *Journal of biomechanical engineering*, *137*(2), 020905.

Hodges, J., Rippe, C., Case, S. W., & Lattimer, B. Y. (2017). Predicting the structural response

of a compartment fire using full-field heat transfer measurements. *Fire Safety Journal*, *91*, 471-479.

Issa, C. A., & Izadifard, R. A. (2021). Numerical simulation of the experimental behavior of RC beams at elevated temperatures. *Advanced Modeling and Simulation in Engineering Sciences*, *8*(1), 12.

Izzet, A. F., Oukaili, N., & Harbi, N. A. (2021). Post-fire serviceability and residual strength of composite post-tensioned concrete T-beams. *SN Applied Sciences*, *3*(2), 158.

Jensen, J., Jensen, J. L., Bitsch, N., Bitsch, N., Bitsch, N., Narasimhan, H., & Narasimhan, H. (2021). *Efficient Fire Hazard Mitigation for Suspension Bridge Cables*. 235–244. https://doi.org/10.1007/978-3-030-59169-4_20

Jhavar, S., Paul, C. P., & Jain, N. K. (2013). Causes of failure and repairing options for dies and molds: A review. *Engineering Failure Analysis*, *34*, 519-535.

Jincheng Liu, Liu, J., Jin-Cheng Liu, Kang Hai Tan, Tan, K. H., Yao Yao, & Yao, Y. (2018). A new perspective on nature of fire-induced spalling in concrete. *Construction and Building Materials*, *184*, 581–590. https://doi.org/10.1016/j.conbuildmat.2018.06.204

Kamil, G. M., Liang, Q. Q., & Hadi, M. N. (2019). Numerical analysis of axially loaded rectangular concrete-filled steel tubular short columns at elevated temperatures. *Engineering Structures*, *180*, 89-102.

Kashi, E., Kashi, E., Bahoosh, M., Bahoosh, M., & Bahoosh, M. (2020). Jet fire assessment in

complex environments using computational fluid dynamics. *Brazilian Journal of Chemical Engineering*, *37*(1), 203–212. https://doi.org/10.1007/s43153-019-00003-y

Khan, M. A., Khan, A. A., Domada, R., & Usmani, A. (2021, December). Fire hazard assessment, performance evaluation, and fire resistance enhancement of bridges. In *Structures* (Vol. 34, pp. 4704-4714). Elsevier.

Klingsch, E. W. (2014). Explosive spalling of concrete in fire. *IBK Bericht*, *356*.

Kodur, V. K. R., & Dwaikat, M. (2008). A numerical model for predicting the fire resistance of reinforced concrete beams. *Cement and Concrete Composites*, *30*(5), 431-443.

Kodur, V., & Gil, A. (2024). Fire hazard in concrete bridges: review, assessment and mitigation strategies. *Structure and Infrastructure Engineering*, *20*(10), 1577-1594.

Koric, S., Hibbeler, L. C., & Thomas, B. G. (2009). Explicit coupled thermo-mechanical finite element model of steel solidification. *International Journal for Numerical Methods in Engineering*, *78*(1), 1-31.

Kragh, E., Kragh, E., Narasimhan, H., Narasimhan, H., Jensen, J., & Jensen, J. L. (2020). Fire Protection of Bridge Cables. *Structural Engineering International*, *30*(4), 530–533. https://doi.org/10.1080/10168664.2020.1716653

Kuna, M., & Kuna, M. (2013). *Finite Elements in Fracture Mechanics*. https://doi.org/10.1007/978-94-007-6680-8.

Lacković, L. (2021). *Behavior of concrete structures subjected to static and dynamic loading after fire exposure* (Doctoral dissertation, Dissertation, Stuttgart, Universität Stuttgart, 2021).

Li, W. Q., & Qu, Z. G. (2015). Experimental study of effective thermal conductivity of stainless

steel fiber felt. *Applied Thermal Engineering*, *86*, 119-126.

Li, Y. (2018). *Material properties and explosive spalling of ultra-high performance concrete in fire* (Doctoral dissertation).

Liu, Z., Li, G. Q., Paya-Zaforteza, I., Cai, C. S., & Huang, Q. (2023). Fire hazards in bridges: state of the art, recent progress, and current research gaps. *Journal of Bridge Engineering*, *28*(7), 03123003.

Liu, C., Yang, M., Wang, P., Li, K., Gao, X., & Miao, J. (2024). Experimental and analytical

study on post-fire residual flexural behavior of corroded reinforced concrete beams after various cooling methods. *Engineering Structures*, *316*, 118577.

Liu, Z., Luo, S., & Jiang, M. (2025). Study on the Temperature Model and Influence Effect of

Uncovered Steel Box Girder with Large Height–Width Ratio and Straight Web Plate. *Buildings*, *15*(11), 1818

Lourenço, P. B., & Gaetani, A. (2022). *Finite element analysis for building assessment: Advanced use and practical recommendations*. Routledge.

Luo, Z., Luo, Z., Luo, Z., Zhao, Y. F., & Zhao, Y. (2018). A survey of finite element analysis of temperature and thermal stress fields in powder bed fusion Additive Manufacturing. *Additive Manufacturing*, *21*, 318–332. https://doi.org/10.1016/j.addma.2018.03.022

Marcé-Nogué, J., Nogué, J. M., Terricabras, J. F., Terricabras, J. F., Espert, L. G., Espert, L. G., Romero, M. S., & Romero, M. S. (2020). *Improving mesh generation in finite element analysis for functional morphology approaches*. *30*(1), 117–132. https://doi.org/10.7203/sjp.30.1.17227.

Maragkos, G., & Beji, T. (2021). Review of convective heat transfer modelling in CFD simulations of fire-driven flows. *Applied sciences*, *11*(11), 5240.

Masiero, A. G. (2024). Fire response of precast prestressed and conventional concrete bridge girders. Doctoral dissertation, Michigan State University.

Matlock, D. K., Kang, S., De Moor, E., & Speer, J. G. (2020). Applications of rapid thermal processing to advanced high strength sheet steel developments. *Materials Characterization*, *166*, 110397.

Memon, S. A., Shah, S. F. A., Khushnood, R. A., & Baloch, W. L. (2019). Durability of sustainable concrete subjected to elevated temperature–A review. *Construction and Building Materials*, *199*, 435–455.

Miah, J. (2017). *The effect of compressive loading and cement type on the fire spalling behaviour of concrete*. Université de Pau et des Pays de l'Adour-Laboratoire SIAME.

Millard, A., & Pimienta, P. (2019). *Modelling of concrete behaviour at high temperature*. Cham, Germany: Springer International Publishing.

Mohammed, H., Ahmed, H., Kurda, R., Alyousef, R., & Deifalla, A. F. (2022). Heat-induced spalling of concrete: A review of the influencing factors and their importance to the phenomenon. *Materials*, *15*(5), 1693.

More, S. T., & Bindu, R. S. (2015). Effect of mesh size on finite element analysis of plate structure. *International Journal of Engineering Science and Innovative Technology*, *4*(3), 181-185.

Mostafaei, H., Mostafaei, H., Kashef, A., Kashef, A., Sultan, M. A., Sultan, M., McCartney, C., McCartney, C., Leroux, P., Leroux, P., Cowalchuk, R., & Cowalchuk, R. (2014). *Resilience of Critical Infrastructure to Extreme Fires—Gaps and Challenges*.

Narang, V. A. (2005). *Heat transfer analysis in steel structures* (Doctoral dissertation, Worcester Polytechnic Institute).

Neupane, D. (2020). Structural analysis technique of simple steel structures exposed in fire using ABAQUS.

Nicoletta, B., Kotsovinos, P., & Gales, J. (2020). Review of the fire risk, hazard, and thermomechanical response of bridges in fire. *Canadian Journal of Civil Engineering*, *47*(4), 363–381.

Okunola, O. H., & Okunola, O. H. (2019). Spatial analysis of disaster statistics in selected cities of Nigeria. *International Journal of Emergency Management*, *15*(4), 299. https://doi.org/10.1504/ijem.2019.10025949

Oliveira, P., Oliveira, P. N., Fonseca, E. M. M., Fonseca, E. M. M., Campilho, R. D. S. G.,

Campilho, R. D. S. G., Campilho, R. D. S. G., Piloto, P. A. G., & Piloto, P. A. G. (2021). Analytical Equations Applied to the Study of Steel Profiles under Fire According to Different Nominal Temperature-Time Curves. *Mathematical & Computational Applications*, *26*(2), 48. https://doi.org/10.3390/mca26020048

Park, J., Park, J., Cho, Y., Cho, Y. K., Shim, J. K., & Shim, J. W. (2018). *Resilient Fire Prevention and Management Strategies for Structures and Materials Stored under Urban Bridges*. 584–593. https://doi.org/10.1061/9780784481288.057

Parthasarathi, N. (2024). Transient state analysis of rehabilitated RC beams using finite element modelling and prediction using an artificial neural network. *Engineering Research Express*, *6*(2), 025109.

Peris-Sayol, G., Peris-Sayol, G., Payá-Zaforteza, I., Paya-Zaforteza, I., Balasch-Parisi, S., Balasch-Parisi, S., Alós-Moya, J., & Alos-Moya, J. (2017). Detailed Analysis of the Causes of Bridge Fires and Their Associated Damage Levels. *Journal of Performance of Constructed Facilities*, *31*(3), 04016108. https://doi.org/10.1061/(asce)cf.1943-5509.0000977

Petrini, F., Francesco, P., Gkoumas, K., Konstantinos, G., Rossi, C., Claudio, R., Bontempi, F., & Franco, B. (2020). Multi-Hazard Assessment of Bridges in Case of Hazard Chain: State of Play and Application to Vehicle-Pier Collision Followed by Fire. *Frontiers in Built Environment*. https://doi.org/10.3389/fbuil.2020.580854

Piekarska, W., Kubiak, M., & Saternus, Z. (2010). Application of Abaqus to analysis of the temperature field in elements heated by moving heat sources. *Archives of foundry engineering*, *10*(4), 177-182

Pipinato, A., Collin, P., & Hallmark, R. (2019). Prolonging the Lifetime of Old Steel and Steel–Concrete Bridges: Assessment Procedures and Retrofitting Interventions. *Structural Engineering International*, *29*(4), 507–518.

Rashid, F. L., Al-Obaidi, M. A., Dulaimi, A., Bernardo, L. F. A., Eleiwi, M. A., Mahood, H. B., & Hashim, A. (2023). A review of recent improvements, developments, effects, and challenges on using phase-change materials in concrete for thermal energy storage and release. *Journal of Composites Science*, *7*(9), 352.

Rackauskaite, E., Kotsovinos, P., Jeffers, A., & Rein, G. (2019). Computational analysis of thermal and structural failure criteria of a multi-storey steel frame exposed to fire. *Engineering Structures*, *180*, 524-543.

Reddy, J. N., & Reddy, J. N. (2015). *An Introduction to Nonlinear Finite Element Analysis: With applications to heat transfer, fluid mechanics, and solid mechanics*.

Rodrigue, J.-P. (2020). *The geography of transport systems*. Routledge.

Rzeszut, K., & Lukasz, P. (2013). Classes of Cross-Sections of Steel Structrural Elements in the Fire Situation. *Procedia Engineering*, *57*, 967-976.

Saari, N. B. (2019). *Behaviour and design of structural steel cross-sections in fire* (Doctoral dissertation, Imperial College London).

Selden, K. L., & Varma, A. H. (2016). Composite beams under fire loading: numerical modeling of behavior. *Journal of Structural Fire Engineering*, *7*(2), 142-157.

Sharma, D. P., Beigi-Mohammadi, N., Geng, H., Dixon, D., Madro, R., Emmenegger, P., Tobar, C., Li, J., & Leon-Garcia, A. (2024). Statistical and Machine Learning Models for Predicting Fire and Other Emergency Events in the City of Edmonton. *IEEE Access*. https://doi.org/10.1109/access.2024.3390089

Siddique, M., Khaled, A. R., Abdulhafiz, N. I., & Boukhary, A. Y. (2010). Recent advances in heat transfer enhancements: a review report. *International Journal of Chemical Engineering*, *2010*(1), 106461

Siebers, R., & Fischer, D. (2016). Sustainable steel construction. *Sustainable Steel Buildings: A Practical Guide for Structures and Envelopes*, 97.

Silva, D. de, Gallo, M., Falco, L. D., & Nigro, E. (2023). Fire risk assessment of bridges: From state of the art to structural vulnerability mitigation. *Journal of Civil Structural Health Monitoring*. https://doi.org/10.1007/s13349-023-00670-z.

So, H.-S. (2016). Spalling prevention of high performance concrete at high temperatures. In *High Performance Concrete Technology and Applications*. IntechOpen.

Son, Y. K., Kim, C.-S., & Kim, H. K. (2022). Fire Risk Evaluation of Cable Bridges due to Vehicle Fires. *IABSE Congress, Nanjing 2022: Bridges and Structures: Connection, Integration and Harmonisation*. https://doi.org/10.2749/nanjing.2022.1404

Song, C., Zhang, G., Li, X., & Kodur, V. (2021). Experimental and numerical study on failure mechanism of steel-concrete composite bridge girders under fuel fire exposure. *Engineering Structures*, *247*, 113230.

Structures in Fire Forum. (2024). *Framework for fire risk assessment of bridges*. United Kingdom instance.

Tang, M. S., Kadir, A. A., & Ngadiman, N. H. A. (2020, April). Simulation analysis of different bone scaffold porous structures for fused deposition modelling fabrication process. In *IOP Conference Series: Materials Science and Engineering* (Vol. 788, No. 1, p. 012023). IOP Publishing

Vácha, J., Kyzlík, P., Both, I., & Wald, F. (2016). Beams with corrugated web at elevated temperature, analytical and numerical models for heat transfer. *Fire Safety Journal*, *86*, 83-94.

Vaxman, A., Vaxman, A., Campen, M., Campen, M., Diamanti, O., Diamanti, O., Panozzo, D., Panozzo, D., Bommes, D., Bommes, D., Hildebrandt, K., Hildebrandt, K., Ben-Chen, M., & Ben-Chen, M. (2016). Directional field synthesis, design, and

processing. *Computer Graphics Forum*, *35*(2), 545–572. https://doi.org/10.1111/cgf.12864

Wang, X., Li, F., Yang, Q., & He, A. (2013). FEM analysis for residual stress prediction in hot

rolled steel strip during the run-out table cooling. *Applied Mathematical Modelling*, *37*(1-2), 586-609.

Watson, K. A., Brown, A. O., Hackett, R. K., & Pham, A. (2012, June). Finite element analysis

learning modules for an undergraduate heat transfer course: Implementation and assessment. In *2012 ASEE Annual Conference & Exposition* (pp. 25-638).

Wickström, U. (2016). *Temperature calculation in fire safety engineering*. Cham, Switzerland:

Springer.

Winful, D. A. A. A. (2018). *Structural fire design considerations for high strength steel* (Doctoral dissertation, Brunel University London).

Wong, M. B. (2017). Temperature analysis of partially heated steel members in fire. *Journal of Constructional Steel Research*, *128*, 1-6

Xia, Y., Chen, B., Weng, S., Ni, Y. Q., & Xu, Y. L. (2012). Temperature effect on vibration properties of civil structures: a literature review and case studies. *Journal of civil structural health monitoring*, *2*(1), 29-46

Yu, M., Chen, Q., Yao, X., Guo, X., Hao, T., & Wang, H. (2021). High-Temperature Properties

of a Long-Span Double-Deck Suspension Bridge under a Tanker Fire. Advances in Civil Engineering, 2021(1), 2631346.

Yun, T. S., Jeong, Y. J., Han, T. S., & Youm, K. S. (2013). Evaluation of thermal conductivity

for thermally insulated concretes. *Energy and Buildings*, *61*, 125-132.

Zehfuß, J., Zehfuss, J., Hosser, D., & Hosser, D. (2007). A parametric natural fire model for the structural fire design of multi-storey buildings. *Fire Safety Journal*, *42*(2), 115–126. https://doi.org/10.1016/j.firesaf.2006.08.004

Zhang, J., & Haghighat, F. (2009). Convective heat transfer prediction in large rectangular cross-sectional area Earth-to-Air Heat Exchangers. *Building and environment*, *44*(9), 1892-1898.

Zhang, B. (2011). Effects of moisture evaporation (weight loss) on fracture properties of high performance concrete subjected to high temperatures. *Fire Safety Journal*, *46*(8), 543 549.

Zhang, G., Yuan, Z., Ding, Y., Xu, F., Tang, C., & Wang, S. (2024). Fire behavior of composite

steel truss bridge girders: numerical investigation and design strategies. Advances in Bridge Engineering, 5(1), 36.

Zhang, H. Y., Li, Q. Y., Kodur, V., & Lv, H. R. (2021). Effect of cracking and residual deformation on behavior of concrete beams with different scales under fire exposure. *Engineering Structures*, *245*, 112886.

Zhou, M., & Peng, X. (2024). Shear behavior of prismatic and tapered prestressed concrete girders with corrugated steel webs exposed to vehicle fire. Engineering Structures, 308, 118004.

Zhou, L., Wanyan, R., & Li, S. (2024). Review on convective and radiation heat transfer between bridges and external environments. *Advances in Structural Engineering*, *27*(8), 1285-1302.

Zhu, S., Zhu, S., Levinson, D., Levinson, D., Liu, H., Liu, H. X., Harder, K. A., & Harder, K. A. (2010). The Traffic and Behavioral Effects of the I-35W Mississippi River Bridge Collapse. *Transportation Research Part A-Policy and Practice*. https://doi.org/10.1016/j.tra.2010.07.001.

Zou, Q., Pool, K., & Chen, S. (2020). Performance of suspension bridge hangers exposed to hazardous material fires considering wind effects. *Advances in Bridge Engineering*, *1*(1), 2.

APPENDIX A

BRIDGE FIRE INCIDENCE OVER THE YEARS

This table contains data used in Figure 2.2 for bridge fire incidence over the years.

DATE	LOCATION	CAUSES	REFERENCE
2024	Lagos, Nigeria	Ignition of petrol tanker	(Punch News Article, 2024)
2024	Lagos, Nigeria	Tanker fell and caught fire	(tvc News Article, 2024)
2023	Lagos, Nigeria	Ignition of petrol tanker	(Vanguard, News Article, 2024)
2023	Russia	Attack with 2-suicide sea drones	(Wikipedia.com, 2023)
2023	Anambra, Nigeria	Fuel tanker rams into vehicles and caught fire	(News Article, 2023)
2022	Lagos, Nigeria	Shelters under the bridge caught fire	(Vanguard, News Article, 2022)
2022	Russia	Bomb loaded onto a truck	(Wikipedia.com, 2022)
2021	Lagos, Nigeria	Electrical fault on petrol tanker	(Punch News Article, 2021)
2021	Lagos, Nigeria	Collision of tanker	(Punch News Article, 2021)
2021	Lagos, Nigeria	Explosion of petrol tanker	(Punch News Article, 2021)
2021	Lagos, Nigeria	Collision of trailer and car	(Punch News Article, 2021)
2020	Lagos-Ibadan, Nigeria	Collision of trailer and tankers	(Punch News Article, 2020)
2020	Kentucky, USA	2-truck collision	(Jiayu *et al*., 2021)
2019	Alberta, Canada	Arson	(Sharma *et al*., 2024)
2019	Apapa-Oshodi, Nigeria	Tanker explosion	(Okunola & Okunola, 2019)

DATE	LOCATION	CAUSES	REFERENCE
2018	Lagos, Nigeria	Explosion of petrol tanker	(Punch News Article, 2018)
2017	Madison County, USA	Arson	(Jiayu *et al*., 2021)
2017	Georgia, USA	Arson	(Jiayu *et al*., 2021)
2016	Alberta, Canada	Arson	(Jiayu *et al*., 2021)
2016	Saskatchewan, Canada	Arson	(Jiayu *et al*., 2021)
2015	Ohio, USA	Tanker truck	(Jiayu *et al*., 2021)
2014	California, USA	Metal cutting ignition on wooden support	(Jiayu *et al*., 2021)
2014	Franklin, USA	Explosion of petrol tanker	(Jiayu *et al*., 2021)
2014	Cairo, Egypt	Gas cylinder explosion	(Jiayu *et al*., 2021)
2013	Denmark		(Kragh *et al*., 2020)
2013	P.A, USA	Diesel tanker explosion	(Peris-Sayol *et al*., 2017)
2013	N.Y.C, USA	Tractor to trailer collision	(Jiayu *et al*., 2021)
2013	Texas, USA	Unknown	(Jiayu *et al*., 2021)
2012	Rouen, France	Tanker and truck collision	(Jiayu *et al*., 2021)
2012	Dormagen, Germany	Plastics stored under bridge caught fire	(Peris-Sayol *et al*., 2017)
2011	California, USA	Tanker and truck collision	(Jiayu *et al*., 2021)
2011	China	Unknown	(Jiayu *et al*., 2021)
2011	North London, UK	Arson	(Jiayu *et al*., 2021)
2010	South Korean	Tanker truck under the viaduct	(Jiayu *et al*., 2021)
2009	USA	Speeding car and fuel tanker collision	(Jiayu *et al*., 2021)
2007	Mexico	Truck collision with 2-school buses	(Peris-Sayol *et al*., 2017)
2007	California, USA	Tanker overturned	(Jiayu *et al*., 2021)
2006	USA	Fuel truck	(Jiayu *et al*., 2021)
2006	N.Y.C, USA	Tanker caught fire	(Jiayu *et al*., 2021)

DATE	LOCATION	CAUSES	REFERENCE
2005	Greece	Unknown	(Peris-Sayol *et al*., 2017)
2004	New Cologne, Germany	Car collided with tanker	(Jiayu *et al*., 2021)
2003	Surrey, UK	Vehicle caught fire	(Jiayu *et al*., 2021)
2002	Kansas, USA	Vehicle caught fire	(Jiayu *et al*., 2021)
2002	Birmingham, USA	Tanker collided with piers of the overpass	(Jiayu *et al*., 2021)

APPENDIX B

STEEL I-BEAM ANALYSIS AND DESIGN

In accordance with EN1993-1-1:2005 incorporating Corrigenda February 2006 and April 2009 and the recommended values TEDDS calculation

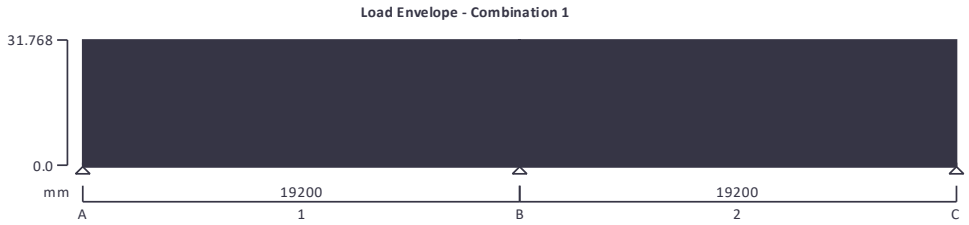

Library item: Show beam analysis drawing

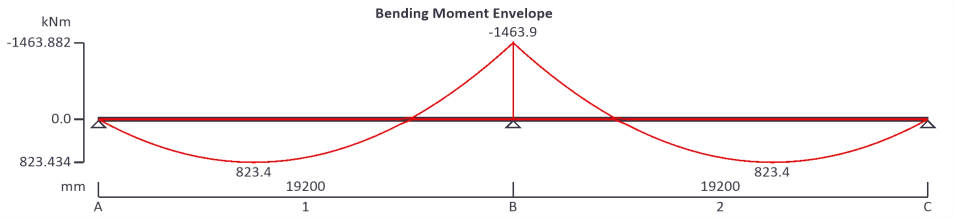

Library item: Show beam analysis drawing

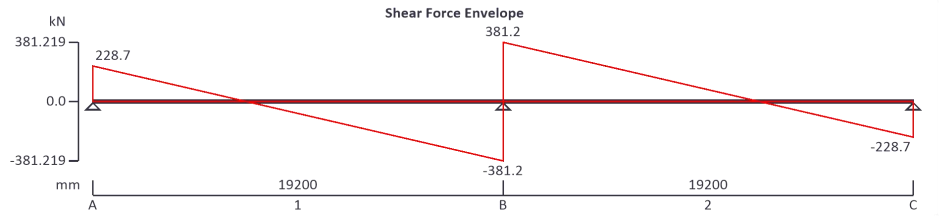

Library item: Show beam analysis drawing

Support conditions

Support A Vertically restrained

Rotationally free

Support B Vertically restrained

Rotationally free

Support C Vertically restrained

Rotationally free

Applied loading

Beam loads Variable full UDL 5 kN/m

Permanent full UDL 16.5 kN/m

Permanent self weight of beam × 1

Load combinations

Load combination 1 Support A Permanent × 1.35

Variable × 1.50

Permanent × 1.35

Variable × 1.50

Support B Permanent × 1.35

Variable × 1.50

Permanent × 1.35

Variable × 1.50

Support C Permanent × 1.35

Variable × 1.50

Analysis results

Maximum moment; M_{max} = 823.4 kNm; M_{min} = -1463.9 kNm

Maximum moment span 1; M_{s1_max} = 823.4 kNm; M_{s1_min} = -1463.9 kNm

Maximum moment span 2; M_{s2_max} = 823.4 kNm; M_{s2_min} = -1463.9 kNm

Maximum shear; V_{max} = 381.2 kN; V_{min} = -381.2 kN

Maximum shear span 1; V_{s1_max} = 228.7 kN; V_{s1_min} = -381.2 kN

Maximum shear span 2; V_{s2_max} = 381.2 kN; V_{s2_min} = -228.7 kN

Deflection; δ_{max} = 17.4 mm; δ_{min} = 0 mm

Deflection span 1; δ_{s1_max} = 17.4 mm; δ_{s1_min} = 0 mm

Deflection span 2; δ_{s2_max} = 17.4 mm; δ_{s2_min} = 0 mm

Maximum reaction at support A; R_{A_max} = 228.7 kN; R_{A_min} = 228.7 kN

Unfactored permanent load reaction at support A; $R_{A\_Permanent}$ = 129.4 kN

Unfactored variable load reaction at support A; $R_{A\_Variable}$ = 36 kN

Maximum reaction at support B; R_{B_max} = 762.4 kN; R_{B_min} = 762.4 kN

Unfactored permanent load reaction at support B; $R_{B\_Permanent}$ = 431.4 kN

Unfactored variable load reaction at support B; $R_{B\_Variable}$ = 120 kN

Maximum reaction at support C; R_{C_max} = 228.7 kN; R_{C_min} = 228.7 kN

Unfactored permanent load reaction at support C; $R_{C\_Permanent}$ = 129.4 kN

Unfactored variable load reaction at support C; $R_{C\_Variable}$ = 36 kN

Section details

Section type; UKB 533x312x150 (Tata Steel Advance)

Steel grade; S355

From table 3.1: Nominal values of yield strength f_y and ultimate tensile strength f_u for hot rolled structural steel

Nominal thickness of element; $t = \max(t_f, t_w) = 20.3$ mm

Nominal yield strength; $f_y = 355$ N/mm^2

Nominal ultimate tensile strength; $f_u = 510$ N/mm^2

Modulus of elasticity; E = 210000 N/mm^2

Library item: Section details output

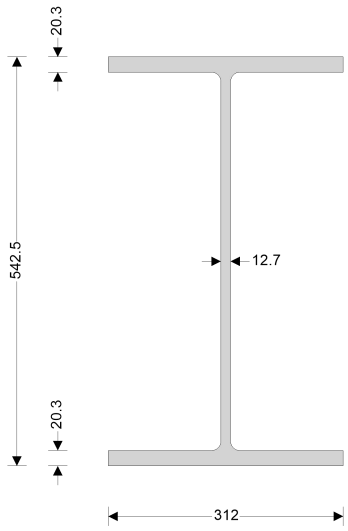

Library item: Show beam section sketch

Partial factors - Section 6.1

Resistance of cross-sections; $\gamma_{M0} = 1.00$

Resistance of members to instability; $\gamma_{M1} = 1.00$

Resistance of tensile members to fracture; $\gamma_{M2} = 1.25$

Library item: Partial factors

Lateral restraint

Library item: Lateral restraint header

Span 1 has full lateral restraint

Library item: Lateral restraint output

Span 2 has full lateral restraint

Library item: Lateral restraint output

Effective length factors

Effective length factor in major axis; $K_y = 1.000$

Effective length factor in minor axis; $K_z = 1.000$

Effective length factor for torsion; $K_{LT.A} = 1.000$;

Library item: Effective length factor output

$K_{LT.B} = 1.000$;

Library item: Eff length factor x1 output

$K_{LT.C} = 1.000$;

Library item: Eff length factor x1 output

Classification of cross sections - Section 5.5

$\varepsilon = \sqrt{[235\ N/mm^2 / f_y]} = 0.81$

Library item: Classification heading

Internal compression parts subject to bending - Table 5.2 (sheet 1 of 3)

Width of section; $c = d = 476.5$ mm

$c / t_w = 46.1 \times \varepsilon <= 72 \times \varepsilon$; Class 1

Library item: Internal bend class output

Outstand flanges - Table 5.2 (sheet 2 of 3)

Width of section; $c = (b - t_w - 2 \times r) / 2 = 137$ mm

$c / t_f = 8.3 \times \varepsilon <= 9 \times \varepsilon$; Class 1

Library item: Outstand flange class output

Section is class 1

Library item: Classification result

Check shear - Section 6.2.6

Library item: Design shear header

Height of web; $h_w = h - 2 \times t_f = 501.9$ mm

Shear area factor; $\eta = 1.000$

$h_w / t_w < 72 \times \varepsilon / \eta$

Library item: Shear slenderness output

Shear buckling resistance can be ignored

Library item: General results output

Design shear force; $V_{Ed} = \max(\text{abs}(V_{max}), \text{abs}(V_{min})) = 381.2$ kN

Shear area - cl 6.2.6(3); $A_v = \max(A - 2 \times b \times t_f + (t_w + 2 \times r) \times t_f, \eta \times h_w \times t_w) = 7286$ mm^2

Design shear resistance - cl 6.2.6(2); $V_{c,Rd} = V_{pl,Rd} = A_v \times (f_y / \sqrt{[3]}) / \gamma_{M0} = 1493.3$ kN

Library item: Shear resistance plastic output

PASS - Design shear resistance exceeds design shear force

Library item: General results output

Check bending moment at span 1 major (y-y) axis - Section 6.2.5

Design bending moment; $M_{Ed} = \max(\text{abs}(M_{s1\_max}), \text{abs}(M_{s1\_min})) = 1463.9$ kNm

Library item: Design bending header

Design bending resistance moment - eq 6.13; $M_{c,Rd} = M_{pl,Rd} = W_{pl,y} \times f_y / \gamma_{M0} = 1470.3$ kNm

Library item: Design bending moment output

PASS - Design bending resistance moment exceeds design bending moment

Library item: General results output

Check vertical deflection - Section 7.2.1

Consider deflection due to variable loads

Limiting deflection; $\delta_{lim} = L_{s1} / 360 = 53.3$ mm

Maximum deflection span 1; $\delta = \max(\text{abs}(\delta_{max}), \text{abs}(\delta_{min})) = 17.414$ mm

Library item: Deflection output

PASS - Maximum deflection does not exceed deflection limit

Library item: General results output

APPENDIX C

STEEL I-BEAM INCREMENT RESULTS FROM ABAQUS

The following images are the increment results from Abaqus for the Steel I-Beam analysis

test_heat_transfer Monitor

Job: test_heat_transfer Status: Completed

Step	Increment	Att	Severe Discon Iter	Equil Iter	Total Iter	Total Time/Freq	Step Time/LPF	Time/LPF Inc
1	1	1	0	1	1	1	1	1
1	2	1	0	1	1	2	2	1
1	3	1	0	1	1	3	3	1
1	4	1	0	1	1	5	5	2
1	5	1	0	1	1	9	9	4
1	6	1	0	1	1	14	14	5
1	7	1	0	1	1	19	19	5
1	8	1	0	1	1	24	24	5
1	9	1	0	1	1	29	29	5
1	10	1	0	1	1	34	34	5
1	11	1	0	1	1	39	39	5
1	12	1	0	1	1	44	44	5
1	13	1	0	1	1	49	49	5
1	14	1	0	1	1	54	54	5
1	15	1	0	1	1	59	59	5
1	16	1	0	1	1	64	64	5
1	17	1	0	1	1	69	69	5
1	18	1	0	1	1	74	74	5
1	19	1	0	1	1	79	79	5
1	20	1	0	1	1	84	84	5
1	21	1	0	1	1	89	89	5
1	22	1	0	1	1	94	94	5
1	23	1	0	1	1	99	99	5
1	24	1	0	1	1	104	104	5
1	25	1	0	1	1	109	109	5
1	26	1	0	1	1	114	114	5
1	27	1	0	1	1	119	119	5
1	28	1	0	1	1	124	124	5
1	29	1	0	1	1	129	129	5
1	30	1	0	1	1	134	134	5

Search Text

Text to find: Match case Next Previous

Kill Dismiss

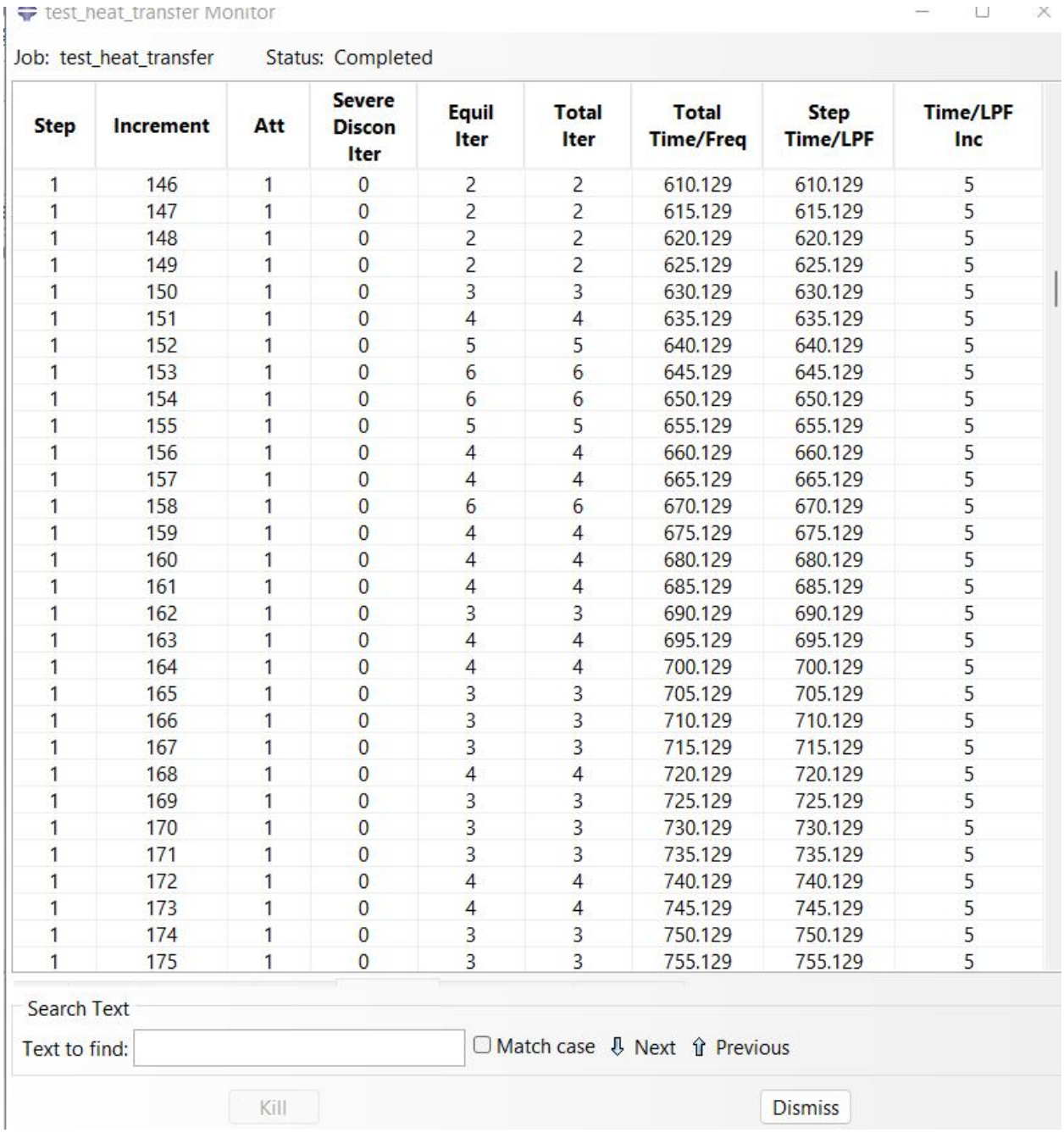

Step	Increment	Att	Severe Discon Iter	Equil Iter	Total Iter	Total Time/Freq	Step Time/LPF	Time/LPF Inc
1	146	1	0	2	2	610.129	610.129	5
1	147	1	0	2	2	615.129	615.129	5
1	148	1	0	2	2	620.129	620.129	5
1	149	1	0	2	2	625.129	625.129	5
1	150	1	0	3	3	630.129	630.129	5
1	151	1	0	4	4	635.129	635.129	5
1	152	1	0	5	5	640.129	640.129	5
1	153	1	0	6	6	645.129	645.129	5
1	154	1	0	6	6	650.129	650.129	5
1	155	1	0	5	5	655.129	655.129	5
1	156	1	0	4	4	660.129	660.129	5
1	157	1	0	4	4	665.129	665.129	5
1	158	1	0	6	6	670.129	670.129	5
1	159	1	0	4	4	675.129	675.129	5
1	160	1	0	4	4	680.129	680.129	5
1	161	1	0	4	4	685.129	685.129	5
1	162	1	0	3	3	690.129	690.129	5
1	163	1	0	4	4	695.129	695.129	5
1	164	1	0	4	4	700.129	700.129	5
1	165	1	0	3	3	705.129	705.129	5
1	166	1	0	3	3	710.129	710.129	5
1	167	1	0	3	3	715.129	715.129	5
1	168	1	0	4	4	720.129	720.129	5
1	169	1	0	3	3	725.129	725.129	5
1	170	1	0	3	3	730.129	730.129	5
1	171	1	0	3	3	735.129	735.129	5
1	172	1	0	4	4	740.129	740.129	5
1	173	1	0	4	4	745.129	745.129	5
1	174	1	0	3	3	750.129	750.129	5
1	175	1	0	3	3	755.129	755.129	5

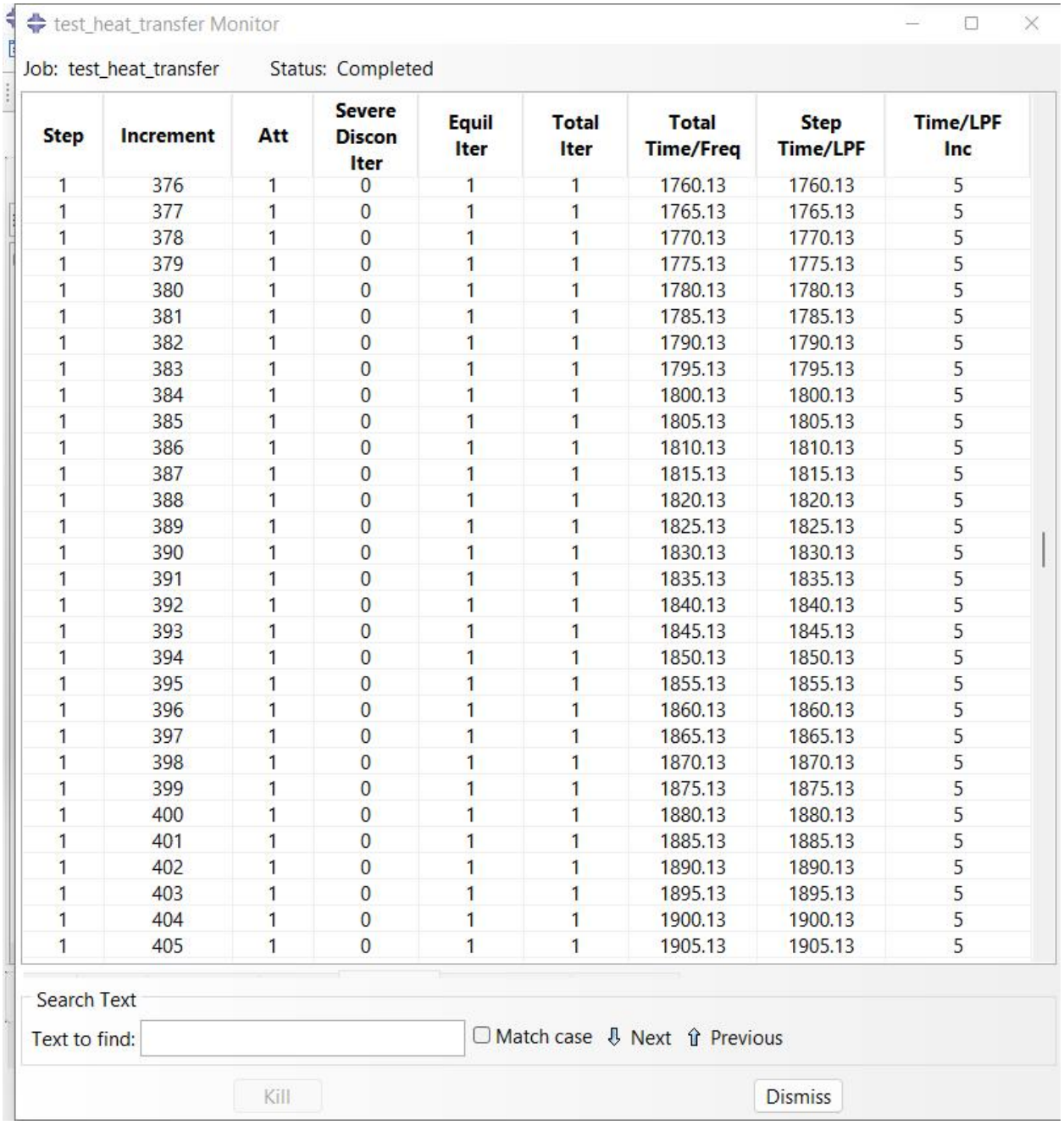

Step	Increment	Att	Severe Discon Iter	Equil Iter	Total Iter	Total Time/Freq	Step Time/LPF	Time/LPF Inc
1	376	1	0	1	1	1760.13	1760.13	5
1	377	1	0	1	1	1765.13	1765.13	5
1	378	1	0	1	1	1770.13	1770.13	5
1	379	1	0	1	1	1775.13	1775.13	5
1	380	1	0	1	1	1780.13	1780.13	5
1	381	1	0	1	1	1785.13	1785.13	5
1	382	1	0	1	1	1790.13	1790.13	5
1	383	1	0	1	1	1795.13	1795.13	5
1	384	1	0	1	1	1800.13	1800.13	5
1	385	1	0	1	1	1805.13	1805.13	5
1	386	1	0	1	1	1810.13	1810.13	5
1	387	1	0	1	1	1815.13	1815.13	5
1	388	1	0	1	1	1820.13	1820.13	5
1	389	1	0	1	1	1825.13	1825.13	5
1	390	1	0	1	1	1830.13	1830.13	5
1	391	1	0	1	1	1835.13	1835.13	5
1	392	1	0	1	1	1840.13	1840.13	5
1	393	1	0	1	1	1845.13	1845.13	5
1	394	1	0	1	1	1850.13	1850.13	5
1	395	1	0	1	1	1855.13	1855.13	5
1	396	1	0	1	1	1860.13	1860.13	5
1	397	1	0	1	1	1865.13	1865.13	5
1	398	1	0	1	1	1870.13	1870.13	5
1	399	1	0	1	1	1875.13	1875.13	5
1	400	1	0	1	1	1880.13	1880.13	5
1	401	1	0	1	1	1885.13	1885.13	5
1	402	1	0	1	1	1890.13	1890.13	5
1	403	1	0	1	1	1895.13	1895.13	5
1	404	1	0	1	1	1900.13	1900.13	5
1	405	1	0	1	1	1905.13	1905.13	5

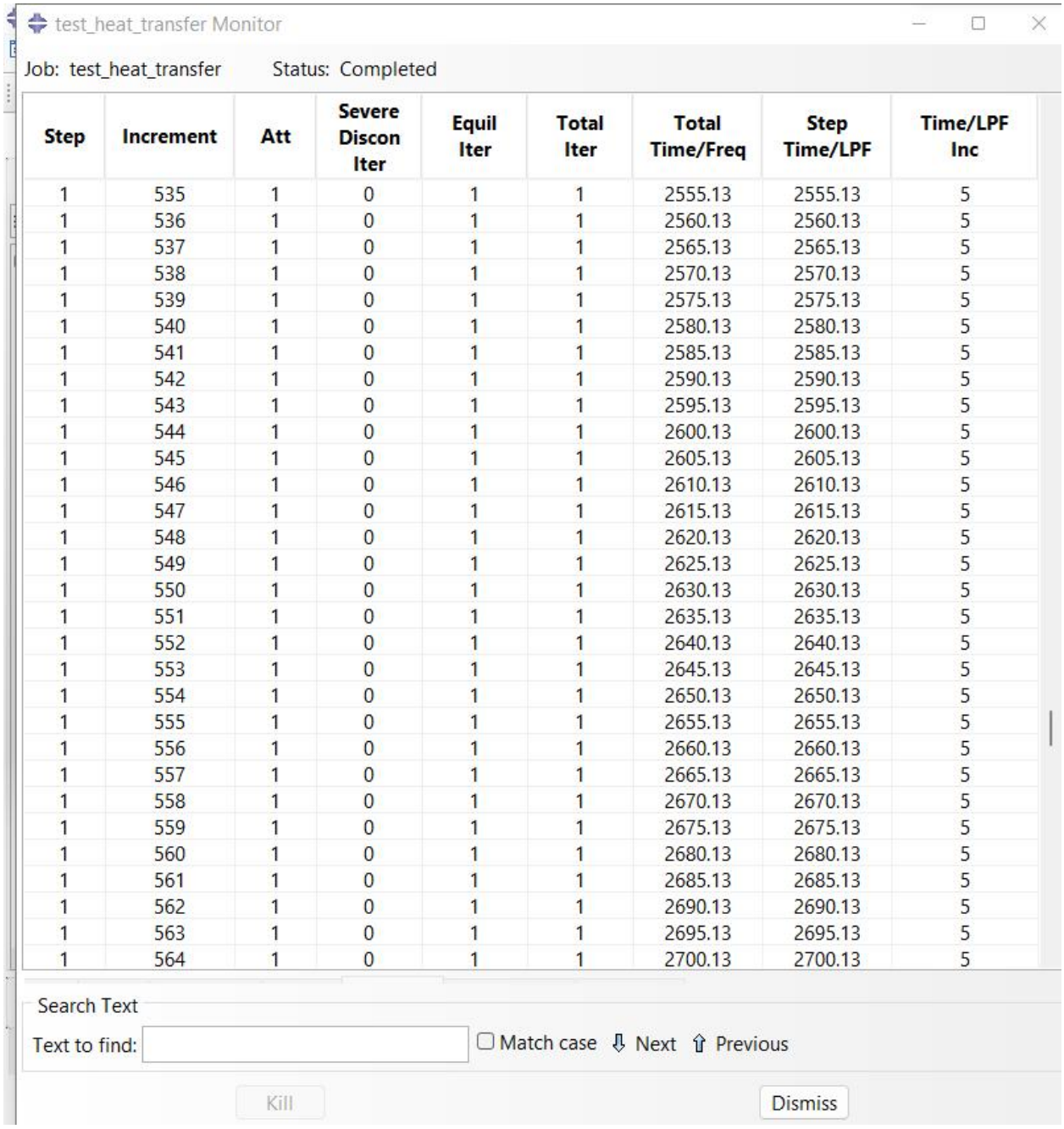

Step	Increment	Att	Severe Discon Iter	Equil Iter	Total Iter	Total Time/Freq	Step Time/LPF	Time/LPF Inc
1	535	1	0	1	1	2555.13	2555.13	5
1	536	1	0	1	1	2560.13	2560.13	5
1	537	1	0	1	1	2565.13	2565.13	5
1	538	1	0	1	1	2570.13	2570.13	5
1	539	1	0	1	1	2575.13	2575.13	5
1	540	1	0	1	1	2580.13	2580.13	5
1	541	1	0	1	1	2585.13	2585.13	5
1	542	1	0	1	1	2590.13	2590.13	5
1	543	1	0	1	1	2595.13	2595.13	5
1	544	1	0	1	1	2600.13	2600.13	5
1	545	1	0	1	1	2605.13	2605.13	5
1	546	1	0	1	1	2610.13	2610.13	5
1	547	1	0	1	1	2615.13	2615.13	5
1	548	1	0	1	1	2620.13	2620.13	5
1	549	1	0	1	1	2625.13	2625.13	5
1	550	1	0	1	1	2630.13	2630.13	5
1	551	1	0	1	1	2635.13	2635.13	5
1	552	1	0	1	1	2640.13	2640.13	5
1	553	1	0	1	1	2645.13	2645.13	5
1	554	1	0	1	1	2650.13	2650.13	5
1	555	1	0	1	1	2655.13	2655.13	5
1	556	1	0	1	1	2660.13	2660.13	5
1	557	1	0	1	1	2665.13	2665.13	5
1	558	1	0	1	1	2670.13	2670.13	5
1	559	1	0	1	1	2675.13	2675.13	5
1	560	1	0	1	1	2680.13	2680.13	5
1	561	1	0	1	1	2685.13	2685.13	5
1	562	1	0	1	1	2690.13	2690.13	5
1	563	1	0	1	1	2695.13	2695.13	5
1	564	1	0	1	1	2700.13	2700.13	5

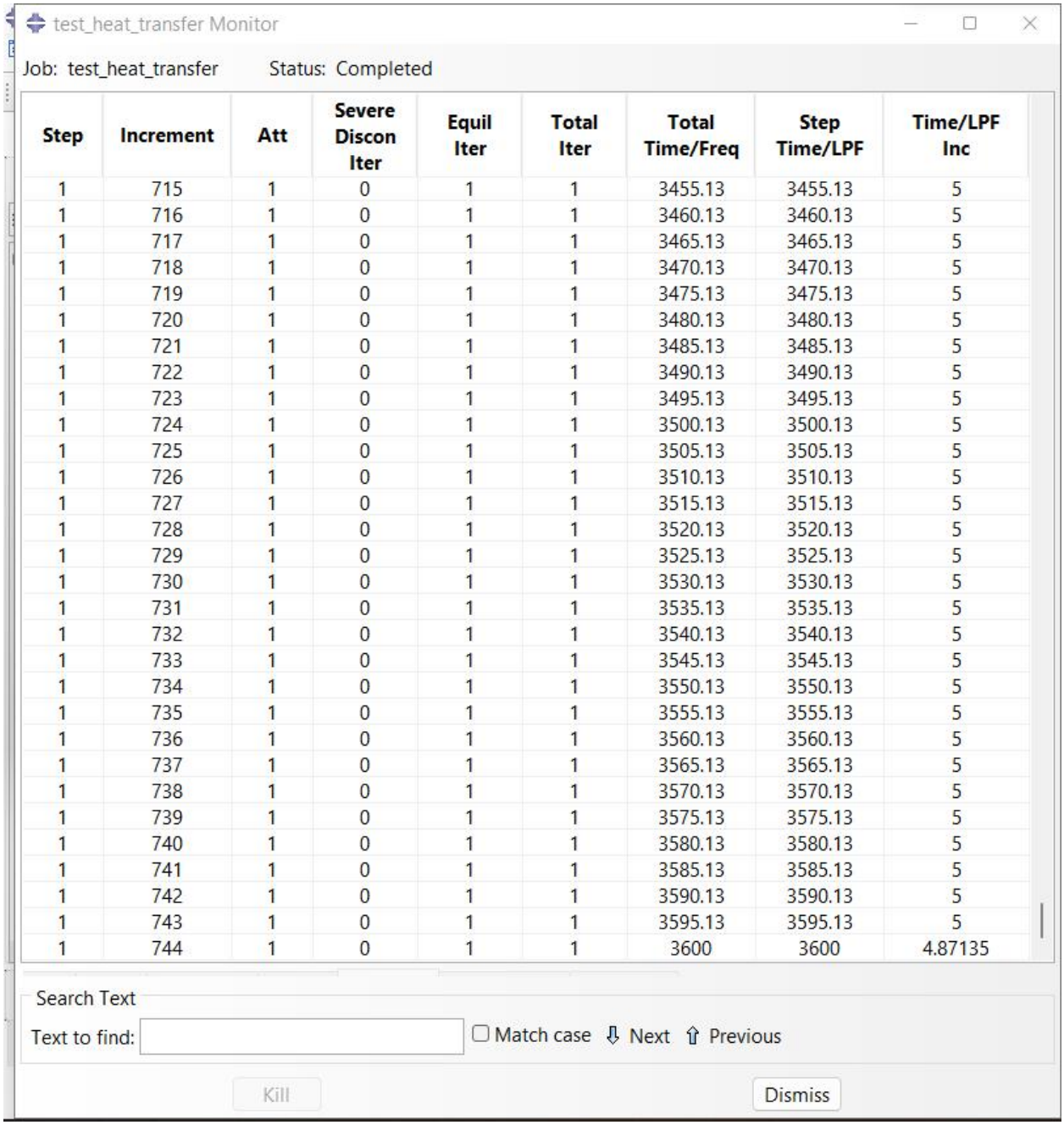

Step	Increment	Att	Severe Discon Iter	Equil Iter	Total Iter	Total Time/Freq	Step Time/LPF	Time/LPF Inc
1	715	1	0	1	1	3455.13	3455.13	5
1	716	1	0	1	1	3460.13	3460.13	5
1	717	1	0	1	1	3465.13	3465.13	5
1	718	1	0	1	1	3470.13	3470.13	5
1	719	1	0	1	1	3475.13	3475.13	5
1	720	1	0	1	1	3480.13	3480.13	5
1	721	1	0	1	1	3485.13	3485.13	5
1	722	1	0	1	1	3490.13	3490.13	5
1	723	1	0	1	1	3495.13	3495.13	5
1	724	1	0	1	1	3500.13	3500.13	5
1	725	1	0	1	1	3505.13	3505.13	5
1	726	1	0	1	1	3510.13	3510.13	5
1	727	1	0	1	1	3515.13	3515.13	5
1	728	1	0	1	1	3520.13	3520.13	5
1	729	1	0	1	1	3525.13	3525.13	5
1	730	1	0	1	1	3530.13	3530.13	5
1	731	1	0	1	1	3535.13	3535.13	5
1	732	1	0	1	1	3540.13	3540.13	5
1	733	1	0	1	1	3545.13	3545.13	5
1	734	1	0	1	1	3550.13	3550.13	5
1	735	1	0	1	1	3555.13	3555.13	5
1	736	1	0	1	1	3560.13	3560.13	5
1	737	1	0	1	1	3565.13	3565.13	5
1	738	1	0	1	1	3570.13	3570.13	5
1	739	1	0	1	1	3575.13	3575.13	5
1	740	1	0	1	1	3580.13	3580.13	5
1	741	1	0	1	1	3585.13	3585.13	5
1	742	1	0	1	1	3590.13	3590.13	5
1	743	1	0	1	1	3595.13	3595.13	5
1	744	1	0	1	1	3600	3600	4.87135

APPENDIX D

CONCRETE I-BEAM ANALYSIS AND DESIGN

In accordance with EN1992-1-1:2004 incorporating Corrigenda January 2008 and the recommended values

Analysis

Geometry (m) - Concrete (C35 2500 Quartzite) - T 200x960x500x200

Span	Length (m)	Section	Start Support	End Support
1	19.2	T 200x960x500x200	Fixed	Roller Pin X
2	19.2	T 200x960x500x200	Roller Pin X	Fixed
T 200x960x500x200: A = 2520 cm^2, I_y = 2154674 cm^4, I_z = 259000 cm^4, A_y = 1000 cm^2, A_z = 1920 cm^2				
Concrete (C35 2500 Quartzite): Density 2500 kg/m^3, Youngs 34.0771462 kN/mm^2, Shear 14.1988109 kN/mm^2, Thermal 0.00001 C^{-1}				

Loading

Self weight included

Permanent - Loading (kN/m)

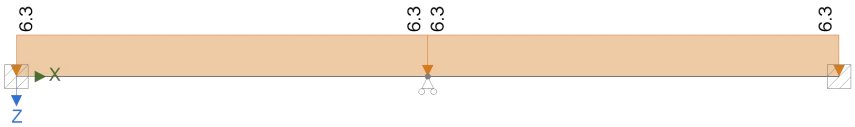

Imposed - Loading (kN/m)

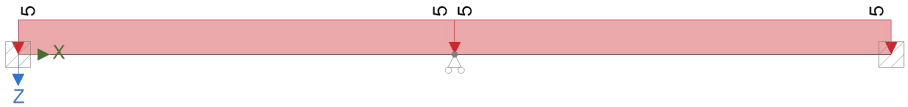

Load combination factors

Load combination	Self Weight	Permanent	Imposed	LoadCase4

Load combination	Self Weight	Permanent	Imposed	LoadCase4
1.35G + 1.5Q + 1.5RQ (Strength)	1.35	1.35	1.50	1.35
1.0G + 1.0Q + 1.0RQ (Service)	1.00	1.00	1.00	1.00
1.0G + 1.0 $_2$Q (Quasi)	1.00	1.00	0.30	1.00

Member Loads

Member	Load case	Load Type	Orientation	Description
Beam	Permanent	UDL	GlobalZ	6.3 kN/m
Beam	Imposed	UDL	GlobalZ	5 kN/m

Results; Forces

Strength combinations - Moment envelope (kNm)

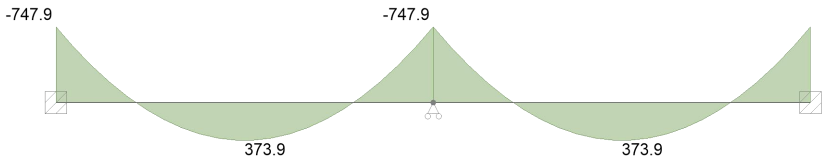

Strength combinations - Shear envelope (kN)

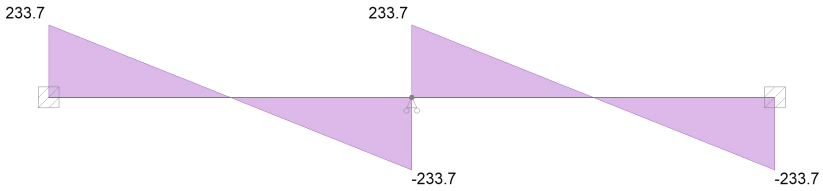

Concrete details -Concrete strength class; C35/45

Aggregate type; Quartzite

Aggregate adjustment factor - cl.3.1.3(2); AAF = 1.0

Characteristic compressive cylinder strength; f_{ck} = 35 N/mm^2

Mean value of compressive cylinder strength; $f_{cm} = f_{ck} + 8$ N/mm^2 = 43 N/mm^2

Mean value of axial tensile strength; $f_{ctm} = 0.3$ N/mm^2 × $(f_{ck}/ 1$ N/mm$^2)^{2/3}$ = 3.2 N/mm^2

Secant modulus of elasticity of concrete; $E_{cm} = 22\ kN/mm^2 \times [f_{cm}/10\ N/mm^2]^{0.3} \times AAF = 34077\ N/mm^2$

Ultimate strain - Table 3.1; $\varepsilon_{cu2} = 0.0035$

Shortening strain - Table 3.1; $\varepsilon_{cu3} = 0.0035$

Effective compression zone height factor; $\lambda = 0.80$

Effective strength factor; $\eta = 1.00$

Coefficient k_1; $k_1 = 0.44$

Coefficient k_2; $k_2 = 1.25 \times (0.6 + 0.0014 / \varepsilon_{cu2}) = 1.25$

Coefficient k_3; $k_3 = 0.54$

Coefficient k_4; $k_4 = 1.25 \times (0.6 + 0.0014 / \varepsilon_{cu2}) = 1.25$

Partial factor for concrete -Table 2.1N; $\gamma_C = 1.50$

Compressive strength coefficient - cl.3.1.6(1); $\alpha_{cc} = 1.00$

Design compressive concrete strength - exp.3.15; $f_{cd} = \alpha_{cc} \times f_{ck} / \gamma_C = 23.3\ N/mm^2$

Compressive strength coefficient - cl.3.1.6(1); $\alpha_{ccw} = 1.00$

Design compressive concrete strength - exp.3.15; $f_{cwd} = \alpha_{ccw} \times f_{ck} / \gamma_C = 23.3\ N/mm^2$

Maximum aggregate size; $h_{agg} = 20\ mm$

Monolithic simple support moment factor; $\beta_1 = 0.15$

Reinforcement details

Characteristic yield strength of reinforcement; $f_{yk} = 460\ N/mm^2$

Partial factor for reinforcing steel - Table 2.1N; $\gamma_S = 1.15$

Design yield strength of reinforcement; $f_{yd} = f_{yk} / \gamma_S = 400\ N/mm^2$

Nominal cover to reinforcement

Nominal cover to top reinforcement; $c_{nom\_t} = 35\ mm$

Nominal cover to bottom reinforcement; $c_{nom\_b} = 35\ mm$

Nominal cover to side reinforcement;c_{nom_s} = 35 mm

Fire resistance

Standard fire resistance period; R = 60 min

Number of sides exposed to fire; 3

Minimum width of beam - EN1992-1-2 Table 5.6; b_{min} = 120 mm

Beam - Span 1

Flanged section details

Section width; b = 200 mm

Section depth; h = 960 mm

Maximum available flange width; b_f = 750 mm

Flange depth; h_f = 150 mm

Allowance for holes; b_{hole} = 0 mm

PASS - Minimum dimensions for fire resistance met

Moment design

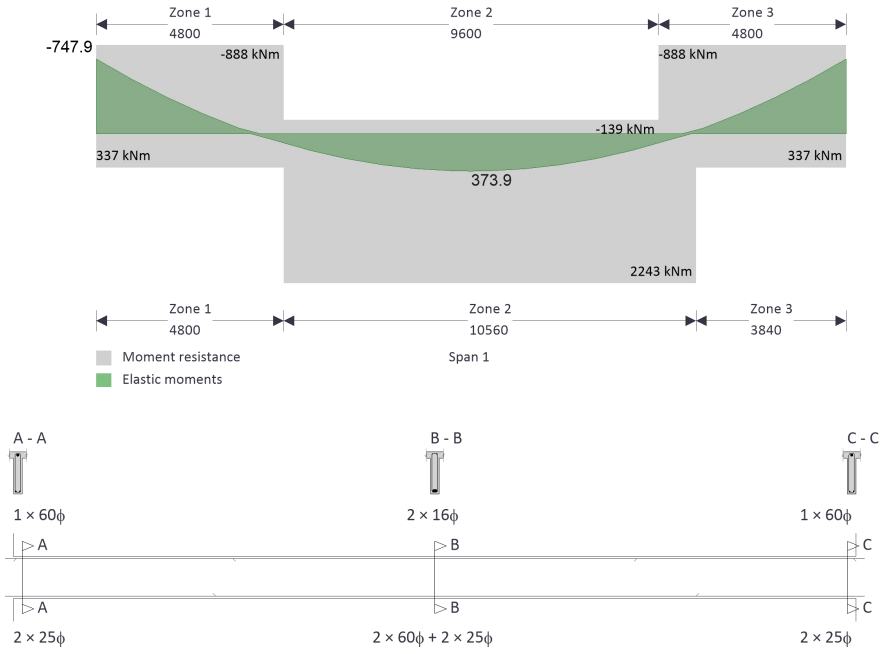

Zone 1 (0 mm - 4800 mm) Positive moment - section 6.1

Design bending moment; $M = abs(M_{m1\_s1\_z1\_max\_red}) = 93.5$ kNm

Distance between points of zero moment; $L_0 = 0.85 \times L_{m1\_s1} = 16320$ mm

Maximum flange outstand; $b_1 = (b_f - b) / 2 = 275$ mm

Effective flange outstand; $b_{eff,1} = \min(0.2 \times b_1 + 0.1 \times L_0, 0.2 \times L_0, b_1) = 275$ mm

Effective flange width; $b_{eff} = 2 \times b_{eff,1} + b = 750$ mm

Effective depth of tension reinforcement; $d = 905$ mm

Redistribution ratio; $\delta = \min(M_{pos\_red\_z1} / M_{pos\_z1}, 1) = 1.000$

$K = M / (b_{eff} \times d^2 \times f_{ck}) = 0.004$

$K' = (2 \times \eta \times \alpha_{cc} / \gamma_C) \times (1 - \lambda \times (\delta - k_1) / (2 \times k_2)) \times (\lambda \times (\delta - k_1) / (2 \times k_2)) = 0.196$

Lever arm; $z = \min(0.5 \times d \times [1 + (1 - 2 \times K / (\eta \times \alpha_{cc} / \gamma_C))^{0.5}], 0.95 \times d) = 859$ mm

Depth of neutral axis; $x = 2 \times (d - z) / \lambda = 113$ mm

$\lambda x <= h_f$ - Compression block wholly within the depth of flange

K' > K - No compression reinforcement is required

Area of tension reinforcement required; $A_{s,req} = \max(M / (f_{yd} \times z), A_{s,min}) = 328$ mm^2

Tension reinforcement provided; $2 \times 25\phi$

Area of tension reinforcement provided; $A_{s,prov} = 982$ mm^2

Minimum area of reinforcement - exp.9.1N; $A_{s,min} = \max(0.26 \times f_{ctm} / f_{yk}, 0.0013) \times b \times d = 328$ mm^2

Maximum area of reinforcement - cl.9.2.1.1(3); $A_{s,max} = 0.04 \times b \times h = 7680$ mm^2

PASS - Area of reinforcement provided is greater than area of reinforcement required

Crack control - Section 7.3

Maximum crack width; $w_k = 0.3$ mm

Design value modulus of elasticity reinf – 3.2.7(4); $E_s = 200000$ N/mm^2

Mean value of concrete tensile strength; $f_{ct,eff} = f_{ctm} = 3.2$ N/mm^2

Stress distribution coefficient; $k_c = 0.4$

Non-uniform self-equilibrating stress coefficient; $k = \min(\max(1 + (300\ mm - \min(h, b)) \times 0.35 / 500\ mm, 0.65), 1) = 1.00$

Actual tension bar spacing; $s_{bar} = (b - (2 \times (c_{nom\_s} + \phi_{m1\_s1\_z1\_v}) + \phi_{m1\_s1\_z1\_b\_L1} \times N_{m1\_s1\_z1\_b\_L1})) / (N_{m1\_s1\_z1\_b\_L1} - 1) + \phi_{m1\_s1\_z1\_b\_L1} = 89\ mm$

Maximum stress permitted - Table 7.3N; $\sigma_s = 329\ N/mm^2$

Steel to concrete modulus of elast. ratio; $\alpha_{cr} = E_s / E_{cm} = 5.87$

Distance of the Elastic NA from bottom of beam; $y = (b \times h^2 / 2 + A_{s,prov} \times (\alpha_{cr} - 1) \times (h - d) + (b_{eff} - b) \times h_f \times (h - h_f/2)) / (b \times h + A_{s,prov} \times (\alpha_{cr} - 1) + (b_{eff} - b) \times h_f) = 592\ mm$

Area of concrete in the tensile zone; $A_{ct} = b \times y = 118474\ mm^2$

Minimum area of reinforcement required - exp.7.1; $A_{sc,min} = k_c \times k \times f_{ct,eff} \times A_{ct} / \sigma_s = 463\ mm^2$

PASS - Area of tension reinforcement provided exceeds minimum required for crack control

Quasi-permanent moment; $M_{QP} = \max(\beta_1 \times \text{abs}(M_{m1\_s1\_z2\_neg\_quasi}), \text{abs}(M_{m1\_s1\_z1\_pos\_quasi})) = 53.7kNm$

Permanent load ratio; $R_{PL} = M_{QP} / M = 0.57$

Service stress in reinforcement; $\sigma_{sr} = f_{yd} \times A_{s,req} / A_{s,prov} \times R_{PL} = 77\ N/mm^2$

Maximum bar spacing - Tables 7.3N; $s_{bar,max} = 300\ mm$

PASS - Maximum bar spacing exceeds actual bar spacing for crack control

Zone 1 (0 mm - 4800 mm) Negative moment - section 6.1

Design bending moment; $M = \max(\beta_1 \times \text{abs}(M_{m1\_s1\_max\_red}), \text{abs}(M_{m1\_s1\_z1\_min\_red})) = 747.9\ kNm$

Effective depth of tension reinforcement; $d = 887\ mm$

Redistribution ratio; $\delta = \min(M_{neg\_red\_z1} / M_{neg\_z1}, 1) = 1.000$

$K = M / (b \times d^2 \times f_{ck}) = 0.136$

$$K' = (2 \times \eta \times \alpha_{cc} / \gamma_C) \times (1 - \lambda \times (\delta - k_1) / (2 \times k_2)) \times (\lambda \times (\delta - k_1) / (2 \times k_2)) = 0.196$$

K' > K - No compression reinforcement is required

Lever arm; $z = \min(0.5 \times d \times [1 + (1 - 2 \times K / (\eta \times \alpha_{cc} / \gamma_C))^{0.5}], 0.95 \times d) = 785$ mm

Depth of neutral axis; $x = 2 \times (d - z) / \lambda = 255$ mm

Area of tension reinforcement required; $A_{s,req} = M / (f_{yd} \times z) = 2382$ mm^2

Tension reinforcement provided; $1 \times 60\phi$

Area of tension reinforcement provided; $A_{s,prov} = 2827$ mm^2

Minimum area of reinforcement - exp.9.1N; $A_{s,min} = \max(0.26 \times f_{ctm} / f_{yk}, 0.0013) \times b \times d = 322$ mm^2

Maximum area of reinforcement - cl.9.2.1.1(3); $A_{s,max} = 0.04 \times b \times h = 7680$ mm^2

PASS - Area of reinforcement provided is greater than area of reinforcement required

Minimum bar spacing (Section 8.2)

Bottom bar spacing; $s_{bot} = (b - (2 \times (c_{nom\_s} + \phi_{m1\_s1\_z1\_v}) + \phi_{m1\_s1\_z1\_b\_L1} \times N_{m1\_s1\_z1\_b\_L1})) / (N_{m1\_s1\_z1\_b\_L1} - 1) = 64.0$ mm

Minimum allowable bottom bar spacing; $s_{bot,min} = \max(\phi_{m1\_s1\_z1\_b\_L1} \times k_{s1}, h_{agg} + k_{s2}, 20\text{mm}) = 25.0$ mm

PASS - Actual bar spacing exceeds minimum allowable

Zone 2 (4800 mm - 15360 mm) Positive moment - section 6.1

Design bending moment; $M = \text{abs}(M_{m1\_s1\_z2\_max\_red}) = 373.9$ kNm

Distance between points of zero moment; $L_0 = 0.85 \times L_{m1\_s1} = 16320$ mm

Maximum flange outstand; $b_1 = (b_f - b) / 2 = 275$ mm

Effective flange outstand; $b_{eff,1} = \min(0.2 \times b_1 + 0.1 \times L_0, 0.2 \times L_0, b_1) = 275$ mm

Effective flange width; $b_{eff} = 2 \times b_{eff,1} + b = 750$ mm

Effective depth of tension reinforcement; $d = 890$ mm

Redistribution ratio; $\delta = \min(M_{pos\_red\_z2} / M_{pos\_z2}, 1) = 1.000$

$K = M / (b_{eff} \times d^2 \times f_{ck}) = 0.018$

$K' = (2 \times \eta \times \alpha_{cc} / \gamma_C) \times (1 - \lambda \times (\delta - k_1) / (2 \times k_2)) \times (\lambda \times (\delta - k_1) / (2 \times k_2)) = 0.196$

Lever arm; $z = \min(0.5 \times d \times [1 + (1 - 2 \times K / (\eta \times \alpha_{cc} / \gamma_C))^{0.5}], 0.95 \times d) = 845$ mm

Depth of neutral axis; $x = 2 \times (d - z) / \lambda = 111$ mm

$\lambda x <= h_f$ - Compression block wholly within the depth of flange

K' > K - No compression reinforcement is required

Area of tension reinforcement required; $A_{s,req} = \max(M / (f_{yd} \times z), A_{s,min}) = 1106$ mm^2

Tension reinforcement provided; $2 \times 60\phi + 2 \times 25\phi$

Area of tension reinforcement provided; $A_{s,prov} = 6637$ mm^2

Minimum area of reinforcement - exp.9.1N; $A_{s,min} = \max(0.26 \times f_{ctm} / f_{yk}, 0.0013) \times b \times d = 323$ mm^2

Maximum area of reinforcement - cl.9.2.1.1(3); $A_{s,max} = 0.04 \times b \times h = 7680$ mm^2

PASS - Area of reinforcement provided is greater than area of reinforcement required

Crack control - Section 7.3

Maximum crack width; $w_k = 0.3$ mm

Design value modulus of elasticity reinf – 3.2.7(4); $E_s = 200000$ N/mm^2

Mean value of concrete tensile strength; $f_{ct,eff} = f_{ctm} = 3.2$ N/mm^2

Stress distribution coefficient; $k_c = 0.4$

Non-uniform self-equilibrating stress coefficient; $k = \min(\max(1 + (300 \text{ mm} - \min(h, b)) \times 0.35 / 500 \text{ mm}, 0.65), 1) = 1.00$

Actual tension bar spacing; $s_{bar} = (b - (2 \times (c_{nom\_s} + \phi_{m1\_s1\_z2\_v}) + \phi_{m1\_s1\_z2\_b\_L1} \times N_{m1\_s1\_z2\_b\_L1} + \phi_{m1\_s1\_z1\_b\_L1} \times N_{m1\_s1\_z1\_b\_L1})) / ((N_{m1\_s1\_z2\_b\_L1} + N_{m1\_s1\_z1\_b\_L1}) - 1) + \phi_{m1\_s1\_z2\_b\_L1} = 41.3$ mm

Maximum stress permitted - Table 7.3N; $\sigma_s = 360$ N/mm^2

Steel to concrete modulus of elast. ratio; $\alpha_{cr} = E_s / E_{cm} = 5.87$

Distance of the Elastic NA from bottom of beam; $y = (b \times h^2 / 2 + A_{s,prov} \times (\alpha_{cr} - 1) \times (h - d) + (b_{eff} - b) \times h_f \times (h - h_f/2)) / (b \times h + A_{s,prov} \times (\alpha_{cr} - 1) + (b_{eff} - b) \times h_f) = 546$ mm

Area of concrete in the tensile zone; $A_{ct} = b \times y = 109153$ mm^2

Minimum area of reinforcement required - exp.7.1; $A_{sc,min} = k_c \times k \times f_{ct,eff} \times A_{ct} / \sigma_s = 389$ mm^2

PASS - Area of tension reinforcement provided exceeds minimum required for crack control

Quasi-permanent moment; $M_{QP} = \text{abs}(M_{m1_s1_z2_pos_quasi}) = 214.7$kNm

Permanent load ratio; $R_{PL} = M_{QP} / M = 0.57$

Service stress in reinforcement; $\sigma_{sr} = f_{yd} \times A_{s,req} / A_{s,prov} \times R_{PL} = 38$ N/mm^2

Maximum bar spacing - Tables 7.3N; $s_{bar,max} = 300$ mm

PASS - Maximum bar spacing exceeds actual bar spacing for crack control

Deflection control - Section 7.4

Reference reinforcement ratio; $\rho_{m0} = (f_{ck} / 1 \text{ N/mm}^2)^{0.5} / 1000 = 0.00592$

Required tension reinforcement ratio; $\rho_m = A_{s,req} / (b_{eff} \times d) = 0.00166$

Required compression reinforcement ratio; $\rho'_m = A_{s2,req} / (b_{eff} \times d) = 0.00000$

Structural system factor - Table 7.4N; $K_b = 1.3$

Basic allowable span to depth ratio ; $\text{span\_to\_depth}_{basic} = K_b \times [11 + 1.5 \times (f_{ck} / 1 \text{ N/mm}^2)^{0.5} \times \rho_{m0} / \rho_m + 3.2 \times (f_{ck} / 1 \text{ N/mm}^2)^{0.5} \times (\rho_{m0} / \rho_m - 1)^{1.5}] = 156.753$

Reinforcement factor - exp.7.17; $K_s = \min(A_{s,prov} / A_{s,req} \times 500 \text{ N/mm}^2 / f_{yk}, 1.5) = 1.500$

Flange width factor; $F1 = \text{if}(b_{eff} / b > 3, 0.8, 1) = 0.800$

Long span supporting brittle partition factor; $F2 = 1 = 1.000$

Allowable span to depth ratio; $\text{span\_to\_depth}_{allow} = \min(\text{span\_to\_depth}_{basic} \times K_s \times F1 \times F2, 40 \times K_b) = 52.000$

Actual span to depth ratio; $\text{span\_to\_depth}_{actual} = L_{m1\_s1} / d = 21.583$

PASS - Actual span to depth ratio is within the allowable limit

Minimum bar spacing (Section 8.2)

Top bar spacing; $s_{top} = (b - (2 \times (c_{nom\_s} + \phi_{m1\_s1\_z2\_v}) + \phi_{m1\_s1\_z2\_t\_L1} \times N_{m1\_s1\_z2\_t\_L1})) / (N_{m1\_s1\_z2\_t\_L1} - 1) = 82.0$ mm

Minimum allowable top bar spacing; $s_{top,min} = \max(\phi_{m1\_s1\_z2\_t\_L1} \times k_{s1}, h_{agg} + k_{s2}, 20mm) = 25.0$ mm

PASS - Actual bar spacing exceeds minimum allowable

Bottom bar spacing; $s_{bot} = (b - (2 \times (c_{nom\_s} + \phi_{m1\_s1\_z2\_v}) + \phi_{m1\_s1\_z2\_b\_L1} \times N_{m1\_s1\_z2\_b\_L1} + \phi_{m1\_s1\_z1\_b\_L1} \times N_{m1\_s1\_z1\_b\_L1})) / ((N_{m1\_s1\_z2\_b\_L1} + N_{m1\_s1\_z1\_b\_L1}) - 1) = -18.7$ mm

Minimum allowable bottom bar spacing; $s_{bot,min} = \max(\phi_{m1\_s1\_z2\_b\_L1} \times k_{s1}, h_{agg} + k_{s2}, 20mm) = 60.0$ mm

Zone 3 (14400 mm - 19200 mm) Negative moment - section 6.1

Design bending moment; $M = \text{abs}(M_{m1\_s1\_z3\_min\_red}) = 747.9$ kNm

Effective depth of tension reinforcement; $d = 887$ mm

Redistribution ratio; $\delta = \min(M_{neg\_red\_z3} / M_{neg\_z3}, 1) = 1.000$

$K = M / (b \times d^2 \times f_{ck}) = 0.136$

$K' = (2 \times \eta \times \alpha_{cc} / \gamma_C) \times (1 - \lambda \times (\delta - k_1) / (2 \times k_2)) \times (\lambda \times (\delta - k_1) / (2 \times k_2)) = 0.196$

K' > K - No compression reinforcement is required

Lever arm; $z = \min(0.5 \times d \times [1 + (1 - 2 \times K / (\eta \times \alpha_{cc} / \gamma_C))^{0.5}], 0.95 \times d) = 785$ mm

Depth of neutral axis; $x = 2 \times (d - z) / \lambda = 255$ mm

Area of tension reinforcement required; $A_{s,req} = M / (f_{yd} \times z) = 2382$ mm^2

Tension reinforcement provided; $1 \times 60\phi$

Area of tension reinforcement provided; $A_{s,prov} = 2827$ mm^2

Minimum area of reinforcement - exp.9.1N; $A_{s,min} = \max(0.26 \times f_{ctm} / f_{yk}, 0.0013) \times b \times d = 322$ mm^2

Maximum area of reinforcement - cl.9.2.1.1(3); $A_{s,max} = 0.04 \times b \times h = 7680$ mm^2

PASS - Area of reinforcement provided is greater than area of reinforcement required

Minimum bar spacing (Section 8.2)

Bottom bar spacing; $s_{bot} = (b - (2 \times (c_{nom\_s} + \phi_{m1\_s1\_z3\_v}) + \phi_{m1\_s1\_z3\_b\_L1} \times N_{m1\_s1\_z3\_b\_L1})) / (N_{m1\_s1\_z3\_b\_L1} - 1) = 64.0$ mm

Minimum allowable bottom bar spacing; $s_{bot,min} = \max(\phi_{m1\_s1\_z3\_b\_L1} \times k_{s1}, h_{agg} + k_{s2}, 20mm) = 25.0$ mm

PASS - Actual bar spacing exceeds minimum allowable

Shear design

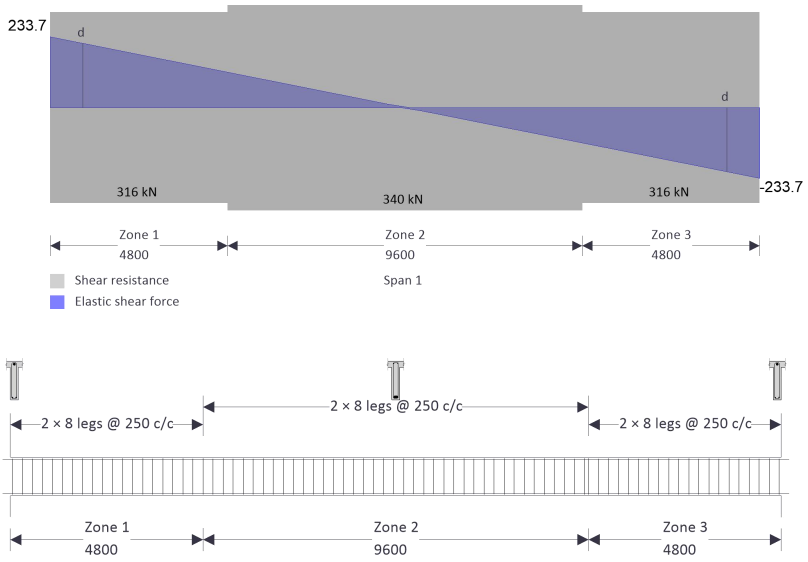

Angle of comp. shear strut for maximum shear; $\theta_{max} = 45$ deg

Strength reduction factor - cl.6.2.3(3); $v_1 = 0.6 \times (1 - f_{ck} / 250\ N/mm^2) = 0.516$

Compression chord coefficient - cl.6.2.3(3); $\alpha_{cw} = 1.00$

Minimum area of shear reinforcement - exp.9.5N; $A_{sv,min} = 0.08\ N/mm^2 \times b \times (f_{ck} / 1\ N/mm^2)^{0.5} / f_{yk} = 206\ mm^2/m$

Zone 1 (0 mm - 4800 mm) shear - section 6.2

Design shear force at support ; $V_{Ed,max} = \max(abs(V_{z1\_max}), abs(V_{z1\_red\_max})) = 234$ kN

Min lever arm in shear zone; $z = 785$ mm

Maximum design shear resistance - exp.6.9; $V_{Rd,max} = \alpha_{cw} \times b \times z \times v_1 \times f_{cwd} / (\cot(\theta_{max}) + \tan(\theta_{max})) = 945$ kN

PASS - Design shear force at support is less than maximum design shear resistance

Design shear force at 887mm from support; $V_{Ed} = 212$ kN

Design shear stress; $v_{Ed} = V_{Ed} / (b \times z) = 1.351$ N/mm^2

Angle of concrete compression strut - cl.6.2.3; $\theta = \min(\max(0.5 \times \text{Asin}(\min(2 \times v_{Ed} / (\alpha_{cw} \times f_{cwd} \times v_1),1)), 21.8 \text{ deg}), 45\text{deg}) = 21.8$ deg

Area of shear reinforcement required - exp.6.8; $A_{sv,des} = v_{Ed} \times b / (f_{yd} \times \cot(\theta)) = 270$ mm^2/m

Area of shear reinforcement required; $A_{sv,req} = \max(A_{sv,min}, A_{sv,des}) = 270$ mm^2/m

Shear reinforcement provided; 2 × 8 legs @ 250 c/c

Area of shear reinforcement provided; $A_{sv,prov} = 402$ mm^2/m

PASS - Area of shear reinforcement provided exceeds minimum required

Maximum longitudinal spacing - exp.9.6N; $s_{vl,max} = 0.75 \times d = 665$ mm

PASS - Longitudinal spacing of shear reinforcement provided is less than maximum

Zone 2 (4800 mm - 14400 mm) shear - section 6.2

Design shear force at support ; $V_{Ed,max} = \max(\text{abs}(V_{z2\_max}), \text{abs}(V_{z2\_red\_max})) = 117$ kN

Min lever arm in shear zone; $z = 845$ mm

Maximum design shear resistance - exp.6.9; $V_{Rd,max} = \alpha_{cw} \times b \times z \times v_1 \times f_{cwd} / (\cot(\theta_{max}) + \tan(\theta_{max})) = 1018$ kN

PASS - Design shear force at support is less than maximum design shear resistance

Design shear force within zone; $V_{Ed} = 117$ kN

Design shear stress; $v_{Ed} = V_{Ed} / (b \times z) = 0.691$ N/mm^2

Angle of concrete compression strut - cl.6.2.3; $\theta = \min(\max(0.5 \times \text{Asin}(\min(2 \times v_{Ed} / (\alpha_{cw} \times f_{cwd} \times v_1),1)), 21.8 \text{ deg}), 45\text{deg}) = 21.8$ deg

Area of shear reinforcement required - exp.6.8; $A_{sv,des} = v_{Ed} \times b / (f_{yd} \times \cot(\theta)) = 138$ mm^2/m

Area of shear reinforcement required; $A_{sv,req} = \max(A_{sv,min}, A_{sv,des}) = 206$ mm^2/m

Shear reinforcement provided; 2 × 8 legs @ 250 c/c

Area of shear reinforcement provided; $A_{sv,prov} = 402$ mm^2/m

PASS - Area of shear reinforcement provided exceeds minimum required

Maximum longitudinal spacing - exp.9.6N; $s_{vl,max} = 0.75 \times d = 667$ mm

PASS - Longitudinal spacing of shear reinforcement provided is less than maximum

Zone 3 (14400 mm - 19200 mm) shear - section 6.2

Design shear force at support ; $V_{Ed,max} = \max(\text{abs}(V_{z3\_max}), \text{abs}(V_{z3\_red\_max})) = 234$ kN

Min lever arm in shear zone; z = 785 mm

Maximum design shear resistance - exp.6.9; $V_{Rd,max} = \alpha_{cw} \times b \times z \times v_1 \times f_{cwd} / (\cot(\theta_{max}) + \tan(\theta_{max})) = 945$ kN

PASS - Design shear force at support is less than maximum design shear resistance

Design shear force at 887mm from support; $V_{Ed} = 212$ kN

Design shear stress; $v_{Ed} = V_{Ed} / (b \times z) = 1.351$ N/mm^2

Angle of concrete compression strut - cl.6.2.3; $\theta = \min(\max(0.5 \times \text{Asin}(\min(2 \times v_{Ed} / (\alpha_{cw} \times f_{cwd} \times v_1),1)), 21.8 \text{ deg}), 45\text{deg}) = 21.8$ deg

Area of shear reinforcement required - exp.6.8; $A_{sv,des} = v_{Ed} \times b / (f_{yd} \times \cot(\theta)) = 270$ mm^2/m

Area of shear reinforcement required; $A_{sv,req} = \max(A_{sv,min}, A_{sv,des}) = 270$ mm^2/m

Shear reinforcement provided; 2 × 8 legs @ 250 c/c

Area of shear reinforcement provided; $A_{sv,prov} = 402$ mm^2/m

PASS - Area of shear reinforcement provided exceeds minimum required

Maximum longitudinal spacing - exp.9.6N; $s_{vl,max} = 0.75 \times d = 665$ mm

PASS - Longitudinal spacing of shear reinforcement provided is less than maximum

Beam - Span 2

Flanged section details

Section width; b = 200 mm

Section depth; h = 960 mm

Maximum available flange width; b_f = 750 mm

Flange depth; h_f = 150 mm

Allowance for holes; b_{hole} = 0 mm

PASS - Minimum dimensions for fire resistance met

Moment design

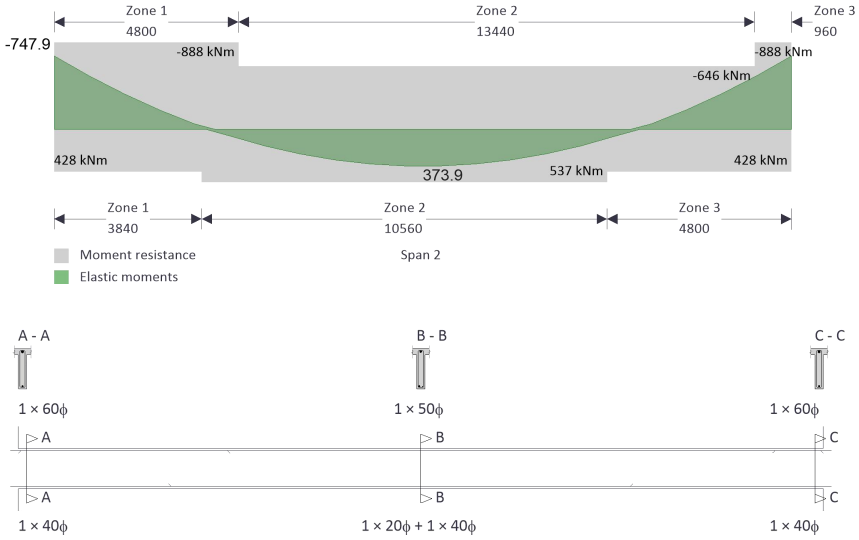

Zone 1 (0 mm - 4800 mm) Negative moment - section 6.1

Design bending moment; $M = abs(M_{m1\_s2\_z1\_min\_red})$ = 747.9 kNm

Effective depth of tension reinforcement; d = 887 mm

Redistribution ratio; $\delta = min(M_{neg\_red\_z1} / M_{neg\_z1}, 1)$ = 1.000

$K = M / (b \times d^2 \times f_{ck})$ = 0.136

$K' = (2 \times \eta \times \alpha_{cc} / \gamma_C) \times (1 - \lambda \times (\delta - k_1) / (2 \times k_2)) \times (\lambda \times (\delta - k_1) / (2 \times k_2))$ = 0.196

K' > K - No compression reinforcement is required

Lever arm; $z = \min(0.5 \times d \times [1 + (1 - 2 \times K / (\eta \times \alpha_{cc} / \gamma_C))^{0.5}], 0.95 \times d) = 785$ mm

Depth of neutral axis; $x = 2 \times (d - z) / \lambda = 255$ mm

Area of tension reinforcement required; $A_{s,req} = M / (f_{yd} \times z) = 2382$ mm^2

Tension reinforcement provided; $1 \times 60\phi$

Area of tension reinforcement provided; $A_{s,prov} = 2827$ mm^2

Minimum area of reinforcement - exp.9.1N; $A_{s,min} = \max(0.26 \times f_{ctm} / f_{yk}, 0.0013) \times b \times d = 322$ mm^2

Maximum area of reinforcement - cl.9.2.1.1(3); $A_{s,max} = 0.04 \times b \times h = 7680$ mm^2

PASS - Area of reinforcement provided is greater than area of reinforcement required

Zone 2 (3840 mm - 14400 mm) Positive moment - section 6.1

Design bending moment; $M = \text{abs}(M_{m1\_s2\_z2\_max\_red}) = 373.9$ kNm

Distance between points of zero moment; $L_0 = 0.85 \times L_{m1\_s2} = 16320$ mm

Maximum flange outstand; $b_1 = (b_f - b) / 2 = 275$ mm

Effective flange outstand; $b_{eff,1} = \min(0.2 \times b_1 + 0.1 \times L_0, 0.2 \times L_0, b_1) = 275$ mm

Effective flange width; $b_{eff} = 2 \times b_{eff,1} + b = 750$ mm

Effective depth of tension reinforcement; $d = 899$ mm

Redistribution ratio; $\delta = \min(M_{pos\_red\_z2} / M_{pos\_z2}, 1) = 1.000$

$K = M / (b_{eff} \times d^2 \times f_{ck}) = 0.018$

$K' = (2 \times \eta \times \alpha_{cc} / \gamma_C) \times (1 - \lambda \times (\delta - k_1) / (2 \times k_2)) \times (\lambda \times (\delta - k_1) / (2 \times k_2)) = 0.196$

Lever arm; $z = \min(0.5 \times d \times [1 + (1 - 2 \times K / (\eta \times \alpha_{cc} / \gamma_C))^{0.5}], 0.95 \times d) = 854$ mm

Depth of neutral axis; $x = 2 \times (d - z) / \lambda = 112$ mm

$\lambda x <= h_f$ - Compression block wholly within the depth of flange

K' > K - No compression reinforcement is required

Area of tension reinforcement required; $A_{s,req} = \max(M / (f_{yd} \times z), A_{s,min}) = 1095$ mm^2

Tension reinforcement provided; $1 \times 20\phi + 1 \times 40\phi$

Area of tension reinforcement provided; $A_{s,prov} = 1571\ mm^2$

Minimum area of reinforcement - exp.9.1N; $A_{s,min} = \max(0.26 \times f_{ctm} / f_{yk}, 0.0013) \times b \times d = 326\ mm^2$

Maximum area of reinforcement - cl.9.2.1.1(3); $A_{s,max} = 0.04 \times b \times h = 7680\ mm^2$

PASS - Area of reinforcement provided is greater than area of reinforcement required

Crack control - Section 7.3

Maximum crack width; $w_k = 0.3\ mm$

Design value modulus of elasticity reinf – 3.2.7(4); $E_s = 200000\ N/mm^2$

Mean value of concrete tensile strength; $f_{ct,eff} = f_{ctm} = 3.2\ N/mm^2$

Stress distribution coefficient; $k_c = 0.4$

Non-uniform self-equilibrating stress coefficient; $k = \min(\max(1 + (300\ mm - \min(h, b)) \times 0.35 / 500\ mm, 0.65), 1) = 1.00$

Actual tension bar spacing; $s_{bar} = (b - (2 \times (c_{nom\_s} + \phi_{m1\_s2\_z2\_v}) + \phi_{m1\_s2\_z2\_b\_L1} \times N_{m1\_s2\_z2\_b\_L1} + \phi_{m1\_s2\_z1\_b\_L1} \times N_{m1\_s2\_z1\_b\_L1})) / ((N_{m1\_s2\_z2\_b\_L1} + N_{m1\_s2\_z1\_b\_L1}) - 1) + \phi_{m1\_s2\_z1\_b\_L1} = 94\ mm$

Maximum stress permitted - Table 7.3N; $\sigma_s = 325\ N/mm^2$

Steel to concrete modulus of elast. ratio; $\alpha_{cr} = E_s / E_{cm} = 5.87$

Distance of the Elastic NA from bottom of beam; $y = (b \times h^2 / 2 + A_{s,prov} \times (\alpha_{cr} - 1) \times (h - d) + (b_{eff} - b) \times h_f \times (h - h_f/2)) / (b \times h + A_{s,prov} \times (\alpha_{cr} - 1) + (b_{eff} - b) \times h_f) = 587\ mm$

Area of concrete in the tensile zone; $A_{ct} = b \times y = 117413\ mm^2$

Minimum area of reinforcement required - exp.7.1; $A_{sc,min} = k_c \times k \times f_{ct,eff} \times A_{ct} / \sigma_s = 464\ mm^2$

PASS - Area of tension reinforcement provided exceeds minimum required for crack control

Quasi-permanent moment; $M_{QP} = \text{abs}(M_{m1\_s2\_z2\_pos\_quasi}) = 214.7kNm$

Permanent load ratio; $R_{PL} = M_{QP} / M = 0.57$

Service stress in reinforcement; $\sigma_{sr} = f_{yd} \times A_{s,req} / A_{s,prov} \times R_{PL} = 160\ N/mm^2$

Maximum bar spacing - Tables 7.3N; $s_{bar,max} = 299.9$ mm

PASS - Maximum bar spacing exceeds actual bar spacing for crack control

Deflection control - Section 7.4

Reference reinforcement ratio; $\rho_{m0} = (f_{ck} / 1\ N/mm^2)^{0.5} / 1000 = 0.00592$

Required tension reinforcement ratio; $\rho_m = A_{s,req} / (b_{eff} \times d) = 0.00162$

Required compression reinforcement ratio; $\rho'_m = A_{s2,req} / (b_{eff} \times d) = 0.00000$

Structural system factor - Table 7.4N; $K_b = 1.3$

Basic allowable span to depth ratio ; $span\_to\_depth_{basic} = K_b \times [11 + 1.5 \times (f_{ck} / 1\ N/mm^2)^{0.5} \times \rho_{m0} / \rho_m + 3.2 \times (f_{ck} / 1\ N/mm^2)^{0.5} \times (\rho_{m0} / \rho_m - 1)^{1.5}] = 162.152$

Reinforcement factor - exp.7.17; $K_s = \min(A_{s,prov} / A_{s,req} \times 500\ N/mm^2 / f_{yk}, 1.5) = 1.500$

Flange width factor; $F1 = if(b_{eff} / b > 3, 0.8, 1) = 0.800$

Long span supporting brittle partition factor; $F2 = 1 = 1.000$

Allowable span to depth ratio; $span\_to\_depth_{allow} = \min(span\_to\_depth_{basic} \times K_s \times F1 \times F2, 40 \times K_b) = 52.000$

Actual span to depth ratio; $span\_to\_depth_{actual} = L_{m1\_s2} / d = 21.357$

PASS - Actual span to depth ratio is within the allowable limit

Zone 2 (4800 mm - 18240 mm) Negative moment - section 6.1

Design bending moment; $M = abs(M_{m1\_s2\_z2\_min\_red}) = 534.7$ kNm

Effective depth of tension reinforcement; $d = 892$ mm

Redistribution ratio; $\delta = \min(M_{neg\_red\_z2} / M_{neg\_z2}, 1) = 1.000$

$K = M / (b \times d^2 \times f_{ck}) = 0.096$

$K' = (2 \times \eta \times \alpha_{cc} / \gamma_C) \times (1 - \lambda \times (\delta - k_1) / (2 \times k_2)) \times (\lambda \times (\delta - k_1) / (2 \times k_2)) = 0.196$

K' > K - No compression reinforcement is required

Lever arm; $z = \min(0.5 \times d \times [1 + (1 - 2 \times K / (\eta \times \alpha_{cc} / \gamma_C))^{0.5}], 0.95 \times d) = 822$ mm

Depth of neutral axis; $x = 2 \times (d - z) / \lambda = 174$ mm

Area of tension reinforcement required; $A_{s,req} = M / (f_{yd} \times z) = 1626$ mm^2

Tension reinforcement provided; $1 \times 50\phi$

Area of tension reinforcement provided; $A_{s,prov} = 1963$ mm^2

Minimum area of reinforcement - exp.9.1N; $A_{s,min} = \max(0.26 \times f_{ctm} / f_{yk}, 0.0013) \times b \times d = 324$ mm^2

Maximum area of reinforcement - cl.9.2.1.1(3); $A_{s,max} = 0.04 \times b \times h = 7680$ mm^2

PASS - Area of reinforcement provided is greater than area of reinforcement required

Deflection control - Section 7.4

Reference reinforcement ratio; $\rho_{m0} = (f_{ck} / 1\ \text{N/mm}^2)^{0.5} / 1000 = 0.00592$

Required tension reinforcement ratio; $\rho_m = A_{s,req} / (b \times d) = 0.00911$

Required compression reinforcement ratio; $\rho'_m = A_{s2,req} / (b \times d) = 0.00000$

Structural system factor - Table 7.4N; $K_b = 1.3$

Basic allowable span to depth ratio ; $\text{span\_to\_depth}_{basic} = K_b \times [11 + 1.5 \times (f_{ck} / 1\ \text{N/mm}^2)^{0.5} \times \rho_{m0} / (\rho_m - \rho'_m) + (f_{ck} / 1\ \text{N/mm}^2)^{0.5} \times (\rho'_m / \rho_{m0})^{0.5} / 12] = 21.790$

Reinforcement factor - exp.7.17; $K_s = \min(A_{s,prov} / A_{s,req} \times 500\ \text{N/mm}^2 / f_{yk}, 1.5) = 1.313$

Flange width factor; $F1 = 1 = 1.000$

Long span supporting brittle partition factor; $F2 = 1 = 1.000$

Allowable span to depth ratio; $\text{span\_to\_depth}_{allow} = \min(\text{span\_to\_depth}_{basic} \times K_s \times F1 \times F2, 40 \times K_b) = 28.605$

Actual span to depth ratio; $\text{span\_to\_depth}_{actual} = L_{m1\_s2} / d = 21.525$

PASS - Actual span to depth ratio is within the allowable limit

Minimum bar spacing (Section 8.2)

Bottom bar spacing; $s_{bot} = (b - (2 \times (c_{nom\_s} + \phi_{m1\_s2\_z2\_v}) + \phi_{m1\_s2\_z2\_b\_L1} \times N_{m1\_s2\_z2\_b\_L1} + \phi_{m1\_s2\_z1\_b\_L1} \times N_{m1\_s2\_z1\_b\_L1})) / ((N_{m1\_s2\_z2\_b\_L1} + N_{m1\_s2\_z1\_b\_L1}) - 1) = 54.0$ mm

Minimum allowable bottom bar spacing; $s_{bot,min} = \max(\phi_{m1\_s2\_z1\_b\_L1} \times k_{s1}, h_{agg} + k_{s2}, 20mm) = 40.0$ mm

PASS - Actual bar spacing exceeds minimum allowable

Zone 3 (14400 mm - 19200 mm) Positive moment - section 6.1

Design bending moment; $M = \text{abs}(M_{m1\_s2\_z3\_max\_red}) = 93.5$ kNm

Distance between points of zero moment; $L_0 = 0.85 \times L_{m1\_s2} = 16320$ mm

Maximum flange outstand; $b_1 = (b_f - b) / 2 = 275$ mm

Effective flange outstand; $b_{eff,1} = \min(0.2 \times b_1 + 0.1 \times L_0, 0.2 \times L_0, b_1) = 275$ mm

Effective flange width; $b_{eff} = 2 \times b_{eff,1} + b = 750$ mm

Effective depth of tension reinforcement; $d = 897$ mm

Redistribution ratio; $\delta = \min(M_{pos\_red\_z3} / M_{pos\_z3}, 1) = 1.000$

$K = M / (b_{eff} \times d^2 \times f_{ck}) = 0.004$

$K' = (2 \times \eta \times \alpha_{cc} / \gamma_C) \times (1 - \lambda \times (\delta - k_1) / (2 \times k_2)) \times (\lambda \times (\delta - k_1) / (2 \times k_2)) = 0.196$

Lever arm; $z = \min(0.5 \times d \times [1 + (1 - 2 \times K / (\eta \times \alpha_{cc} / \gamma_C))^{0.5}], 0.95 \times d) = 852$ mm

Depth of neutral axis; $x = 2 \times (d - z) / \lambda = 112$ mm

$\lambda x <= h_f$ - Compression block wholly within the depth of flange

$K' > K$ - No compression reinforcement is required

Area of tension reinforcement required; $A_{s,req} = \max(M / (f_{yd} \times z), A_{s,min}) = 325$ mm^2

Tension reinforcement provided; $1 \times 40\phi$

Area of tension reinforcement provided; $A_{s,prov} = 1257$ mm^2

Minimum area of reinforcement - exp.9.1N; $A_{s,min} = \max(0.26 \times f_{ctm} / f_{yk}, 0.0013) \times b \times d = 325$ mm^2

Maximum area of reinforcement - cl.9.2.1.1(3); $A_{s,max} = 0.04 \times b \times h = 7680\ mm^2$

PASS - Area of reinforcement provided is greater than area of reinforcement required

Crack control - Section 7.3

Maximum crack width; $w_k = 0.3\ mm$

Design value modulus of elasticity reinf – 3.2.7(4); $E_s = 200000\ N/mm^2$

Mean value of concrete tensile strength; $f_{ct,eff} = f_{ctm} = 3.2\ N/mm^2$

Stress distribution coefficient; $k_c = 0.4$

Non-uniform self-equilibrating stress coefficient; $k = \min(\max(1 + (300\ mm - \min(h, b)) \times 0.35 / 500\ mm, 0.65), 1) = 1.00$

Actual tension bar spacing; $s_{bar} = b + \phi_{m1\_s2\_z3\_b\_L1} = 240\ mm$

Maximum stress permitted - Table 7.3N; $\sigma_s = 208\ N/mm^2$

Steel to concrete modulus of elast. ratio; $\alpha_{cr} = E_s / E_{cm} = 5.87$

Distance of the Elastic NA from bottom of beam; $y = (b \times h^2 / 2 + A_{s,prov} \times (\alpha_{cr} - 1) \times (h - d) + (b_{eff} - b) \times h_f \times (h - h_f/2)) / (b \times h + A_{s,prov} \times (\alpha_{cr} - 1) + (b_{eff} - b) \times h_f) = 590\ mm$

Area of concrete in the tensile zone; $A_{ct} = b \times y = 117995\ mm^2$

Minimum area of reinforcement required - exp.7.1; $A_{sc,min} = k_c \times k \times f_{ct,eff} \times A_{ct} / \sigma_s = 728\ mm^2$

PASS - Area of tension reinforcement provided exceeds minimum required for crack control

Quasi-permanent moment; $M_{QP} = \max(\beta_1 \times \text{abs}(M_{m1\_s2\_z2\_neg\_quasi}), \text{abs}(M_{m1\_s2\_z3\_pos\_quasi})) = 53.7kNm$

Permanent load ratio; $R_{PL} = M_{QP} / M = 0.57$

Service stress in reinforcement; $\sigma_{sr} = f_{yd} \times A_{s,req} / A_{s,prov} \times R_{PL} = 59\ N/mm^2$

Maximum bar spacing - Tables 7.3N; $s_{bar,max} = 300\ mm$

PASS - Maximum bar spacing exceeds actual bar spacing for crack control

Zone 3 (18240 mm - 19200 mm) Negative moment - section 6.1

Design bending moment; $M = \max(\beta_1 \times \text{abs}(M_{m1\_s2\_max\_red}), \text{abs}(M_{m1\_s2\_z3\_min\_red})) = 747.9$ kNm

Effective depth of tension reinforcement; $d = 887$ mm

Redistribution ratio; $\delta = \min(M_{neg\_red\_z3} / M_{neg\_z3}, 1) = 1.000$

$K = M / (b \times d^2 \times f_{ck}) = 0.136$

$K' = (2 \times \eta \times \alpha_{cc} / \gamma_C) \times (1 - \lambda \times (\delta - k_1) / (2 \times k_2)) \times (\lambda \times (\delta - k_1) / (2 \times k_2)) = 0.196$

K' > K - No compression reinforcement is required

Lever arm; $z = \min(0.5 \times d \times [1 + (1 - 2 \times K / (\eta \times \alpha_{cc} / \gamma_C))^{0.5}], 0.95 \times d) = 785$ mm

Depth of neutral axis; $x = 2 \times (d - z) / \lambda = 255$ mm

Area of tension reinforcement required; $A_{s,req} = M / (f_{yd} \times z) = 2382$ mm^2

Tension reinforcement provided; $1 \times 60\phi$

Area of tension reinforcement provided; $A_{s,prov} = 2827$ mm^2

Minimum area of reinforcement - exp.9.1N; $A_{s,min} = \max(0.26 \times f_{ctm} / f_{yk}, 0.0013) \times b \times d = 322$ mm^2

Maximum area of reinforcement - cl.9.2.1.1(3); $A_{s,max} = 0.04 \times b \times h = 7680$ mm^2

PASS - Area of reinforcement provided is greater than area of reinforcement required

Shear design

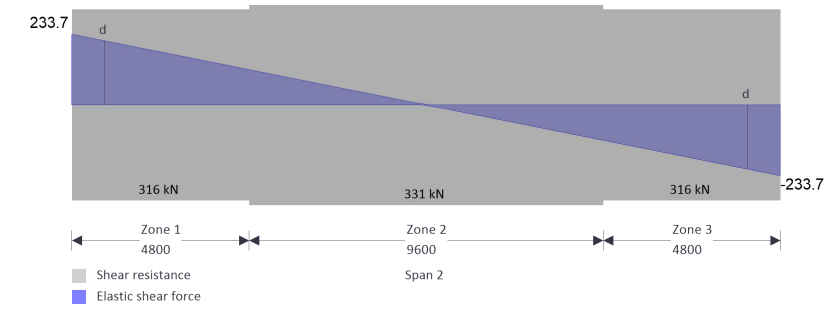

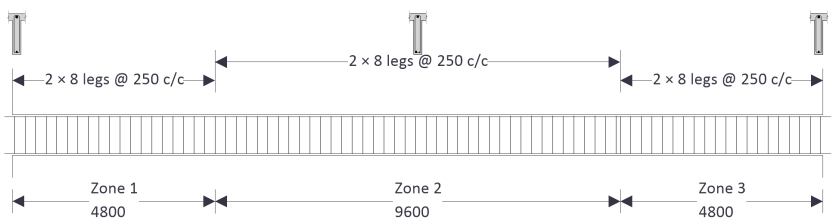

Angle of comp. shear strut for maximum shear; $\theta_{max} = 45$ deg

Strength reduction factor - cl.6.2.3(3); $v_1 = 0.6 \times (1 - f_{ck} / 250\ N/mm^2) = 0.516$

Compression chord coefficient - cl.6.2.3(3); $\alpha_{cw} = 1.00$

Minimum area of shear reinforcement - exp.9.5N; $A_{sv,min} = 0.08\ N/mm^2 \times b \times (f_{ck} / 1\ N/mm^2)^{0.5} / f_{yk} = 206\ mm^2/m$

Zone 1 (0 mm - 4800 mm) shear - section 6.2

Design shear force at support ; $V_{Ed,max} = \max(abs(V_{z1\_max}), abs(V_{z1\_red\_max})) = 234$ kN

Min lever arm in shear zone; $z = 785$ mm

Maximum design shear resistance - exp.6.9; $V_{Rd,max} = \alpha_{cw} \times b \times z \times v_1 \times f_{cwd} / (\cot(\theta_{max}) + \tan(\theta_{max})) = 945$ kN

PASS - Design shear force at support is less than maximum design shear resistance

Design shear force at 887mm from support; $V_{Ed} = 212$ kN

Design shear stress; $v_{Ed} = V_{Ed} / (b \times z) = 1.351\ N/mm^2$

Angle of concrete compression strut - cl.6.2.3; $\theta = \min(\max(0.5 \times \text{Asin}(\min(2 \times v_{Ed} / (\alpha_{cw} \times f_{cwd} \times v_1),1)), 21.8\ deg), 45deg) = 21.8$ deg

Area of shear reinforcement required - exp.6.8; $A_{sv,des} = v_{Ed} \times b / (f_{yd} \times \cot(\theta)) = 270\ mm^2/m$

Area of shear reinforcement required; $A_{sv,req} = \max(A_{sv,min}, A_{sv,des}) = 270\ mm^2/m$

Shear reinforcement provided; 2 × 8 legs @ 250 c/c

Area of shear reinforcement provided; $A_{sv,prov} = 402\ mm^2/m$

PASS - Area of shear reinforcement provided exceeds minimum required

Maximum longitudinal spacing - exp.9.6N; $s_{vl,max} = 0.75 \times d = 665$ mm

PASS - Longitudinal spacing of shear reinforcement provided is less than maximum

Zone 2 (4800 mm - 14400 mm) shear - section 6.2

Design shear force at support ; $V_{Ed,max} = \max(abs(V_{z2\_max}), abs(V_{z2\_red\_max})) = 117$ kN

Min lever arm in shear zone; z = 822 mm

Maximum design shear resistance - exp.6.9; $V_{Rd,max} = \alpha_{cw} \times b \times z \times v_1 \times f_{cwd} / (\cot(\theta_{max}) + \tan(\theta_{max})) = 990$ kN

PASS - Design shear force at support is less than maximum design shear resistance

Design shear force within zone; $V_{Ed} = 117$ kN

Design shear stress; $v_{Ed} = V_{Ed} / (b \times z) = 0.711$ N/mm^2

Angle of concrete compression strut - cl.6.2.3; $\theta = \min(\max(0.5 \times \text{Asin}(\min(2 \times v_{Ed} / (\alpha_{cw} \times f_{cwd} \times v_1),1)), 21.8 \text{ deg}), 45\text{deg}) = 21.8$ deg

Area of shear reinforcement required - exp.6.8; $A_{sv,des} = v_{Ed} \times b / (f_{yd} \times \cot(\theta)) = 142$ mm^2/m

Area of shear reinforcement required; $A_{sv,req} = \max(A_{sv,min}, A_{sv,des}) = 206$ mm^2/m

Shear reinforcement provided; 2 × 8 legs @ 250 c/c

Area of shear reinforcement provided; $A_{sv,prov} = 402$ mm^2/m

PASS - Area of shear reinforcement provided exceeds minimum required

Maximum longitudinal spacing - exp.9.6N; $s_{vl,max} = 0.75 \times d = 669$ mm

PASS - Longitudinal spacing of shear reinforcement provided is less than maximum

Zone 3 (14400 mm - 19200 mm) shear - section 6.2

Design shear force at support ; $V_{Ed,max} = \max(\text{abs}(V_{z3\_max}), \text{abs}(V_{z3\_red\_max})) = 234$ kN

Min lever arm in shear zone; z = 785 mm

Maximum design shear resistance - exp.6.9; $V_{Rd,max} = \alpha_{cw} \times b \times z \times v_1 \times f_{cwd} / (\cot(\theta_{max}) + \tan(\theta_{max})) = 945$ kN

PASS - Design shear force at support is less than maximum design shear resistance

Design shear force at 887mm from support; $V_{Ed} = 212$ kN

Design shear stress; $v_{Ed} = V_{Ed} / (b \times z) = 1.351$ N/mm^2

Angle of concrete compression strut - cl.6.2.3; $\theta = \min(\max(0.5 \times \text{Asin}(\min(2 \times v_{Ed} / (\alpha_{cw} \times f_{cwd} \times v_1),1)), 21.8 \text{ deg}), 45\text{deg}) = 21.8$ deg

Area of shear reinforcement required - exp.6.8; $A_{sv,des} = v_{Ed} \times b / (f_{yd} \times \cot(\theta)) = 270$ mm^2/m

Area of shear reinforcement required; $A_{sv,req} = \max(A_{sv,min}, A_{sv,des}) = 270$ mm^2/m

Shear reinforcement provided; 2 × 8 legs @ 250 c/c

Area of shear reinforcement provided; $A_{sv,prov} = 402$ mm^2/m

PASS - Area of shear reinforcement provided exceeds minimum required

Maximum longitudinal spacing - exp.9.6N; $s_{vl,max} = 0.75 \times d = 665$ mm

PASS - Longitudinal spacing of shear reinforcement provided is less than maximum

APPENDIX E

CONCRETE I-BEAM INCREMENT RESULTS FROM ABAQUS

The following images are the increment results from Abaqus for the Concrete I-Beam analysis.

heat_transfer Monitor

Job: heat_transfer Status: Completed

Step	Increment	Att	Severe Discon Iter	Equil Iter	Total Iter	Total Time/Freq	Step Time/LPF	Time/LPF Inc
1	1	1	0	2	2	1	1	1
1	2	1	0	1	1	2	2	1
1	3	1	0	1	1	3	3	1
1	4	1	0	2	2	5	5	2
1	5	1	0	2	2	7.58627	7.58627	2.58627
1	6	1	0	1	1	10.1725	10.1725	2.58627
1	7	1	0	1	1	12.7588	12.7588	2.58627
1	8	1	0	1	1	15.3451	15.3451	2.58627
1	9	1	0	1	1	17.9313	17.9313	2.58627
1	10	1	0	1	1	20.5176	20.5176	2.58627
1	11	1	0	1	1	23.1039	23.1039	2.58627
1	12	1	0	1	1	25.6901	25.6901	2.58627
1	13	1	0	1	1	28.2764	28.2764	2.58627
1	14	1	0	1	1	30.8627	30.8627	2.58627
1	15	1	0	1	1	33.4489	33.4489	2.58627
1	16	1	0	1	1	36.0352	36.0352	2.58627
1	17	1	0	1	1	38.6215	38.6215	2.58627
1	18	1	0	1	1	41.2077	41.2077	2.58627
1	19	1	0	1	1	43.794	43.794	2.58627
1	20	1	0	1	1	46.3803	46.3803	2.58627
1	21	1	0	1	1	48.9665	48.9665	2.58627
1	22	1	0	1	1	51.5528	51.5528	2.58627
1	23	1	0	1	1	54.1391	54.1391	2.58627
1	24	1	0	1	1	56.7253	56.7253	2.58627
1	25	1	0	1	1	59.3116	59.3116	2.58627
1	26	1	0	1	1	61.8979	61.8979	2.58627
1	27	1	0	1	1	64.4841	64.4841	2.58627
1	28	1	0	1	1	67.0704	67.0704	2.58627
1	29	1	0	1	1	69.6567	69.6567	2.58627
1	30	1	0	1	1	72.2429	72.2429	2.58627

Search Text

Text to find: Match case Next Previous

Kill Dismiss

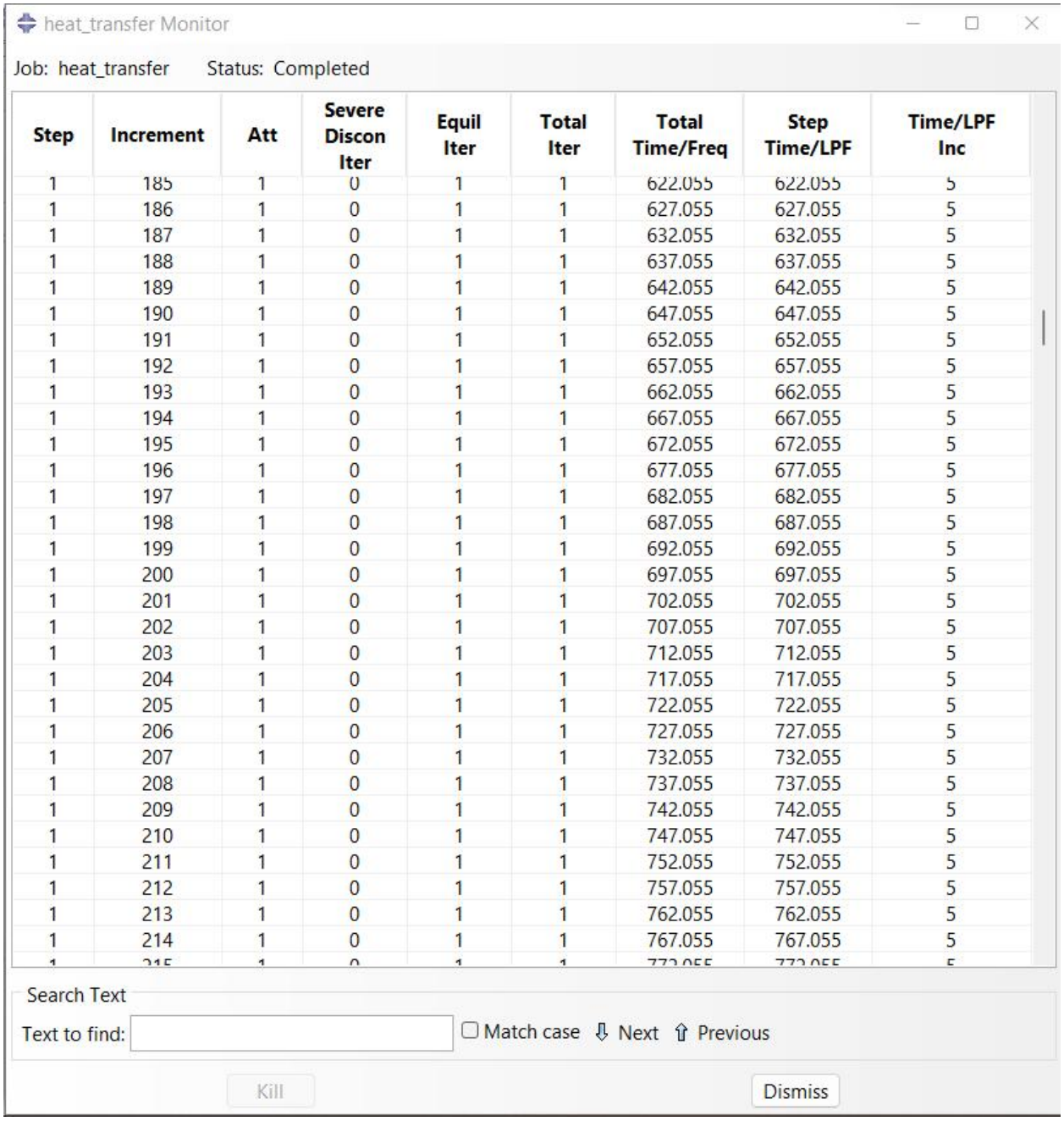
heat_transfer Monitor
Job: heat_transfer Status: Completed
Step
Increment
Att
Severe Discon Iter
Equil Iter
Total Iter
Total Time/Freq
Step Time/LPF
Time/LPF Inc
1 185 1 0 1 1 622.055 622.055 5
1 186 1 0 1 1 627.055 627.055 5
1 187 1 0 1 1 632.055 632.055 5
1 188 1 0 1 1 637.055 637.055 5
1 189 1 0 1 1 642.055 642.055 5
1 190 1 0 1 1 647.055 647.055 5
1 191 1 0 1 1 652.055 652.055 5
1 192 1 0 1 1 657.055 657.055 5
1 193 1 0 1 1 662.055 662.055 5
1 194 1 0 1 1 667.055 667.055 5
1 195 1 0 1 1 672.055 672.055 5
1 196 1 0 1 1 677.055 677.055 5
1 197 1 0 1 1 682.055 682.055 5
1 198 1 0 1 1 687.055 687.055 5
1 199 1 0 1 1 692.055 692.055 5
1 200 1 0 1 1 697.055 697.055 5
1 201 1 0 1 1 702.055 702.055 5
1 202 1 0 1 1 707.055 707.055 5
1 203 1 0 1 1 712.055 712.055 5
1 204 1 0 1 1 717.055 717.055 5
1 205 1 0 1 1 722.055 722.055 5
1 206 1 0 1 1 727.055 727.055 5
1 207 1 0 1 1 732.055 732.055 5
1 208 1 0 1 1 737.055 737.055 5
1 209 1 0 1 1 742.055 742.055 5
1 210 1 0 1 1 747.055 747.055 5
1 211 1 0 1 1 752.055 752.055 5
1 212 1 0 1 1 757.055 757.055 5
1 213 1 0 1 1 762.055 762.055 5
1 214 1 0 1 1 767.055 767.055 5
Search Text
Text to find:
Match case
Next
Previous
Kill
Dismiss

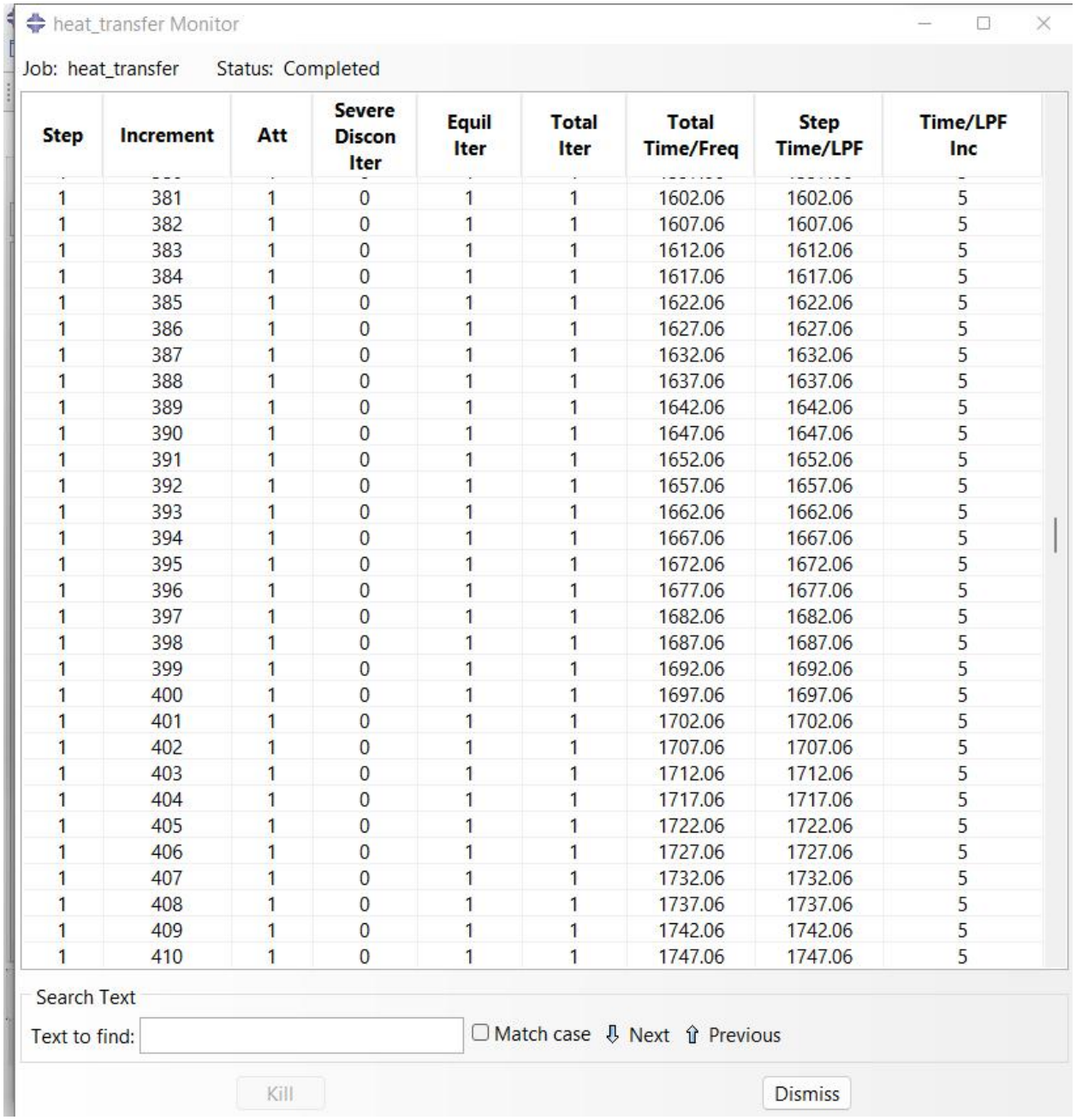

Step	Increment	Att	Severe Discon Iter	Equil Iter	Total Iter	Total Time/Freq	Step Time/LPF	Time/LPF Inc
1	381	1	0	1	1	1602.06	1602.06	5
1	382	1	0	1	1	1607.06	1607.06	5
1	383	1	0	1	1	1612.06	1612.06	5
1	384	1	0	1	1	1617.06	1617.06	5
1	385	1	0	1	1	1622.06	1622.06	5
1	386	1	0	1	1	1627.06	1627.06	5
1	387	1	0	1	1	1632.06	1632.06	5
1	388	1	0	1	1	1637.06	1637.06	5
1	389	1	0	1	1	1642.06	1642.06	5
1	390	1	0	1	1	1647.06	1647.06	5
1	391	1	0	1	1	1652.06	1652.06	5
1	392	1	0	1	1	1657.06	1657.06	5
1	393	1	0	1	1	1662.06	1662.06	5
1	394	1	0	1	1	1667.06	1667.06	5
1	395	1	0	1	1	1672.06	1672.06	5
1	396	1	0	1	1	1677.06	1677.06	5
1	397	1	0	1	1	1682.06	1682.06	5
1	398	1	0	1	1	1687.06	1687.06	5
1	399	1	0	1	1	1692.06	1692.06	5
1	400	1	0	1	1	1697.06	1697.06	5
1	401	1	0	1	1	1702.06	1702.06	5
1	402	1	0	1	1	1707.06	1707.06	5
1	403	1	0	1	1	1712.06	1712.06	5
1	404	1	0	1	1	1717.06	1717.06	5
1	405	1	0	1	1	1722.06	1722.06	5
1	406	1	0	1	1	1727.06	1727.06	5
1	407	1	0	1	1	1732.06	1732.06	5
1	408	1	0	1	1	1737.06	1737.06	5
1	409	1	0	1	1	1742.06	1742.06	5
1	410	1	0	1	1	1747.06	1747.06	5

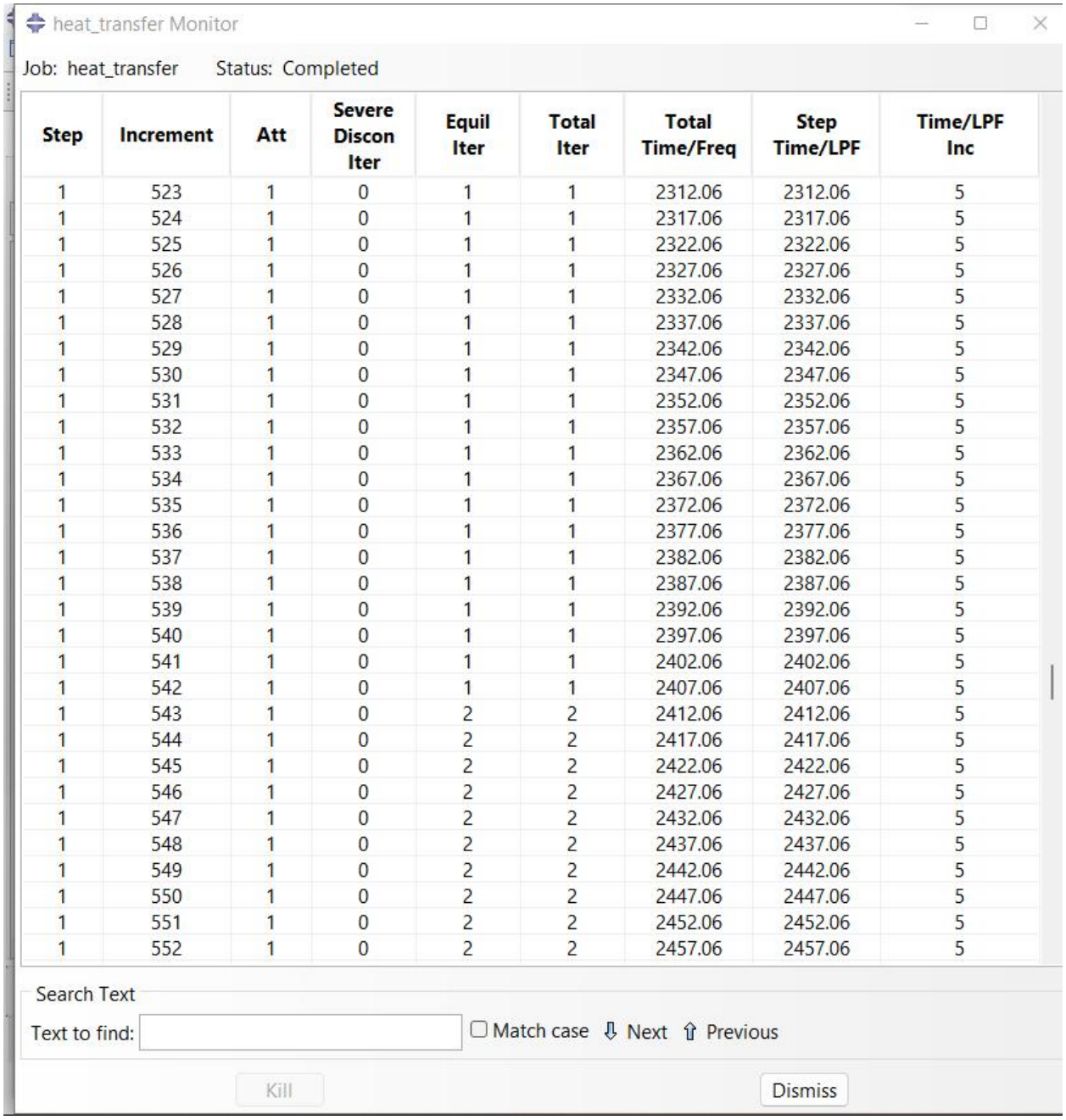

Step	Increment	Att	Severe Discon Iter	Equil Iter	Total Iter	Total Time/Freq	Step Time/LPF	Time/LPF Inc
1	523	1	0	1	1	2312.06	2312.06	5
1	524	1	0	1	1	2317.06	2317.06	5
1	525	1	0	1	1	2322.06	2322.06	5
1	526	1	0	1	1	2327.06	2327.06	5
1	527	1	0	1	1	2332.06	2332.06	5
1	528	1	0	1	1	2337.06	2337.06	5
1	529	1	0	1	1	2342.06	2342.06	5
1	530	1	0	1	1	2347.06	2347.06	5
1	531	1	0	1	1	2352.06	2352.06	5
1	532	1	0	1	1	2357.06	2357.06	5
1	533	1	0	1	1	2362.06	2362.06	5
1	534	1	0	1	1	2367.06	2367.06	5
1	535	1	0	1	1	2372.06	2372.06	5
1	536	1	0	1	1	2377.06	2377.06	5
1	537	1	0	1	1	2382.06	2382.06	5
1	538	1	0	1	1	2387.06	2387.06	5
1	539	1	0	1	1	2392.06	2392.06	5
1	540	1	0	1	1	2397.06	2397.06	5
1	541	1	0	1	1	2402.06	2402.06	5
1	542	1	0	1	1	2407.06	2407.06	5
1	543	1	0	2	2	2412.06	2412.06	5
1	544	1	0	2	2	2417.06	2417.06	5
1	545	1	0	2	2	2422.06	2422.06	5
1	546	1	0	2	2	2427.06	2427.06	5
1	547	1	0	2	2	2432.06	2432.06	5
1	548	1	0	2	2	2437.06	2437.06	5
1	549	1	0	2	2	2442.06	2442.06	5
1	550	1	0	2	2	2447.06	2447.06	5
1	551	1	0	2	2	2452.06	2452.06	5
1	552	1	0	2	2	2457.06	2457.06	5

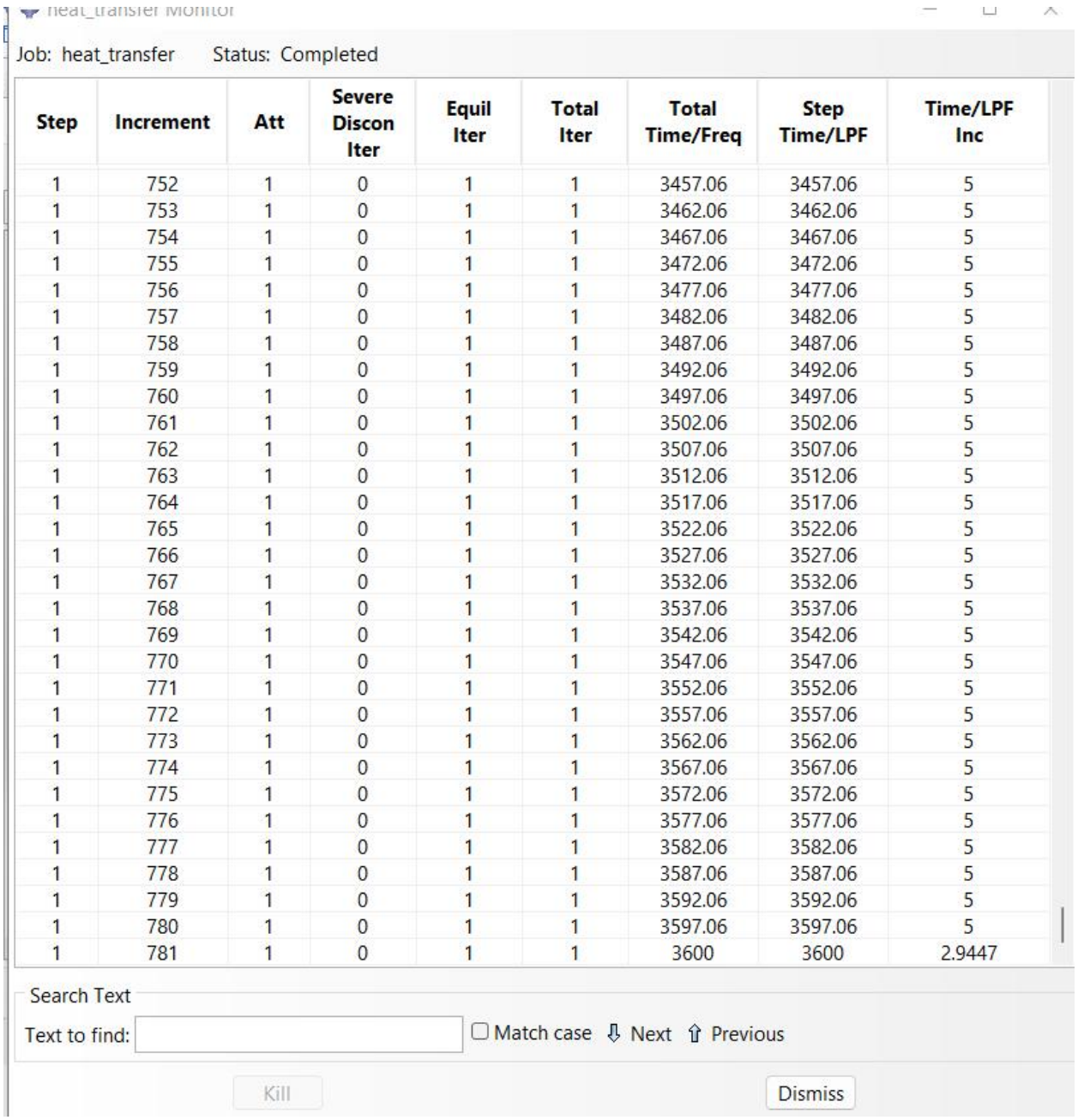

Step	Increment	Att	Severe Discon Iter	Equil Iter	Total Iter	Total Time/Freq	Step Time/LPF	Time/LPF Inc
1	752	1	0	1	1	3457.06	3457.06	5
1	753	1	0	1	1	3462.06	3462.06	5
1	754	1	0	1	1	3467.06	3467.06	5
1	755	1	0	1	1	3472.06	3472.06	5
1	756	1	0	1	1	3477.06	3477.06	5
1	757	1	0	1	1	3482.06	3482.06	5
1	758	1	0	1	1	3487.06	3487.06	5
1	759	1	0	1	1	3492.06	3492.06	5
1	760	1	0	1	1	3497.06	3497.06	5
1	761	1	0	1	1	3502.06	3502.06	5
1	762	1	0	1	1	3507.06	3507.06	5
1	763	1	0	1	1	3512.06	3512.06	5
1	764	1	0	1	1	3517.06	3517.06	5
1	765	1	0	1	1	3522.06	3522.06	5
1	766	1	0	1	1	3527.06	3527.06	5
1	767	1	0	1	1	3532.06	3532.06	5
1	768	1	0	1	1	3537.06	3537.06	5
1	769	1	0	1	1	3542.06	3542.06	5
1	770	1	0	1	1	3547.06	3547.06	5
1	771	1	0	1	1	3552.06	3552.06	5
1	772	1	0	1	1	3557.06	3557.06	5
1	773	1	0	1	1	3562.06	3562.06	5
1	774	1	0	1	1	3567.06	3567.06	5
1	775	1	0	1	1	3572.06	3572.06	5
1	776	1	0	1	1	3577.06	3577.06	5
1	777	1	0	1	1	3582.06	3582.06	5
1	778	1	0	1	1	3587.06	3587.06	5
1	779	1	0	1	1	3592.06	3592.06	5
1	780	1	0	1	1	3597.06	3597.06	5
1	781	1	0	1	1	3600	3600	2.9447

APPENDIX F

CONCRETE RECTANGULAR BEAM ANALYSIS AND DESIGN

In accordance with EN1992-1-1:2004 incorporating Corrigenda January 2008 and the recommended values

Analysis

Geometry (m) - Concrete (C35 2500 Quartzite) - R 300x700

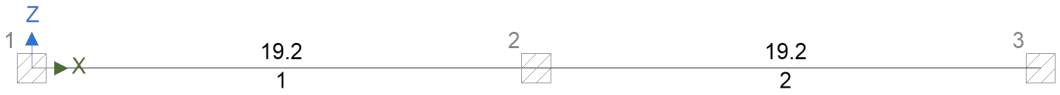

Span	Length (m)	Section	Start Support	End Support
1	19.2	R 300x700	Fixed	Fixed
2	19.2	R 300x700	Fixed	Fixed
R 300x700: A = 2100 cm^2, I_y = 857500 cm^4, I_z = 157500 cm^4, A_y = 1750 cm^2, A_z = 1750 cm^2				
Concrete (C35 2500 Quartzite): Density 2500 kg/m^3, Youngs 34.0771462 kN/mm^2, Shear 14.1988109 kN/mm^2, Thermal 0.00001 $°C^{-1}$				

Loading

Self weight included

Permanent - Loading (kN/m)

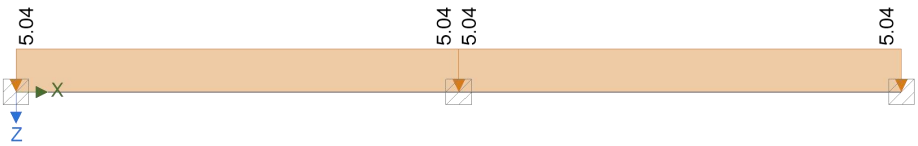

Imposed - Loading (kN/m)

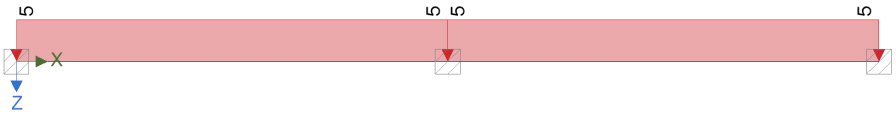

Load combination factors

Load combination	Self Weight	Permanent	Imposed	LoadCase4
1.35G + 1.5Q + 1.5RQ (Strength)	1.35	1.35	1.50	1.35
1.0G + 1.0Q + 1.0RQ (Service)	1.00	1.00	1.00	1.00
1.0G + 1.0ψ_2Q (Quasi)	1.00	1.00	0.30	1.00

Member Loads

Member	Load case	Load Type	Orientation	Description
Beam	Permanent	UDL	GlobalZ	5.04 kN/m
Beam	Imposed	UDL	GlobalZ	5 kN/m

Results; Forces

Strength combinations - Moment envelope (kNm)

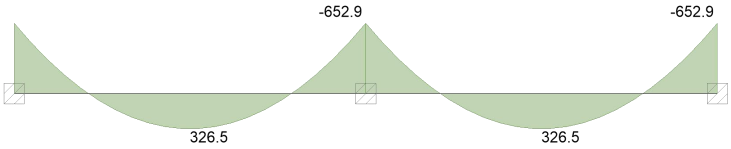

Strength combinations - Shear envelope (kN)

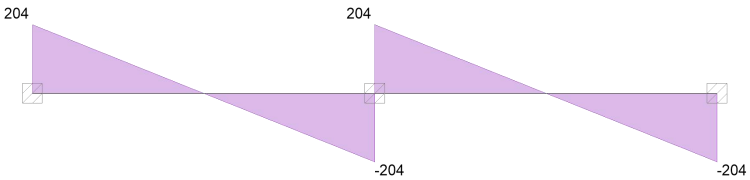

Concrete details - Concrete strength class; C35/45

Aggregate type; Quartzite

Aggregate adjustment factor - cl.3.1.3(2); AAF = 1.0

Characteristic compressive cylinder strength; f_{ck} = 35 N/mm^2

Mean value of compressive cylinder strength; $f_{cm} = f_{ck}$ + 8 N/mm^2 = 43 N/mm^2

Mean value of axial tensile strength; f_{ctm} = 0.3 N/mm^2 × (f_{ck}/ 1 N/mm^2)$^{2/3}$ = 3.2 N/mm^2

Secant modulus of elasticity of concrete; E_{cm} = 22 kN/mm^2×[f_{cm}/10 N/mm^2]$^{0.3}$ × AAF = 34077 N/mm^2

Ultimate strain - Table 3.1; $\varepsilon_{cu2} = 0.0035$

Shortening strain - Table 3.1; $\varepsilon_{cu3} = 0.0035$

Effective compression zone height factor; $\lambda = 0.80$

Effective strength factor; $\eta = 1.00$

Coefficient k_1; $k_1 = 0.44$

Coefficient k_2; $k_2 = 1.25 \times (0.6 + 0.0014 / \varepsilon_{cu2}) = 1.25$

Coefficient k_3; $k_3 = 0.54$

Coefficient k_4; $k_4 = 1.25 \times (0.6 + 0.0014 / \varepsilon_{cu2}) = 1.25$

Partial factor for concrete -Table 2.1N; $\gamma_C = 1.50$

Compressive strength coefficient - cl.3.1.6(1); $\alpha_{cc} = 1.00$

Design compressive concrete strength - exp.3.15; $f_{cd} = \alpha_{cc} \times f_{ck} / \gamma_C = 23.3$ N/mm^2

Compressive strength coefficient - cl.3.1.6(1); $\alpha_{ccw} = 1.00$

Design compressive concrete strength - exp.3.15; $f_{cwd} = \alpha_{ccw} \times f_{ck} / \gamma_C = 23.3$ N/mm^2

Maximum aggregate size; $h_{agg} = 20$ mm

Monolithic simple support moment factor; $\beta_1 = 0.15$

Reinforcement details

Characteristic yield strength of reinforcement; $f_{yk} = 460$ N/mm^2

Partial factor for reinforcing steel - Table 2.1N; $\gamma_S = 1.15$

Design yield strength of reinforcement; $f_{yd} = f_{yk} / \gamma_S = 400$ N/mm^2

Nominal cover to reinforcement

Nominal cover to top reinforcement; $c_{nom\_t} = 35$ mm

Nominal cover to bottom reinforcement; $c_{nom\_b} = 35$ mm

Nominal cover to side reinforcement;$c_{nom\_s} = 35$ mm

Fire resistance

Standard fire resistance period; R = 60 min

Number of sides exposed to fire; 3

Minimum width of beam - EN1992-1-2 Table 5.6; b_{min} = 120 mm

Beam - Span 1

Rectangular section details

Section width; b = 300 mm

Section depth; h = 700 mm

PASS - Minimum dimensions for fire resistance met

Moment design

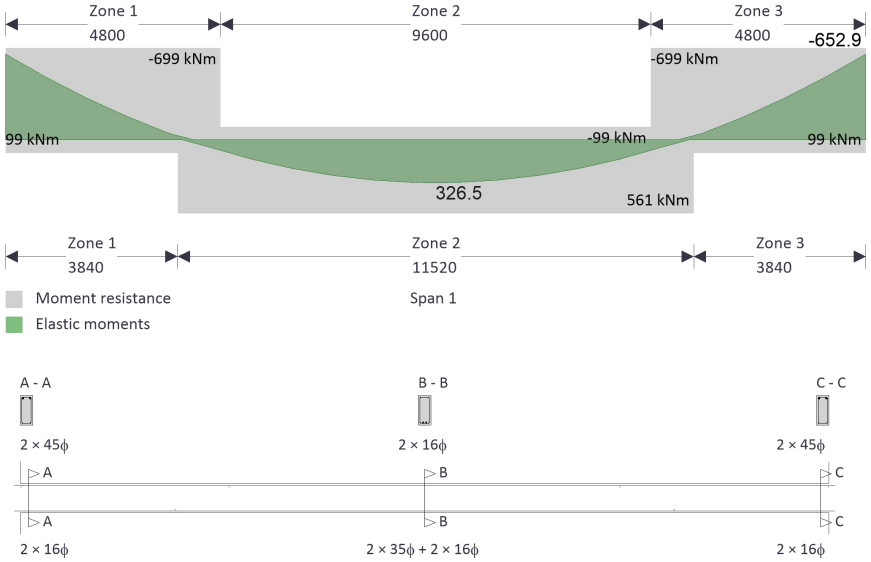

Zone 1 (0 mm - 4800 mm) Negative moment - section 6.1

Design bending moment; $M = \max(\beta_1 \times \text{abs}(M_{m1\_s1\_max\_red}), \text{abs}(M_{m1\_s1\_z1\_min\_red})) = 652.9$ kNm

Effective depth of tension reinforcement; d = 635 mm

Redistribution ratio; $\delta = \min(M_{neg\_red\_z1} / M_{neg\_z1}, 1) = 1.000$

$$K = M / (b \times d^2 \times f_{ck}) = 0.154$$

$$K' = (2 \times \eta \times \alpha_{cc} / \gamma_C) \times (1 - \lambda \times (\delta - k_1) / (2 \times k_2)) \times (\lambda \times (\delta - k_1) / (2 \times k_2)) = 0.196$$

K' > K - No compression reinforcement is required

Lever arm; $z = \min(0.5 \times d \times [1 + (1 - 2 \times K / (\eta \times \alpha_{cc} / \gamma_C))^{0.5}], 0.95 \times d) = 550$ mm

Depth of neutral axis; $x = 2 \times (d - z) / \lambda = 212$ mm

Area of tension reinforcement required; $A_{s,req} = M / (f_{yd} \times z) = 2970$ mm^2

Tension reinforcement provided; $2 \times 45\phi$

Area of tension reinforcement provided; $A_{s,prov} = 3181$ mm^2

Minimum area of reinforcement - exp.9.1N; $A_{s,min} = \max(0.26 \times f_{ctm} / f_{yk}, 0.0013) \times b \times d = 345$ mm^2

Maximum area of reinforcement - cl.9.2.1.1(3); $A_{s,max} = 0.04 \times b \times h = 8400$ mm^2

PASS - Area of reinforcement provided is greater than area of reinforcement required

Crack control - Section 7.3

Maximum crack width; $w_k = 0.3$ mm

Design value modulus of elasticity reinf – 3.2.7(4); $E_s = 200000$ N/mm^2

Mean value of concrete tensile strength; $f_{ct,eff} = f_{ctm} = 3.2$ N/mm^2

Stress distribution coefficient; $k_c = 0.4$

Non-uniform self-equilibrating stress coefficient; $k = \min(\max(1 + (300 \text{ mm} - \min(h, b)) \times 0.35 / 500 \text{ mm}, 0.65), 1) = 1.00$

Actual tension bar spacing; $s_{bar} = (b - (2 \times (c_{nom\_s} + \phi_{m1\_s1\_z1\_v}) + \phi_{m1\_s1\_z1\_t\_L1} \times N_{m1\_s1\_z1\_t\_L1})) / (N_{m1\_s1\_z1\_t\_L1} - 1) + \phi_{m1\_s1\_z1\_t\_L1} = 169$ mm

Maximum stress permitted - Table 7.3N; $\sigma_s = 265$ N/mm^2

Steel to concrete modulus of elast. ratio; $\alpha_{cr} = E_s / E_{cm} = 5.87$

Distance of the Elastic NA from bottom of beam; $y = (b \times h^2 / 2 + A_{s,prov} \times (\alpha_{cr} - 1) \times (h - d)) / (b \times h + A_{s,prov} \times (\alpha_{cr} - 1)) = 330$ mm

Area of concrete in the tensile zone; $A_{ct} = b \times y = 99138$ mm^2

Minimum area of reinforcement required - exp.7.1; $A_{sc,min} = k_c \times k \times f_{ct,eff} \times A_{ct} / \sigma_s = 481$ mm^2

PASS - Area of tension reinforcement provided exceeds minimum required for crack control

Quasi-permanent moment; $M_{QP} = \max(\beta_1 \times \text{abs}(M_{m1\_s1\_z2\_pos\_quasi}), \text{abs}(M_{m1\_s1\_z1\_neg\_quasi})) = 359.1\text{kNm}$

Permanent load ratio; $R_{PL} = M_{QP} / M = 0.55$

Service stress in reinforcement; $\sigma_{sr} = f_{yd} \times A_{s,req} / A_{s,prov} \times R_{PL} = 205\ \text{N/mm}^2$

Maximum bar spacing - Tables 7.3N; $s_{bar,max} = 243.3$ mm

PASS - Maximum bar spacing exceeds actual bar spacing for crack control

Minimum bar spacing (Section 8.2)

Top bar spacing; $s_{top} = (b - (2 \times (c_{nom\_s} + \phi_{m1\_s1\_z1\_v}) + \phi_{m1\_s1\_z1\_t\_L1} \times N_{m1\_s1\_z1\_t\_L1})) / (N_{m1\_s1\_z1\_t\_L1} - 1) = 124.0$ mm

Minimum allowable top bar spacing; $s_{top,min} = \max(\phi_{m1\_s1\_z1\_t\_L1} \times k_{s1}, h_{agg} + k_{s2}, 20\text{mm}) = 45.0$ mm

PASS - Actual bar spacing exceeds minimum allowable

Bottom bar spacing; $s_{bot} = (b - (2 \times (c_{nom\_s} + \phi_{m1\_s1\_z1\_v}) + \phi_{m1\_s1\_z1\_b\_L1} \times N_{m1\_s1\_z1\_b\_L1})) / (N_{m1\_s1\_z1\_b\_L1} - 1) = 182.0$ mm

Minimum allowable bottom bar spacing; $s_{bot,min} = \max(\phi_{m1\_s1\_z1\_b\_L1} \times k_{s1}, h_{agg} + k_{s2}, 20\text{mm}) = 25.0$ mm

PASS - Actual bar spacing exceeds minimum allowable

Zone 2 (3840 mm - 15360 mm) Positive moment - section 6.1

Design bending moment; $M = \text{abs}(M_{m1\_s1\_z2\_max\_red}) = 326.5$ kNm

Effective depth of tension reinforcement; $d = 641$ mm

Redistribution ratio; $\delta = \min(M_{pos\_red\_z2} / M_{pos\_z2}, 1) = 1.000$

$K = M / (b \times d^2 \times f_{ck}) = 0.076$

$K' = (2 \times \eta \times \alpha_{cc} / \gamma_C) \times (1 - \lambda \times (\delta - k_1) / (2 \times k_2)) \times (\lambda \times (\delta - k_1) / (2 \times k_2)) = 0.196$

K' > K - No compression reinforcement is required

Lever arm; $z = \min(0.5 \times d \times [1 + (1 - 2 \times K / (\eta \times \alpha_{cc} / \gamma_C))^{0.5}], 0.95 \times d) = 602$ mm

Depth of neutral axis; $x = 2 \times (d - z) / \lambda = 97$ mm

Area of tension reinforcement required; $A_{s,req} = M / (f_{yd} \times z) = 1355$ mm^2

Tension reinforcement provided; $2 \times 35\phi + 2 \times 16\phi$

Area of tension reinforcement provided; $A_{s,prov} = 2326$ mm^2

Minimum area of reinforcement - exp.9.1N; $A_{s,min} = \max(0.26 \times f_{ctm} / f_{yk}, 0.0013) \times b \times d = 349$ mm^2

Maximum area of reinforcement - cl.9.2.1.1(3); $A_{s,max} = 0.04 \times b \times h = 8400$ mm^2

PASS - Area of reinforcement provided is greater than area of reinforcement required

Crack control - Section 7.3

Maximum crack width; $w_k = 0.3$ mm

Design value modulus of elasticity reinf – 3.2.7(4); $E_s = 200000$ N/mm^2

Mean value of concrete tensile strength; $f_{ct,eff} = f_{ctm} = 3.2$ N/mm^2

Stress distribution coefficient; $k_c = 0.4$

Non-uniform self-equilibrating stress coefficient; $k = \min(\max(1 + (300 \text{ mm} - \min(h, b)) \times 0.35 / 500 \text{ mm}, 0.65), 1) = 1.00$

Actual tension bar spacing; $s_{bar} = (b - (2 \times (c_{nom\_s} + \phi_{m1\_s1\_z2\_v}) + \phi_{m1\_s1\_z2\_b\_L1} \times N_{m1\_s1\_z2\_b\_L1} + \phi_{m1\_s1\_z1\_b\_L1} \times N_{m1\_s1\_z1\_b\_L1})) / ((N_{m1\_s1\_z2\_b\_L1} + N_{m1\_s1\_z1\_b\_L1}) - 1) + \phi_{m1\_s1\_z2\_b\_L1} = 72.3$ mm

Maximum stress permitted - Table 7.3N; $\sigma_s = 342$ N/mm^2

Steel to concrete modulus of elast. ratio; $\alpha_{cr} = E_s / E_{cm} = 5.87$

Distance of the Elastic NA from bottom of beam; $y = (b \times h^2 / 2 + A_{s,prov} \times (\alpha_{cr} - 1) \times (h - d)) / (b \times h + A_{s,prov} \times (\alpha_{cr} - 1)) = 335$ mm

Area of concrete in the tensile zone; $A_{ct} = b \times y = 100530$ mm^2

Minimum area of reinforcement required - exp.7.1; $A_{sc,min} = k_c \times k \times f_{ct,eff} \times A_{ct} / \sigma_s = 377$ mm^2

PASS - Area of tension reinforcement provided exceeds minimum required for crack control

Quasi-permanent moment; $M_{QP} = abs(M_{m1\_s1\_z2\_pos\_quasi}) = 179.5kNm$

Permanent load ratio; $R_{PL} = M_{QP} / M = 0.55$

Service stress in reinforcement; $\sigma_{sr} = f_{yd} \times A_{s,req} / A_{s,prov} \times R_{PL} = 128$ N/mm^2

Maximum bar spacing - Tables 7.3N; $s_{bar,max} = 300$ mm

PASS - Maximum bar spacing exceeds actual bar spacing for crack control

Deflection control - Section 7.4

Reference reinforcement ratio; $\rho_{m0} = (f_{ck} / 1\ N/mm^2)^{0.5} / 1000 = 0.00592$

Required tension reinforcement ratio; $\rho_m = A_{s,req} / (b \times d) = 0.00704$

Required compression reinforcement ratio; $\rho'_m = A_{s2,req} / (b \times d) = 0.00000$

Structural system factor - Table 7.4N; $K_b = 1.3$

Basic allowable span to depth ratio ; $span\_to\_depth_{basic} = K_b \times [11 + 1.5 \times (f_{ck} / 1\ N/mm^2)^{0.5} \times \rho_{m0} / (\rho_m - \rho'_m) + (f_{ck} / 1\ N/mm^2)^{0.5} \times (\rho'_m / \rho_{m0})^{0.5} / 12] = 23.990$

Reinforcement factor - exp.7.17; $K_s = \min(A_{s,prov} / A_{s,req} \times 500\ N/mm^2 / f_{yk}, 1.5) = 1.500$

Flange width factor; $F1 = 1 = 1.000$

Long span supporting brittle partition factor; $F2 = 1 = 1.000$

Allowable span to depth ratio; $span\_to\_depth_{allow} = \min(span\_to\_depth_{basic} \times K_s \times F1 \times F2, 40 \times K_b) = 35.984$

Actual span to depth ratio; $span\_to\_depth_{actual} = L_{m1\_s1} / d = 29.947$

PASS - Actual span to depth ratio is within the allowable limit

Minimum bar spacing (Section 8.2)

Top bar spacing; $s_{top} = (b - (2 \times (c_{nom\_s} + \phi_{m1\_s1\_z2\_v}) + \phi_{m1\_s1\_z2\_t\_L1} \times N_{m1\_s1\_z2\_t\_L1})) / (N_{m1\_s1\_z2\_t\_L1} - 1) = 182.0$ mm

Minimum allowable top bar spacing; $s_{top,min} = \max(\phi_{m1\_s1\_z2\_t\_L1} \times k_{s1}, h_{agg} + k_{s2}, 20mm) = 25.0$ mm

PASS - Actual bar spacing exceeds minimum allowable

Bottom bar spacing; $s_{bot} = (b - (2 \times (c_{nom\_s} + \phi_{m1\_s1\_z2\_v}) + \phi_{m1\_s1\_z2\_b\_L1} \times N_{m1\_s1\_z2\_b\_L1} + \phi_{m1\_s1\_z1\_b\_L1} \times N_{m1\_s1\_z1\_b\_L1})) / ((N_{m1\_s1\_z2\_b\_L1} + N_{m1\_s1\_z1\_b\_L1}) - 1) = 37.3$ mm

Minimum allowable bottom bar spacing; $s_{bot,min} = \max(\phi_{m1\_s1\_z2\_b\_L1} \times k_{s1}, h_{agg} + k_{s2}, 20mm) = 35.0$ mm

PASS - Actual bar spacing exceeds minimum allowable

Zone 3 (14400 mm - 19200 mm) Negative moment - section 6.1

Design bending moment; $M = abs(M_{m1\_s1\_z3\_min\_red}) = 652.9$ kNm

Effective depth of tension reinforcement; $d = 635$ mm

Redistribution ratio; $\delta = \min(M_{neg\_red\_z3} / M_{neg\_z3}, 1) = 1.000$

$K = M / (b \times d^2 \times f_{ck}) = 0.154$

$K' = (2 \times \eta \times \alpha_{cc} / \gamma_C) \times (1 - \lambda \times (\delta - k_1) / (2 \times k_2)) \times (\lambda \times (\delta - k_1) / (2 \times k_2)) = 0.196$

K' > K - No compression reinforcement is required

Lever arm; $z = \min(0.5 \times d \times [1 + (1 - 2 \times K / (\eta \times \alpha_{cc} / \gamma_C))^{0.5}], 0.95 \times d) = 550$ mm

Depth of neutral axis; $x = 2 \times (d - z) / \lambda = 212$ mm

Area of tension reinforcement required; $A_{s,req} = M / (f_{yd} \times z) = 2970$ mm^2

Tension reinforcement provided; $2 \times 45\phi$

Area of tension reinforcement provided; $A_{s,prov} = 3181$ mm^2

Minimum area of reinforcement - exp.9.1N; $A_{s,min} = \max(0.26 \times f_{ctm} / f_{yk}, 0.0013) \times b \times d = 345$ mm^2

Maximum area of reinforcement - cl.9.2.1.1(3); $A_{s,max} = 0.04 \times b \times h = 8400$ mm^2

PASS - Area of reinforcement provided is greater than area of reinforcement required

Crack control - Section 7.3

Maximum crack width; $w_k = 0.3$ mm

Design value modulus of elasticity reinf – 3.2.7(4); $E_s = 200000$ N/mm^2

Mean value of concrete tensile strength; $f_{ct,eff} = f_{ctm} = 3.2$ N/mm^2

Stress distribution coefficient; $k_c = 0.4$

Non-uniform self-equilibrating stress coefficient; $k = \min(\max(1 + (300\text{ mm} - \min(h, b)) \times 0.35 / 500\text{ mm}, 0.65), 1) = 1.00$

Actual tension bar spacing; $s_{bar} = (b - (2 \times (c_{nom\_s} + \phi_{m1\_s1\_z3\_v}) + \phi_{m1\_s1\_z3\_t\_L1} \times N_{m1\_s1\_z3\_t\_L1})) / (N_{m1\_s1\_z3\_t\_L1} - 1) + \phi_{m1\_s1\_z3\_t\_L1} = 169$ mm

Maximum stress permitted - Table 7.3N; $\sigma_s = 265$ N/mm^2

Steel to concrete modulus of elast. ratio; $\alpha_{cr} = E_s / E_{cm} = 5.87$

Distance of the Elastic NA from bottom of beam; $y = (b \times h^2 / 2 + A_{s,prov} \times (\alpha_{cr} - 1) \times (h - d)) / (b \times h + A_{s,prov} \times (\alpha_{cr} - 1)) = 330$ mm

Area of concrete in the tensile zone; $A_{ct} = b \times y = 99138$ mm^2

Minimum area of reinforcement required - exp.7.1; $A_{sc,min} = k_c \times k \times f_{ct,eff} \times A_{ct} / \sigma_s = 481$ mm^2

PASS - Area of tension reinforcement provided exceeds minimum required for crack control

Quasi-permanent moment; $M_{QP} = \text{abs}(M_{m1_s1_z3_neg_quasi}) = 359.1$kNm

Permanent load ratio; $R_{PL} = M_{QP} / M = 0.55$

Service stress in reinforcement; $\sigma_{sr} = f_{yd} \times A_{s,req} / A_{s,prov} \times R_{PL} = 205$ N/mm^2

Maximum bar spacing - Tables 7.3N; $s_{bar,max} = 243.3$ mm

PASS - Maximum bar spacing exceeds actual bar spacing for crack control

Minimum bar spacing (Section 8.2)

Top bar spacing; $s_{top} = (b - (2 \times (c_{nom\_s} + \phi_{m1\_s1\_z3\_v}) + \phi_{m1\_s1\_z3\_t\_L1} \times N_{m1\_s1\_z3\_t\_L1})) / (N_{m1\_s1\_z3\_t\_L1} - 1) = 124.0$ mm

Minimum allowable top bar spacing; $s_{top,min} = \max(\phi_{m1\_s1\_z3\_t\_L1} \times k_{s1}, h_{agg} + k_{s2}, 20mm) = 45.0$ mm

PASS - Actual bar spacing exceeds minimum allowable

Bottom bar spacing; $s_{bot} = (b - (2 \times (c_{nom\_s} + \phi_{m1\_s1\_z3\_v}) + \phi_{m1\_s1\_z3\_b\_L1} \times N_{m1\_s1\_z3\_b\_L1})) / (N_{m1\_s1\_z3\_b\_L1} - 1) = 182.0$ mm

Minimum allowable bottom bar spacing; $s_{bot,min} = \max(\phi_{m1\_s1\_z3\_b\_L1} \times k_{s1}, h_{agg} + k_{s2}, 20mm) = 25.0$ mm

PASS - Actual bar spacing exceeds minimum allowable

Shear design

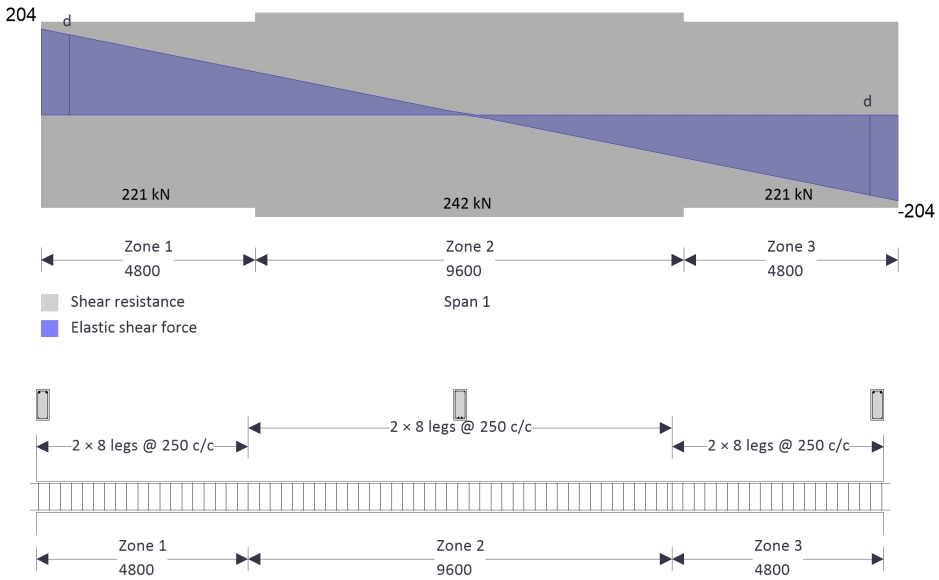

Angle of comp. shear strut for maximum shear; $\theta_{max} = 45$ deg

Strength reduction factor - cl.6.2.3(3); $v_1 = 0.6 \times (1 - f_{ck} / 250\ N/mm^2) = 0.516$

Compression chord coefficient - cl.6.2.3(3); $\alpha_{cw} = 1.00$

Minimum area of shear reinforcement - exp.9.5N; $A_{sv,min} = 0.08\ N/mm^2 \times b \times (f_{ck} / 1\ N/mm^2)^{0.5} / f_{yk} = 309\ mm^2/m$

Zone 1 (0 mm - 4800 mm) shear - section 6.2

Design shear force at support ; $V_{Ed,max} = \max(abs(V_{z1\_max}), abs(V_{z1\_red\_max})) = 204$ kN

Min lever arm in shear zone; $z = 550$ mm

Maximum design shear resistance - exp.6.9; $V_{Rd,max} = \alpha_{cw} \times b \times z \times v_1 \times f_{cwd} / (\cot(\theta_{max}) + \tan(\theta_{max})) = 993$ kN

PASS - Design shear force at support is less than maximum design shear resistance

Design shear force at 635mm from support; $V_{Ed} = 191$ kN

Design shear stress; $v_{Ed} = V_{Ed} / (b \times z) = 1.156$ N/mm^2

Angle of concrete compression strut - cl.6.2.3; $\theta = \min(\max(0.5 \times \text{Asin}(\min(2 \times v_{Ed} / (\alpha_{cw} \times f_{cwd} \times v_1),1)), 21.8 \text{ deg}), 45\text{deg}) = 21.8$ deg

Area of shear reinforcement required - exp.6.8; $A_{sv,des} = v_{Ed} \times b / (f_{yd} \times \cot(\theta)) = 347$ mm^2/m

Area of shear reinforcement required; $A_{sv,req} = \max(A_{sv,min}, A_{sv,des}) = 347$ mm^2/m

Shear reinforcement provided; 2 × 8 legs @ 250 c/c

Area of shear reinforcement provided; $A_{sv,prov} = 402$ mm^2/m

PASS - Area of shear reinforcement provided exceeds minimum required

Maximum longitudinal spacing - exp.9.6N; $s_{vl,max} = 0.75 \times d = 476$ mm

PASS - Longitudinal spacing of shear reinforcement provided is less than maximum

Zone 2 (4800 mm - 14400 mm) shear - section 6.2

Design shear force at support ; $V_{Ed,max} = \max(\text{abs}(V_{z2\_max}), \text{abs}(V_{z2\_red\_max})) = 102$ kN

Min lever arm in shear zone; $z = 602$ mm

Maximum design shear resistance - exp.6.9; $V_{Rd,max} = \alpha_{cw} \times b \times z \times v_1 \times f_{cwd} / (\cot(\theta_{max}) + \tan(\theta_{max})) = 1088$ kN

PASS - Design shear force at support is less than maximum design shear resistance

Design shear force within zone; $V_{Ed} = 102$ kN

Design shear stress; $v_{Ed} = V_{Ed} / (b \times z) = 0.564$ N/mm^2

Angle of concrete compression strut - cl.6.2.3; $\theta = \min(\max(0.5 \times \text{Asin}(\min(2 \times v_{Ed} / (\alpha_{cw} \times f_{cwd} \times v_1),1)), 21.8 \text{ deg}), 45\text{deg}) = 21.8$ deg

Area of shear reinforcement required - exp.6.8; $A_{sv,des} = v_{Ed} \times b / (f_{yd} \times \cot(\theta)) = 169$ mm^2/m

Area of shear reinforcement required; $A_{sv,req} = \max(A_{sv,min}, A_{sv,des}) = 309$ mm^2/m

Shear reinforcement provided; 2 × 8 legs @ 250 c/c

Area of shear reinforcement provided; $A_{sv,prov} = 402$ mm^2/m

PASS - Area of shear reinforcement provided exceeds minimum required

Maximum longitudinal spacing - exp.9.6N; $s_{vl,max} = 0.75 \times d = 481$ mm

PASS - Longitudinal spacing of shear reinforcement provided is less than maximum

Zone 3 (14400 mm - 19200 mm) shear - section 6.2

Design shear force at support ; $V_{Ed,max} = \max(\text{abs}(V_{z3\_max}), \text{abs}(V_{z3\_red\_max})) = 204$ kN

Min lever arm in shear zone; z = 550 mm

Maximum design shear resistance - exp.6.9; $V_{Rd,max} = \alpha_{cw} \times b \times z \times v_1 \times f_{cwd} / (\cot(\theta_{max}) + \tan(\theta_{max})) = 993$ kN

PASS - Design shear force at support is less than maximum design shear resistance

Design shear force at 635mm from support; $V_{Ed} = 191$ kN

Design shear stress; $v_{Ed} = V_{Ed} / (b \times z) = 1.156$ N/mm^2

Angle of concrete compression strut - cl.6.2.3; $\theta = \min(\max(0.5 \times \text{Asin}(\min(2 \times v_{Ed} / (\alpha_{cw} \times f_{cwd} \times v_1),1)), 21.8 \text{ deg}), 45\text{deg}) = 21.8$ deg

Area of shear reinforcement required - exp.6.8; $A_{sv,des} = v_{Ed} \times b / (f_{yd} \times \cot(\theta)) = 347$ mm^2/m

Area of shear reinforcement required; $A_{sv,req} = \max(A_{sv,min}, A_{sv,des}) = 347$ mm^2/m

Shear reinforcement provided; 2 × 8 legs @ 250 c/c

Area of shear reinforcement provided; $A_{sv,prov} = 402$ mm^2/m

PASS - Area of shear reinforcement provided exceeds minimum required

Maximum longitudinal spacing - exp.9.6N; $s_{vl,max} = 0.75 \times d = 476$ mm

PASS - Longitudinal spacing of shear reinforcement provided is less than maximum

Beam - Span 2

Rectangular section details

Section width; b = 300 mm

Section depth; h = 700 mm

PASS - Minimum dimensions for fire resistance met

Moment design

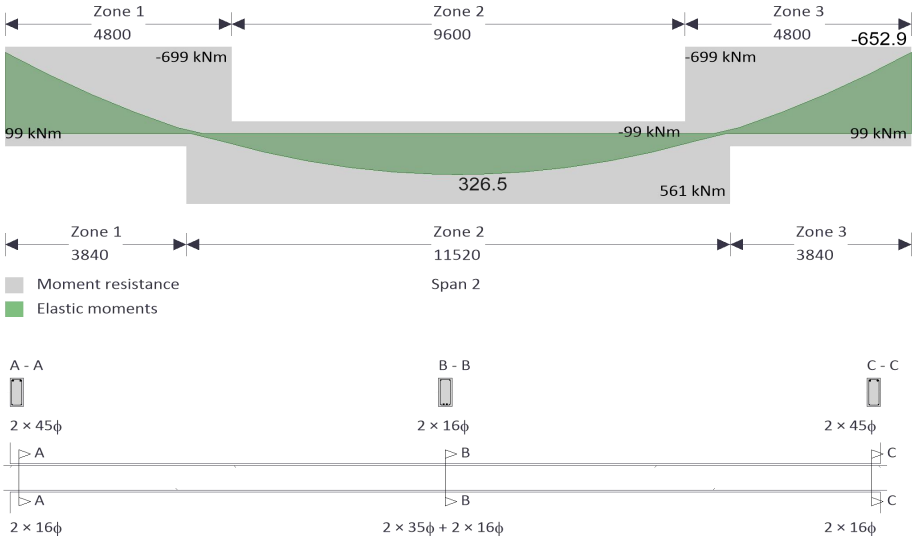

Zone 1 (0 mm - 4800 mm) Negative moment - section 6.1

Design bending moment; $M = abs(M_{m1\_s2\_z1\_min\_red}) = 652.9$ kNm

Effective depth of tension reinforcement; $d = 635$ mm

Redistribution ratio; $\delta = min(M_{neg\_red\_z1} / M_{neg\_z1}, 1) = 1.000$

$K = M / (b \times d^2 \times f_{ck}) = 0.154$

$K' = (2 \times \eta \times \alpha_{cc} / \gamma_C) \times (1 - \lambda \times (\delta - k_1) / (2 \times k_2)) \times (\lambda \times (\delta - k_1) / (2 \times k_2)) = 0.196$

K' > K - No compression reinforcement is required

Lever arm; $z = min(0.5 \times d \times [1 + (1 - 2 \times K / (\eta \times \alpha_{cc} / \gamma_C))^{0.5}], 0.95 \times d) = 550$ mm

Depth of neutral axis; $x = 2 \times (d - z) / \lambda = 212$ mm

Area of tension reinforcement required; $A_{s,req} = M / (f_{yd} \times z) = 2970$ mm^2

Tension reinforcement provided; $2 \times 45\phi$

Area of tension reinforcement provided; $A_{s,prov} = 3181\ mm^2$

Minimum area of reinforcement - exp.9.1N; $A_{s,min} = \max(0.26 \times f_{ctm} / f_{yk}, 0.0013) \times b \times d = 345\ mm^2$

Maximum area of reinforcement - cl.9.2.1.1(3); $A_{s,max} = 0.04 \times b \times h = 8400\ mm^2$

PASS - Area of reinforcement provided is greater than area of reinforcement required

Crack control - Section 7.3

Maximum crack width; $w_k = 0.3\ mm$

Design value modulus of elasticity reinf – 3.2.7(4); $E_s = 200000\ N/mm^2$

Mean value of concrete tensile strength; $f_{ct,eff} = f_{ctm} = 3.2\ N/mm^2$

Stress distribution coefficient; $k_c = 0.4$

Non-uniform self-equilibrating stress coefficient; $k = \min(\max(1 + (300\ mm - \min(h, b)) \times 0.35 / 500\ mm, 0.65), 1) = 1.00$

Actual tension bar spacing; $s_{bar} = (b - (2 \times (c_{nom\_s} + \phi_{m1\_s2\_z1\_v}) + \phi_{m1\_s2\_z1\_t\_L1} \times N_{m1\_s2\_z1\_t\_L1})) / (N_{m1\_s2\_z1\_t\_L1} - 1) + \phi_{m1\_s2\_z1\_t\_L1} = 169\ mm$

Maximum stress permitted - Table 7.3N; $\sigma_s = 265\ N/mm^2$

Steel to concrete modulus of elast. ratio; $\alpha_{cr} = E_s / E_{cm} = 5.87$

Distance of the Elastic NA from bottom of beam; $y = (b \times h^2 / 2 + A_{s,prov} \times (\alpha_{cr} - 1) \times (h - d)) / (b \times h + A_{s,prov} \times (\alpha_{cr} - 1)) = 330\ mm$

Area of concrete in the tensile zone; $A_{ct} = b \times y = 99138\ mm^2$

Minimum area of reinforcement required - exp.7.1; $A_{sc,min} = k_c \times k \times f_{ct,eff} \times A_{ct} / \sigma_s = 481\ mm^2$

PASS - Area of tension reinforcement provided exceeds minimum required for crack control

Quasi-permanent moment; $M_{QP} = \text{abs}(M_{m1\_s2\_z1\_neg\_quasi}) = 359.1kNm$

Permanent load ratio; $R_{PL} = M_{QP} / M = 0.55$

Service stress in reinforcement; $\sigma_{sr} = f_{yd} \times A_{s,req} / A_{s,prov} \times R_{PL} = 205$ N/mm^2

Maximum bar spacing - Tables 7.3N;$s_{bar,max} = 243.3$ mm

PASS - Maximum bar spacing exceeds actual bar spacing for crack control

Minimum bar spacing (Section 8.2)

Top bar spacing; $s_{top} = (b - (2 \times (c_{nom\_s} + \phi_{m1\_s2\_z1\_v}) + \phi_{m1\_s2\_z1\_t\_L1} \times N_{m1\_s2\_z1\_t\_L1})) / (N_{m1\_s2\_z1\_t\_L1} - 1) = 124.0$ mm

Minimum allowable top bar spacing; $s_{top,min} = \max(\phi_{m1\_s2\_z1\_t\_L1} \times k_{s1}, h_{agg} + k_{s2}, 20\text{mm}) = 45.0$ mm

PASS - Actual bar spacing exceeds minimum allowable

Bottom bar spacing; $s_{bot} = (b - (2 \times (c_{nom\_s} + \phi_{m1\_s2\_z1\_v}) + \phi_{m1\_s2\_z1\_b\_L1} \times N_{m1\_s2\_z1\_b\_L1})) / (N_{m1\_s2\_z1\_b\_L1} - 1) = 182.0$ mm

Minimum allowable bottom bar spacing; $s_{bot,min} = \max(\phi_{m1\_s2\_z1\_b\_L1} \times k_{s1}, h_{agg} + k_{s2}, 20\text{mm}) = 25.0$ mm

PASS - Actual bar spacing exceeds minimum allowable

Zone 2 (3840 mm - 15360 mm) Positive moment - section 6.1

Design bending moment; $M = \text{abs}(M_{m1\_s2\_z2\_max\_red}) = 326.5$ kNm

Effective depth of tension reinforcement; $d = 641$ mm

Redistribution ratio; $\delta = \min(M_{pos\_red\_z2} / M_{pos\_z2}, 1) = 1.000$

$K = M / (b \times d^2 \times f_{ck}) = 0.076$

$K' = (2 \times \eta \times \alpha_{cc} / \gamma_C) \times (1 - \lambda \times (\delta - k_1) / (2 \times k_2)) \times (\lambda \times (\delta - k_1) / (2 \times k_2)) = 0.196$

K' > K - No compression reinforcement is required

Lever arm; $z = \min(0.5 \times d \times [1 + (1 - 2 \times K / (\eta \times \alpha_{cc} / \gamma_C))^{0.5}], 0.95 \times d) = 602$ mm

Depth of neutral axis; $x = 2 \times (d - z) / \lambda = 97$ mm

Area of tension reinforcement required; $A_{s,req} = M / (f_{yd} \times z) = 1355$ mm^2

Tension reinforcement provided; $2 \times 35\phi + 2 \times 16\phi$

Area of tension reinforcement provided; $A_{s,prov} = 2326\ mm^2$

Minimum area of reinforcement - exp.9.1N; $A_{s,min} = \max(0.26 \times f_{ctm} / f_{yk}, 0.0013) \times b \times d = 349\ mm^2$

Maximum area of reinforcement - cl.9.2.1.1(3); $A_{s,max} = 0.04 \times b \times h = 8400\ mm^2$

PASS - Area of reinforcement provided is greater than area of reinforcement required

Crack control - Section 7.3

Maximum crack width; $w_k = 0.3\ mm$

Design value modulus of elasticity reinf – 3.2.7(4); $E_s = 200000\ N/mm^2$

Mean value of concrete tensile strength; $f_{ct,eff} = f_{ctm} = 3.2\ N/mm^2$

Stress distribution coefficient; $k_c = 0.4$

Non-uniform self-equilibrating stress coefficient; $k = \min(\max(1 + (300\ mm - \min(h, b)) \times 0.35 / 500\ mm, 0.65), 1) = 1.00$

Actual tension bar spacing; $s_{bar} = (b - (2 \times (c_{nom\_s} + \phi_{m1\_s2\_z2\_v}) + \phi_{m1\_s2\_z2\_b\_L1} \times N_{m1\_s2\_z2\_b\_L1} + \phi_{m1\_s2\_z1\_b\_L1} \times N_{m1\_s2\_z1\_b\_L1})) / ((N_{m1\_s2\_z2\_b\_L1} + N_{m1\_s2\_z1\_b\_L1}) - 1) + \phi_{m1\_s2\_z2\_b\_L1} = 72.3\ mm$

Maximum stress permitted - Table 7.3N; $\sigma_s = 342\ N/mm^2$

Steel to concrete modulus of elast. ratio; $\alpha_{cr} = E_s / E_{cm} = 5.87$

Distance of the Elastic NA from bottom of beam; $y = (b \times h^2 / 2 + A_{s,prov} \times (\alpha_{cr} - 1) \times (h - d)) / (b \times h + A_{s,prov} \times (\alpha_{cr} - 1)) = 335\ mm$

Area of concrete in the tensile zone; $A_{ct} = b \times y = 100530\ mm^2$

Minimum area of reinforcement required - exp.7.1; $A_{sc,min} = k_c \times k \times f_{ct,eff} \times A_{ct} / \sigma_s = 377\ mm^2$

PASS - Area of tension reinforcement provided exceeds minimum required for crack control

Quasi-permanent moment; $M_{QP} = \text{abs}(M_{m1\_s2\_z2\_pos\_quasi}) = 179.5kNm$

Permanent load ratio; $R_{PL} = M_{QP} / M = 0.55$

Service stress in reinforcement; $\sigma_{sr} = f_{yd} \times A_{s,req} / A_{s,prov} \times R_{PL} = 128$ N/mm^2

Maximum bar spacing - Tables 7.3N;$s_{bar,max} = 300$ mm

PASS - Maximum bar spacing exceeds actual bar spacing for crack control

Deflection control - Section 7.4

Reference reinforcement ratio; $\rho_{m0} = (f_{ck} / 1 \text{ N/mm}^2)^{0.5} / 1000 = 0.00592$

Required tension reinforcement ratio; $\rho_m = A_{s,req} / (b \times d) = 0.00704$

Required compression reinforcement ratio; $\rho'_m = A_{s2,req} / (b \times d) = 0.00000$

Structural system factor - Table 7.4N; $K_b = 1.3$

Basic allowable span to depth ratio ; $span\_to\_depth_{basic} = K_b \times [11 + 1.5 \times (f_{ck} / 1 \text{ N/mm}^2)^{0.5} \times \rho_{m0} / (\rho_m - \rho'_m) + (f_{ck} / 1 \text{ N/mm}^2)^{0.5} \times (\rho'_m / \rho_{m0})^{0.5} / 12] = 23.990$

Reinforcement factor - exp.7.17; $K_s = \min(A_{s,prov} / A_{s,req} \times 500 \text{ N/mm}^2 / f_{yk}, 1.5) = 1.500$

Flange width factor; F1 = 1 = 1.000

Long span supporting brittle partition factor; F2 = 1 = 1.000

Allowable span to depth ratio; $span\_to\_depth_{allow} = \min(span\_to\_depth_{basic} \times K_s \times F1 \times F2, 40 \times K_b) = 35.984$

Actual span to depth ratio; $span\_to\_depth_{actual} = L_{m1\_s2} / d = 29.947$

PASS - Actual span to depth ratio is within the allowable limit

Minimum bar spacing (Section 8.2)

Top bar spacing; $s_{top} = (b - (2 \times (c_{nom\_s} + \phi_{m1\_s2\_z2\_v}) + \phi_{m1\_s2\_z2\_t\_L1} \times N_{m1\_s2\_z2\_t\_L1})) / (N_{m1\_s2\_z2\_t\_L1} - 1) = 182.0$ mm

Minimum allowable top bar spacing; $s_{top,min} = \max(\phi_{m1\_s2\_z2\_t\_L1} \times k_{s1}, h_{agg} + k_{s2}, 20\text{mm}) = 25.0$ mm

PASS - Actual bar spacing exceeds minimum allowable

Bottom bar spacing; $s_{bot} = (b - (2 \times (c_{nom\_s} + \phi_{m1\_s2\_z2\_v}) + \phi_{m1\_s2\_z2\_b\_L1} \times N_{m1\_s2\_z2\_b\_L1} + \phi_{m1\_s2\_z1\_b\_L1} \times N_{m1\_s2\_z1\_b\_L1})) / ((N_{m1\_s2\_z2\_b\_L1} + N_{m1\_s2\_z1\_b\_L1}) - 1) = 37.3$ mm

Minimum allowable bottom bar spacing; $s_{bot,min} = \max(\phi_{m1\_s2\_z2\_b\_L1} \times k_{s1}, h_{agg} + k_{s2}, 20mm) = 35.0$ mm

PASS - Actual bar spacing exceeds minimum allowable

Zone 3 (14400 mm - 19200 mm) Negative moment - section 6.1

Design bending moment; $M = \max(\beta_1 \times \text{abs}(M_{m1\_s2\_max\_red}), \text{abs}(M_{m1\_s2\_z3\_min\_red})) = 652.9$ kNm

Effective depth of tension reinforcement; $d = 635$ mm

Redistribution ratio; $\delta = \min(M_{neg\_red\_z3} / M_{neg\_z3}, 1) = 1.000$

$K = M / (b \times d^2 \times f_{ck}) = 0.154$

$K' = (2 \times \eta \times \alpha_{cc} / \gamma_C) \times (1 - \lambda \times (\delta - k_1) / (2 \times k_2)) \times (\lambda \times (\delta - k_1) / (2 \times k_2)) = 0.196$

K' > K - No compression reinforcement is required

Lever arm; $z = \min(0.5 \times d \times [1 + (1 - 2 \times K / (\eta \times \alpha_{cc} / \gamma_C))^{0.5}], 0.95 \times d) = 550$ mm

Depth of neutral axis; $x = 2 \times (d - z) / \lambda = 212$ mm

Area of tension reinforcement required; $A_{s,req} = M / (f_{yd} \times z) = 2970$ mm^2

Tension reinforcement provided; $2 \times 45\phi$

Area of tension reinforcement provided; $A_{s,prov} = 3181$ mm^2

Minimum area of reinforcement - exp.9.1N; $A_{s,min} = \max(0.26 \times f_{ctm} / f_{yk}, 0.0013) \times b \times d = 345$ mm^2

Maximum area of reinforcement - cl.9.2.1.1(3); $A_{s,max} = 0.04 \times b \times h = 8400$ mm^2

PASS - Area of reinforcement provided is greater than area of reinforcement required

Crack control - Section 7.3

Maximum crack width; $w_k = 0.3$ mm

Design value modulus of elasticity reinf – 3.2.7(4); $E_s = 200000$ N/mm^2

Mean value of concrete tensile strength; $f_{ct,eff} = f_{ctm} = 3.2$ N/mm^2

Stress distribution coefficient; $k_c = 0.4$

Non-uniform self-equilibrating stress coefficient; $k = \min(\max(1 + (300\text{ mm} - \min(h, b)) \times 0.35 / 500\text{ mm}, 0.65), 1) = 1.00$

Actual tension bar spacing; $s_{bar} = (b - (2 \times (c_{nom\_s} + \phi_{m1\_s2\_z3\_v}) + \phi_{m1\_s2\_z3\_t\_L1} \times N_{m1\_s2\_z3\_t\_L1})) / (N_{m1\_s2\_z3\_t\_L1} - 1) + \phi_{m1\_s2\_z3\_t\_L1} = 169$ mm

Maximum stress permitted - Table 7.3N; $\sigma_s = 265$ N/mm^2

Steel to concrete modulus of elast. ratio; $\alpha_{cr} = E_s / E_{cm} = 5.87$

Distance of the Elastic NA from bottom of beam; $y = (b \times h^2 / 2 + A_{s,prov} \times (\alpha_{cr} - 1) \times (h - d)) / (b \times h + A_{s,prov} \times (\alpha_{cr} - 1)) = 330$ mm

Area of concrete in the tensile zone; $A_{ct} = b \times y = 99138$ mm^2

Minimum area of reinforcement required - exp.7.1; $A_{sc,min} = k_c \times k \times f_{ct,eff} \times A_{ct} / \sigma_s = 481$ mm^2

PASS - Area of tension reinforcement provided exceeds minimum required for crack control

Quasi-permanent moment; $M_{QP} = \max(\beta_1 \times \text{abs}(M_{m1_s2_z2_pos_quasi}), \text{abs}(M_{m1_s2_z3_neg_quasi})) = 359.1$kNm

Permanent load ratio; $R_{PL} = M_{QP} / M = 0.55$

Service stress in reinforcement; $\sigma_{sr} = f_{yd} \times A_{s,req} / A_{s,prov} \times R_{PL} = 205$ N/mm^2

Maximum bar spacing - Tables 7.3N; $s_{bar,max} = 243.3$ mm

PASS - Maximum bar spacing exceeds actual bar spacing for crack control

Minimum bar spacing (Section 8.2)

Top bar spacing; $s_{top} = (b - (2 \times (c_{nom\_s} + \phi_{m1\_s2\_z3\_v}) + \phi_{m1\_s2\_z3\_t\_L1} \times N_{m1\_s2\_z3\_t\_L1})) / (N_{m1\_s2\_z3\_t\_L1} - 1) = 124.0$ mm

Minimum allowable top bar spacing; $s_{top,min} = \max(\phi_{m1\_s2\_z3\_t\_L1} \times k_{s1}, h_{agg} + k_{s2}, 20\text{mm}) = 45.0$ mm

PASS - Actual bar spacing exceeds minimum allowable

Bottom bar spacing; $s_{bot} = (b - (2 \times (c_{nom\_s} + \phi_{m1\_s2\_z3\_v}) + \phi_{m1\_s2\_z3\_b\_L1} \times N_{m1\_s2\_z3\_b\_L1})) / (N_{m1\_s2\_z3\_b\_L1} - 1) = 182.0$ mm

Minimum allowable bottom bar spacing; $s_{bot,min} = \max(\phi_{m1\_s2\_z3\_b\_L1} \times k_{s1}, h_{agg} + k_{s2}, 20mm) = 25.0$ mm

PASS - Actual bar spacing exceeds minimum allowable

Shear design

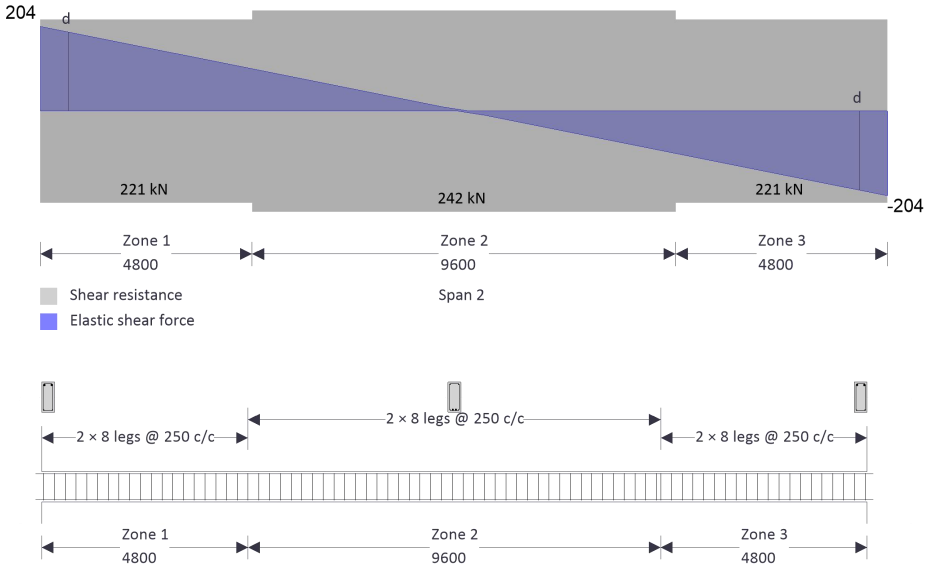

Angle of comp. shear strut for maximum shear; $\theta_{max} = 45$ deg

Strength reduction factor - cl.6.2.3(3); $v_1 = 0.6 \times (1 - f_{ck} / 250\ N/mm^2) = 0.516$

Compression chord coefficient - cl.6.2.3(3); $\alpha_{cw} = 1.00$

Minimum area of shear reinforcement - exp.9.5N; $A_{sv,min} = 0.08\ N/mm^2 \times b \times (f_{ck} / 1\ N/mm^2)^{0.5} / f_{yk} = 309\ mm^2/m$

Zone 1 (0 mm - 4800 mm) shear - section 6.2

Design shear force at support ; $V_{Ed,max} = \max(abs(V_{z1\_max}), abs(V_{z1\_red\_max})) = 204$ kN

Min lever arm in shear zone; $z = 550$ mm

Maximum design shear resistance - exp.6.9; $V_{Rd,max} = \alpha_{cw} \times b \times z \times v_1 \times f_{cwd} / (\cot(\theta_{max}) + \tan(\theta_{max})) = 993$ kN

PASS - Design shear force at support is less than maximum design shear resistance

Design shear force at 635mm from support; $V_{Ed} = 191$ kN

Design shear stress; $v_{Ed} = V_{Ed} / (b \times z) = 1.156$ N/mm^2

Angle of concrete compression strut - cl.6.2.3; $\theta = \min(\max(0.5 \times \text{Asin}(\min(2 \times v_{Ed} / (\alpha_{cw} \times f_{cwd} \times v_1),1)), 21.8 \text{ deg}), 45\text{deg}) = 21.8$ deg

Area of shear reinforcement required - exp.6.8; $A_{sv,des} = v_{Ed} \times b / (f_{yd} \times \cot(\theta)) = 347$ mm^2/m

Area of shear reinforcement required; $A_{sv,req} = \max(A_{sv,min}, A_{sv,des}) = 347$ mm^2/m

Shear reinforcement provided; 2 × 8 legs @ 250 c/c

Area of shear reinforcement provided; $A_{sv,prov} = 402$ mm^2/m

PASS - Area of shear reinforcement provided exceeds minimum required

Maximum longitudinal spacing - exp.9.6N; $s_{vl,max} = 0.75 \times d = 476$ mm

PASS - Longitudinal spacing of shear reinforcement provided is less than maximum

Zone 2 (4800 mm - 14400 mm) shear - section 6.2

Design shear force at support ; $V_{Ed,max} = \max(\text{abs}(V_{z2\_max}), \text{abs}(V_{z2\_red\_max})) = 102$ kN

Min lever arm in shear zone; $z = 602$ mm

Maximum design shear resistance - exp.6.9; $V_{Rd,max} = \alpha_{cw} \times b \times z \times v_1 \times f_{cwd} / (\cot(\theta_{max}) + \tan(\theta_{max})) = 1088$ kN

PASS - Design shear force at support is less than maximum design shear resistance

Design shear force within zone; $V_{Ed} = 102$ kN

Design shear stress; $v_{Ed} = V_{Ed} / (b \times z) = 0.564$ N/mm^2

Angle of concrete compression strut - cl.6.2.3; $\theta = \min(\max(0.5 \times \text{Asin}(\min(2 \times v_{Ed} / (\alpha_{cw} \times f_{cwd} \times v_1),1)), 21.8 \text{ deg}), 45\text{deg}) = 21.8$ deg

Area of shear reinforcement required - exp.6.8; $A_{sv,des} = v_{Ed} \times b / (f_{yd} \times \cot(\theta)) = 169$ mm^2/m

Area of shear reinforcement required; $A_{sv,req} = \max(A_{sv,min}, A_{sv,des}) = 309$ mm^2/m

Shear reinforcement provided; 2 × 8 legs @ 250 c/c

Area of shear reinforcement provided; $A_{sv,prov} = 402$ mm^2/m

PASS - Area of shear reinforcement provided exceeds minimum required

Maximum longitudinal spacing - exp.9.6N; $s_{vl,max} = 0.75 \times d = 481$ mm

PASS - Longitudinal spacing of shear reinforcement provided is less than maximum

Zone 3 (14400 mm - 19200 mm) shear - section 6.2

Design shear force at support ; $V_{Ed,max} = \max(\text{abs}(V_{z3\_max}), \text{abs}(V_{z3\_red\_max})) = 204$ kN

Min lever arm in shear zone; z = 550 mm

Maximum design shear resistance - exp.6.9; $V_{Rd,max} = \alpha_{cw} \times b \times z \times v_1 \times f_{cwd} / (\cot(\theta_{max}) + \tan(\theta_{max})) = 993$ kN

PASS - Design shear force at support is less than maximum design shear resistance

Design shear force at 635mm from support; $V_{Ed} = 191$ kN

Design shear stress; $v_{Ed} = V_{Ed} / (b \times z) = 1.156$ N/mm^2

Angle of concrete compression strut - cl.6.2.3; $\theta = \min(\max(0.5 \times \text{Asin}(\min(2 \times v_{Ed} / (\alpha_{cw} \times f_{cwd} \times v_1),1)), 21.8 \text{ deg}), 45\text{deg}) = 21.8$ deg

Area of shear reinforcement required - exp.6.8; $A_{sv,des} = v_{Ed} \times b / (f_{yd} \times \cot(\theta)) = 347$ mm^2/m

Area of shear reinforcement required; $A_{sv,req} = \max(A_{sv,min}, A_{sv,des}) = 347$ mm^2/m

Shear reinforcement provided; 2 × 8 legs @ 250 c/c

Area of shear reinforcement provided; $A_{sv,prov} = 402$ mm^2/m

PASS - Area of shear reinforcement provided exceeds minimum required

Maximum longitudinal spacing - exp.9.6N; $s_{vl,max} = 0.75 \times d = 476$ mm

PASS - Longitudinal spacing of shear reinforcement provided is less than maximum

APPENDIX G

CONCRETE RECTANGULAR BEAM INCREMENT RESULTS FROM ABAQUS

The following images are the increment results from Abaqus for the Concrete Rectangular Beam analysis.

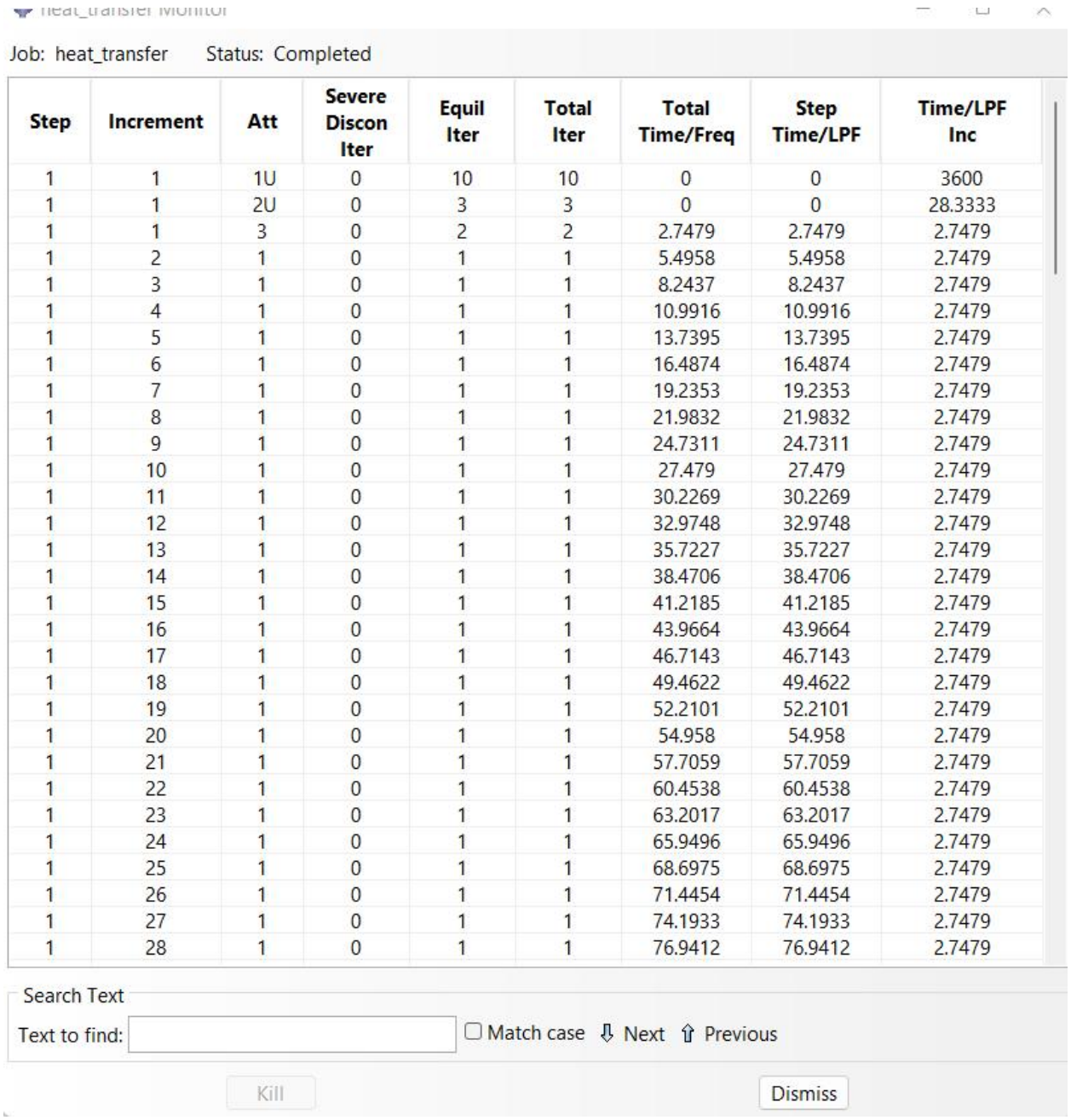

heat_transfer Monitor

Job: heat_transfer Status: Completed

Step	Increment	Att	Severe Discon Iter	Equil Iter	Total Iter	Total Time/Freq	Step Time/LPF	Time/LPF Inc
1	1	1U	0	10	10	0	0	3600
1	1	2U	0	3	3	0	0	28.3333
1	1	3	0	2	2	2.7479	2.7479	2.7479
1	2	1	0	1	1	5.4958	5.4958	2.7479
1	3	1	0	1	1	8.2437	8.2437	2.7479
1	4	1	0	1	1	10.9916	10.9916	2.7479
1	5	1	0	1	1	13.7395	13.7395	2.7479
1	6	1	0	1	1	16.4874	16.4874	2.7479
1	7	1	0	1	1	19.2353	19.2353	2.7479
1	8	1	0	1	1	21.9832	21.9832	2.7479
1	9	1	0	1	1	24.7311	24.7311	2.7479
1	10	1	0	1	1	27.479	27.479	2.7479
1	11	1	0	1	1	30.2269	30.2269	2.7479
1	12	1	0	1	1	32.9748	32.9748	2.7479
1	13	1	0	1	1	35.7227	35.7227	2.7479
1	14	1	0	1	1	38.4706	38.4706	2.7479
1	15	1	0	1	1	41.2185	41.2185	2.7479
1	16	1	0	1	1	43.9664	43.9664	2.7479
1	17	1	0	1	1	46.7143	46.7143	2.7479
1	18	1	0	1	1	49.4622	49.4622	2.7479
1	19	1	0	1	1	52.2101	52.2101	2.7479
1	20	1	0	1	1	54.958	54.958	2.7479
1	21	1	0	1	1	57.7059	57.7059	2.7479
1	22	1	0	1	1	60.4538	60.4538	2.7479
1	23	1	0	1	1	63.2017	63.2017	2.7479
1	24	1	0	1	1	65.9496	65.9496	2.7479
1	25	1	0	1	1	68.6975	68.6975	2.7479
1	26	1	0	1	1	71.4454	71.4454	2.7479
1	27	1	0	1	1	74.1933	74.1933	2.7479
1	28	1	0	1	1	76.9412	76.9412	2.7479

Search Text

Text to find: Match case Next Previous

Kill Dismiss

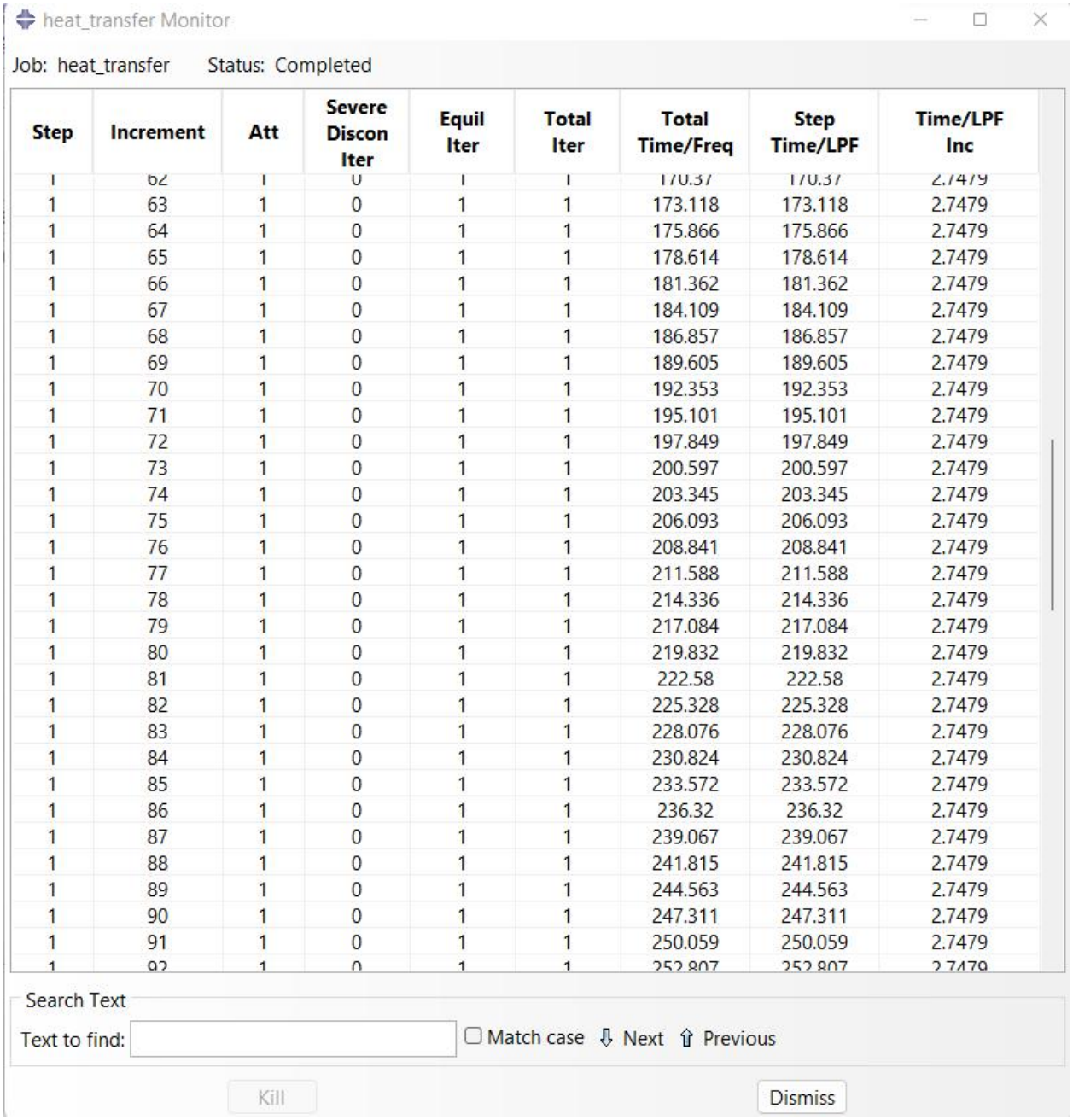

Step	Increment	Att	Severe Discon Iter	Equil Iter	Total Iter	Total Time/Freq	Step Time/LPF	Time/LPF Inc
1	62	1	0	1	1	170.37	170.37	2.7479
1	63	1	0	1	1	173.118	173.118	2.7479
1	64	1	0	1	1	175.866	175.866	2.7479
1	65	1	0	1	1	178.614	178.614	2.7479
1	66	1	0	1	1	181.362	181.362	2.7479
1	67	1	0	1	1	184.109	184.109	2.7479
1	68	1	0	1	1	186.857	186.857	2.7479
1	69	1	0	1	1	189.605	189.605	2.7479
1	70	1	0	1	1	192.353	192.353	2.7479
1	71	1	0	1	1	195.101	195.101	2.7479
1	72	1	0	1	1	197.849	197.849	2.7479
1	73	1	0	1	1	200.597	200.597	2.7479
1	74	1	0	1	1	203.345	203.345	2.7479
1	75	1	0	1	1	206.093	206.093	2.7479
1	76	1	0	1	1	208.841	208.841	2.7479
1	77	1	0	1	1	211.588	211.588	2.7479
1	78	1	0	1	1	214.336	214.336	2.7479
1	79	1	0	1	1	217.084	217.084	2.7479
1	80	1	0	1	1	219.832	219.832	2.7479
1	81	1	0	1	1	222.58	222.58	2.7479
1	82	1	0	1	1	225.328	225.328	2.7479
1	83	1	0	1	1	228.076	228.076	2.7479
1	84	1	0	1	1	230.824	230.824	2.7479
1	85	1	0	1	1	233.572	233.572	2.7479
1	86	1	0	1	1	236.32	236.32	2.7479
1	87	1	0	1	1	239.067	239.067	2.7479
1	88	1	0	1	1	241.815	241.815	2.7479
1	89	1	0	1	1	244.563	244.563	2.7479
1	90	1	0	1	1	247.311	247.311	2.7479
1	91	1	0	1	1	250.059	250.059	2.7479
1	92	1	0	1	1	252.807	252.807	2.7479

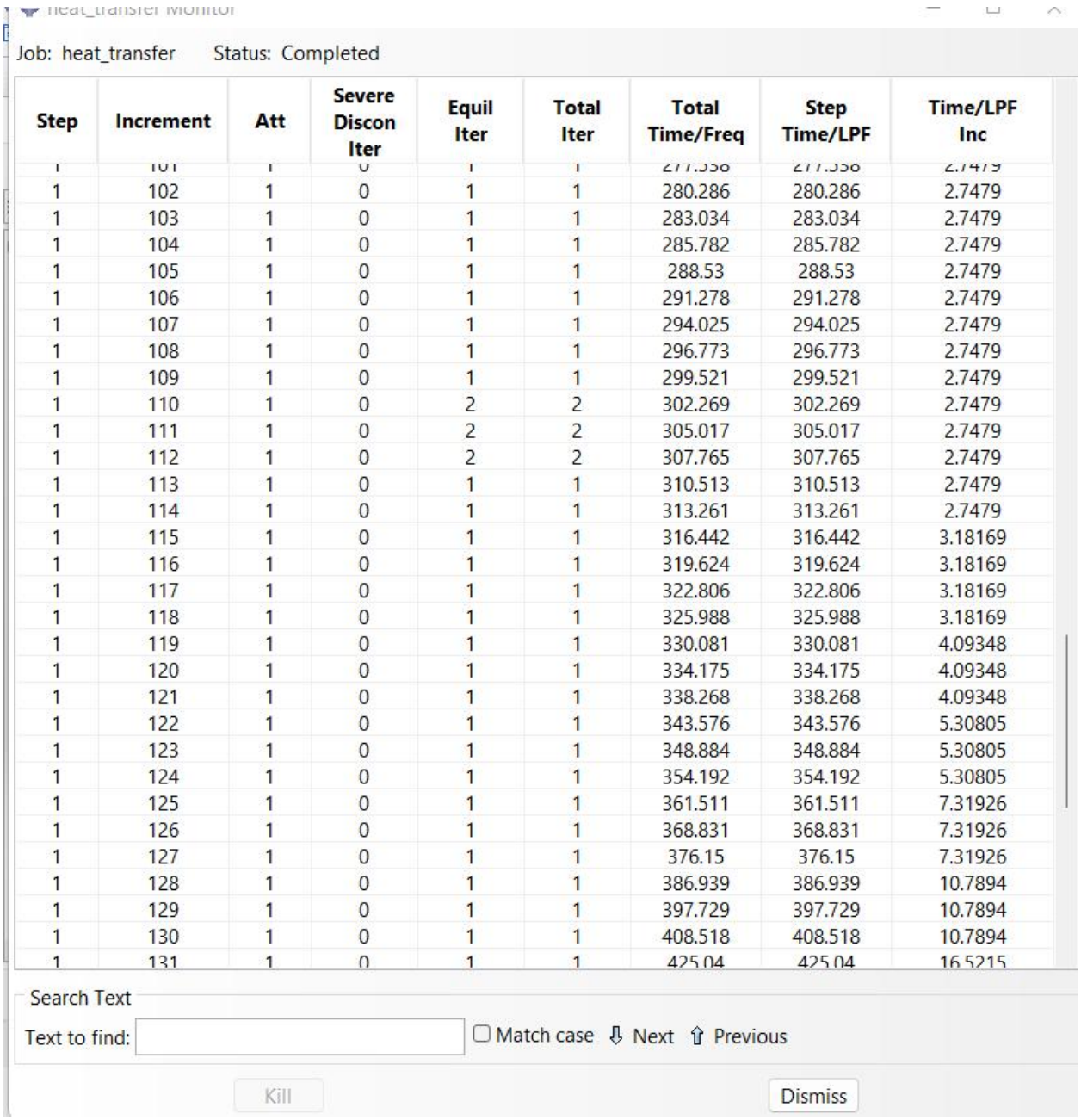

heat_transfer Monitor

Job: heat_transfer Status: Completed

Step	Increment	Att	Severe Discon Iter	Equil Iter	Total Iter	Total Time/Freq	Step Time/LPF	Time/LPF Inc
1	101	1	0	1	1	277.358	277.358	2.7479
1	102	1	0	1	1	280.286	280.286	2.7479
1	103	1	0	1	1	283.034	283.034	2.7479
1	104	1	0	1	1	285.782	285.782	2.7479
1	105	1	0	1	1	288.53	288.53	2.7479
1	106	1	0	1	1	291.278	291.278	2.7479
1	107	1	0	1	1	294.025	294.025	2.7479
1	108	1	0	1	1	296.773	296.773	2.7479
1	109	1	0	1	1	299.521	299.521	2.7479
1	110	1	0	2	2	302.269	302.269	2.7479
1	111	1	0	2	2	305.017	305.017	2.7479
1	112	1	0	2	2	307.765	307.765	2.7479
1	113	1	0	1	1	310.513	310.513	2.7479
1	114	1	0	1	1	313.261	313.261	2.7479
1	115	1	0	1	1	316.442	316.442	3.18169
1	116	1	0	1	1	319.624	319.624	3.18169
1	117	1	0	1	1	322.806	322.806	3.18169
1	118	1	0	1	1	325.988	325.988	3.18169
1	119	1	0	1	1	330.081	330.081	4.09348
1	120	1	0	1	1	334.175	334.175	4.09348
1	121	1	0	1	1	338.268	338.268	4.09348
1	122	1	0	1	1	343.576	343.576	5.30805
1	123	1	0	1	1	348.884	348.884	5.30805
1	124	1	0	1	1	354.192	354.192	5.30805
1	125	1	0	1	1	361.511	361.511	7.31926
1	126	1	0	1	1	368.831	368.831	7.31926
1	127	1	0	1	1	376.15	376.15	7.31926
1	128	1	0	1	1	386.939	386.939	10.7894
1	129	1	0	1	1	397.729	397.729	10.7894
1	130	1	0	1	1	408.518	408.518	10.7894
1	131	1	0	1	1	425.04	425.04	16.5215

Search Text

Text to find: Match case Next Previous

Kill Dismiss

heat_transfer Monitor

Job: heat_transfer Status: Completed

Step	Increment	Att	Severe Discon Iter	Equil Iter	Total Iter	Total Time/Freq	Step Time/LPF	Time/LPF Inc
1	128	1	0	1	1	386.939	386.939	10.7894
1	129	1	0	1	1	397.729	397.729	10.7894
1	130	1	0	1	1	408.518	408.518	10.7894
1	131	1	0	1	1	425.04	425.04	16.5215
1	132	1	0	1	1	441.561	441.561	16.5215
1	133	1	0	1	1	458.083	458.083	16.5215
1	134	1	0	1	1	481.484	481.484	23.401
1	135	1	0	1	1	504.885	504.885	23.401
1	136	1	0	1	1	528.286	528.286	23.401
1	137	1	0	1	1	555.409	555.409	27.1234
1	138	1	0	1	1	582.533	582.533	27.1234
1	139	1	0	2	2	609.656	609.656	27.1234
1	140	1	0	2	2	636.779	636.779	27.1234
1	141	1	0	1	1	663.903	663.903	27.1234
1	142	1	0	1	1	707.627	707.627	43.7241
1	143	1	0	1	1	751.351	751.351	43.7241
1	144	1	0	1	1	795.075	795.075	43.7241
1	145	1	0	1	1	857.896	857.896	62.8209
1	146	1	0	2	2	920.717	920.717	62.8209
1	147	1	0	2	2	983.538	983.538	62.8209
1	148	1	0	1	1	1046.36	1046.36	62.8209
1	149	1	0	1	1	1170.08	1170.08	123.72
1	150	1	0	2	2	1293.8	1293.8	123.72
1	151	1	0	2	2	1417.52	1417.52	123.72
1	152	1	0	2	2	1603.1	1603.1	185.579
1	153	1	0	2	2	1881.47	1881.47	278.369
1	154	1	0	2	2	2159.83	2159.83	278.369
1	155	1	0	2	2	2577.39	2577.39	417.553
1	156	1	0	2	2	3203.72	3203.72	626.33
1	157	1	0	3	3	3600	3600	396.282

Search Text

Text to find: Match case Next Previous

Kill Dismiss

APPENDIX H

COMPOSITE GIRDER ANALYSIS AND DESIGN

In accordance with EN1992-1-1:2004 incorporating Corrigenda January 2008 and the recommended values

Analysis

Geometry (m) - Concrete (C35 2500 Quartzite)

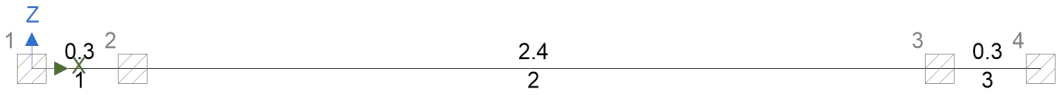

Span	Length (m)	Section	Start Support	End Support
1	0.3	R 300x700	Fixed	Fixed
2	2.4	R 2400x300	Fixed	Fixed
3	0.3	R 300x700	Fixed	Fixed
R 300x700: A = 2100 cm^2, I_y = 857500 cm^4, I_z = 157500 cm^4, A_y = 1750 cm^2, A_z = 1750 cm^2				
R 2400x300: A = 7200 cm^2, I_y = 540000 cm^4, I_z = 3.×10^7 cm^4, A_y = 6000 cm^2, A_z = 6000 cm^2				
Concrete (C35 2500 Quartzite): Density 2500 kg/m^3, Youngs 34.0771462 kN/mm^2, Shear 14.1988109 kN/mm^2, Thermal 0.00001 $°C^{-1}$				

Loading

Self weight included

Permanent - Loading (kN/m)

Imposed - Loading (kN/m)

Load combination factors

Load combination	Self Weight	Permanent	Imposed	LoadCase 4
1.35G + 1.5Q + 1.5RQ (Strength)	1.35	1.35	1.50	1.35
1.0G + 1.0Q + 1.0RQ (Service)	1.00	1.00	1.00	1.00
1.0G + 1.0ψ_2Q (Quasi)	1.00	1.00	0.30	1.00

Member Loads

Member	Load case	Load Type	Orientation	Description
Beam	Permanent	UDL	GlobalZ	0.5 kN/m
Beam	Imposed	UDL	GlobalZ	0.5 kN/m

Results; Forces

Strength combinations - Moment envelope (kNm)

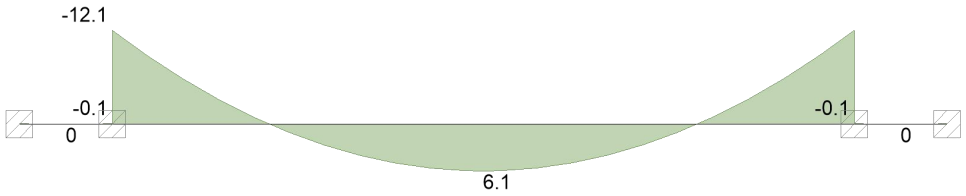

Strength combinations - Shear envelope (kN)

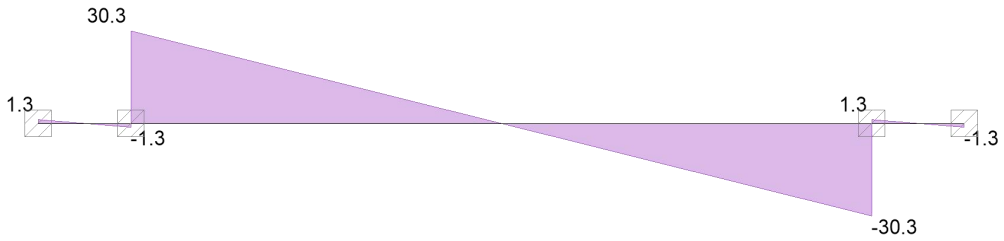

Concrete details - Concrete strength class; C35/45

Aggregate type; Quartzite

Aggregate adjustment factor - cl.3.1.3(2); AAF = 1.0

Characteristic compressive cylinder strength; f_{ck} = 35 N/mm^2

Mean value of compressive cylinder strength; $f_{cm} = f_{ck}$ + 8 N/mm^2 = 43 N/mm^2

Mean value of axial tensile strength; f_{ctm} = 0.3 N/mm^2 × (f_{ck}/ 1 N/mm^2)$^{2/3}$ = 3.2 N/mm^2

Secant modulus of elasticity of concrete; $E_{cm} = 22\ kN/mm^2 \times [f_{cm}/10\ N/mm^2]^{0.3} \times AAF = 34077\ N/mm^2$

Ultimate strain - Table 3.1; $\varepsilon_{cu2} = 0.0035$

Shortening strain - Table 3.1; $\varepsilon_{cu3} = 0.0035$

Effective compression zone height factor; $\lambda = 0.80$

Effective strength factor; $\eta = 1.00$

Coefficient k_1; $k_1 = 0.44$

Coefficient k_2; $k_2 = 1.25 \times (0.6 + 0.0014 / \varepsilon_{cu2}) = 1.25$

Coefficient k_3; $k_3 = 0.54$

Coefficient k_4; $k_4 = 1.25 \times (0.6 + 0.0014 / \varepsilon_{cu2}) = 1.25$

Partial factor for concrete -Table 2.1N; $\gamma_C = 1.50$

Compressive strength coefficient - cl.3.1.6(1); $\alpha_{cc} = 1.00$

Design compressive concrete strength - exp.3.15; $f_{cd} = \alpha_{cc} \times f_{ck} / \gamma_C = 23.3\ N/mm^2$

Compressive strength coefficient - cl.3.1.6(1); $\alpha_{ccw} = 1.00$

Design compressive concrete strength - exp.3.15; $f_{cwd} = \alpha_{ccw} \times f_{ck} / \gamma_C = 23.3\ N/mm^2$

Maximum aggregate size; $h_{agg} = 20\ mm$

Monolithic simple support moment factor; $\beta_1 = 0.15$

Reinforcement details

Characteristic yield strength of reinforcement; $f_{yk} = 460\ N/mm^2$

Partial factor for reinforcing steel - Table 2.1N; $\gamma_S = 1.15$

Design yield strength of reinforcement; $f_{yd} = f_{yk} / \gamma_S = 400\ N/mm^2$

Nominal cover to reinforcement

Nominal cover to top reinforcement; $c_{nom\_t} = 35\ mm$

Nominal cover to bottom reinforcement; $c_{nom\_b} = 35\ mm$

Nominal cover to side reinforcement;c_{nom_s} = 35 mm

Fire resistance

Standard fire resistance period; R = 60 min

Number of sides exposed to fire; 3

Minimum width of beam - EN1992-1-2 Table 5.6; b_{min} = 120 mm

Beam - Span 1

Rectangular section details

Section width; b = 300 mm

Section depth; h = 700 mm

PASS - Minimum dimensions for fire resistance met

Moment design

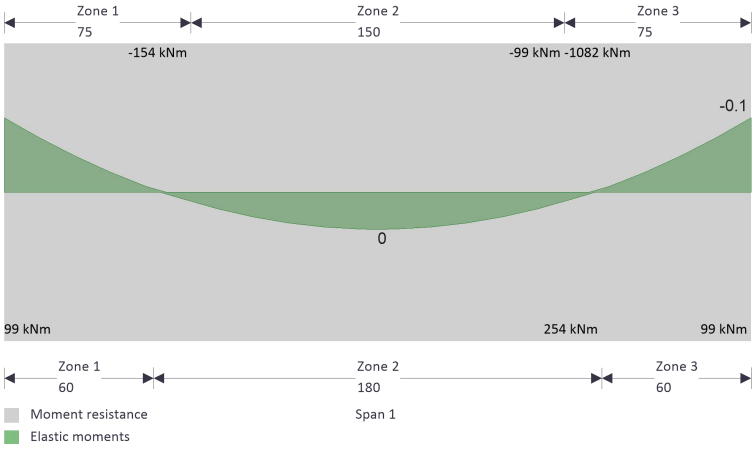

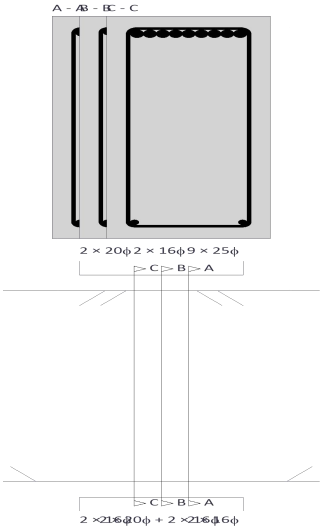

Zone 1 (0 mm - 75 mm) Negative moment - section 6.1

Design bending moment; $M = \max(\beta_1 \times \text{abs}(M_{m1\_s1\_max\_red}), \text{abs}(M_{m1\_s1\_z1\_min\_red})) = 0.1$ kNm

Effective depth of tension reinforcement; $d = 647$ mm

Redistribution ratio; $\delta = \min(M_{neg\_red\_z1} / M_{neg\_z1}, 1) = 1.000$

$K = M / (b \times d^2 \times f_{ck}) = 0.000$

$K' = (2 \times \eta \times \alpha_{cc} / \gamma_C) \times (1 - \lambda \times (\delta - k_1) / (2 \times k_2)) \times (\lambda \times (\delta - k_1) / (2 \times k_2)) = 0.196$

K' > K - No compression reinforcement is required

Lever arm; $z = \min(0.5 \times d \times [1 + (1 - 2 \times K / (\eta \times \alpha_{cc} / \gamma_C))^{0.5}], 0.95 \times d) = 615$ mm

Depth of neutral axis; $x = 2 \times (d - z) / \lambda = 81$ mm

Area of tension reinforcement required; $A_{s,req} = M / (f_{yd} \times z) = 0$ mm^2

Tension reinforcement provided; $2 \times 20\phi$

Area of tension reinforcement provided; $A_{s,prov} = 628$ mm^2

Minimum area of reinforcement - exp.9.1N; $A_{s,min} = \max(0.26 \times f_{ctm} / f_{yk}, 0.0013) \times b \times d = 352$ mm^2

Maximum area of reinforcement - cl.9.2.1.1(3); $A_{s,max} = 0.04 \times b \times h = 8400$ mm^2

PASS - Area of reinforcement provided is greater than area of reinforcement required

Crack control - Section 7.3

Maximum crack width; $w_k = 0.3$ mm

Design value modulus of elasticity reinf – 3.2.7(4); $E_s = 200000$ N/mm^2

Mean value of concrete tensile strength; $f_{ct,eff} = f_{ctm} = 3.2$ N/mm^2

Stress distribution coefficient; $k_c = 0.4$

Non-uniform self-equilibrating stress coefficient; $k = \min(\max(1 + (300 \text{ mm} - \min(h, b)) \times 0.35 / 500 \text{ mm}, 0.65), 1) = 1.00$

Actual tension bar spacing; $s_{bar} = (b - (2 \times (c_{nom\_s} + \phi_{m1\_s1\_z1\_v}) + \phi_{m1\_s1\_z1\_t\_L1} \times N_{m1\_s1\_z1\_t\_L1})) / (N_{m1\_s1\_z1\_t\_L1} - 1) + \phi_{m1\_s1\_z1\_t\_L1} = 194$ mm

Maximum stress permitted - Table 7.3N; $\sigma_s = 245$ N/mm^2

Steel to concrete modulus of elast. ratio; $\alpha_{cr} = E_s / E_{cm} = 5.87$

Distance of the Elastic NA from bottom of beam; $y = (b \times h^2 / 2 + A_{s,prov} \times (\alpha_{cr} - 1) \times (h - d)) / (b \times h + A_{s,prov} \times (\alpha_{cr} - 1)) = 346$ mm

Area of concrete in the tensile zone; $A_{ct} = b \times y = 103721$ mm^2

Minimum area of reinforcement required - exp.7.1; $A_{sc,min} = k_c \times k \times f_{ct,eff} \times A_{ct} / \sigma_s = 544$ mm^2

PASS - Area of tension reinforcement provided exceeds minimum required for crack control

Quasi-permanent moment; $M_{QP} = \max(\beta_1 \times \text{abs}(M_{m1_s1_z2_pos_quasi}), \text{abs}(M_{m1_s1_z1_neg_quasi})) = 0.0$kNm

Permanent load ratio; $R_{PL} = M_{QP} / M = 0.69$

Service stress in reinforcement; $\sigma_{sr} = f_{yd} \times A_{s,req} / A_{s,prov} \times R_{PL} = 0$ N/mm^2

Maximum bar spacing - Tables 7.3N;$s_{bar,max} = 300$ mm

PASS - Maximum bar spacing exceeds actual bar spacing for crack control

Minimum bar spacing (Section 8.2)

Top bar spacing; $s_{top} = (b - (2 \times (c_{nom\_s} + \phi_{m1\_s1\_z1\_v}) + \phi_{m1\_s1\_z1\_t\_L1} \times N_{m1\_s1\_z1\_t\_L1})) / (N_{m1\_s1\_z1\_t\_L1} - 1) = 174.0$ mm

Minimum allowable top bar spacing; $s_{top,min} = \max(\phi_{m1\_s1\_z1\_t\_L1} \times k_{s1}, h_{agg} + k_{s2}, 20\text{mm}) = 25.0$ mm

PASS - Actual bar spacing exceeds minimum allowable

Bottom bar spacing; $s_{bot} = (b - (2 \times (c_{nom\_s} + \phi_{m1\_s1\_z1\_v}) + \phi_{m1\_s1\_z1\_b\_L1} \times N_{m1\_s1\_z1\_b\_L1})) / (N_{m1\_s1\_z1\_b\_L1} - 1) = 182.0$ mm

Minimum allowable bottom bar spacing; $s_{bot,min} = \max(\phi_{m1\_s1\_z1\_b\_L1} \times k_{s1}, h_{agg} + k_{s2}, 20\text{mm}) = 25.0$ mm

PASS - Actual bar spacing exceeds minimum allowable

Zone 2 (60 mm - 240 mm) Positive moment - section 6.1

Design bending moment; $M = abs(M_{m1\_s1\_z2\_max\_red}) = 0.0$ kNm

Effective depth of tension reinforcement; $d = 648$ mm

Redistribution ratio; $\delta = \min(M_{pos\_red\_z2} / M_{pos\_z2}, 1) = 1.000$

$K = M / (b \times d^2 \times f_{ck}) = 0.000$

$K' = (2 \times \eta \times \alpha_{cc} / \gamma_C) \times (1 - \lambda \times (\delta - k_1) / (2 \times k_2)) \times (\lambda \times (\delta - k_1) / (2 \times k_2)) = 0.196$

K' > K - No compression reinforcement is required

Lever arm; $z = \min(0.5 \times d \times [1 + (1 - 2 \times K / (\eta \times \alpha_{cc} / \gamma_C))^{0.5}], 0.95 \times d) = 615$ mm

Depth of neutral axis; $x = 2 \times (d - z) / \lambda = 81$ mm

Area of tension reinforcement required; $A_{s,req} = M / (f_{yd} \times z) = 0$ mm^2

Tension reinforcement provided; $2 \times 20\phi + 2 \times 16\phi$

Area of tension reinforcement provided; $A_{s,prov} = 1030$ mm^2

Minimum area of reinforcement - exp.9.1N; $A_{s,min} = \max(0.26 \times f_{ctm} / f_{yk}, 0.0013) \times b \times d = 353$ mm^2

Maximum area of reinforcement - cl.9.2.1.1(3); $A_{s,max} = 0.04 \times b \times h = 8400$ mm^2

PASS - Area of reinforcement provided is greater than area of reinforcement required

Crack control - Section 7.3

Maximum crack width; $w_k = 0.3$ mm

Design value modulus of elasticity reinf – 3.2.7(4); $E_s = 200000$ N/mm^2

Mean value of concrete tensile strength; $f_{ct,eff} = f_{ctm} = 3.2$ N/mm^2

Stress distribution coefficient; $k_c = 0.4$

Non-uniform self-equilibrating stress coefficient; $k = \min(\max(1 + (300 \text{ mm} - \min(h, b)) \times 0.35 / 500 \text{ mm}, 0.65), 1) = 1.00$

Actual tension bar spacing; $s_{bar} = (b - (2 \times (c_{nom\_s} + \phi_{m1\_s1\_z2\_v}) + \phi_{m1\_s1\_z2\_b\_L1} \times N_{m1\_s1\_z2\_b\_L1} + \phi_{m1\_s1\_z1\_b\_L1} \times N_{m1\_s1\_z1\_b\_L1})) / ((N_{m1\_s1\_z2\_b\_L1} + N_{m1\_s1\_z1\_b\_L1}) - 1) + \phi_{m1\_s1\_z2\_b\_L1} = 67.3$ mm

Maximum stress permitted - Table 7.3N; $\sigma_s = 346$ N/mm^2

Steel to concrete modulus of elast. ratio; $\alpha_{cr} = E_s / E_{cm} = 5.87$

Distance of the Elastic NA from bottom of beam; $y = (b \times h^2 / 2 + A_{s,prov} \times (\alpha_{cr} - 1) \times (h - d)) / (b \times h + A_{s,prov} \times (\alpha_{cr} - 1)) = 343$ mm

Area of concrete in the tensile zone; $A_{ct} = b \times y = 102915$ mm^2

Minimum area of reinforcement required - exp.7.1; $A_{sc,min} = k_c \times k \times f_{ct,eff} \times A_{ct} / \sigma_s = 382$ mm^2

PASS - Area of tension reinforcement provided exceeds minimum required for crack control

Quasi-permanent moment; $M_{QP} = \text{abs}(M_{m1_s1_z2_pos_quasi}) = 0.0$kNm

Permanent load ratio; $R_{PL} = M_{QP} / M = 0.69$

Service stress in reinforcement; $\sigma_{sr} = f_{yd} \times A_{s,req} / A_{s,prov} \times R_{PL} = 0$ N/mm^2

Maximum bar spacing - Tables 7.3N; $s_{bar,max} = 300$ mm

PASS - Maximum bar spacing exceeds actual bar spacing for crack control

Deflection control - Section 7.4

Reference reinforcement ratio; $\rho_{m0} = (f_{ck} / 1 \text{ N/mm}^2)^{0.5} / 1000 = 0.00592$

Required tension reinforcement ratio; $\rho_m = A_{s,req} / (b \times d) = 0.00000$

Required compression reinforcement ratio; $\rho'_m = A_{s2,req} / (b \times d) = 0.00000$

Structural system factor - Table 7.4N; $K_b = 1.3$

Basic allowable span to depth ratio ; $\text{span\_to\_depth}_{basic} = K_b \times [11 + 1.5 \times (f_{ck} / 1 \text{ N/mm}^2)^{0.5} \times \rho_{m0} / \rho_m + 3.2 \times (f_{ck} / 1 \text{ N/mm}^2)^{0.5} \times (\rho_{m0} / \rho_m - 1)^{1.5}] = 21150798.947$

Reinforcement factor - exp.7.17; $K_s = \min(A_{s,prov} / A_{s,req} \times 500 \text{ N/mm}^2 / f_{yk}, 1.5) = 1.500$

Flange width factor; $F1 = 1 = 1.000$

Long span supporting brittle partition factor; $F2 = 1 = 1.000$

Allowable span to depth ratio; $span\_to\_depth_{allow} = \min(span\_to\_depth_{basic} \times K_s \times F1 \times F2, 40 \times K_b) = 52.000$

Actual span to depth ratio; $span\_to\_depth_{actual} = L_{m1\_s1} / d = 0.463$

PASS - Actual span to depth ratio is within the allowable limit

Minimum bar spacing (Section 8.2)

Top bar spacing; $s_{top} = (b - (2 \times (c_{nom\_s} + \phi_{m1\_s1\_z2\_v}) + \phi_{m1\_s1\_z2\_t\_L1} \times N_{m1\_s1\_z2\_t\_L1})) / (N_{m1\_s1\_z2\_t\_L1} - 1) = 182.0$ mm

Minimum allowable top bar spacing; $s_{top,min} = \max(\phi_{m1\_s1\_z2\_t\_L1} \times k_{s1}, h_{agg} + k_{s2}, 20mm) = 25.0$ mm

PASS - Actual bar spacing exceeds minimum allowable

Bottom bar spacing; $s_{bot} = (b - (2 \times (c_{nom\_s} + \phi_{m1\_s1\_z2\_v}) + \phi_{m1\_s1\_z2\_b\_L1} \times N_{m1\_s1\_z2\_b\_L1} + \phi_{m1\_s1\_z1\_b\_L1} \times N_{m1\_s1\_z1\_b\_L1})) / ((N_{m1\_s1\_z2\_b\_L1} + N_{m1\_s1\_z1\_b\_L1}) - 1) = 47.3$ mm

Minimum allowable bottom bar spacing; $s_{bot,min} = \max(\phi_{m1\_s1\_z2\_b\_L1} \times k_{s1}, h_{agg} + k_{s2}, 20mm) = 25.0$ mm

PASS - Actual bar spacing exceeds minimum allowable

Zone 3 (225 mm - 300 mm) Negative moment - section 6.1

Design bending moment; $M = abs(M_{m1\_s1\_z3\_min\_red}) = 0.1$ kNm

Effective depth of tension reinforcement; $d = 645$ mm

Redistribution ratio; $\delta = \min(M_{neg\_red\_z3} / M_{neg\_z3}, 1) = 1.000$

$K = M / (b \times d^2 \times f_{ck}) = 0.000$

$K' = (2 \times \eta \times \alpha_{cc} / \gamma_C) \times (1 - \lambda \times (\delta - k_1) / (2 \times k_2)) \times (\lambda \times (\delta - k_1) / (2 \times k_2)) = 0.196$

K' > K - No compression reinforcement is required

Lever arm; $z = \min(0.5 \times d \times [1 + (1 - 2 \times K / (\eta \times \alpha_{cc} / \gamma_C))^{0.5}], 0.95 \times d) = 612$ mm

Depth of neutral axis; $x = 2 \times (d - z) / \lambda = 81$ mm

Area of tension reinforcement required; $A_{s,req} = M / (f_{yd} \times z) = 0$ mm^2

Tension reinforcement provided; $9 \times 25\phi$

Area of tension reinforcement provided; $A_{s,prov} = 4418$ mm^2

Minimum area of reinforcement - exp.9.1N; $A_{s,min} = \max(0.26 \times f_{ctm} / f_{yk}, 0.0013) \times b \times d = 351$ mm^2

Maximum area of reinforcement - cl.9.2.1.1(3); $A_{s,max} = 0.04 \times b \times h = 8400$ mm^2

PASS - Area of reinforcement provided is greater than area of reinforcement required

Crack control - Section 7.3

Maximum crack width; $w_k = 0.3$ mm

Design value modulus of elasticity reinf – 3.2.7(4); $E_s = 200000$ N/mm^2

Mean value of concrete tensile strength; $f_{ct,eff} = f_{ctm} = 3.2$ N/mm^2

Stress distribution coefficient; $k_c = 0.4$

Non-uniform self-equilibrating stress coefficient; $k = \min(\max(1 + (300 \text{ mm} - \min(h, b)) \times 0.35 / 500 \text{ mm}, 0.65), 1) = 1.00$

Actual tension bar spacing; $s_{bar} = (b - (2 \times (c_{nom\_s} + \phi_{m1\_s1\_z3\_v}) + \phi_{m1\_s1\_z3\_t\_L1} \times N_{m1\_s1\_z3\_t\_L1})) / (N_{m1\_s1\_z3\_t\_L1} - 1) + \phi_{m1\_s1\_z3\_t\_L1} = 23.6$ mm

Maximum stress permitted - Table 7.3N; $\sigma_s = 360$ N/mm^2

Steel to concrete modulus of elast. ratio; $\alpha_{cr} = E_s / E_{cm} = 5.87$

Distance of the Elastic NA from bottom of beam; $y = (b \times h^2 / 2 + A_{s,prov} \times (\alpha_{cr} - 1) \times (h - d)) / (b \times h + A_{s,prov} \times (\alpha_{cr} - 1)) = 323$ mm

Area of concrete in the tensile zone; $A_{ct} = b \times y = 96791$ mm^2

Minimum area of reinforcement required - exp.7.1; $A_{sc,min} = k_c \times k \times f_{ct,eff} \times A_{ct} / \sigma_s = 345$ mm^2

PASS - Area of tension reinforcement provided exceeds minimum required for crack control

Quasi-permanent moment; $M_{QP} = \text{abs}(M_{m1_s1_z3_neg_quasi}) = 0.0$kNm

Permanent load ratio; $R_{PL} = M_{QP} / M = 0.69$

Service stress in reinforcement; $\sigma_{sr} = f_{yd} \times A_{s,req} / A_{s,prov} \times R_{PL} = 0$ N/mm^2

Maximum bar spacing - Tables 7.3N; $s_{bar,max} = 300$ mm

PASS - Maximum bar spacing exceeds actual bar spacing for crack control

Minimum bar spacing (Section 8.2)

Top bar spacing; $s_{top} = (b - (2 \times (c_{nom\_s} + \phi_{m1\_s1\_z3\_v}) + \phi_{m1\_s1\_z3\_t\_L1} \times N_{m1\_s1\_z3\_t\_L1})) / (N_{m1\_s1\_z3\_t\_L1} - 1) = -1.4$ mm

Minimum allowable top bar spacing; $s_{top,min} = \max(\phi_{m1\_s1\_z3\_t\_L1} \times k_{s1}, h_{agg} + k_{s2}, 20mm) = 25.0$ mm

Bottom bar spacing; $s_{bot} = (b - (2 \times (c_{nom\_s} + \phi_{m1\_s1\_z3\_v}) + \phi_{m1\_s1\_z3\_b\_L1} \times N_{m1\_s1\_z3\_b\_L1})) / (N_{m1\_s1\_z3\_b\_L1} - 1) = 182.0$ mm

Minimum allowable bottom bar spacing; $s_{bot,min} = \max(\phi_{m1\_s1\_z3\_b\_L1} \times k_{s1}, h_{agg} + k_{s2}, 20mm) = 25.0$ mm

PASS - Actual bar spacing exceeds minimum allowable

Shear design

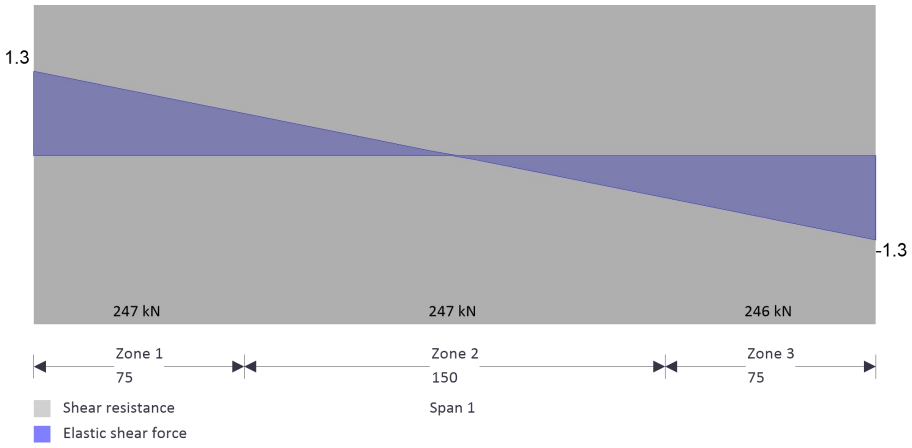

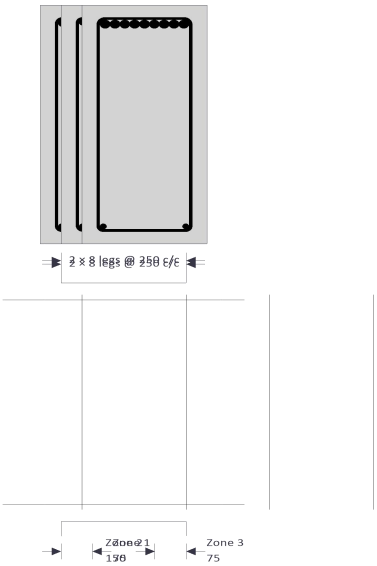

Angle of comp. shear strut for maximum shear; $\theta_{max} = 45$ deg

Strength reduction factor - cl.6.2.3(3); $v_1 = 0.6 \times (1 - f_{ck} / 250\ N/mm^2) = 0.516$

Compression chord coefficient - cl.6.2.3(3); $\alpha_{cw} = 1.00$

Minimum area of shear reinforcement - exp.9.5N; $A_{sv,min} = 0.08\ N/mm^2 \times b \times (f_{ck} / 1\ N/mm^2)^{0.5} / f_{yk} = 309\ mm^2/m$

Zone 1 (0 mm - 75 mm) shear - section 6.2

Design shear force at support ; $V_{Ed,max} = \max(\text{abs}(V_{z1\_max}), \text{abs}(V_{z1\_red\_max})) = 39$ kN

Min lever arm in shear zone; $z = 615$ mm

Maximum design shear resistance - exp.6.9; $V_{Rd,max} = \alpha_{cw} \times b \times z \times v_1 \times f_{cwd} / (\cot(\theta_{max}) + \tan(\theta_{max})) = 1110$ kN

PASS - Design shear force at support is less than maximum design shear resistance

Design shear force at support; $V_{Ed} = 39$ kN

Design shear stress; $v_{Ed} = V_{Ed} / (b \times z) = 0.211\ N/mm^2$

Angle of concrete compression strut - cl.6.2.3; $\theta = \min(\max(0.5 \times \text{Asin}(\min(2 \times v_{Ed} / (\alpha_{cw} \times f_{cwd} \times v_1),1)), 21.8\ \text{deg}), 45\text{deg}) = 21.8$ deg

Area of shear reinforcement required - exp.6.8; $A_{sv,des} = v_{Ed} \times b / (f_{yd} \times \cot(\theta)) = 63\ mm^2/m$

Area of shear reinforcement required; $A_{sv,req} = \max(A_{sv,min}, A_{sv,des}) = 309$ mm^2/m

Shear reinforcement provided; 2 × 8 legs @ 250 c/c

Area of shear reinforcement provided; $A_{sv,prov} = 402$ mm^2/m

PASS - Area of shear reinforcement provided exceeds minimum required

Maximum longitudinal spacing - exp.9.6N; $s_{vl,max} = 0.75 \times d = 485$ mm

PASS - Longitudinal spacing of shear reinforcement provided is less than maximum

Zone 2 (75 mm - 225 mm) shear - section 6.2

Design shear force at support ; $V_{Ed,max} = \max(\text{abs}(V_{z2\_max}), \text{abs}(V_{z2\_red\_max})) = 41$ kN

Min lever arm in shear zone; z = 615 mm

Maximum design shear resistance - exp.6.9; $V_{Rd,max} = \alpha_{cw} \times b \times z \times v_1 \times f_{cwd} / (\cot(\theta_{max}) + \tan(\theta_{max})) = 1111$ kN

PASS - Design shear force at support is less than maximum design shear resistance

Design shear force within zone; $V_{Ed} = 41$ kN

Design shear stress; $v_{Ed} = V_{Ed} / (b \times z) = 0.221$ N/mm^2

Angle of concrete compression strut - cl.6.2.3; $\theta = \min(\max(0.5 \times \text{Asin}(\min(2 \times v_{Ed} / (\alpha_{cw} \times f_{cwd} \times v_1),1)), 21.8 \text{ deg}), 45\text{deg}) = 21.8$ deg

Area of shear reinforcement required - exp.6.8; $A_{sv,des} = v_{Ed} \times b / (f_{yd} \times \cot(\theta)) = 66$ mm^2/m

Area of shear reinforcement required; $A_{sv,req} = \max(A_{sv,min}, A_{sv,des}) = 309$ mm^2/m

Shear reinforcement provided; 2 × 8 legs @ 250 c/c

Area of shear reinforcement provided; $A_{sv,prov} = 402$ mm^2/m

PASS - Area of shear reinforcement provided exceeds minimum required

Maximum longitudinal spacing - exp.9.6N; $s_{vl,max} = 0.75 \times d = 486$ mm

PASS - Longitudinal spacing of shear reinforcement provided is less than maximum

Zone 3 (225 mm - 300 mm) shear - section 6.2

Design shear force at support ; $V_{Ed,max} = \max(\text{abs}(V_{z3\_max}), \text{abs}(V_{z3\_red\_max})) = 41$ kN

Min lever arm in shear zone; $z = 612$ mm

Maximum design shear resistance - exp.6.9; $V_{Rd,max} = \alpha_{cw} \times b \times z \times v_1 \times f_{cwd} / (\cot(\theta_{max}) + \tan(\theta_{max})) = 1106$ kN

PASS - Design shear force at support is less than maximum design shear resistance

Design shear force at support; $V_{Ed} = 41$ kN

Design shear stress; $v_{Ed} = V_{Ed} / (b \times z) = 0.226$ N/mm^2

Angle of concrete compression strut - cl.6.2.3; $\theta = \min(\max(0.5 \times \text{Asin}(\min(2 \times v_{Ed} / (\alpha_{cw} \times f_{cwd} \times v_1),1)), 21.8 \text{ deg}), 45\text{deg}) = 21.8$ deg

Area of shear reinforcement required - exp.6.8; $A_{sv,des} = v_{Ed} \times b / (f_{yd} \times \cot(\theta)) = 68$ mm^2/m

Area of shear reinforcement required; $A_{sv,req} = \max(A_{sv,min}, A_{sv,des}) = 309$ mm^2/m

Shear reinforcement provided; 2 × 8 legs @ 250 c/c

Area of shear reinforcement provided; $A_{sv,prov} = 402$ mm^2/m

PASS - Area of shear reinforcement provided exceeds minimum required

Maximum longitudinal spacing - exp.9.6N; $s_{vl,max} = 0.75 \times d = 483$ mm

PASS - Longitudinal spacing of shear reinforcement provided is less than maximum

Beam - Span 2

Rectangular section details

Section width; $b = 2400$ mm

Section depth; $h = 300$ mm

PASS - Minimum dimensions for fire resistance met

Moment design

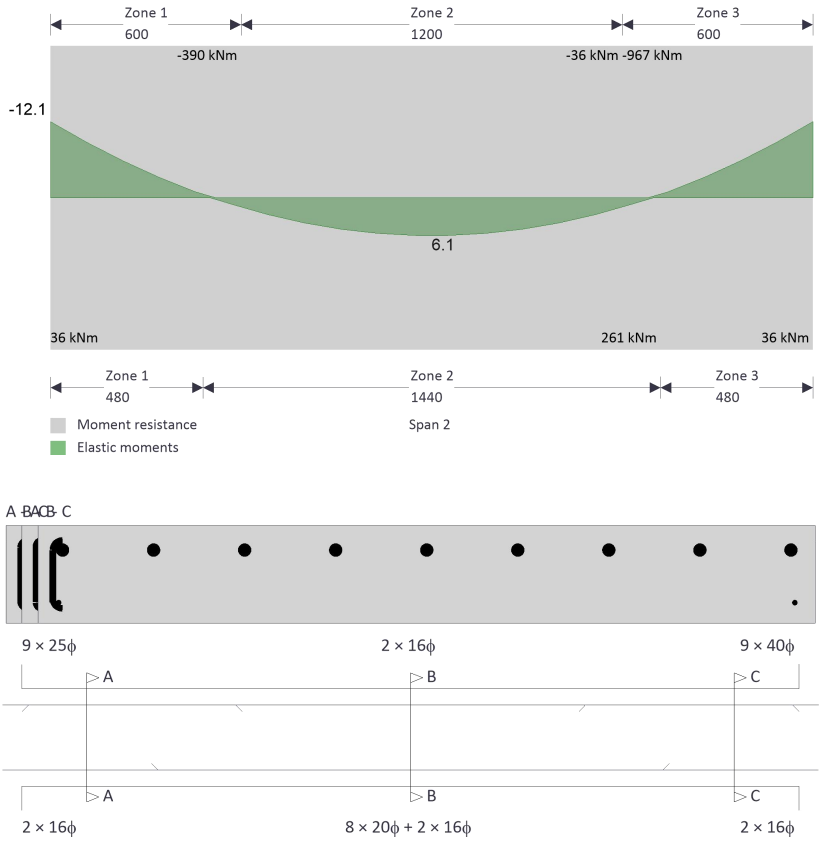

Zone 1 (0 mm - 600 mm) Negative moment - section 6.1

Design bending moment; $M = abs(M_{m1\_s2\_z1\_min\_red}) = 12.1$ kNm

Effective depth of tension reinforcement; $d = 232$ mm

Redistribution ratio; $\delta = min(M_{neg\_red\_z1} / M_{neg\_z1}, 1) = 1.000$

$K = M / (b \times d^2 \times f_{ck}) = 0.003$

$K' = (2 \times \eta \times \alpha_{cc} / \gamma_C) \times (1 - \lambda \times (\delta - k_1) / (2 \times k_2)) \times (\lambda \times (\delta - k_1) / (2 \times k_2)) = 0.196$

K' > K - No compression reinforcement is required

Lever arm; $z = min(0.5 \times d \times [1 + (1 - 2 \times K / (\eta \times \alpha_{cc} / \gamma_C))^{0.5}], 0.95 \times d) = 221$ mm

Depth of neutral axis; $x = 2 \times (d - z) / \lambda = 29$ mm

Area of tension reinforcement required; $A_{s,req} = M / (f_{yd} \times z) = 137$ mm^2

Tension reinforcement provided; $9 \times 25\phi$

Area of tension reinforcement provided; $A_{s,prov} = 4418$ mm^2

Minimum area of reinforcement - exp.9.1N; $A_{s,min} = \max(0.26 \times f_{ctm} / f_{yk}, 0.0013) \times b \times d = 1012\ mm^2$

Maximum area of reinforcement - cl.9.2.1.1(3); $A_{s,max} = 0.04 \times b \times h = 28800\ mm^2$

PASS - Area of reinforcement provided is greater than area of reinforcement required

Crack control - Section 7.3

Maximum crack width; $w_k = 0.3\ mm$

Design value modulus of elasticity reinf – 3.2.7(4); $E_s = 200000\ N/mm^2$

Mean value of concrete tensile strength; $f_{ct,eff} = f_{ctm} = 3.2\ N/mm^2$

Stress distribution coefficient; $k_c = 0.4$

Non-uniform self-equilibrating stress coefficient; $k = \min(\max(1 + (300\ mm - \min(h, b)) \times 0.35 / 500\ mm, 0.65), 1) = 1.00$

Actual tension bar spacing; $s_{bar} = (b - (2 \times (c_{nom\_s} + \phi_{m1\_s2\_z1\_v}) + \phi_{m1\_s2\_z1\_t\_L1} \times N_{m1\_s2\_z1\_t\_L1})) / (N_{m1\_s2\_z1\_t\_L1} - 1) + \phi_{m1\_s2\_z1\_t\_L1} = 283.1\ mm$

Maximum stress permitted - Table 7.3N; $\sigma_s = 174\ N/mm^2$

Steel to concrete modulus of elast. ratio; $\alpha_{cr} = E_s / E_{cm} = 5.87$

Distance of the Elastic NA from bottom of beam; $y = (b \times h^2 / 2 + A_{s,prov} \times (\alpha_{cr} - 1) \times (h - d)) / (b \times h + A_{s,prov} \times (\alpha_{cr} - 1)) = 148\ mm$

Area of concrete in the tensile zone; $A_{ct} = b \times y = 354256\ mm^2$

Minimum area of reinforcement required - exp.7.1; $A_{sc,min} = k_c \times k \times f_{ct,eff} \times A_{ct} / \sigma_s = 2622\ mm^2$

PASS - Area of tension reinforcement provided exceeds minimum required for crack control

Quasi-permanent moment; $M_{QP} = \text{abs}(M_{m1\_s2\_z1\_neg\_quasi}) = 8.8kNm$

Permanent load ratio; $R_{PL} = M_{QP} / M = 0.72$

Service stress in reinforcement; $\sigma_{sr} = f_{yd} \times A_{s,req} / A_{s,prov} \times R_{PL} = 9\ N/mm^2$

Maximum bar spacing - Tables 7.3N; $s_{bar,max} = 300\ mm$

PASS - Maximum bar spacing exceeds actual bar spacing for crack control

Minimum bar spacing (Section 8.2)

Top bar spacing; $s_{top} = (b - (2 \times (c_{nom\_s} + \phi_{m1\_s2\_z1\_v}) + \phi_{m1\_s2\_z1\_t\_L1} \times N_{m1\_s2\_z1\_t\_L1})) / (N_{m1\_s2\_z1\_t\_L1} - 1) = 258.1$ mm

Minimum allowable top bar spacing; $s_{top,min} = \max(\phi_{m1\_s2\_z1\_t\_L1} \times k_{s1}, h_{agg} + k_{s2}, 20mm) = 25.0$ mm

PASS - Actual bar spacing exceeds minimum allowable

Bottom bar spacing; $s_{bot} = (b - (2 \times (c_{nom\_s} + \phi_{m1\_s2\_z1\_v}) + \phi_{m1\_s2\_z1\_b\_L1} \times N_{m1\_s2\_z1\_b\_L1})) / (N_{m1\_s2\_z1\_b\_L1} - 1) = 2258.0$ mm

Minimum allowable bottom bar spacing; $s_{bot,min} = \max(\phi_{m1\_s2\_z1\_b\_L1} \times k_{s1}, h_{agg} + k_{s2}, 20mm) = 25.0$ mm

PASS - Actual bar spacing exceeds minimum allowable

Zone 2 (480 mm - 1920 mm) Positive moment - section 6.1

Design bending moment; $M = \text{abs}(M_{m1\_s2\_z2\_max\_red}) = 6.1$ kNm

Effective depth of tension reinforcement; $d = 235$ mm

Redistribution ratio; $\delta = \min(M_{pos\_red\_z2} / M_{pos\_z2}, 1) = 1.000$

$K = M / (b \times d^2 \times f_{ck}) = 0.001$

$K' = (2 \times \eta \times \alpha_{cc} / \gamma_C) \times (1 - \lambda \times (\delta - k_1) / (2 \times k_2)) \times (\lambda \times (\delta - k_1) / (2 \times k_2)) = 0.196$

K' > K - No compression reinforcement is required

Lever arm; $z = \min(0.5 \times d \times [1 + (1 - 2 \times K / (\eta \times \alpha_{cc} / \gamma_C))^{0.5}], 0.95 \times d) = 224$ mm

Depth of neutral axis; $x = 2 \times (d - z) / \lambda = 29$ mm

Area of tension reinforcement required; $A_{s,req} = M / (f_{yd} \times z) = 68$ mm^2

Tension reinforcement provided; $8 \times 20\phi + 2 \times 16\phi$

Area of tension reinforcement provided; $A_{s,prov} = 2915$ mm^2

Minimum area of reinforcement - exp.9.1N; $A_{s,min} = \max(0.26 \times f_{ctm} / f_{yk}, 0.0013) \times b \times d = 1024\ mm^2$

Maximum area of reinforcement - cl.9.2.1.1(3); $A_{s,max} = 0.04 \times b \times h = 28800\ mm^2$

PASS - Area of reinforcement provided is greater than area of reinforcement required

Crack control - Section 7.3

Maximum crack width; $w_k = 0.3\ mm$

Design value modulus of elasticity reinf – 3.2.7(4); $E_s = 200000\ N/mm^2$

Mean value of concrete tensile strength; $f_{ct,eff} = f_{ctm} = 3.2\ N/mm^2$

Stress distribution coefficient; $k_c = 0.4$

Non-uniform self-equilibrating stress coefficient; $k = \min(\max(1 + (300\ mm - \min(h, b)) \times 0.35 / 500\ mm, 0.65), 1) = 1.00$

Actual tension bar spacing; $s_{bar} = (b - (2 \times (c_{nom\_s} + \phi_{m1\_s2\_z2\_v}) + \phi_{m1\_s2\_z2\_b\_L1} \times N_{m1\_s2\_z2\_b\_L1} + \phi_{m1\_s2\_z1\_b\_L1} \times N_{m1\_s2\_z1\_b\_L1})) / ((N_{m1\_s2\_z2\_b\_L1} + N_{m1\_s2\_z1\_b\_L1}) - 1) + \phi_{m1\_s2\_z2\_b\_L1} = 253.1\ mm$

Maximum stress permitted - Table 7.3N; $\sigma_s = 198\ N/mm^2$

Steel to concrete modulus of elast. ratio; $\alpha_{cr} = E_s / E_{cm} = 5.87$

Distance of the Elastic NA from bottom of beam; $y = (b \times h^2 / 2 + A_{s,prov} \times (\alpha_{cr} - 1) \times (h - d)) / (b \times h + A_{s,prov} \times (\alpha_{cr} - 1)) = 148\ mm$

Area of concrete in the tensile zone; $A_{ct} = b \times y = 356043\ mm^2$

Minimum area of reinforcement required - exp.7.1; $A_{sc,min} = k_c \times k \times f_{ct,eff} \times A_{ct} / \sigma_s = 2315\ mm^2$

PASS - Area of tension reinforcement provided exceeds minimum required for crack control

Quasi-permanent moment; $M_{QP} = \text{abs}(M_{m1\_s2\_z2\_pos\_quasi}) = 4.4kNm$

Permanent load ratio; $R_{PL} = M_{QP} / M = 0.72$

Service stress in reinforcement; $\sigma_{sr} = f_{yd} \times A_{s,req} / A_{s,prov} \times R_{PL} = 7\ N/mm^2$

Maximum bar spacing - Tables 7.3N;$s_{bar,max}$ = 300 mm

PASS - Maximum bar spacing exceeds actual bar spacing for crack control

Deflection control - Section 7.4

Reference reinforcement ratio; $\rho_{m0} = (f_{ck} / 1\ N/mm^2)^{0.5} / 1000 = 0.00592$

Required tension reinforcement ratio; $\rho_m = A_{s,req} / (b \times d) = 0.00012$

Required compression reinforcement ratio; $\rho'_m = A_{s2,req} / (b \times d) = 0.00000$

Structural system factor - Table 7.4N; $K_b = 1.5$

Basic allowable span to depth ratio ; $span\_to\_depth_{basic} = K_b \times [11 + 1.5 \times (f_{ck} / 1\ N/mm^2)^{0.5} \times \rho_{m0} / \rho_m + 3.2 \times (f_{ck} / 1\ N/mm^2)^{0.5} \times (\rho_{m0} / \rho_m - 1)^{1.5}] = 10197.116$

Reinforcement factor - exp.7.17; $K_s = \min(A_{s,prov} / A_{s,req} \times 500\ N/mm^2 / f_{yk}, 1.5) = 1.500$

Flange width factor; F1 = 1 = 1.000

Long span supporting brittle partition factor; F2 = 1 = 1.000

Allowable span to depth ratio; $span\_to\_depth_{allow} = \min(span\_to\_depth_{basic} \times K_s \times F1 \times F2, 40 \times K_b) = 60.000$

Actual span to depth ratio; $span\_to\_depth_{actual} = L_{m1\_s2} / d = 10.201$

PASS - Actual span to depth ratio is within the allowable limit

Minimum bar spacing (Section 8.2)

Top bar spacing; $s_{top} = (b - (2 \times (c_{nom\_s} + \phi_{m1\_s2\_z2\_v}) + \phi_{m1\_s2\_z2\_t\_L1} \times N_{m1\_s2\_z2\_t\_L1})) / (N_{m1\_s2\_z2\_t\_L1} - 1) = 2258.0$ mm

Minimum allowable top bar spacing; $s_{top,min} = \max(\phi_{m1\_s2\_z2\_t\_L1} \times k_{s1}, h_{agg} + k_{s2}, 20mm) = 25.0$ mm

PASS - Actual bar spacing exceeds minimum allowable

Bottom bar spacing; $s_{bot} = (b - (2 \times (c_{nom\_s} + \phi_{m1\_s2\_z2\_v}) + \phi_{m1\_s2\_z2\_b\_L1} \times N_{m1\_s2\_z2\_b\_L1} + \phi_{m1\_s2\_z1\_b\_L1} \times N_{m1\_s2\_z1\_b\_L1})) / ((N_{m1\_s2\_z2\_b\_L1} + N_{m1\_s2\_z1\_b\_L1}) - 1) = 233.1$ mm

Minimum allowable bottom bar spacing; $s_{bot,min} = \max(\phi_{m1\_s2\_z2\_b\_L1} \times k_{s1}, h_{agg} + k_{s2}, 20mm) = 25.0$ mm

PASS - Actual bar spacing exceeds minimum allowable

Zone 3 (1800 mm - 2400 mm) Negative moment - section 6.1

Design bending moment; $M = \text{abs}(M_{m1\_s2\_z3\_min\_red}) = 12.1$ kNm

Effective depth of tension reinforcement; $d = 225$ mm

Redistribution ratio; $\delta = \min(M_{neg\_red\_z3} / M_{neg\_z3}, 1) = 1.000$

$K = M / (b \times d^2 \times f_{ck}) = 0.003$

$K' = (2 \times \eta \times \alpha_{cc} / \gamma_C) \times (1 - \lambda \times (\delta - k_1) / (2 \times k_2)) \times (\lambda \times (\delta - k_1) / (2 \times k_2)) = 0.196$

K' > K - No compression reinforcement is required

Lever arm; $z = \min(0.5 \times d \times [1 + (1 - 2 \times K / (\eta \times \alpha_{cc} / \gamma_C))^{0.5}], 0.95 \times d) = 214$ mm

Depth of neutral axis; $x = 2 \times (d - z) / \lambda = 28$ mm

Area of tension reinforcement required; $A_{s,req} = M / (f_{yd} \times z) = 142$ mm^2

Tension reinforcement provided; $9 \times 40\phi$

Area of tension reinforcement provided; $A_{s,prov} = 11310$ mm^2

Minimum area of reinforcement - exp.9.1N; $A_{s,min} = \max(0.26 \times f_{ctm} / f_{yk}, 0.0013) \times b \times d = 980$ mm^2

Maximum area of reinforcement - cl.9.2.1.1(3); $A_{s,max} = 0.04 \times b \times h = 28800$ mm^2

PASS - Area of reinforcement provided is greater than area of reinforcement required

Crack control - Section 7.3

Maximum crack width; $w_k = 0.3$ mm

Design value modulus of elasticity reinf – 3.2.7(4); $E_s = 200000$ N/mm^2

Mean value of concrete tensile strength; $f_{ct,eff} = f_{ctm} = 3.2$ N/mm^2

Stress distribution coefficient; $k_c = 0.4$

Non-uniform self-equilibrating stress coefficient; $k = \min(\max(1 + (300\ mm - \min(h, b)) \times 0.35 / 500\ mm, 0.65), 1) = 1.00$

Actual tension bar spacing; $s_{bar} = (b - (2 \times (c_{nom\_s} + \phi_{m1\_s2\_z3\_v}) + \phi_{m1\_s2\_z3\_t\_L1} \times N_{m1\_s2\_z3\_t\_L1})) / (N_{m1\_s2\_z3\_t\_L1} - 1) + \phi_{m1\_s2\_z3\_t\_L1} = 281.3\ mm$

Maximum stress permitted - Table 7.3N; $\sigma_s = 175\ N/mm^2$

Steel to concrete modulus of elast. ratio; $\alpha_{cr} = E_s / E_{cm} = 5.87$

Distance of the Elastic NA from bottom of beam; $y = (b \times h^2 / 2 + A_{s,prov} \times (\alpha_{cr} - 1) \times (h - d)) / (b \times h + A_{s,prov} \times (\alpha_{cr} - 1)) = 145\ mm$

Area of concrete in the tensile zone; $A_{ct} = b \times y = 347211\ mm^2$

Minimum area of reinforcement required - exp.7.1; $A_{sc,min} = k_c \times k \times f_{ct,eff} \times A_{ct} / \sigma_s = 2548\ mm^2$

PASS - Area of tension reinforcement provided exceeds minimum required for crack control

Quasi-permanent moment; $M_{QP} = \text{abs}(M_{m1\_s2\_z3\_neg\_quasi}) = 8.8kNm$

Permanent load ratio; $R_{PL} = M_{QP} / M = 0.72$

Service stress in reinforcement; $\sigma_{sr} = f_{yd} \times A_{s,req} / A_{s,prov} \times R_{PL} = 4\ N/mm^2$

Maximum bar spacing - Tables 7.3N; $s_{bar,max} = 300\ mm$

PASS - Maximum bar spacing exceeds actual bar spacing for crack control

Minimum bar spacing (Section 8.2)

Top bar spacing; $s_{top} = (b - (2 \times (c_{nom\_s} + \phi_{m1\_s2\_z3\_v}) + \phi_{m1\_s2\_z3\_t\_L1} \times N_{m1\_s2\_z3\_t\_L1})) / (N_{m1\_s2\_z3\_t\_L1} - 1) = 241.3\ mm$

Minimum allowable top bar spacing; $s_{top,min} = \max(\phi_{m1\_s2\_z3\_t\_L1} \times k_{s1}, h_{agg} + k_{s2}, 20mm) = 40.0\ mm$

PASS - Actual bar spacing exceeds minimum allowable

Bottom bar spacing; $s_{bot} = (b - (2 \times (c_{nom\_s} + \phi_{m1\_s2\_z3\_v}) + \phi_{m1\_s2\_z3\_b\_L1} \times N_{m1\_s2\_z3\_b\_L1})) / (N_{m1\_s2\_z3\_b\_L1} - 1) = 2258.0\ mm$

Minimum allowable bottom bar spacing; $s_{bot,min} = \max(\phi_{m1\_s2\_z3\_b\_L1} \times k_{s1}, h_{agg} + k_{s2}, 20mm) = 25.0$ mm

PASS - Actual bar spacing exceeds minimum allowable

Shear design

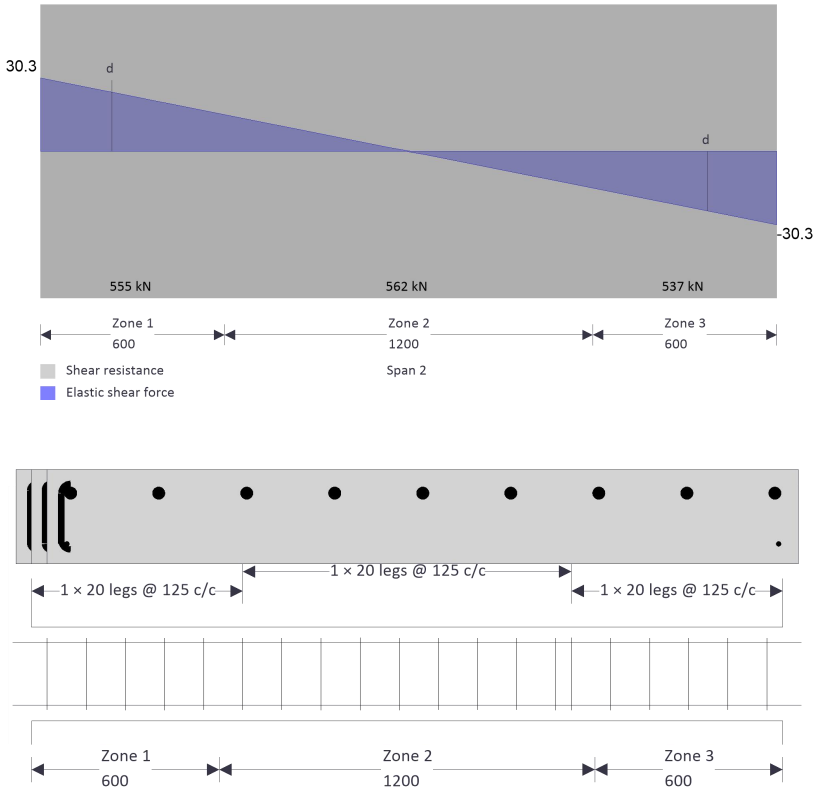

Angle of comp. shear strut for maximum shear; $\theta_{max} = 45$ deg

Strength reduction factor - cl.6.2.3(3); $v_1 = 0.6 \times (1 - f_{ck} / 250\ N/mm^2) = 0.516$

Compression chord coefficient - cl.6.2.3(3); $\alpha_{cw} = 1.00$

Minimum area of shear reinforcement - exp.9.5N; $A_{sv,min} = 0.08\ N/mm^2 \times b \times (f_{ck} / 1\ N/mm^2)^{0.5} / f_{yk} = 2469\ mm^2/m$

Zone 1 (0 mm - 600 mm) shear - section 6.2

Design shear force at support ; $V_{Ed,max} = \max(abs(V_{z1\_max}), abs(V_{z1\_red\_max})) = 35$ kN

Min lever arm in shear zone; $z = 221$ mm

Maximum design shear resistance - exp.6.9; $V_{Rd,max} = \alpha_{cw} \times b \times z \times v_1 \times f_{cwd} / (\cot(\theta_{max}) + \tan(\theta_{max})) = 3191$ kN

PASS - Design shear force at support is less than maximum design shear resistance

Design shear force at 232mm from support; $V_{Ed} = 29$ kN

Design shear stress; $v_{Ed} = V_{Ed} / (b \times z) = 0.056$ N/mm^2

Angle of concrete compression strut - cl.6.2.3; $\theta = \min(\max(0.5 \times \text{Asin}(\min(2 \times v_{Ed} / (\alpha_{cw} \times f_{cwd} \times v_1),1)), 21.8 \text{ deg}), 45\text{deg}) = 21.8$ deg

Area of shear reinforcement required - exp.6.8; $A_{sv,des} = v_{Ed} \times b / (f_{yd} \times \cot(\theta)) = 133$ mm^2/m

Area of shear reinforcement required; $A_{sv,req} = \max(A_{sv,min}, A_{sv,des}) = 2469$ mm^2/m

Shear reinforcement provided; 1 × 20 legs @ 125 c/c

Area of shear reinforcement provided; $A_{sv,prov} = 2513$ mm^2/m

PASS - Area of shear reinforcement provided exceeds minimum required

Maximum longitudinal spacing - exp.9.6N; $s_{vl,max} = 0.75 \times d = 174$ mm

PASS - Longitudinal spacing of shear reinforcement provided is less than maximum

Zone 2 (600 mm - 1800 mm) shear - section 6.2

Design shear force at support ; $V_{Ed,max} = \max(\text{abs}(V_{z2\_max}), \text{abs}(V_{z2\_red\_max})) = 20$ kN

Min lever arm in shear zone; $z = 224$ mm

Maximum design shear resistance - exp.6.9; $V_{Rd,max} = \alpha_{cw} \times b \times z \times v_1 \times f_{cwd} / (\cot(\theta_{max}) + \tan(\theta_{max})) = 3229$ kN

PASS - Design shear force at support is less than maximum design shear resistance

Design shear force within zone; $V_{Ed} = 20$ kN

Design shear stress; $v_{Ed} = V_{Ed} / (b \times z) = 0.038$ N/mm^2

Angle of concrete compression strut - cl.6.2.3; $\theta = \min(\max(0.5 \times \text{Asin}(\min(2 \times v_{Ed} / (\alpha_{cw} \times f_{cwd} \times v_1),1)), 21.8 \text{ deg}), 45\text{deg}) = 21.8$ deg

Area of shear reinforcement required - exp.6.8; $A_{sv,des} = v_{Ed} \times b / (f_{yd} \times \cot(\theta)) = 90$ mm^2/m

Area of shear reinforcement required; $A_{sv,req} = \max(A_{sv,min}, A_{sv,des}) = 2469$ mm^2/m

Shear reinforcement provided; 1 × 20 legs @ 125 c/c

Area of shear reinforcement provided; $A_{sv,prov} = 2513$ mm^2/m

PASS - Area of shear reinforcement provided exceeds minimum required

Maximum longitudinal spacing - exp.9.6N; $s_{vl,max} = 0.75 \times d = 176$ mm

PASS - Longitudinal spacing of shear reinforcement provided is less than maximum

Zone 3 (1800 mm - 2400 mm) shear - section 6.2

Design shear force at support ; $V_{Ed,max} = \max(\text{abs}(V_{z3\_max}), \text{abs}(V_{z3\_red\_max})) = 30$ kN

Min lever arm in shear zone; $z = 214$ mm

Maximum design shear resistance - exp.6.9; $V_{Rd,max} = \alpha_{cw} \times b \times z \times v_1 \times f_{cwd} / (\cot(\theta_{max}) + \tan(\theta_{max})) = 3088$ kN

PASS - Design shear force at support is less than maximum design shear resistance

Design shear force at 225mm from support; $V_{Ed} = 25$ kN

Design shear stress; $v_{Ed} = V_{Ed} / (b \times z) = 0.048$ N/mm^2

Angle of concrete compression strut - cl.6.2.3; $\theta = \min(\max(0.5 \times \text{Asin}(\min(2 \times v_{Ed} / (\alpha_{cw} \times f_{cwd} \times v_1),1)), 21.8 \text{ deg}), 45\text{deg}) = 21.8$ deg

Area of shear reinforcement required - exp.6.8; $A_{sv,des} = v_{Ed} \times b / (f_{yd} \times \cot(\theta)) = 115$ mm^2/m

Area of shear reinforcement required; $A_{sv,req} = \max(A_{sv,min}, A_{sv,des}) = 2469$ mm^2/m

Shear reinforcement provided; 1 × 20 legs @ 125 c/c

Area of shear reinforcement provided; $A_{sv,prov} = 2513$ mm^2/m

PASS - Area of shear reinforcement provided exceeds minimum required

Maximum longitudinal spacing - exp.9.6N; $s_{vl,max} = 0.75 \times d = 169$ mm

PASS - Longitudinal spacing of shear reinforcement provided is less than maximum

Beam - Span 3

Rectangular section details

Section width; b = 300 mm

Section depth; h = 700 mm

PASS - Minimum dimensions for fire resistance met

Moment design

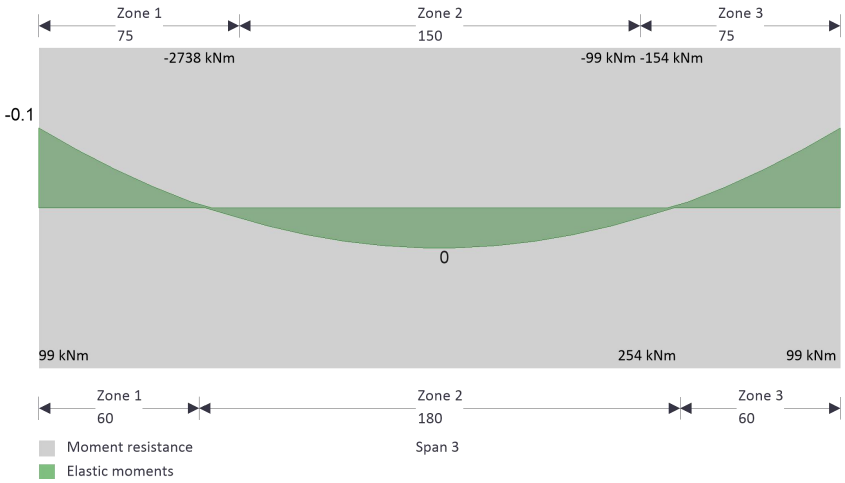

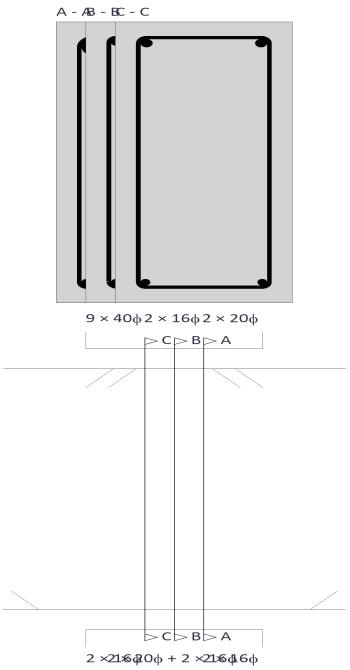

Zone 1 (0 mm - 75 mm) Negative moment - section 6.1

Design bending moment; $M = abs(M_{m1\_s3\_z1\_min\_red}) = 0.1$ kNm

Effective depth of tension reinforcement; d = 637 mm

Redistribution ratio; $\delta = \min(M_{neg\_red\_z1} / M_{neg\_z1}, 1) = 1.000$

$K = M / (b \times d^2 \times f_{ck}) = 0.000$

$K' = (2 \times \eta \times \alpha_{cc} / \gamma_C) \times (1 - \lambda \times (\delta - k_1) / (2 \times k_2)) \times (\lambda \times (\delta - k_1) / (2 \times k_2)) = 0.196$

K' > K - No compression reinforcement is required

Lever arm; $z = \min(0.5 \times d \times [1 + (1 - 2 \times K / (\eta \times \alpha_{cc} / \gamma_C))^{0.5}], 0.95 \times d) = 605$ mm

Depth of neutral axis; $x = 2 \times (d - z) / \lambda = 80$ mm

Area of tension reinforcement required; $A_{s,req} = M / (f_{yd} \times z) = 0$ mm^2

Tension reinforcement provided; $9 \times 40\phi$

Area of tension reinforcement provided; $A_{s,prov} = 11310$ mm^2

Minimum area of reinforcement - exp.9.1N; $A_{s,min} = \max(0.26 \times f_{ctm} / f_{yk}, 0.0013) \times b \times d = 347$ mm^2

Maximum area of reinforcement - cl.9.2.1.1(3); $A_{s,max} = 0.04 \times b \times h = 8400$ mm^2

Crack control - Section 7.3

Maximum crack width; $w_k = 0.3$ mm

Design value modulus of elasticity reinf – 3.2.7(4); $E_s = 200000$ N/mm^2

Mean value of concrete tensile strength; $f_{ct,eff} = f_{ctm} = 3.2$ N/mm^2

Stress distribution coefficient; $k_c = 0.4$

Non-uniform self-equilibrating stress coefficient; $k = \min(\max(1 + (300 \text{ mm} - \min(h, b)) \times 0.35 / 500 \text{ mm}, 0.65), 1) = 1.00$

Actual tension bar spacing; $s_{bar} = (b - (2 \times (c_{nom\_s} + \phi_{m1\_s3\_z1\_v}) + \phi_{m1\_s3\_z1\_t\_L1} \times N_{m1\_s3\_z1\_t\_L1})) / (N_{m1\_s3\_z1\_t\_L1} - 1) + \phi_{m1\_s3\_z1\_t\_L1} = 21.7$ mm

Maximum stress permitted - Table 7.3N; $\sigma_s = 360$ N/mm^2

Steel to concrete modulus of elast. ratio; $\alpha_{cr} = E_s / E_{cm} = 5.87$

Distance of the Elastic NA from bottom of beam; $y = (b \times h^2 / 2 + A_{s,prov} \times (\alpha_{cr} - 1) \times (h - d)) / (b \times h + A_{s,prov} \times (\alpha_{cr} - 1)) = 290$ mm

Area of concrete in the tensile zone; $A_{ct} = b \times y = 87113\ mm^2$

Minimum area of reinforcement required - exp.7.1; $A_{sc,min} = k_c \times k \times f_{ct,eff} \times A_{ct} / \sigma_s = 311\ mm^2$

PASS - Area of tension reinforcement provided exceeds minimum required for crack control

Quasi-permanent moment; $M_{QP} = abs(M_{m1\_s3\_z1\_neg\_quasi}) = 0.0kNm$

Permanent load ratio; $R_{PL} = M_{QP} / M = 0.69$

Service stress in reinforcement; $\sigma_{sr} = f_{yd} \times A_{s,req} / A_{s,prov} \times R_{PL} = 0\ N/mm^2$

Maximum bar spacing - Tables 7.3N;$s_{bar,max} = 300\ mm$

PASS - Maximum bar spacing exceeds actual bar spacing for crack control

Minimum bar spacing (Section 8.2)

Top bar spacing; $s_{top} = (b - (2 \times (c_{nom\_s} + \phi_{m1\_s3\_z1\_v}) + \phi_{m1\_s3\_z1\_t\_L1} \times N_{m1\_s3\_z1\_t\_L1})) / (N_{m1\_s3\_z1\_t\_L1} - 1) = -18.3\ mm$

Minimum allowable top bar spacing; $s_{top,min} = max(\phi_{m1\_s3\_z1\_t\_L1} \times k_{s1}, h_{agg} + k_{s2}, 20mm) = 40.0\ mm$

Bottom bar spacing; $s_{bot} = (b - (2 \times (c_{nom\_s} + \phi_{m1\_s3\_z1\_v}) + \phi_{m1\_s3\_z1\_b\_L1} \times N_{m1\_s3\_z1\_b\_L1})) / (N_{m1\_s3\_z1\_b\_L1} - 1) = 182.0\ mm$

Minimum allowable bottom bar spacing; $s_{bot,min} = max(\phi_{m1\_s3\_z1\_b\_L1} \times k_{s1}, h_{agg} + k_{s2}, 20mm) = 25.0\ mm$

PASS - Actual bar spacing exceeds minimum allowable

Zone 2 (60 mm - 240 mm) Positive moment - section 6.1

Design bending moment; $M = abs(M_{m1\_s3\_z2\_max\_red}) = 0.0\ kNm$

Effective depth of tension reinforcement; $d = 648\ mm$

Redistribution ratio; $\delta = min(M_{pos\_red\_z2} / M_{pos\_z2}, 1) = 1.000$

$K = M / (b \times d^2 \times f_{ck}) = 0.000$

$K' = (2 \times \eta \times \alpha_{cc} / \gamma_C) \times (1 - \lambda \times (\delta - k_1) / (2 \times k_2)) \times (\lambda \times (\delta - k_1) / (2 \times k_2)) = 0.196$

K' > K - No compression reinforcement is required

Lever arm; $z = \min(0.5 \times d \times [1 + (1 - 2 \times K / (\eta \times \alpha_{cc} / \gamma_C))^{0.5}], 0.95 \times d) = 615$ mm

Depth of neutral axis; $x = 2 \times (d - z) / \lambda = 81$ mm

Area of tension reinforcement required; $A_{s,req} = M / (f_{yd} \times z) = 0$ mm^2

Tension reinforcement provided; $2 \times 20\phi + 2 \times 16\phi$

Area of tension reinforcement provided; $A_{s,prov} = 1030$ mm^2

Minimum area of reinforcement - exp.9.1N; $A_{s,min} = \max(0.26 \times f_{ctm} / f_{yk}, 0.0013) \times b \times d = 353$ mm^2

Maximum area of reinforcement - cl.9.2.1.1(3); $A_{s,max} = 0.04 \times b \times h = 8400$ mm^2

PASS - Area of reinforcement provided is greater than area of reinforcement required

Crack control - Section 7.3

Maximum crack width; $w_k = 0.3$ mm

Design value modulus of elasticity reinf – 3.2.7(4); $E_s = 200000$ N/mm^2

Mean value of concrete tensile strength; $f_{ct,eff} = f_{ctm} = 3.2$ N/mm^2

Stress distribution coefficient; $k_c = 0.4$

Non-uniform self-equilibrating stress coefficient; $k = \min(\max(1 + (300 \text{ mm} - \min(h, b)) \times 0.35 / 500 \text{ mm}, 0.65), 1) = 1.00$

Actual tension bar spacing; $s_{bar} = (b - (2 \times (c_{nom\_s} + \phi_{m1\_s3\_z2\_v}) + \phi_{m1\_s3\_z2\_b\_L1} \times N_{m1\_s3\_z2\_b\_L1} + \phi_{m1\_s3\_z1\_b\_L1} \times N_{m1\_s3\_z1\_b\_L1})) / ((N_{m1\_s3\_z2\_b\_L1} + N_{m1\_s3\_z1\_b\_L1}) - 1) + \phi_{m1\_s3\_z2\_b\_L1} = 67.3$ mm

Maximum stress permitted - Table 7.3N; $\sigma_s = 346$ N/mm^2

Steel to concrete modulus of elast. ratio; $\alpha_{cr} = E_s / E_{cm} = 5.87$

Distance of the Elastic NA from bottom of beam; $y = (b \times h^2 / 2 + A_{s,prov} \times (\alpha_{cr} - 1) \times (h - d)) / (b \times h + A_{s,prov} \times (\alpha_{cr} - 1)) = 343$ mm

Area of concrete in the tensile zone; $A_{ct} = b \times y = 102915$ mm^2

Minimum area of reinforcement required - exp.7.1; $A_{sc,min} = k_c \times k \times f_{ct,eff} \times A_{ct} / \sigma_s = 382$ mm^2

PASS - Area of tension reinforcement provided exceeds minimum required for crack control

Quasi-permanent moment; $M_{QP} = abs(M_{m1\_s3\_z2\_pos\_quasi}) = 0.0kNm$

Permanent load ratio; $R_{PL} = M_{QP} / M = 0.69$

Service stress in reinforcement; $\sigma_{sr} = f_{yd} \times A_{s,req} / A_{s,prov} \times R_{PL} = 0$ N/mm^2

Maximum bar spacing - Tables 7.3N;$s_{bar,max} = 300$ mm

PASS - Maximum bar spacing exceeds actual bar spacing for crack control

Deflection control - Section 7.4

Reference reinforcement ratio; $\rho_{m0} = (f_{ck} / 1\ N/mm^2)^{0.5} / 1000 = 0.00592$

Required tension reinforcement ratio; $\rho_m = A_{s,req} / (b \times d) = 0.00000$

Required compression reinforcement ratio; $\rho'_m = A_{s2,req} / (b \times d) = 0.00000$

Structural system factor - Table 7.4N; $K_b = 1.3$

Basic allowable span to depth ratio ; $span\_to\_depth_{basic} = K_b \times [11 + 1.5 \times (f_{ck} / 1\ N/mm^2)^{0.5} \times \rho_{m0} / \rho_m + 3.2 \times (f_{ck} / 1\ N/mm^2)^{0.5} \times (\rho_{m0} / \rho_m - 1)^{1.5}] = 21150798.947$

Reinforcement factor - exp.7.17; $K_s = \min(A_{s,prov} / A_{s,req} \times 500\ N/mm^2 / f_{yk}, 1.5) = 1.500$

Flange width factor; $F1 = 1 = 1.000$

Long span supporting brittle partition factor; $F2 = 1 = 1.000$

Allowable span to depth ratio; $span\_to\_depth_{allow} = \min(span\_to\_depth_{basic} \times K_s \times F1 \times F2, 40 \times K_b) = 52.000$

Actual span to depth ratio; $span\_to\_depth_{actual} = L_{m1\_s3} / d = 0.463$

PASS - Actual span to depth ratio is within the allowable limit

Minimum bar spacing (Section 8.2)

Top bar spacing; $s_{top} = (b - (2 \times (c_{nom\_s} + \phi_{m1\_s3\_z2\_v}) + \phi_{m1\_s3\_z2\_t\_L1} \times N_{m1\_s3\_z2\_t\_L1})) / (N_{m1\_s3\_z2\_t\_L1} - 1) = 182.0$ mm

Minimum allowable top bar spacing; $s_{top,min} = \max(\phi_{m1\_s3\_z2\_t\_L1} \times k_{s1}, h_{agg} + k_{s2}, 20mm) = 25.0$ mm

PASS - Actual bar spacing exceeds minimum allowable

Bottom bar spacing; $s_{bot} = (b - (2 \times (c_{nom\_s} + \phi_{m1\_s3\_z2\_v}) + \phi_{m1\_s3\_z2\_b\_L1} \times N_{m1\_s3\_z2\_b\_L1} + \phi_{m1\_s3\_z1\_b\_L1} \times N_{m1\_s3\_z1\_b\_L1})) / ((N_{m1\_s3\_z2\_b\_L1} + N_{m1\_s3\_z1\_b\_L1}) - 1) = 47.3$ mm

Minimum allowable bottom bar spacing; $s_{bot,min} = \max(\phi_{m1\_s3\_z2\_b\_L1} \times k_{s1}, h_{agg} + k_{s2}, 20mm) = 25.0$ mm

PASS - Actual bar spacing exceeds minimum allowable

Zone 3 (225 mm - 300 mm) Negative moment - section 6.1

Design bending moment; $M = \max(\beta_1 \times \text{abs}(M_{m1\_s3\_max\_red}), \text{abs}(M_{m1\_s3\_z3\_min\_red})) = 0.1$ kNm

Effective depth of tension reinforcement; $d = 647$ mm

Redistribution ratio; $\delta = \min(M_{neg\_red\_z3} / M_{neg\_z3}, 1) = 1.000$

$K = M / (b \times d^2 \times f_{ck}) = 0.000$

$K' = (2 \times \eta \times \alpha_{cc} / \gamma_C) \times (1 - \lambda \times (\delta - k_1) / (2 \times k_2)) \times (\lambda \times (\delta - k_1) / (2 \times k_2)) = 0.196$

K' > K - No compression reinforcement is required

Lever arm; $z = \min(0.5 \times d \times [1 + (1 - 2 \times K / (\eta \times \alpha_{cc} / \gamma_C))^{0.5}], 0.95 \times d) = 615$ mm

Depth of neutral axis; $x = 2 \times (d - z) / \lambda = 81$ mm

Area of tension reinforcement required; $A_{s,req} = M / (f_{yd} \times z) = 0$ mm^2

Tension reinforcement provided; $2 \times 20\phi$

Area of tension reinforcement provided; $A_{s,prov} = 628$ mm^2

Minimum area of reinforcement - exp.9.1N; $A_{s,min} = \max(0.26 \times f_{ctm} / f_{yk}, 0.0013) \times b \times d = 352$ mm^2

Maximum area of reinforcement - cl.9.2.1.1(3); $A_{s,max} = 0.04 \times b \times h = 8400$ mm^2

PASS - Area of reinforcement provided is greater than area of reinforcement required

Crack control - Section 7.3

Maximum crack width; $w_k = 0.3$ mm

Design value modulus of elasticity reinf – 3.2.7(4); $E_s = 200000$ N/mm^2

Mean value of concrete tensile strength; $f_{ct,eff} = f_{ctm} = 3.2$ N/mm^2

Stress distribution coefficient; $k_c = 0.4$

Non-uniform self-equilibrating stress coefficient; $k = \min(\max(1 + (300\text{ mm} - \min(h, b)) \times 0.35 / 500\text{ mm}, 0.65), 1) = 1.00$

Actual tension bar spacing; $s_{bar} = (b - (2 \times (c_{nom\_s} + \phi_{m1\_s3\_z3\_v}) + \phi_{m1\_s3\_z3\_t\_L1} \times N_{m1\_s3\_z3\_t\_L1})) / (N_{m1\_s3\_z3\_t\_L1} - 1) + \phi_{m1\_s3\_z3\_t\_L1} = 194$ mm

Maximum stress permitted - Table 7.3N; $\sigma_s = 245$ N/mm^2

Steel to concrete modulus of elast. ratio; $\alpha_{cr} = E_s / E_{cm} = 5.87$

Distance of the Elastic NA from bottom of beam; $y = (b \times h^2 / 2 + A_{s,prov} \times (\alpha_{cr} - 1) \times (h - d)) / (b \times h + A_{s,prov} \times (\alpha_{cr} - 1)) = 346$ mm

Area of concrete in the tensile zone; $A_{ct} = b \times y = 103721$ mm^2

Minimum area of reinforcement required - exp.7.1; $A_{sc,min} = k_c \times k \times f_{ct,eff} \times A_{ct} / \sigma_s = 544$ mm^2

PASS - Area of tension reinforcement provided exceeds minimum required for crack control

Quasi-permanent moment; $M_{QP} = \max(\beta_1 \times \text{abs}(M_{m1_s3_z2_pos_quasi}), \text{abs}(M_{m1_s3_z3_neg_quasi})) = 0.0$kNm

Permanent load ratio; $R_{PL} = M_{QP} / M = 0.69$

Service stress in reinforcement; $\sigma_{sr} = f_{yd} \times A_{s,req} / A_{s,prov} \times R_{PL} = 0$ N/mm^2

Maximum bar spacing - Tables 7.3N; $s_{bar,max} = 300$ mm

PASS - Maximum bar spacing exceeds actual bar spacing for crack control

Minimum bar spacing (Section 8.2)

Top bar spacing; $s_{top} = (b - (2 \times (c_{nom\_s} + \phi_{m1\_s3\_z3\_v}) + \phi_{m1\_s3\_z3\_t\_L1} \times N_{m1\_s3\_z3\_t\_L1})) / (N_{m1\_s3\_z3\_t\_L1} - 1) = 174.0$ mm

Minimum allowable top bar spacing; $s_{top,min} = \max(\phi_{m1\_s3\_z3\_t\_L1} \times k_{s1}, h_{agg} + k_{s2}, 20mm) = 25.0$ mm

PASS - Actual bar spacing exceeds minimum allowable

Bottom bar spacing; $s_{bot} = (b - (2 \times (c_{nom\_s} + \phi_{m1\_s3\_z3\_v}) + \phi_{m1\_s3\_z3\_b\_L1} \times N_{m1\_s3\_z3\_b\_L1})) / (N_{m1\_s3\_z3\_b\_L1} - 1) = 182.0$ mm

Minimum allowable bottom bar spacing; $s_{bot,min} = \max(\phi_{m1\_s3\_z3\_b\_L1} \times k_{s1}, h_{agg} + k_{s2}, 20mm) = 25.0$ mm

PASS - Actual bar spacing exceeds minimum allowable

Shear design

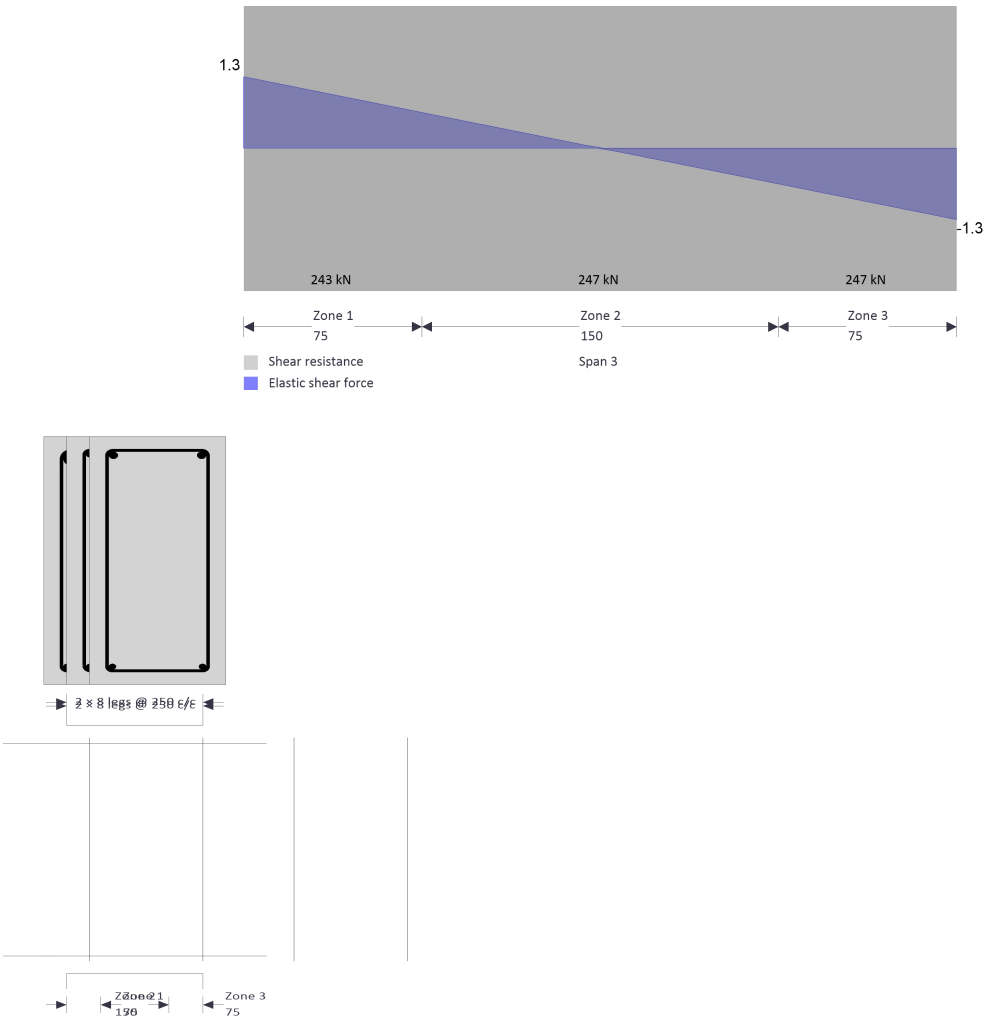

Angle of comp. shear strut for maximum shear; $\theta_{max} = 45$ deg

Strength reduction factor - cl.6.2.3(3); $v_1 = 0.6 \times (1 - f_{ck} / 250\ N/mm^2) = 0.516$

Compression chord coefficient - cl.6.2.3(3); $\alpha_{cw} = 1.00$

Minimum area of shear reinforcement - exp.9.5N; $A_{sv,min} = 0.08\ N/mm^2 \times b \times (f_{ck} / 1\ N/mm^2)^{0.5} / f_{yk} = 309\ mm^2/m$

Zone 1 (0 mm - 75 mm) shear - section 6.2

Design shear force at support ; $V_{Ed,max} = \max(abs(V_{z1\_max}), abs(V_{z1\_red\_max})) = 1$ kN

Min lever arm in shear zone; $z = 605$ mm

Maximum design shear resistance - exp.6.9; $V_{Rd,max} = \alpha_{cw} \times b \times z \times v_1 \times f_{cwd} / (\cot(\theta_{max}) + \tan(\theta_{max})) = 1093$ kN

PASS - Design shear force at support is less than maximum design shear resistance

Design shear force at support; $V_{Ed} = 1$ kN

Design shear stress; $v_{Ed} = V_{Ed} / (b \times z) = 0.007\ N/mm^2$

Angle of concrete compression strut - cl.6.2.3; $\theta = \min(\max(0.5 \times \text{Asin}(\min(2 \times v_{Ed} / (\alpha_{cw} \times f_{cwd} \times v_1),1)), 21.8\ deg), 45deg) = 21.8$ deg

Area of shear reinforcement required - exp.6.8; $A_{sv,des} = v_{Ed} \times b / (f_{yd} \times \cot(\theta)) = 2\ mm^2/m$

Area of shear reinforcement required; $A_{sv,req} = \max(A_{sv,min}, A_{sv,des}) = 309\ mm^2/m$

Shear reinforcement provided; 2 × 8 legs @ 250 c/c

Area of shear reinforcement provided; $A_{sv,prov} = 402\ mm^2/m$

PASS - Area of shear reinforcement provided exceeds minimum required

Maximum longitudinal spacing - exp.9.6N; $s_{vl,max} = 0.75 \times d = 478$ mm

PASS - Longitudinal spacing of shear reinforcement provided is less than maximum

Zone 2 (75 mm - 225 mm) shear - section 6.2

Design shear force at support ; $V_{Ed,max} = \max(abs(V_{z2\_max}), abs(V_{z2\_red\_max})) = 1$ kN

Min lever arm in shear zone; z = 615 mm

Maximum design shear resistance - exp.6.9; $V_{Rd,max} = \alpha_{cw} \times b \times z \times v_1 \times f_{cwd} / (\cot(\theta_{max}) + \tan(\theta_{max})) = 1111$ kN

PASS - Design shear force at support is less than maximum design shear resistance

Design shear force within zone; $V_{Ed} = 1$ kN

Design shear stress; $v_{Ed} = V_{Ed} / (b \times z) = 0.003$ N/mm^2

Angle of concrete compression strut - cl.6.2.3; $\theta = \min(\max(0.5 \times \text{Asin}(\min(2 \times v_{Ed} / (\alpha_{cw} \times f_{cwd} \times v_1),1)), 21.8 \text{ deg}), 45\text{deg}) = 21.8$ deg

Area of shear reinforcement required - exp.6.8; $A_{sv,des} = v_{Ed} \times b / (f_{yd} \times \cot(\theta)) = 1$ mm^2/m

Area of shear reinforcement required; $A_{sv,req} = \max(A_{sv,min}, A_{sv,des}) = 309$ mm^2/m

Shear reinforcement provided; 2 × 8 legs @ 250 c/c

Area of shear reinforcement provided; $A_{sv,prov} = 402$ mm^2/m

PASS - Area of shear reinforcement provided exceeds minimum required

Maximum longitudinal spacing - exp.9.6N; $s_{vl,max} = 0.75 \times d = 486$ mm

PASS - Longitudinal spacing of shear reinforcement provided is less than maximum

Zone 3 (225 mm - 300 mm) shear - section 6.2

Design shear force at support ; $V_{Ed,max} = \max(\text{abs}(V_{z3\_max}), \text{abs}(V_{z3\_red\_max})) = 1$ kN

Min lever arm in shear zone; z = 615 mm

Maximum design shear resistance - exp.6.9; $V_{Rd,max} = \alpha_{cw} \times b \times z \times v_1 \times f_{cwd} / (\cot(\theta_{max}) + \tan(\theta_{max})) = 1110$ kN

PASS - Design shear force at support is less than maximum design shear resistance

Design shear force at support;$V_{Ed} = 1$ kN

Design shear stress; $v_{Ed} = V_{Ed} / (b \times z) = 0.007$ N/mm^2

Angle of concrete compression strut - cl.6.2.3; $\theta = \min(\max(0.5 \times \text{Asin}(\min(2 \times v_{Ed} / (\alpha_{cw} \times f_{cwd} \times v_1),1)), 21.8 \text{ deg}), 45\text{deg}) = 21.8$ deg

Area of shear reinforcement required - exp.6.8; $A_{sv,des} = v_{Ed} \times b / (f_{yd} \times \cot(\theta)) = 2$ mm^2/m

Area of shear reinforcement required; $A_{sv,req} = \max(A_{sv,min}, A_{sv,des}) = 309$ mm^2/m

Shear reinforcement provided; 2 × 8 legs @ 250 c/c

Area of shear reinforcement provided; $A_{sv,prov} = 402$ mm^2/m

PASS - Area of shear reinforcement provided exceeds minimum required

Maximum longitudinal spacing - exp.9.6N; $s_{vl,max} = 0.75 \times d = 485$ mm

PASS - Longitudinal spacing of shear reinforcement provided is less than maximum

APPENDIX I

COMPOSITE GIRDER INCREMENT RESULTS FROM ABAQUS

The following images are the increment results from Abaqus for the Composite Girder analysis.

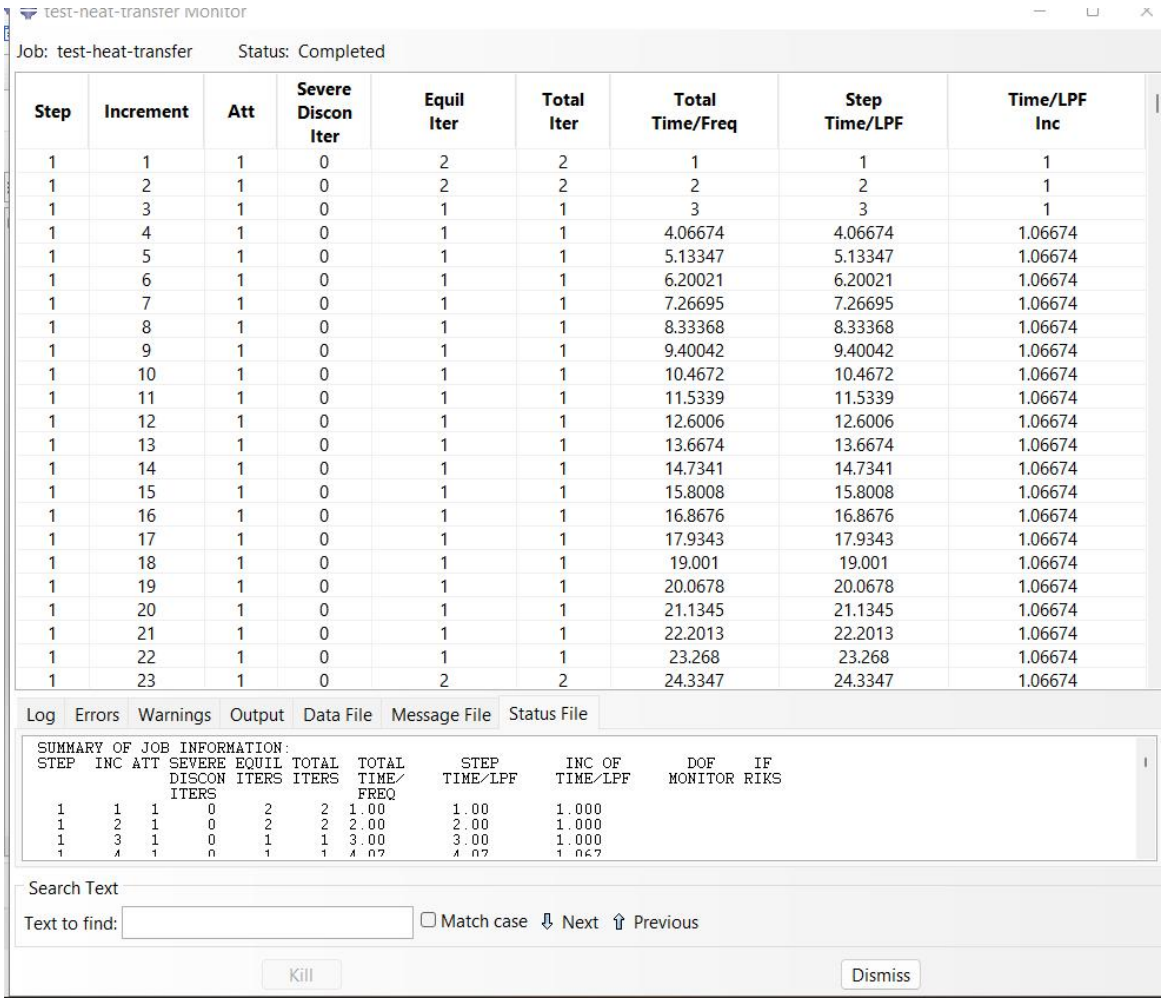
test-heat-transfer Monitor

Job: test-heat-transfer Status: Completed

Step	Increment	Att	Severe Discon Iter	Equil Iter	Total Iter	Total Time/Freq	Step Time/LPF	Time/LPF Inc
1	1	1	0	2	2	1	1	1
1	2	1	0	2	2	2	2	1
1	3	1	0	1	1	3	3	1
1	4	1	0	1	1	4.06674	4.06674	1.06674
1	5	1	0	1	1	5.13347	5.13347	1.06674
1	6	1	0	1	1	6.20021	6.20021	1.06674
1	7	1	0	1	1	7.26695	7.26695	1.06674
1	8	1	0	1	1	8.33368	8.33368	1.06674
1	9	1	0	1	1	9.40042	9.40042	1.06674
1	10	1	0	1	1	10.4672	10.4672	1.06674
1	11	1	0	1	1	11.5339	11.5339	1.06674
1	12	1	0	1	1	12.6006	12.6006	1.06674
1	13	1	0	1	1	13.6674	13.6674	1.06674
1	14	1	0	1	1	14.7341	14.7341	1.06674
1	15	1	0	1	1	15.8008	15.8008	1.06674
1	16	1	0	1	1	16.8676	16.8676	1.06674
1	17	1	0	1	1	17.9343	17.9343	1.06674
1	18	1	0	1	1	19.001	19.001	1.06674
1	19	1	0	1	1	20.0678	20.0678	1.06674
1	20	1	0	1	1	21.1345	21.1345	1.06674
1	21	1	0	1	1	22.2013	22.2013	1.06674
1	22	1	0	1	1	23.268	23.268	1.06674
1	23	1	0	2	2	24.3347	24.3347	1.06674

Log Errors Warnings Output Data File Message File Status File

```
SUMMARY OF JOB INFORMATION:
STEP   INC ATT SEVERE EQUIL TOTAL  TOTAL      STEP       INC OF      DOF    IF
                DISCON ITERS ITERS  TIME/     TIME/LPF   TIME/LPF    MONITOR RIKS
                ITERS               FREQ
  1     1   1      0     2     2  1.00        1.00       1.000
  1     2   1      0     2     2  2.00        2.00       1.000
  1     3   1      0     1     1  3.00        3.00       1.000
  1     4   1      0     1     1  4.07        4.07       1.067
```

Search Text

Text to find: Match case Next Previous

Kill Dismiss

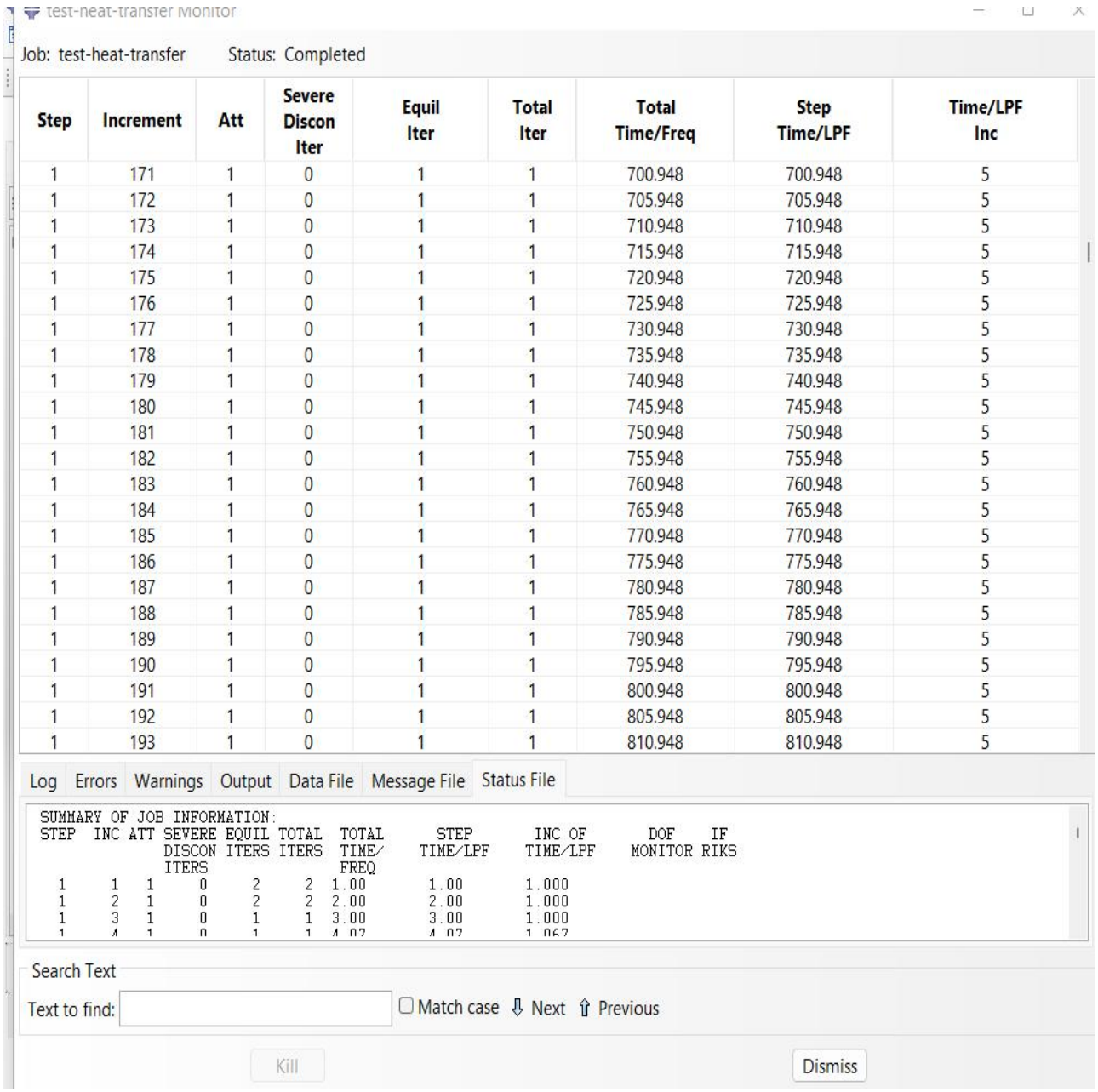

Step	Increment	Att	Severe Discon Iter	Equil Iter	Total Iter	Total Time/Freq	Step Time/LPF	Time/LPF Inc
1	171	1	0	1	1	700.948	700.948	5
1	172	1	0	1	1	705.948	705.948	5
1	173	1	0	1	1	710.948	710.948	5
1	174	1	0	1	1	715.948	715.948	5
1	175	1	0	1	1	720.948	720.948	5
1	176	1	0	1	1	725.948	725.948	5
1	177	1	0	1	1	730.948	730.948	5
1	178	1	0	1	1	735.948	735.948	5
1	179	1	0	1	1	740.948	740.948	5
1	180	1	0	1	1	745.948	745.948	5
1	181	1	0	1	1	750.948	750.948	5
1	182	1	0	1	1	755.948	755.948	5
1	183	1	0	1	1	760.948	760.948	5
1	184	1	0	1	1	765.948	765.948	5
1	185	1	0	1	1	770.948	770.948	5
1	186	1	0	1	1	775.948	775.948	5
1	187	1	0	1	1	780.948	780.948	5
1	188	1	0	1	1	785.948	785.948	5
1	189	1	0	1	1	790.948	790.948	5
1	190	1	0	1	1	795.948	795.948	5
1	191	1	0	1	1	800.948	800.948	5
1	192	1	0	1	1	805.948	805.948	5
1	193	1	0	1	1	810.948	810.948	5

STEP	INC	ATT	SEVERE DISCON ITERS	EQUIL ITERS	TOTAL ITERS	TOTAL TIME/ FREQ	STEP TIME/LPF	INC OF TIME/LPF	DOF MONITOR	IF RIKS
1	1	1	0	2	2	1.00	1.00	1.000		
1	2	1	0	2	2	2.00	2.00	1.000		
1	3	1	0	1	1	3.00	3.00	1.000		
1	4	1	0	1	1	4.07	4.07	1.062		

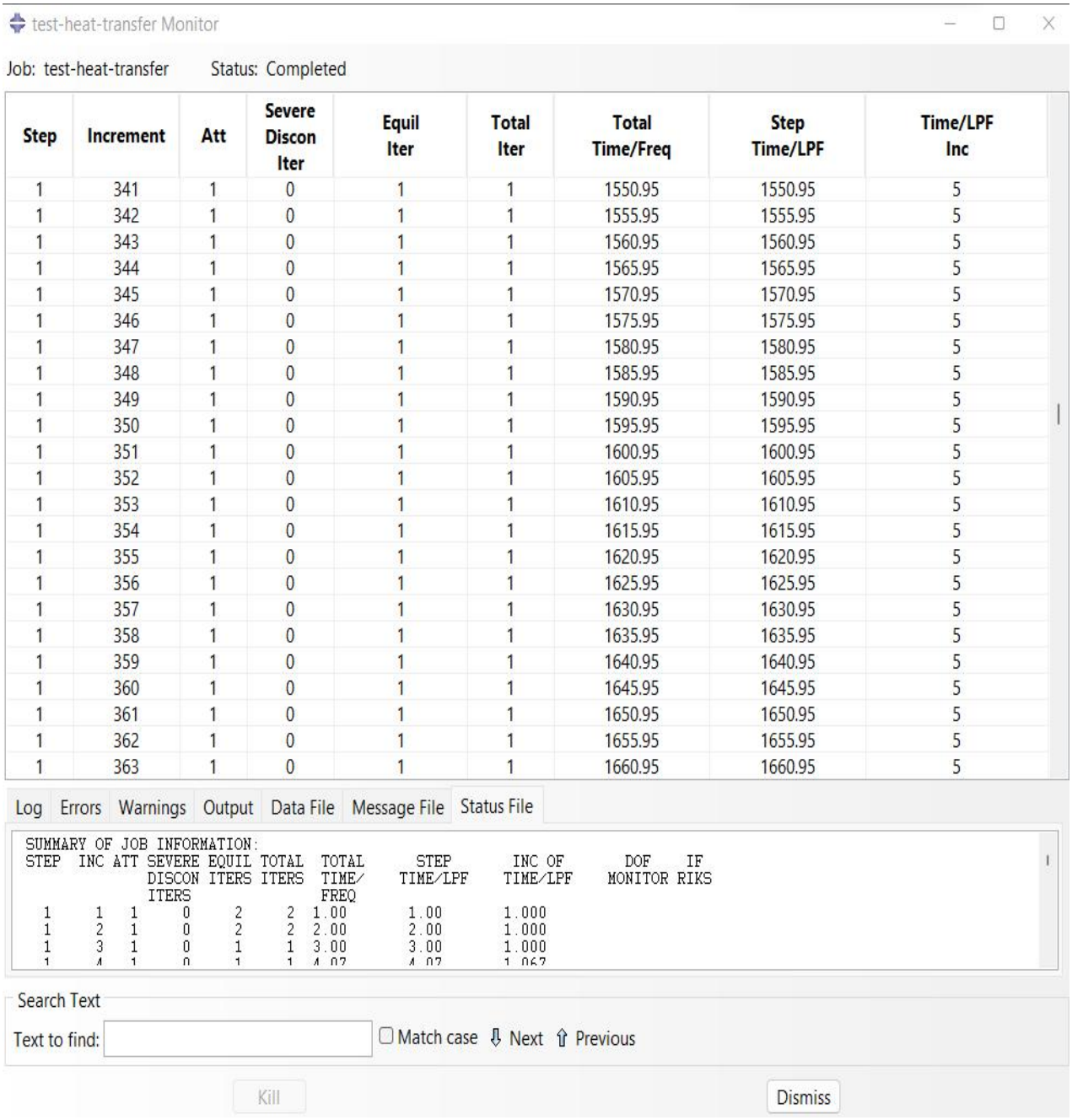

Step	Increment	Att	Severe Discon Iter	Equil Iter	Total Iter	Total Time/Freq	Step Time/LPF	Time/LPF Inc
1	341	1	0	1	1	1550.95	1550.95	5
1	342	1	0	1	1	1555.95	1555.95	5
1	343	1	0	1	1	1560.95	1560.95	5
1	344	1	0	1	1	1565.95	1565.95	5
1	345	1	0	1	1	1570.95	1570.95	5
1	346	1	0	1	1	1575.95	1575.95	5
1	347	1	0	1	1	1580.95	1580.95	5
1	348	1	0	1	1	1585.95	1585.95	5
1	349	1	0	1	1	1590.95	1590.95	5
1	350	1	0	1	1	1595.95	1595.95	5
1	351	1	0	1	1	1600.95	1600.95	5
1	352	1	0	1	1	1605.95	1605.95	5
1	353	1	0	1	1	1610.95	1610.95	5
1	354	1	0	1	1	1615.95	1615.95	5
1	355	1	0	1	1	1620.95	1620.95	5
1	356	1	0	1	1	1625.95	1625.95	5
1	357	1	0	1	1	1630.95	1630.95	5
1	358	1	0	1	1	1635.95	1635.95	5
1	359	1	0	1	1	1640.95	1640.95	5
1	360	1	0	1	1	1645.95	1645.95	5
1	361	1	0	1	1	1650.95	1650.95	5
1	362	1	0	1	1	1655.95	1655.95	5
1	363	1	0	1	1	1660.95	1660.95	5

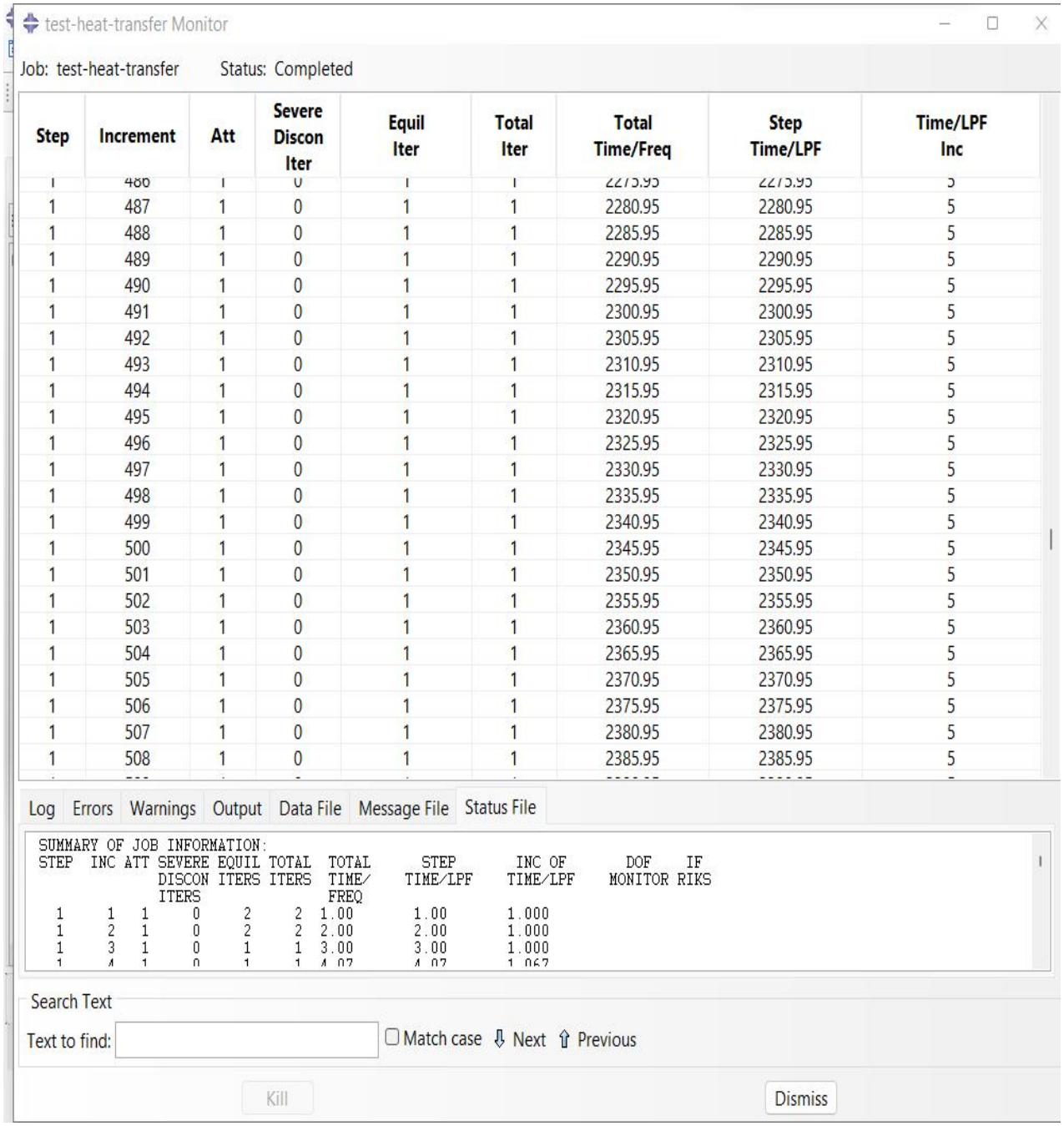
test-heat-transfer Monitor
Job: test-heat-transfer
Status: Completed
Step
Increment
Att
Severe Discon Iter
Equil Iter
Total Iter
Total Time/Freq
Step Time/LPF
Time/LPF Inc
1 487 1 0 1 1 2280.95 2280.95 5
1 488 1 0 1 1 2285.95 2285.95 5
1 489 1 0 1 1 2290.95 2290.95 5
1 490 1 0 1 1 2295.95 2295.95 5
1 491 1 0 1 1 2300.95 2300.95 5
1 492 1 0 1 1 2305.95 2305.95 5
1 493 1 0 1 1 2310.95 2310.95 5
1 494 1 0 1 1 2315.95 2315.95 5
1 495 1 0 1 1 2320.95 2320.95 5
1 496 1 0 1 1 2325.95 2325.95 5
1 497 1 0 1 1 2330.95 2330.95 5
1 498 1 0 1 1 2335.95 2335.95 5
1 499 1 0 1 1 2340.95 2340.95 5
1 500 1 0 1 1 2345.95 2345.95 5
1 501 1 0 1 1 2350.95 2350.95 5
1 502 1 0 1 1 2355.95 2355.95 5
1 503 1 0 1 1 2360.95 2360.95 5
1 504 1 0 1 1 2365.95 2365.95 5
1 505 1 0 1 1 2370.95 2370.95 5
1 506 1 0 1 1 2375.95 2375.95 5
1 507 1 0 1 1 2380.95 2380.95 5
1 508 1 0 1 1 2385.95 2385.95 5
Log
Errors
Warnings
Output
Data File
Message File
Status File
SUMMARY OF JOB INFORMATION:
STEP INC ATT SEVERE DISCON ITERS EQUIL ITERS TOTAL ITERS TOTAL TIME/ FREQ STEP TIME/LPF INC OF TIME/LPF DOF MONITOR IF RIKS
1 1 1 0 2 2 1.00 1.00 1.000
1 2 1 0 2 2 2.00 2.00 1.000
1 3 1 0 1 1 3.00 3.00 1.000
Search Text
Text to find:
Match case
Next
Previous
Kill
Dismiss

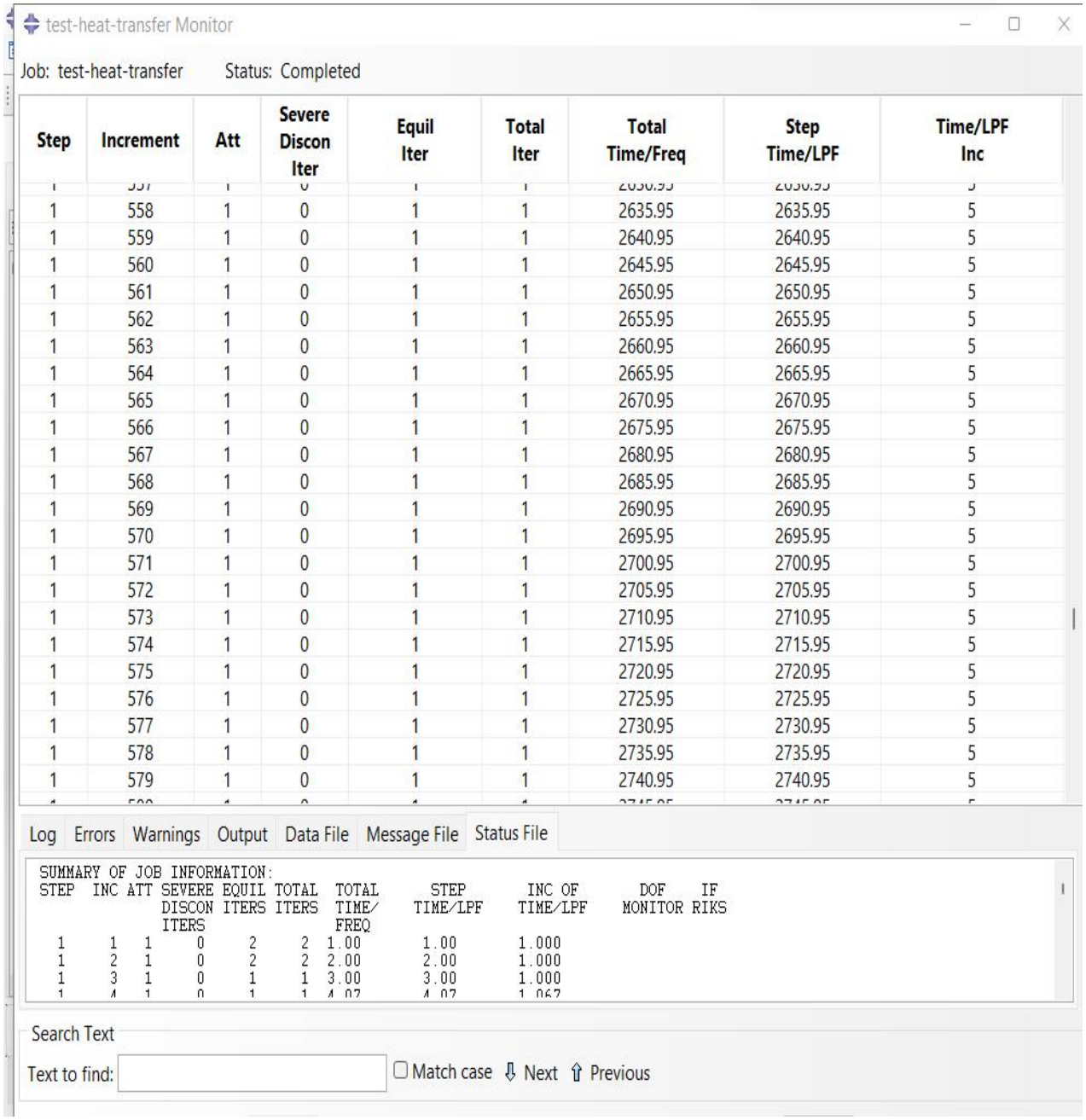
test-heat-transfer Monitor
Job: test-heat-transfer Status: Completed
Step | Increment | Att | Severe Discon Iter | Equil Iter | Total Iter | Total Time/Freq | Step Time/LPF | Time/LPF Inc
1 558 1 0 1 1 2635.95 2635.95 5
1 559 1 0 1 1 2640.95 2640.95 5
1 560 1 0 1 1 2645.95 2645.95 5
1 561 1 0 1 1 2650.95 2650.95 5
1 562 1 0 1 1 2655.95 2655.95 5
1 563 1 0 1 1 2660.95 2660.95 5
1 564 1 0 1 1 2665.95 2665.95 5
1 565 1 0 1 1 2670.95 2670.95 5
1 566 1 0 1 1 2675.95 2675.95 5
1 567 1 0 1 1 2680.95 2680.95 5
1 568 1 0 1 1 2685.95 2685.95 5
1 569 1 0 1 1 2690.95 2690.95 5
1 570 1 0 1 1 2695.95 2695.95 5
1 571 1 0 1 1 2700.95 2700.95 5
1 572 1 0 1 1 2705.95 2705.95 5
1 573 1 0 1 1 2710.95 2710.95 5
1 574 1 0 1 1 2715.95 2715.95 5
1 575 1 0 1 1 2720.95 2720.95 5
1 576 1 0 1 1 2725.95 2725.95 5
1 577 1 0 1 1 2730.95 2730.95 5
1 578 1 0 1 1 2735.95 2735.95 5
1 579 1 0 1 1 2740.95 2740.95 5
Log Errors Warnings Output Data File Message File Status File
SUMMARY OF JOB INFORMATION:
STEP INC ATT SEVERE DISCON ITERS EQUIL ITERS TOTAL ITERS TOTAL TIME/FREQ STEP TIME/LPF INC OF TIME/LPF DOF MONITOR IF RIKS
1 1 1 0 2 2 1.00 1.00 1.000
1 2 1 0 2 2 2.00 2.00 1.000
1 3 1 0 1 1 3.00 3.00 1.000
Search Text
Text to find:
Match case
Next
Previous

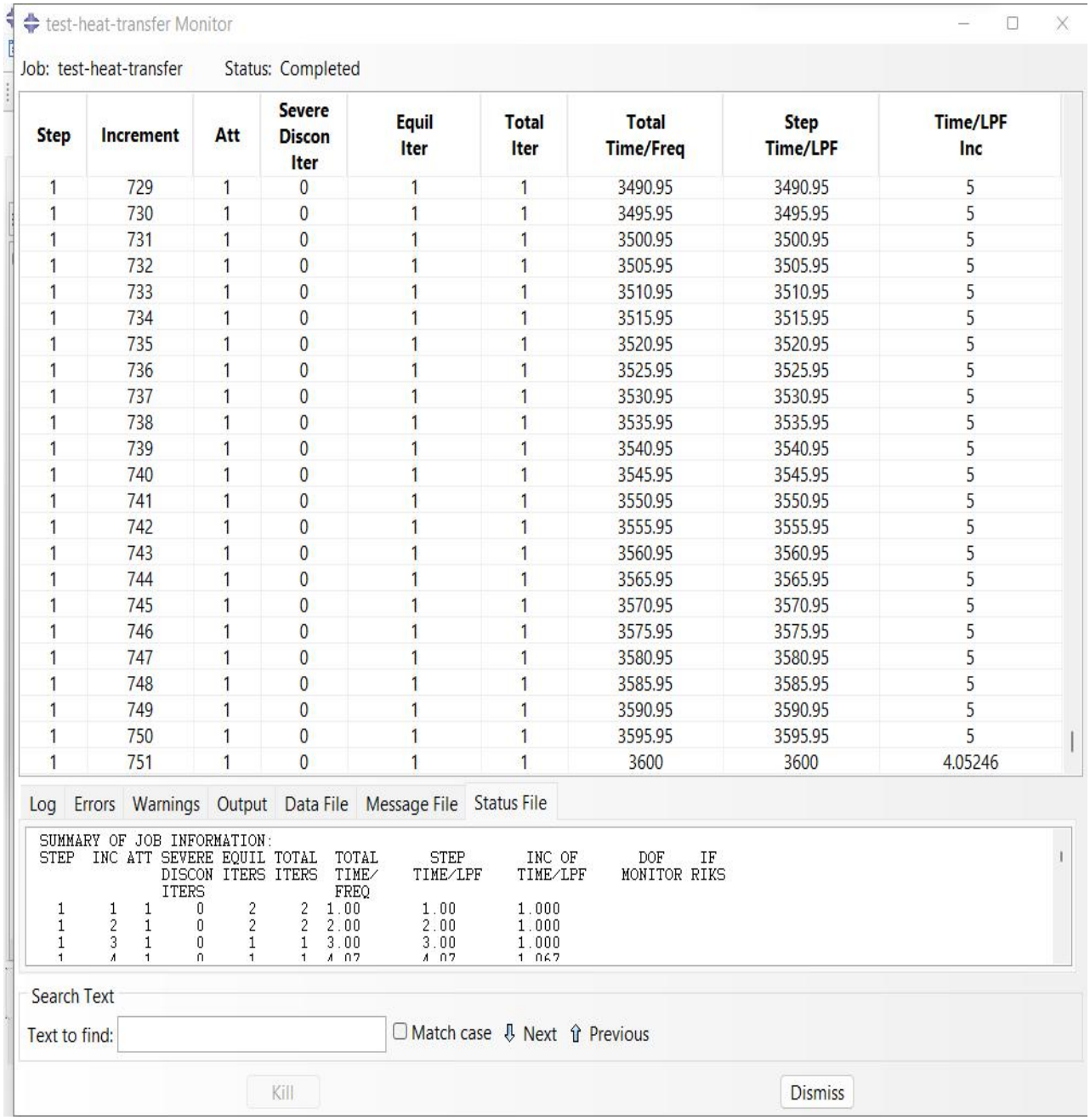

Step	Increment	Att	Severe Discon Iter	Equil Iter	Total Iter	Total Time/Freq	Step Time/LPF	Time/LPF Inc
1	729	1	0	1	1	3490.95	3490.95	5
1	730	1	0	1	1	3495.95	3495.95	5
1	731	1	0	1	1	3500.95	3500.95	5
1	732	1	0	1	1	3505.95	3505.95	5
1	733	1	0	1	1	3510.95	3510.95	5
1	734	1	0	1	1	3515.95	3515.95	5
1	735	1	0	1	1	3520.95	3520.95	5
1	736	1	0	1	1	3525.95	3525.95	5
1	737	1	0	1	1	3530.95	3530.95	5
1	738	1	0	1	1	3535.95	3535.95	5
1	739	1	0	1	1	3540.95	3540.95	5
1	740	1	0	1	1	3545.95	3545.95	5
1	741	1	0	1	1	3550.95	3550.95	5
1	742	1	0	1	1	3555.95	3555.95	5
1	743	1	0	1	1	3560.95	3560.95	5
1	744	1	0	1	1	3565.95	3565.95	5
1	745	1	0	1	1	3570.95	3570.95	5
1	746	1	0	1	1	3575.95	3575.95	5
1	747	1	0	1	1	3580.95	3580.95	5
1	748	1	0	1	1	3585.95	3585.95	5
1	749	1	0	1	1	3590.95	3590.95	5
1	750	1	0	1	1	3595.95	3595.95	5
1	751	1	0	1	1	3600	3600	4.05246